An Investigation of High Performance Metal- Metal Oxide Multilayer Structure for Optoelectronic Applications

This thesis is submitted as a partial fulfillment of the Ph.D. program in Physics

by

VIKAS SHARMA

(ID No. 2011RPH7113)

Department of Physics

MALAVIYA NATIONAL INSTITUTE OF TECHNOLOGY JAIPUR

May 2017

Malaviya National Institute of Technology Jaipur

2017

All Rights Reserved

Dedicated to My Family

Supervisor's Certificate

This is to certify that the thesis titled "An Investigation of High Performance Metal- Metal Oxide Multilayer Structure for Optoelectronic Applications" describes the original research work carried out by Mr. Vikas Sharma (ID No. 2011RPH7113) for the award of the degree of Doctor of Philosophy (Physics) in Malaviya National Institute of Technology Jaipur (India). This work was done by him during the period December 2011 to December 2016 under my supervision.

(Dr. K. Sachdev)
Associate Professor
Department of Physics
MNIT Jaipur (India)

Acknowledgement

"A journey is easier and more memorable when travelled together". These many years have taught me that interdependence is more valuable than independence. In this research work, I have been accompanied and supported by many people. It is a pleasant aspect that I have now an opportunity to express my gratitude for all of them.

First of all, I would like to thank almighty, by whose grace I could achieve this destination.

With the deepest sense of gratitude, I would like to thank my research supervisor, Dr. K. Sachdev, Department of Physics, MNIT Jaipur for her inspiring guidance and encouraging demeanor. Her everlasting enthusiasm, generous support and spiritual dedication towards the work, extending well beyond the office hours, inspired me in all the stages of my research work.

I am greatly indebted to Dr. K Asokan, IUAC, New Delhi, who provided me an opportunity to join his research group, and gave access to the laboratory/ research facilities. His unfailing support and continuous encouragement throughout the research process and during writing thesis made this work accomplishable.

I thank the present and former Heads of Department of Physics, for providing the administrative support and necessary facilities in the Department for accomplishment of my research work. I also thank the faculty members of Department and DREC members with whom I had an opportunity to discuss academics at various stages of my work. I would like to express a deep sense of gratitude to Prof. M.K. Banerjee for his active interest and concern always.

I am indebted to Dr. D. Kanjilal, Director, Inter University Accelerator Centre (IUAC), New Delhi for giving me the opportunity of doing the research work at the center.

I am highly thankful to Dr. R. Singh, Wide Band Gap Semiconductor Lab, IITD for providing experimental facility and useful discussions.

I would like to express my gratefulness to Dr. V. K. Khanna CEERI Pilani and Dr. V. Manjula, BITS, Pilani for providing me motivation and precious blessings.

I am thankful to Dr. Rishi Vyas, Jaipur and Dr. Parmod Kumar, New Delhi for the stimulating discussions, for the sleepless nights of work together before the deadlines, and for all the fun we have had in the last five years.

I also convey my sincere thanks to scientific and technical staff of Materials Research Centre and other non-teaching staff members of Department of Physics and Materials Research Center for their help at various stages of my work.

I acknowledge the support provided my colleagues, Mr. Satyavir Singh, Ms Yogita Kumari, Mr Himanshu Sharma, Mr Rajesh Kumar, Ms Parul Gupta, Ms Surbhi, other lab mates and project students for moral support and for sharing all my good and bad moments in the whole duration of my research work. I am thankful to my friends pursuing research in institutions: IUAC, BITS and IIT Delhi for their useful discussions and support.

I would like to express thanks to alumni of MSc physics of MNIT and all research scholars of MNIT for their kind support, love, care and constant encouragement.

The acknowledgement would remain incomplete without mention of my family members for their faith, kind support, love, patience and constant encouragement which made it possible to reach my goal.

The errors, idiocies and inconsistencies remain my own.

May 2017 Vikas Sharma

List of abbreviation

AFM	Atomic Force Microscopy
EDS	Electron Dispersive Spectroscopy
RBS	Rutherford Back Scattering
SAED	Selective area electron diffraction
SEM	Scanning Electron Microscopy
SHI	Swift Heavy Ion
SnO_2	Tin Oxide
TCE	Transparent Conducting Electrode
TCO	Transparent Conducting Oxide
TEM	Transmission Electron Microscopy
UV-Vis	Ultra Violet- Visible
XAS	X-ray Absorption Spectroscopy
XES	X-ray Emission Spectroscopy
XPS	X-ray Photoelectron Spectroscopy
XRD	X-ray Diffraction
ZnO	Zinc Oxide

Abstract of the thesis

In the present investigation, Dielectric-Metal- Dielectric (DMD) structure viz $SnO_x/Au/SnO_x$, $SnO_2/Ag/SnO_2$ and ZnO/Ag/ZnO are explored for their TCO applications. The present research work discusses the optimization of growth parameters for room temperature fabrication of stacked multilayered structure of typical thickness less than 100 nm exhibiting better or similar electrical conductivity and optical transparency in visible spectrum as compared to ITO substrates. The average transparency of these specimen is about 70%-80% with sheet resistance values in the range of 10-50 Ω/sq.

The individual layer thickness (verified by fitting of RBS spectra) in these stacked multilayered structure is varied to obtain better optoelectronic properties attributed to DMD structures: SnO_x (35 nm)/Au (5 nm)/SnO_x (35 nm), SnO_2 (40 nm)/Ag (9 nm)/SnO_2 (40 nm) and ZnO (40 nm)/Ag (9 nm)/ZnO (40 nm) among all fabricated DMD structures. Workability of these samples at low temperatures is also verified from low temperature Hall measurement which shows electrical stability in the temperature range 80K -350 K.

These structures are further explored for optoelectronic property modification by exposure to gamma radiation, low energy ions (Xe-100 keV) and swift heavy ion (100 MeV O^{7+} or 100 MeV Ag^{7+}) irradiation. The gamma radiation is concluded to deteriorate the transparency of these stacked multilayers. Variation of optical and electrical properties of the samples has been observed by irradiation of low energy and swift heavy ions. This suggests that it is possible to tune these properties which pertain to use of these multilayers as TCO in optoelectronic devices. The irradiated films are also shown to possess electrical stability as evident from low temperature Hall measurement in the temperature range 80K -350 K. Chemical study of the layers in the DMD structure by X-ray photoelectron spectroscopy shows diffusion of the middle metal layer in the metal oxide layers as a result of irradiation controlled by fluence of these energetic ions.

Contents

Supervisor's certificate VI

Acknowledgement VII

List of abbreviation IX

Abstract of the thesis XI

Contents XIII

List of Figures XIX

List of Tables XXIV

Chapter-1 Introduction 1-12

1.1. Introduction 1

1.2. Criteria for Transparent Conducting Oxides 2

1.3. Applications of TCOs 4

1.4. Types of TCO 4

1.5. Alternatives to ITO 5

1.6. Multilayer Transparent Conducting Oxide 6

1.7. Objective of the Thesis 10

Chapter-2 Literature Review 13-26

2.1. Introduction 13

2.2. Historical Development of Transparent Conducting Oxide 13

2.3. Methods and Materials for Transparent Conducting Electrode 15

2.4. Multilayer TCO as Transparent Conducting Electrode 16

2.5. SnO_2 and ZnO as Transparent Conducting Oxide 17

2.6. Effect of Post-Deposition Treatment on TCOs 19

2.7. Modification of Layered Structure by Post Deposition Treatment: Implantation 21

2.8. Modification of Layered Structure by Post Deposition Treatment: Swift Heavy Ion Irradiation 23

Chapter-3 Materials, Methods and Characterization Techniques **27-42**
3.1 Introduction to the TCO Materials 27
3.1.1 Tin Oxide (SnO_2) 28
3.1.2 Zinc Oxide (ZnO) 28
3.1.3 Silver 28
3.1.4 Gold 29
3.2 Methods of Preparation of TCO 30
3.2.1 RF-DC Sputtering 30
3.2.2 E-beam/ Thermal Evaporation 30
3.3 Post Treatment Methods 31
3.3.1 Swift Heavy Ions Irradiation 31
3.3.1.1 Pelletron Accelerator 32
3.3.1.2 Material Science Beam Line 33
3.3.2 Low Energy Ion Implantation 34
3.3.3 Gamma Irradiation 35
3.4 Characterization Techniques 35
3.4.1 X-ray Diffraction (XRD) 35
3.4.2 Rutherford Backscattering Spectrometry (RBS) 36
3.4.3 X-ray Photoelectron Spectroscopy (XPS) 36
3.4.4 Atomic Force Microscopy (AFM) 37
3.4.5 Field Emission Scanning Electron Microscopy (FESEM) 38
3.4.6 Transmission Electron Microscopy (TEM) with EDS 39
3.4.7 UV–Vis Spectroscopy 41
3.4.8 Hall Measurement 41

Chapter-4 Fabrication and Characterization of SnO_2-Ag-SnO_2 Multilayer Thin Films and Their Ion Beam Effects **43-73**
4.1 Introduction 43
4.2 Experimental Study 43
4.3 Results and Discussion 45
4.3.1 X-Ray Diffraction 45
4.3.2 Rutherford Back Scattering 46
4.3.3 Scanning Electron Microscope 46
4.3.4 Atomic Force Microscope 47

4.3.5 Transmission Electron Microscope 49
4.3.6 UV-Vis Spectroscopic Study 50
4.3.7 Hall Measurements 52
4.4 Xe^{+} Ion-Beam (100keV) Effect on SnO_2-Ag-SnO_2 Thin Films 53
4.5 Results and Discussion 54
4.5.1 X-ray Diffraction 54
4.5.2 Rutherford Back Scattering 54
4.5.3 X-ray Photoelectron Spectroscopy 55
4.5.4 Scanning Electron Microscope 57
4.5.5 Atomic Force Microscope 58
4.5.6 UV-Vis Spectroscopic Study 60
4.5.7 Hall Measurements 62
4.6 O^{7+} Ion-Beam (100MeV) Effect on SnO_2-Ag-SnO_2 Thin Films 64
4.7 Results and Discussion 64
4.7.1 X-ray Diffraction 64
4.7.2 Rutherford Back Scattering 65
4.7.3 Raman Spectroscopy 66
4.7.4 SEM and AFM Studies 66
4.7.5 UV-Vis Spectroscopic Study 68
4.7.6 Hall Measurements 70
4.8 Conclusion 71

Chapter-5 Fabrication and Characterization of SnO_x-Au-SnO_x Multilayer Thin Films and Their Irradiation Effects **73-108**
5.1 Introduction 73
5.2 Experimental Details 73
5.3 Investigations on SnO_x/Au/SnO_x 75
5.3.1 X-ray Diffraction Study 75
5.3.2 Morphological Studies 77
5.3.3 XAS and XES Studies 78
5.3.4 Rutherford Back Scattering 81
5.3.5 UV-Vis and Raman Spectroscopy 82
5.3.6 Low-Temperature Hall Study 84

5.4 Irradiation Studies of Multilayered $SnO_x/Au/SnO_x$ TCO Thin Films for 100 MeV O^{7+} Ion Irradiation 87
5.4.1 Introduction 87
5.5 Results and Discussion 87
5.5.1 X-ray Diffraction Study 87
5.5.2 RBS Study 88
5.5.3 Morphological Studies 90
5.5.4 UV-Vis and Raman Study 91
5.5.5 Low Temperature Hall Studies 93
5.5.6 XPS Study 95
5.6 Gamma Irradiation Study of Stacked Multi-Layered $SnO_x/Au/SnO_x$ Thin Films 100
5.6.1 Introduction 100
5.7 Results and Discussion 100
5.7.1 X-ray Diffraction Study 100
5.7.2 AFM Study 101
5.7.3 UV-Vis Study 102
5.7.4 RBS Study 103
5.7.5 XPS Study 104
5.7.6 Hall Studies 105
5.8 Conclusion 107

Chapter-6 Fabrication and Characterization of ZnO-Ag-ZnO Multilayer Thin Films and Their Ion Beam Effects **109-152**
6.1 Introduction 109
6.2 Experimental Study 110
6.3 Results and Discussion 111
6.3.1 X-ray Diffraction 111
6.3.2 Rutherford Back Scattering 113
6.3.3 Scanning Electron Microscope 113
6.3.4 Atomic Force Microscope 115
6.3.5 Transmission Electron Microscope 116
6.3.6 UV-Vis Spectroscopic Study 117
6.3.7 Hall Measurements 119

6.4 Xe^{+} Ion-Beam (100keV) Effect on ZnO-Ag-ZnO Thin Films 121
6.5 Results and Discussion 122
6.5.1 X-ray Diffraction 122
6.5.2 Rutherford Back Scattering 123
6.5.3 X-ray Photoelectron Spectroscopy 124
6.5.4 Scanning Electron Microscope 127
6.5.5 Atomic Force Microscope 129
6.5.6 Transmission Electron Microscope 130
6.5.7 UV-Vis Spectroscopic Study 130
6.5.8 Hall Measurements 133
6.6 Ag^{7+} Ion-Beam (100MeV) Effect on ZnO-Ag-ZnO Thin Films 135
6.7 Results and Discussion 135
6.7.1 X-ray Diffraction 135
6.7.2 Rutherford Back Scattering 137
6.7.3 X-ray Photoelectron Spectroscopy 138
6.7.4 Scanning Electron Microscope 142
6.7.5 Atomic Force Microscope 143
6.7.6 UV-Vis Spectroscopic Study 144
6.7.7 Hall Measurements 148
6.8 Conclusion 151

Chapter-7 Conclusion and Future Work **153-156**
7.1 Conclusion 153
7.2 Scope of Future Work 155

References **157**
Biodata **165**
Declaration **171**

List of figures

3.1 The lattice structure of silver having face centered cubic structure.

3.2 Energy Loss distribution in the 100 MeV swift heavy ion in the target material.

3.3 Schematic diagram of source of negative ions by Cesium Sputtering (SNICS)

3.4 Schematic diagram of low energy ion beam implanter at Inter University Accelerator Centre, New Delhi.

3.5 X-pert pro Panalytical model at MRC, MNITJ.

3.6 (a) Schematic representation of the working of XPS (b) XPS instrument (Omicron ESCA) at MRC, MNITJ.

3.7 (a) Block diagram of Atomic Force Microscopy (b) Multimode Scanning Probe Microscope AFM at MRC, MNITJ.

3.8 (a) Schematic diagram of components of Scanning electron microscope (b) Nova Nano FE-SEM 450 (FEI) at MRC, MNIT Jaipur.

3.9 (a) Schematic representation of components of transmission electron microscope (TEM) (b) Tecnai G2 20(FEI) HR-TEM at MRC, MNITJ.

3.10 UV/Vis/NIR Lambda 750 (Perkin Elmer) Spectrometer at MRC, MNITJ.

3.11 (a) Sample holder used for the Van der Pauw measurements for Hall effect (b) Pictorial representation of the different components of Hall measurement apparatus.

4.1 XRD pattern of SnO_2-Ag-SnO_2 with different Ag thickness (4-30 nm).

4.2 RUMP fitted RBS pattern of SnO_2-Ag-SnO_2 with Ag thickness of 8 nm.

4.3 SEM micrographs of SnO_2-Ag-SnO_2 with different Ag thickness (4-30 nm).

4.4 AFM images of SnO_2-Ag-SnO_2 with different Ag thickness (4-30 nm).

4.5 TEM micrographs of SnO_2-Ag-SnO_2 with different Ag thickness (4-30 nm).

4.6 UV-Vis spectra of SnO_2-Ag-SnO_2 with different Ag thickness (4-30 nm).

4.7 Tauc's plot for SnO_2-Ag-SnO_2 multilayer with varying Ag thickness (4-30 nm).

4.8 Refractive index and extinction coefficient of SnO_2-Ag-SnO_2 with different Ag thickness (4-30 nm).

4.9 Hall measurements of SnO_2-Ag-SnO_2 with different Ag thickness (4-30 nm).

4.10 XRD pattern of pristine and Xe implanted SnO_2-Ag-SnO_2 films.

4.11 Experimental and Rump fitted RBS spectra of pristine and 1E16 Xe implanted SnO_2-Ag-SnO_2 films.

4.12 XPS spectra of pristine and Xe implanted SnO_2-Ag-SnO_2 films.
4.13 SEM images of pristine and Xe implanted SnO_2-Ag-SnO_2 films.
4.14 EDS of pristine and Xe implanted SnO_2-Ag-SnO_2 films.
4.15 AFM images of pristine and Xe implanted SnO_2-Ag-SnO_2 films.
4.16 Variation in surface roughness of pristine and Xe implanted SnO_2-Ag-SnO_2 films.
4.17 Transmittance spectra of pristine and Xe implanted SnO_2-Ag-SnO_2 films.
4.18 Tauc plot for pristine and Xe implanted SnO_2-Ag-SnO_2 films.
4.19 Refractive index and extinction coefficient for pristine and Xe implanted SnO_2-Ag-SnO_2 films.
4.20 Carrier concentration, mobility and sheet resistance for pristine and Xe implanted SnO_2-Ag-SnO_2 films.
4.21 XRD pattern of SnO_2/Ag/SnO_2 pristine and irradiated films.
4.22 RBS spectrum of SnO_2/Ag/SnO_2 film with fitted profile.
4.23 Raman spectra of SnO_2/Ag/SnO_2 pristine and irradiated films.
4.24 SEM (a) and AFM (b) images of the pristine and irradiated SnO_2/Ag/SnO_2 films.
4.25 Transmittance and absorbance spectra of pristine and irradiated SnO_2/Ag/SnO_2 multilayer films.
4.26 Tauc's plot of pristine and irradiated SnO_2/Ag/SnO_2 multilayer films.
5.1 (a) X-ray diffraction pattern of as-deposited SnO_x/Au/SnO_x stacked multilayer (b) X-ray diffraction pattern showing amorphous nature of stacked multilayers for different annealing temperatures.
5.2 (a) SEM image exhibiting a flat topology of stacked multilayer (b) AFM image showing the surface topology of the sandwich layer along with (c) depth histogram.
5.3 (a) O K-edge X-ray absorption spectra of SnO and SnO_2 reference samples along with the stacked TCO multilayer measured in TEY/TFY modes. (b) Sn M-edge spectra for the TCO multilayer compared to references, and (c) XES and XAS of the O K-edges where XES displays a valence band line shape indicating SnO. (d) Magnitude of the band gap energy determined using second derivatives
5.4 RBS spectrum along with a fitted profile of the stacked multilayer.
5.5 UV-Vis curve showing transmittance, absorbance and reflectance for stacked multilayer.
5.6 Raman spectrum of stacked multilayer. Electrical resistivity and sheet resistance as a function of reciprocal temperature.
5.7 Electrical resistivity and sheet resistance as a function of reciprocal temperature

5.8 Sheet resistance, carrier concentration and mobility as a function of reciprocal temperature.

5.9 X-ray Diffraction spectra corresponding to pristine and 100 MeV O^{7+} irradiated stacked multilayer thin films.

5.10 RBS spectra showing experimental and simulated data corresponding to the pristine SnO_x/Au/SnO_x thin film.

5.11 RBS spectra showing experimental and simulated data corresponding to the SnO_x /Au/SnO_x thin film irradiated with fluence of 5×10^{12} ions / cm^2.

5.12 SEM micrographs for pristine (a), irradiated stacked multilayers with fluences 5×10^{11} ions / cm^2 (b), 1×10^{12} ions / cm^2 (c), and 5×10^{12} ions / cm^2 (d).

5.13 AFM micrographs for pristine (a), irradiated stacked multilayers with fluence 5×10^{11} ions / cm^2 (b), 1×10^{12} ions / cm^2 (c), and 5×10^{12} ions / cm^2 (d).

5.14 UV-Vis spectra for pristine (a), irradiated stacked multilayers with fluence 5×10^{11} ions / cm^2, 1×10^{12} ions / cm^2, and 5×10^{12} ions / cm^2

5.15 Raman spectra for pristine and irradiated stacked multilayer.

5.16 Variation of sheet resistance and resistivity of pristine and 100 MeV O^{7+} irradiated stacked multilayers.

5.17 Schematic showing the interface of stacked multilayered structure.

5.18 Variation of sheet resistance, carrier concentration and mobility with reciprocal of temperature corresponding to the SnO_x/Au/SnO_x thin film irradiated with fluence of 5×10^{12} ions / cm^2.

5.19 XPS survey scan of pristine and irradiated (with the highest fluence of 5×10^{12} ions / cm^2) multi-layered SnO_x /Au/SnO_x thin film.

5.20 XPS spectra of O-1s and Sn $3d_{5/2}$ from top layer of pristine and irradiated (with highest fluence of 5×10^{12} ions / cm^2) multi-layered SnO_x /Au/SnO_x thin film.

5.21 XPS spectra of O-1s and Sn $3d_{5/2}$ from Ist interface of pristine and irradiated (with highest fluence of 5×10^{12} ions / cm^2) multi-layered SnO_x /Au/SnO_x thin film.

5.22 XPS spectra of O-1s and Sn $3d_{5/2}$ from IInd interface of pristine and irradiated (with the highest fluence of 5×10^{12} ions / cm^2) multi-layered SnO_x /Au/SnO_x thin film.

5.23 X-ray diffraction spectra corresponding to the pristine and γ-irradiated stacked multi-layered SnO_x/Au/SnO_x thin films at different doses (5 kGy to 100 kGy).

5.24 AFM micrograph showing the topography of the SnO_2 layer in pristine and γ-irradiated stacked multi-layered SnO_x/Au/SnO_x thin films at different doses (5 kGy to 100 kGy)

5.25 Absorbance and transmittance in the visible region for pristine and γ-irradiated stacked multi-layered SnO_x/Au /SnO_x thin films at different doses (5kGy to 100 kGy).
5.26 The RBS spectrum and its fit for pristine stacked multi-layered SnO_x/Au/SnO_x thin film.
5.27 The RBS spectrum and its fit for stacked multi-layered SnO_x/Au/SnO_x thin films irradiated with γ-radiation at a dose of 100 kGy.
5.28 The high-resolution XPS spectra of top layer and I[st] interface post γ-radiation at a dose of 100 kGy showing O-1s and Sn $3d_{5/2}$ region.
5.29 Variation of resistivity and sheet resistivity with dose of γ-radiation.
5.30 The temperature dependence of sheet resistance, carrier concentration and mobility in stacked multilayers of SnO_x /Au/SnO_x post γ-radiation of 100 kGy.
6.1 XRD pattern of ZAZ multilayer with different Ag layer thickness (4-30 nm).
6.2 RBS pattern of ZAZ with Ag thickness 8 nm.
6.3 SEM micrographs of ZAZ with different Ag thickness (4-30 nm).
6.4 EDX micrograph of ZAZ with 8 nm thickness
6.5 AFM images of ZAZ with different Ag thickness (4-30 nm).
6.6 TEM micrographs of ZAZ with 8 nm Ag thickness.
6.7 UV-Vis spectra of ZAZ with different Ag thickness (4-30 nm).
6.8 Tauc's plot for ZAZ multilayers with varying Ag thickness (4-30 nm).
6.9 Refractive index and extinction coefficient for ZAZ multilayer with varying Ag thickness (4-30 nm).
6.10 Hall measurements of ZAZ with different thickness (4-30 nm).
6.11 Haacke's FOM of ZAZ with different Ag thickness (4-30 nm).
6.12 XRD pattern of pristine and Xe ion irradiated ZAZ multilayer thin films.
6.13 RBS spectra of ZAZ multilayer thin films (a) pristine and (b) Xe ion irradiated at a fluence of 1×10^{16} ions/cm^2.
6.14 XPS spectra of pristine and Xe ion implanted at a fluence of 1×10^{16} ions/cm^2 ZAZ multilayer thin films (a) survey scan (b) Zn 2p-edge (c) O 1s-edge (d) Ag 3d-edge.
6.15 SEM micrographs of pristine and Xe ion irradiated ZAZ multilayer thin films.
6.16 Variation of particle size from SEM micrographs of pristine and Xe ion irradiated ZAZ multilayer thin films.
6.17 AFM micrographs of pristine and Xe ion implanted ZAZ multilayer thin films.
6.18 TEM images of Xe ion implanted ZAZ multilayer thin films.

6.19 Transmittance spectra of pristine and Xe ion irradiated ZAZ multilayer thin films in the visible region.
6.20 Bandgap plot of pristine and Xe ion irradiated ZAZ multilayer thin films.
6.21 Calculated refractive index and extinction coefficient spectra of pristine and Xe ion irradiated ZAZ multilayer thin films in the visible region.
6.22 Hall measurement of pristine and Xe ion irradiated ZAZ multilayer thin films for different fluences.
6.23 Calculated Haacke FOM for pristine and Xe ion irradiated ZAZ multilayer thin films.
6.24 XRD pattern of pristine and SHI irradiated ZAZ multilayer structure.
6.25 RBS spectra of pristine and SHI irradiated ZAZ multilayer structure.
6.26 (a) XPS results of pristine and irradiated ZAZ multilayer structure at the top surface (survey scan). (b) XPS results of pristine and irradiated ZAZ multilayer structure of the top surface (short scan for Zn). (c) XPS results of pristine and irradiated ZAZ multilayer structure at the top surface (short scan for O). (d) XPS results of pristine and irradiated ZAZ multilayer structure at middle layer (short scan for Ag).
6.27 SEM images of pristine and SHI irradiated ZAZ multilayer structure with different ion fluences.
6.28 AFM images of pristine and SHI irradiated ZAZ multilayer structure.
6.29 Pristine and SHI irradiated ZAZ multilayer structure (a) Transmittance spectra and (b) optical band gap from Tauc's plot.
6.30 Refractive index and extinction coefficient variation spectra of pristine and SHI irradiated ZAZ multilayer structure.
6.31 Photoluminescence spectra of pristine and SHI irradiated ZAZ multilayer structure.
6.32 Electrical properties of pristine and SHI irradiated ZAZ multilayer structure with a variation in temperature.
6.33 (a) Electrical properties of pristine and SHI irradiated ZAZ multilayer structure at room temperature. (b) FOM for pristine and SHI irradiated ZAZ structure at room temperature.

List of Tables

4.1 Resistivity, carrier concentration, mobility and sheet resistance (R_{sh}) of 100 MeV O^{7+} irradiated SnO_2/Ag/SnO_2 multilayer thin film.

6.1 Physical parameters calculated from XRD pattern for different Ag thickness.

6.2 Various physical parameters calculated from XRD and AFM measurements for implanted ZAZ multilayers.

6.3 Various Parameters calculated for ZnO and Ag from XRD pattern for 100 MeV Ag^{7+} irradiated ZnO/Ag/ZnO multilayer thin films.

6.4 Variation in electrical properties with fluence at room temperature for 100 MeV Ag^{7+} irradiated ZnO/Ag/ZnO multilayer thin films.

Chapter-1

Introduction

1.1 Introduction

Transparent conducting oxides (TCOs) have attracted lot of attention for wide range of applications in industry due to their high transparency in the visible region and very good metallic conductance. Transparent conducting electrodes are one of the crucial components for optoelectronic devices and hence have been widely explored in terms of new materials and enhancement of required properties[1]. Generally, a certain sheet resistance is required to meet the electrical functionality. The sheet resistance needed for electrodes to be used in touch screens is in range of 400–700 Ω/sq while it should be less than 10 Ω/sq for large area flat panel displays and thin film solar cells[2]. Another important parameter of interest is transmittance of materials in the spectral range. This range can be determined based on the sensitivity of human eye, efficiency of absorber material for solar cells, or the emission spectra of active materials used for new lighting technologies. The coexistence of electrical conductivity and optical transparency in these materials depends on the nature, number, and atomic arrangements of metal cations in crystalline or amorphous oxide structures, their morphologies and presence of intrinsic or intentionally introduced defects[3]. TCOs are oxide semiconductors having band gap ≥ 3 eV, which is large enough for optical transparency yet small enough for sufficiently good conductivity. Perfect crystalline stoichiometric TCOs behave as an insulator because of their large band gap. However, presence of defects or vacancies in case of non-stoichiometry in the metal oxide lattice leads to formation of new band structure giving electrical conductivity. These intrinsic

defects are generally attributed to the presence of interstitial metal atoms or oxygen vacancies and behave as electron donor centers. Extrinsic dopants also play an important role in the population of conduction band and their intentional introduction provides sufficient density of charge carriers[4]. TCOs, due to their wide bandgap are generally transparent in the visible (Vis) and near-infrared region (NIR) while these are reflecting and absorptive for thermal infrared radiation (IR) and ultraviolet (UV) range respectively. At longer wavelengths, reflection is due to free electrons or plasma resonance absorption while absorption takes place at shorter wavelengths due to fundamental bandgap transition. TCOs generally do not absorb photons in the in the UV-Vis-NIR region but reflection and interference would also affect the transmission. The optical properties of TCO which include transmission [T], reflection [R], absorption [A], refraction index n, extinction coefficient k, band gap Eg depend upon the type, thickness, uniformity, surface roughness, chemical state and the structure of TCO.

1.2 Criteria for Transparent Conducting Oxides

For a material to be used as TCO, it should be a wide band gap material (> 3eV) with low resistivity (of the order of 1×10^{-4} Ω.cm), have sufficient number of charge carriers and mobility and controlled roughness[5]. Work function of the material is equally important to give proper band alignment with the active layer for use of TCO as electrode in energy conversion devices[6]. Besides the resistivity and transmittance, the choice of substrates (both rigid and flexible substrates as per the technological use) also plays a crucial role in deciding a proper TCO for a particular application. Deposited film morphology, surface roughness and interfaces also affect the optical properties due to reflection losses which include specular and scattered components. The surface

roughness of TCO thin film plays important role in the optical properties of the structure: smoother films have high transparency due to less absorption. The film structure whether crystalline, amorphous or having short range order would play an important role in transparency and conductivity of TCO thin film due to grain boundary scatterings. Furthermore, the chemical structure, bonding between atoms and defect state may also alter the electrical properties.

Electrochromic mirrors widely used in automobiles and "smart" windows should be chemically inert with high transparency and fabricated with low cost materials. Low-emissivity windows in building materials with high transmittance are preferred in cold climates while materials reflecting the NIR part of incident sunlight are used in hot climates[7]. Solar cells require low cost materials with good thermal stability[8]. Furthermore, low cost and durable materials with low resistance are also required for defrosting windows in freezers and airplanes or automobiles windshields[9]. A large number of TCOs exist today and all commonly used transparent conducting materials and their production methods nowadays show some advantages and disadvantages for each application. Till date, there is no transparent conductor that can be used for all such applications.

According to the theory of charge transport in TCO materials, the electrical conductivity (σ) depends upon the concentration (n) and mobility (μ) of charge carriers. Therefore, higher conductivity is expected to come from large carrier concentration and large mobility[10]. However, the mobility is severely restricted by several constraints like scattering from grain boundaries[11], lattice vibrations and neutral and ionized impurities. In commonly used *n*-type TCOs, electrical conductivity of thin films depends on the electron density in the conduction band and the mobility; $\sigma = \mu n e$; where μ is the electron mobility, n is its density, and e is the electron charge.

1.3 Applications of TCOs

Transparent electrode is a key component in optoelectronic devices. Other than solar cell applications[8], it is also required in light emitting diodes[12], displays[13], touch screens[14], perovskite solar cells[15] and has many other potential applications. Organic solar cells and organic LEDs are the most studied devices using novel TCO materials and structures. Touch screen and displays which include liquid crystal are also based on TCO electrodes. Electrochromic materials based window are fabricated over TCO coated thin films. New generation photovoltaics like perovskite and heterojunction solar cells also have TCO as an important part. Recently, TCO electrodes have also been explored in water splitting devices and for sensor applications[16]. There is a continuously increasing demand of TCO which is compatible to flexible optoelectronic devices and has led to fabrication of room temperature deposited TCO on a plastic substrate. In addition to optoelectronic devices, TCOs are now also used in different devices like antenna, MEMS, sensors and energy applications.

1.4 Types of TCO

TCOs can be categorized into two types (*n*-type and *p*-type TCO). Generally, 90% of TCO are *n*- type, where electrons are the majority charge carriers. Few *p*-type TCOs have also been fabricated but are difficult to produce and experimentation has been done only up to research level and has not been commercialized till now[1]. Most commonly studied *p*-type TCOs are $CuInO_2$, $CuGaO_2$, $SrCu_2O_2$ and $CuAlO_2$ etc[17]. Among the large number of available *n*-type TCOs, only ITO[18] and FTO[19] are most common and commercialized TCOs which are used as electrode in most of the applications. Doping is usually done to generate n-type TCO where one element is intentionally added to the host TCO matrix. This creates defect levels due to the

presence of dopant atoms resulting in n-type conduction. The resultant TCO possesses unique properties in terms of good transparency and conductivity simultaneously which are mutually exclusive properties. FTO is fluorine doped tin oxide, while ITO (In_2O_3; Sn) having typically 90% transparency has 10% SnO_2 by weight to make a ternary compound consisting of indium, tin and oxygen. ITO is a highly degenerate semiconductor having wide band gap making it highly conducting as well as transparent. The approximate thickness of ITO coating on glass for electrode application is ~ 300 nm and high temperature sintering is required to show its best results of conductivity and transparency. The most commonly used methods to fabricate ITO films on glass, plastic or other substrates are physical vapor deposition techniques[20]. Other *n*-type TCOs used largely are Al doped ZnO (AZO)[21], Ga doped ZnO (GZO)[22], In doped ZnO (IZO[23]) etc. which are able to achieve low resistivity with high transparency.

1.5 Alternatives to ITO

Scarcity of Indium and more energy consumption during and post deposition has led to an increase in the production cost of ITO coated substrate. Moreover certain drawbacks of ITO[24] such as low mechanical flexibility, high thickness, high temperature processing has led to researchers trying to develop an alternative TCO which can compete with ITO for a wide range of applications[25]. Many alternatives have been explored starting from doped single layer TCO like AZO, IZO, GZO, FTO etc., however conductivity of these doped metal oxides is limited by scattering due to coulomb interaction between ionized donor atoms and free electrons[26]. Other currently studied novel materials for this are CNTs, graphene, graphene oxide[27], conducting polymers[28], metal nanowires[29] and metal grid. It is found that these materials proposed

as an alternative of TCO have certain limitations. High cost in case of CNT, low transparency and high resistivity of polymers and difficulty in production of graphene makes these materials not very practical commercial alternative of ITO. In the past few years stacked multilayer film having a thin metal layer embedded between two metal oxide layers has emerged out as most suitable candidate to be considered as an alternative of ITO for TCO applications[30].

1.6 Multilayer Transparent Conducting Oxide

Various TCOs have been developed till today scaling from very simplistic structures to the most complicated hetero-structures. Such structures have already been in discussion and later discarded for their complex counterparts offering high conductivity, transparency and stability but at the cost of complex manufacturing procedures. The quest for an efficient TCO has led to the need of development of a coating with (1) superior transparency in visible region, (2) excellent conducting properties and (3) good thermal and mechanical stability. The optimization for good transparency and conductivity at the same time has always presented a roadblock for the development of efficient TCOs. Among various structures, stacked multilayer thin films (metal oxide/metal/ metal oxide) have proved to be most suitable candidates[31]. These stacked multilayer structures have attracted great attention as transparent electrode as they exhibit a unique combination of required properties viz. good optical transparency in the visible region and high electrical conductivity, even when the layers are grown at room temperature. In this trilayer structure, the sandwiched metal layer is responsible for the charge transport phenomena and transmittance is enhanced by the dielectric layer having high refractive index[32]. The limitation to higher transmittance is due to reflection losses from metal layer. In the multilayer structure, the oxide layer

acts as anti-reflecting coating. Overall optical transmission of the multilayer structure is enhanced by destructive interference in the beams reflected from the metal-semiconductor interfaces, and constructive interference in the beams transmitted through the stacked multilayer structure and the transparent substrate[33]. In addition, the work function of these multilayer electrodes could be tuned by selecting the dielectric material as per the requirement of the TCO to be used as cathode, anode or an intermediate electrode. It is well known that the thickness of metal oxide and the embedded metal layer play an important role in controlling the electrical conductivity and optical properties of the stacked multilayer. The thickness of metal layer below 10 nm increases the transparency as well as charge transport. In order to realize high transparency and conductivity in the stacked multilayer electrode, it is necessary to deposit a continuous metal layer sandwiched between the two dielectric layers[34]. The growth of ultrathin metal layer deposited on bottom dielectric layer follows the island or Volmer-Weber growth mode, normally followed by systems of metals when grown over insulators[35]. In this mode, nucleation of small clusters takes place directly on the surface of substrates. These clusters then grow into islands which further coalesce to form continuous thin films. The metal mid layer should be above the percolation threshold thickness, uniform, thin and continuous for good conductivity and high transmittance. For isolated islands of Ag resistance of structure will be high and transmittance will also decrease because of scattering.

Metal islands on a flat substrate will grow into uniform thin film under different processes. For low deposition rate, one can imagine atoms will attach to the substrate one by one. The very first atom has high mobility to walk randomly on the substrate, as does the second atom. It is highly possible that two atoms meet and form a larger

island which has lower mobility. This island will then meet the consequent atoms that leads to increase in the size and hence reduction in mobility[36].

The conduction mechanism in these stacked structures is explained by considering a thin continuous layer of metal embedded between two oxide layers thereby forming a DMD structure[37]. The total resistance of this coplanar configuration is generally given by a parallel combination of resistance as: $1 / R_{total} = 1 / R_{metal} + 2 / R_{oxide}$ with $R_{oxide} > 1000\ R_{metal}$, so $R_{total} \approx R_{metal}$. Therefore, the conductivity shown by DMD structure is primarily due to embedded metal film and solely responsible for exhibiting such low values of resistivity as compared to single layer TCO[38]. A critical thickness of the metal film is required to provide a continuous path for conduction of electron[39]. The room temperature resistivity and sheet resistance values for staked layered structure are an indication of a continuous metal inter layer for these multilayers. Charge carrier behavior in middle metal layer is independent of temperature, as these are the valence electrons. The multilayer structure charge mobility is affected by scattering resulting in change in resistivity of structure. The influencing scattering mechanisms are scattering from interface, surface and grain boundary in the sandwich structure. The behavior of middle metal layer can be explained through grain-boundary scattering. For a large grain size, the fraction of grain-boundary area decreases, giving high mobility[40].

Electrical properties of the DMD structure are largely influenced by the metal semiconductor interface in the DMD structure the difference in work function of metal and semiconductor leads to band bending on contact to match the fermi levels[6]. Due to this charge carriers (electrons) transfer from lower work function (generally metals) side to higher work function (oxide) side and a thin accumulation region is created at the interface till thermodynamics equilibrium is achieved. In case of stacked multilayer

structure electrons are transferred from metal (Ag, Au) side to metal oxide (ZnO, SnO_2) side and increase the charge carrier concentration and hence conductivity of metal oxide. This interface phenomenon is dependent on stoichiometry, contamination, defects specially oxygen vacancies and chemical states of both metal and metal oxide layers. The figure below shows transfer of electrons from low work function material to high work function material. Due to this conduction and valence bands of oxide (work function ≥ 5.2 eV) bend downwards and that of metal (work function ≤ 5.1 eV) bend upwards to achieve equilibrium. Reverse bending will occur for a metal having work function more than that of oxide material.

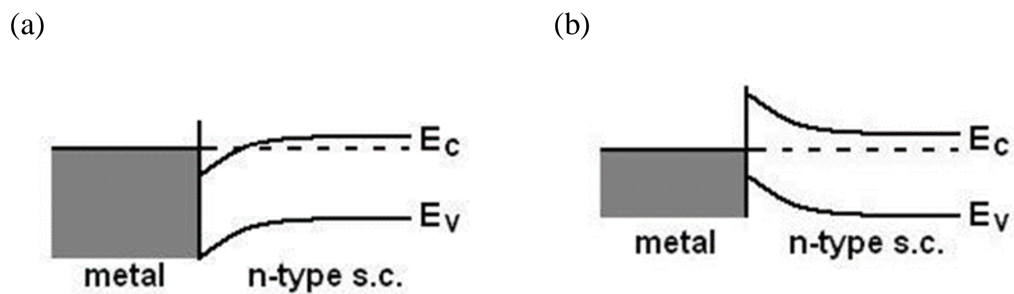

Several combinations have been studied using metal oxides viz SnO_2[41], ZnO[42], TiO_2[43], WO_3[44], graphene oxide etc. along with various highly conducting metals like silver (Ag)[45], gold (Au)[46] and copper (Cu)[14] to form of a multilayer stacked structure of three or more layers. These structures have been fabricated on different substrates including glass, quartz and plastic depending on the type of application. Most of the multilayers have total thickness near or below 100 nm.

1.7 Objective of the Thesis

The stacked multilayer structures have been explored as an alternative of ITO for TCO applications. The present research work is focused on the optimization of growth parameters for room temperature fabrication of stacked multilayered structure

of typical thickness lesser than 100 nm exhibiting better or similar conductivity and transparency in visible spectrum. These multilayer structures are further explored to investigate the effect of gamma radiation, low energy ion (100 keV) and swift heavy ion (100 MeV) irradiation on their optical and electrical properties. Low temperature Hall measurements were carried out to verify the stability of electrical properties of these films in the temperature range 80K -350 K. The main objectives of the present thesis are as follows:

- To fabricate trilayer structure MeO/M/MeO (M-Au/Ag, MeO-ZnO, SnO_2) at room temperature having total thickness ~ 100 nm for superior optical and electrical properties.
- To enhance the optoelectronic properties of the optimized layer by surface treatment.
- To test the stability of optimized trilayer towards ion irradiation using gamma radiation, low energy ion (100 keV) and swift heavy ion (100 MeV) beams.

Thesis plan:

- Chapter 4 describes synthesis of stacked multi-layered SnO_2-Ag-SnO_2 (SAS) structure by varying the thickness of Ag layer along with investigation of the optimized multilayer for 100 keV Xe ion implantation and 100MeV O^{7+} SHI irradiation on SAS structure.
- Chapter 5 details fabrication of tri layer SnO_x-Au-SnO_x structure by evaporation technique. Study of effect of gamma ray radiation of different doses (10-100 kGy) and 100MeV O^{7+} SHI irradiation on SAuS structure is given.

- Chapter 6 gives the synthesis of stacked multi-layered ZnO-Ag-ZnO (ZAZ) structure by varying the thickness of Ag layer. The multilayer films are then investigated for 100 keV Xe ion implantation and 100MeV Ag^{7+} SHI irradiation effect on ZAZ structure in terms of structural, optical and electrical properties.

Chapter-2

Literature Review

2.1 Introduction

Over the past few decades, several new materials and manufacturing techniques have been explored to find a suitable transparent conducting oxide (TCO) that can serve the new and upcoming technological requirements. The following literature survey summarizes the advancement in the field of TCO till date.

2.2 Historical Development of Transparent Conducting Oxide

Investigations on TCO as an electrode was begun in the year 1907 by Badekar *et al.*[47] using thermally oxidized film of cadmium metal. The evaporated CdO, yellowish in color had resistivity ~ 1.2×10^{-3} Ω cm, which is nearly one order of magnitude higher than the resistivity of indium tin oxide (ITO) coated films[48] the best TCO available today. The journey started from Badekar was continued by Holland[49], who reviewed the early work of TCO film in 1953. He produced the thin film using a metallic target and reactive sputtering in oxygen gas. Vossen[50] and Hacke[51] further wrote comprehensive reviews in mid-1970s that included the concept of figure of merit: a unique combination of transparency and conductivity (sheet resistance) to quantify the quality of thin films for TCO applications. Till that time, the main component of TCO material was pure or doped tin oxide. In 1980s Major and Chopra *et al.*[52] published reports on zinc oxide (pure and doped) based TCO. They also used annealing in vacuum and oxygen environment to tune the properties of TCO thin film. They discussed the mechanism of transparent conducting oxide in terms of charge transport. A detailed comparative analysis was done for TCO properties in terms of optical, structural and

electrical properties affected by fabrication techniques, process parameters, composition of the target material and workability in different optical spectrum. In 1990, Islam *et al.*[53] reported electronic structure analysis of TCO layer using advanced techniques like XPS and XRD. Minami *et al.*[54] reported the status and prospects of further development of polycrystalline or amorphous TCO semiconductor used for practical thin film transparent electrode application. Gordon[5], Stadler[17] and Zunger[3] addressed some critical issues related to new TCO material, such as criteria for application and theoretical models in early 21st century. Gordon summarized the basic requirements of TCO for practical applications like synthesis methods, gas environment, annealing temperature and other factors, which affect the performance of TCO in the device. Ellmer *et al.*[1] investigated for different types and dimensions of TCO along with scope of new materials for TCO applications such as metal thin film, carbon based materials etc.

The industrial applications of TCO materials began in the middle of 1940s when researchers used it as a transparent heater in the aeroplane window and for antistatic window applications[55]. In 1960s, the infrared light filters composed of Sn or In_2O_3 increased the lamp efficiency by reducing heat losses in low-pressure sodium discharge lamps[56]. The invention of advanced flat-panel display technology around 1970, increased the use of tin-doped indium oxide (In_2O_3: Sn, abbreviated ITO) for transparent electrodes[57]. Energy crisis initiated the research in non-conventional sources for energy which included solar cell, low emissive windows and light emitting diodes which boosted the use of TCO. Currently, TCO is used in low emissive windows[58], thermochromic devices[59] (used to shadow buildings against direct solar radiation to reduce the heat load) and transparent electrodes[60] for optoelectronic apications.

2.3 Methods and Materials for Transparent Conducting Electrode

In terms of fabrication techniques, physical vapor sputter technology is extensively used for TCO deposition on large area substrates providing upscaling for industrial uses. The sputtering method provides good control over thickness and uniformity of deposited film[61]. High temperature is required for some of the TCOs like ITO and Al doped ZnO (AZO during or after deposition[62]. Other than sputtering, most popular methods for deposition of single or multilayer thin films TCO on different substrates are e-beam and thermal evaporation techniques[63]. Chemical methods like spray pyrolysis[19], spin coating[64], dip coating[65], chemical vapor deposition[66] etc. are also useful for deposition of doped TCO thin films. Main advantages of chemical techniques are low-temperature synthesis and control over doping percentage. But at the same time there are some disadvantages of chemical techniques such as poor thickness control and films produced with high roughness and less conductivity. The rough surface of the electrode adversely affects the device performance as the morphology is transferred to the next active layer and creates an uneven interface[67].

TCO coating quality is usually measured by two parameters: sheet resistance ($R_s = 1/\sigma t$) and optical transmittance (proportional to exp ($-\alpha t$). Here σ is conductivity, α is optical absorption coefficient and t is the thickness. Studies show that these two parameters depend upon the coating material and their resistivity[60]. The properties of TCO thin film are a function of film's thickness and the process parameters[68]. Considering these facts, silver (Ag)[69] with lowest resistivity is the first choice followed by copper (Cu)[70] and gold (Au)[71] for metal based TCOs. Au is favored for its inertness and stability in different environments. Some alloys or mixture of metals like Al-Ag[72], Au-Ag[73] have also been used for particular applications or improvement in metallic layer properties.

In general, TCOs are wide bandgap ($E_g \geq 3$ eV) *n*-type degenerate semiconductors having charge concentration (n) ≈ 2×10^{21} cm^{-3} and mobility (μ) ≈ 100 $cm^2V^{-1}s^{-1}$ with resistivity in the range of 10^{-4}–10^{-3} Ωcm[74]. The conduction property of TCO materials is due to the fact that conduction band is composed of overlapping metal-s-like orbitals in these materials, which leads to broadly dispersed conduction band[75]. Ionized impurity in TCO limits the mobility of charge carriers due to scattering[76]. Clustering of dopants leads to scattering of charges in the semiconductor. Transition metal oxides (SnO_2, ZnO, and TiO_2) are extensively used for TCO applications due to their wide band gap and presence of intrinsic defects which makes them optically transparent as well as electrically conducting[67]. Quantum mechanical phenomena have significantly improved the understanding of charge transport and doping processes of semiconductors (especially oxides). Scientists have investigated the role of intrinsic/extrinsic defects such as vacancies, substitutional and interstitial lattice site defects in TCO properties[11,77]. Hartnagal *et al.*[78] reviewed the growth techniques, properties and applications of TCOs.

2.4 Multilayer TCO as Transparent Conducting Electrode

Recently oxide/metal/oxide stacked multilayer structure[79] has attracted much attention as transparent electrode showing combination of required properties viz. good optical transparency and high electrical conductivity, even when these layers are grown at room temperature[80]. In such kind of structures, the sandwiched metal layer is responsible for the charge transport phenomena[81] and transmittance is enhanced by the oxide (dielectric) layer having high refractive index[82]. In addition, by selecting the oxide material as per the requirement to be used as cathode, anode or an intermediate electrode, the work function of these multilayer structure electrodes could be tuned[44].

Due to these advantages, many studies based on stacked multilayer-structured transparent conducting films such as ITO/Ag/ITO[83], ITO/Au/ITO[84], GZO/Ag/GZO[85], ZnO/Au/ZnO[86], ZTO/Ag/ZTO[87], and GMZO/ Ag/GMZO[88] have been carried out.

The Hybrid metal – TCO multilayer gives superior optical and electrical characteristics compared to that of single layer TCO or a metal electrode. A tri-layer ITO/Ag/ITO[36] anode was investigated for the desired electrical properties with lesser thickness. Some recent reports have described the influence of Ag layer thickness on electrical and optical properties of the trilayer. Yun et al[89]. have reported sheet resistance nearly 3 Ω/□ and transmittance less than 85 % with incorporation of 18 nm AgO layer using ITO as TCO. There have been studies where different combinations of metals with both pure and doped TCO under different process conditions have been tried[90]. Cho et al[87] have reported 80-86% transmittance for Zinc tin oxide (ZTO)/Ag/ZTO, whereas WO_3/Ag/WO_3 system was reported to give 4 Ω/□ sheet resistance[44]. In MoO_3/Ag/MoO_3 system when Ag is replaced by Au, improved efficiency (η) of the anode was reported[91]. Several other combinations were also tried by different groups to enhance various properties like stability in different environments[81], mechanical flexibility[92] and get improved thermal[90] and structural properties[20].

2.5 SnO_2 and ZnO as Transparent Conducting Oxide

ZnO or SnO_2 thin films combined with suitable sandwiched metal films such as Au and Ag are potential and suitable replacements for ITO and other TCO materials[93]. The dominant TCOs have been SnO_2: X, In_2O_3: X and ZnO: X (where X is a dopant) due to their large band gap (> 3eV) and low resistivity (~ 10^{-3} Ω cm)[94]. SnO_2 and ZnO in pure form are highly resistive due to low carrier concentration. The benefit of using

these materials is that the plasma absorption wavelength increases as the charge carrier concentration decreases that results in high infrared transmission. SnO_2 and ZnO exhibits outstanding optical characteristics leading to broad industrial applications of these TCO materials. As the electrical and optical properties of TCOs can be tuned[95], extensive studies have been reported on these systems[64]. However, the transmittance spectrum shape depends strongly on the layer thickness[96] and the oxygen content of metal oxide layer[97] and number of defects present in the system[98]. Enhancement in transmittance in a particular wavelength region can also be achieved by adjusting the film thickness, defect concentration and other preparation parameters[67]. The performance of TCO is important as it affects the performance of the complete device[2].

Several trilayer structure combinations viz., $SnO_2/Ag/SnO_2$[99], $SnO_2/Cu/SnO_2$[100] were studied with different thicknesses of oxide films. The studies conceded that SnO_2 gives best results in terms of optical properties for thickness between 30 to 50 nm in stacked multilayer structure.[101] ZnO/Ag/ZnO[102], ZnO/Cu/ZnO[92], ZnO/Au/ZnO[103], AZO/Ag/AZO[95] are few examples of zinc oxide based stacked multilayer structure studied. Sahu *et. al.*[42] and Mohamed[104] have reported the effect of deposition process of both Ag layer and top ZnO layer on the physical properties of ZnO/Ag/ZnO multilayer system. Thickness of ZnO is found to be around 40 nm for effective trilayer.

Other than these metal oxides (ZnO and SnO_2), deposited multilayer structures of $TiO_2/Ag/TiO_2$ onto flexible substrates at room temperature by sputtering have been reported by Dhar *et al*[43]. The critical thickness (t_c) of Ag mid-layer to form a continuous conducting layer was obtained as ~ 9.5 nm and the multilayer has been optimized to obtain a sheet resistance of 5.7 Ω/sq and an average optical transmittance was ~ 86%

at 550 nm. The Haacke figure of merit (FOM) for t_c was $61.4 \times 10^{-3}\ \Omega^{-1}$/sq, highest value reported so far.

Both Ag and Au have been extensively used for different applications such as for electrodes[73], plasmonic[105] and sensing applications[106]. Both metals show very good conductivity in bulk and thin film form. The metallic film is transparent for thickness below 10 nm[46]. Various reports have shown that Au and Ag films achieve continuity for thickness greater than 5 or 6 nm for gold[107] and greater than 8 nm for silver[108]. Ag is considered as one of most useful material due to its high conductivity, low cost and good band alignment with oxide materials[109], while Au is considered for its stable nature even for high-temperature applications[110]. Few other metals like Cu[111], Ni[112], and Al[113] have also been investigated for use as middle metal layer in oxide/metal/oxide stacked multilayer structure.

2.6 Effect of Post-Deposition Treatment on TCOs

Properties of the metal oxide/metal/ metal oxide coating can be enhanced by controlling the deposition parameters and varying the temperature and atmosphere during post-deposition annealing[79]. ZnS/Au/ZnS[114] was synthesized and investigated for the effect of air annealing on electrical and optical properties; whereas different TCO/metal/TCO structures like ZnO:Al/Au/ZnO:Al[62], SnO_2/Cu/SnO_2[100], ZnO/Ag/ZnO[40], MoO_3/Au/MoO_3[91] were synthesized and investigated for different post-deposition conditions. IZO/Ag/IZO[115] films have been tested for their stability at several temperatures and humidity conditions. Interfacial stability of SnO_2-Ag-SnO_2 tri-layer structure was studied by post process annealing at 100 °C and 200 °C and found that Ag formed hillocks and cracks was formed in SnO_2 layer[116].

Chen *et al.*[65] studied the effect of high-temperature annealing on optical and electrical properties of GZO films deposited by sol-gel method. Annealing in air degraded the films in terms of carrier concentration but enhanced the mobility due to large grain growth which leads to decrease in scattering. Annealing in ambient argon improves the structure, conductivity, mobility and carrier concentration keeping optical transparency ~ 73.8 % after annealing. Yong *et al.*[117] studied the effect of annealing of gold layer on Si substrate and found that surface morphology changes with annealing time and temperature. Initially gold clusters are formed which dissolve later; this study helped to understand the conduction mechanism in metal thin films.

Hong *et al.*[118] investigated effect of UV irradiation and H ion implantation on the ZnO thin films. Results showed that the films show high transparency but low conductivity after UV treatment and hydrogen implantation. The films show low resistivity (1.3×10^{-3} Ωcm) with sufficient mobility maintaining transparency ≥ 80 % in the visible region. Gamma irradiation with ^{60}Co radioisotope on ITO coated glass were performed by Alyamani *et al*[119]. for high doses, up to 250 kGy. With increase in dose, the coating color changed from yellowish to brown and led to decrease in overall transmittance, but increase in refractive index and extinction coefficient. Electrical properties are very much affected by irradiation as seen by increase in conductivity. Primary suggested reason for this was an increase in grain size. Morphology is badly affected as roughness increases up to 5.7 nm after irradiation.

Alford studied gamma radiation effects on IZO thin film transistor and found better electrical reliability of indium -zinc oxide TFT over silicon-based TFT[120]. Yun *et al.*[121] saw the effect of nitrogen doping (≤ 1 %) in the sandwiched metal layer of

ZnO/Cu/ZnO structure and found improvement in the wettability of film and sheet resistance.

2.7 Modification of Layered Structure by Post Deposition Treatment: Implantation

Metal oxide thin films with wide band gap are very sensitive to low energy ion implantation and undergo structural changes at moderate fluences. Low energy ion implantation can alter the structural, optical and electrical properties of the ZnO and SnO_2[76]. The effect of ion implantation on multilayer thin film is required to study the effect of defects and doping. Better understanding of low energy ion interaction with multilayer material and correct selection of implantation parameters such as mass, energy, and fluence of the beam is useful for modifying the surface properties[122]. Low energy ion implantation is a technique with high control for introduction of dopants into targets, especially semiconductors. Short process times, excellent fluence homogeneity over large areas, dopant mass separation during implantation and adjustable doping profile by multiple implantations are the advantages of this technique[123]. Several researchers have studied modification in structural, electrical and optical properties of the ZnO, SnO_2 and other metal- oxide thin films using different of low energy ion implantation.

A significant decrease in sheet resistance has been reported in ITO/Ag/ITO and IZO/Ag/IZO layers after electron beam irradiation on these films, however, improvement in transmittance and increase in optical band gap was reported only for ITO/Ag/ITO with no significant change in these properties for IZO/Ag/IZO[124].

Keshri *et al.*[125] have reported structural, optical and gas sensitivity behaviors of WO_3 films implanted by 100 keV Ar^+ ions. Films has been deposited on unheated corning glass and *n*-type Si (100) substrates by thermal evaporation technique. And Optical transmittance and reflectance spectra of the films in the wavelength range 300 to 1000 nm have been measured. An increase in optical band gap from 2.90 to 3.49 eV has been observed with increase in fluence from 3×10^{15} to 1×10^{17} cm^{-2}. All films, especially the implanted films show good gas sensing behavior in methane environment. The film with a critical fluence of value 1×10^{16} cm^{-2} shows better optical as well as gas sensing properties.

Fromknecht *et al.*[126] implanted He, Hg and Xe ions with different oxidation states in TiO_2 (rutile). The lattice disorders and the lattice site location of the implanted ions were determined using Rutherford backscattering and channeling (RBS-C) spectrometry. The observation of dynamic recovery was proportional to ln*t*, indicating that the activation energy increases with decreasing disorder density. With increasing net charge, the maximum soluble concentration decreases by the formation of impurity-defect complexes probably enforced by charge compensation. The electrical conductivity of the implanted samples increase by many orders of magnitude irrespective of the oxidation state of the implanted species. It was concluded, that the carrier transport occurs by single energy states excitation at low doses and by variable range hopping (VRH) between localized states at high doses.

Implantation studies using low energy ion beam on SnO_2, have attracted considerable interest of researchers. It has been reported that ion implantation with controlled doses and depths can be used as an alternative method of doping. Moreover, the dopant species are confined to within a few hundred Å of the surface with

implantation energies of the order of keV. The Tuquabo group implanted fluorine doped tin oxide films as a TCO with N^+ at various energies between 5 and 40 keV for different ion doses between 10^{14} and 10^{16} ions/cm^2 and investigated the microstructure, optical and electrical properties of the films[127]. Bekisli *et al.* found that hydrogen is an important source of *n*-type conductivity in the transparent conducting oxide SnO_2[128].

ZnO is an important wide-band-gap multifunctional semiconductor and has been used widely for many optoelectronic devices. The role of vacancy clustering and acceptor activation on resistivity evolution in N ion-implanted *n*-type hydrothermally grown bulk ZnO has been studied by the Thomas group where they found that N ion implantation in ZnO at room temperature with 220 keV using doses in the low fluence 10^{15} ion/cm^2 range induces small and big vacancy clusters containing at least 2 and 3–4 Zn vacancies[129]. Buyanova *et al.*[130] study the combined effect of N and O implantation in ZnO with Raman and PL spectroscopy and found that the formation of the involved defects is largely enhanced by co-implantation. There are a number of studies for hydrogen implanted ZnO. Brillson et al.[131] studied the effect of ion fluence on mobility and carrier concentration found that the electrical properties are improved for low fluences, and degraded at higher fluences. Park and Liang studied the optical properties of ZnO with proton implantation and related the change in optical properties with defects and band gap using PL and Raman spectroscopy[132].

2.8 Modification of Layered Structure by Post Deposition Treatment: Swift Heavy Ion Irradiation

Swift heavy ion (SHI) irradiation can drastically modify the structural, optical and electrical properties of the material[133]. The annealing effect induced by the ion beam irradiation can be understood on the basis of thermal spike model[134]. According

to this model, a large amount of heat energy transfer by the projectile ions into the electronic systems takes place when energetic ions pass through the material. The transferred energy is distributed among the electrons and consequently to lattice atoms through the electron-lattice coupling. Deposition of such high energy raises the lattice temperature appreciably along the ion tracks within a very short duration of time ($\sim 10^{-14}$ s) and quenches rapidly. The rise and fall of temperature within a short interval of time generate pressure waves which in turn modifies the crystal structure.

Depending on type, mass and energy of ion and the interacting material state, structure and fabrication parameters, SHI can degrade or enhance the properties of the materials[135]. When SHI interacts with the material, the energy is dissipated through two ways (i) nuclear energy loss (Sn): the ion energy is directly transferred to the host atom, and (ii) electronic energy loss (Se): electronic excitation of host atom by inelastic collisions. The deposition of localized energy is high within a confined volume, resulting in a non-equilibrium state. As the range of SHI is few microns and these films are tens of nanometers thick, the ions pass through the thin film without being deposited.

Researchers from different groups have used different post-deposition processing techniques: thermal annealing[19] and SHI irradiation being the important ones[135]. TiO_2 and SnO_2 films were deposited by RF sputtering and then studied for the effect of Ag^{+15} ion of 200 MeV of different fluences. It was found that with higher fluence, transmittance increases in TiO_2 but not in SnO_2[136]. Chauhan et al. have used 100 MeV Ag ions with higher fluence ($1x10^{13}$ions/cm^2) and have reported an increase in crystallinity and higher value of transmittance for SnO_2 after irradiation[137]. Agarwal et al.[138] reported irradiation of ZnO thin film 100 MeV Au^{+8} ion and a consequent change in morphology and optical properties. Results of this study show that with low

fluence the roughness decreases with release of strain and high disorder exists at high fluence. The band gap and luminescent properties show tuning due to irradiation-induced oxygen vacancies or defects. Hemant et al.[135] studied the SHI irradiation effect on single layer ITO and FTO for rigid and flexible substrates for dye-sensitized solar cell application. They reported reduction of transmittance and conductivity by 15 % due to SHI irradiation at higher fluence of 3×10^{12} ion/ cm^{2,} while a negligible change in properties was seen at lower fluence 3×10^{11} ion/ cm^2. Deshpande et al.[139] have investigated the optical transparency and conductivity behavior of ITO coated films via spray pyrolysis for ion beam irradiation alteration. In that investigation, the resistance decreased from 200 Ω to 60 Ω with a reduction in transparency by about 40 % by SHI irradiation.

Chapter-3

Materials, Methods and Characterization Techniques

3.1 Introduction to the TCO Materials

In the past few decades, different materials have been explored for use as transparent conducting oxides[50]. Among them, only three oxides have emerged to be commercially important as transparent conductors viz. indium oxide, tin oxide, and zinc oxide. By volume, the most deposited TCO today is SnO_2, which has been used as a host material for In and F to produce ITO[140] and FTO[19]. ZnO is also primarily used as TCO in many coatings with Ag or Al doping[141]. The recent processing related improvements and low cost of ZnO makes it an attractive replacement of high-cost In-based TCOs. Non-stoichiometric oxides used as transparent conductors are invariably having anion vacancy, mostly an oxygen vacancy, in perfect crystal[142]. This property of oxides makes them conducting and hence suitable for transparent electrode application as their band gap makes them transparent in visible spectrum. In the present thesis, we have fabricated and investigated multilayer structure using two metal oxides ZnO and SnO_2. Ag and Au have been used as the sandwich metal layer to develop as an alternative for commercially available TCO i.e ITO. This chapter is divided into three sections. The first section is based on brief description of different materials used in the present work. The second section deals with various methods used for deposition of the multilayer structure and the last section of this chapter describes the characterization processes used, to understand the various important physical properties of the DMD structure.

3.1.1 Tin Oxide (SnO_2)

SnO_2 exhibits tetragonal rutile structure with space group D14 (P42/mnm). The unit cell contains six atoms –two tin and four oxygen[143]. Lattice parameters are a = b = 4.737 and c = 3.185 with c/a ratio 0.673. Ionic radii of tin (Sn^{4-}) and oxygen ion (O^{2-}) are 0.71 A^0 and 1.40 A^0 respectively. It is wide band gap (3.6 eV) semiconductor with high stability and is easy to fabricate as thin film[144], making it suitable for many applications from sensing to energy conversion[145].

3.1.2 Zinc Oxide (ZnO)

The II – VI group semiconductor, ZnO shows thermodynamically stable hexagonal wurtzite phase[146]. The hexagonal structure consists of lattice constants a = 3.24 Å & c = 5.19 Å with ratio c/a = 1.66. It has direct wide band gap (3.3 eV) with large excitation energy (60 meV). Radiation hardness property of ZnO and inexpensive production makes it a highly suitable material for different applications in space, energy and optics[147].

3.1.3 Silver

Silver (Ag) is a metallic element having face-centered cubic lattice and atomic number 47. It is the most abundantly used material for transparent conducting electrodes[148]. Ag is a good conductor of heat and electricity, having significantly high electrical and thermal conductivity in comparison to all other materials known. It can also endure high temperatures and is strong, malleable and ductile material. In addition, Ag is also a good reflector of light.

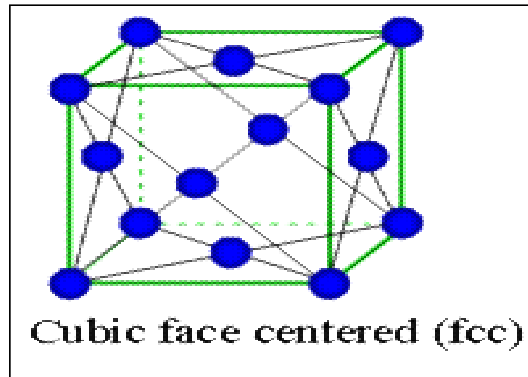

Figure 3.1 The lattice structure of silver having face centered cubic structure.

Although silver tarnishes with time but it still maintains its electrical conductivity. Also, it does not corrode easily, thus avoiding overheating and fire. Ag is most common metal used in transparent conducting electrodes because of its alluring electrical, thermal and optical properties[149]. When the Ag layer thickness is less than 10 nm, it exhibits transparency for visible light. High transmittance values can be achieved using very thin films of Ag[72].

Other than this, alloys of Ag assist in improving the stability of electrode by avoiding any increase in shear resistance. Addition of silver layer to the multilayer enhances its electrical and corrosion properties[150].

3.1.4 Gold

Group 11 element, gold (Au) has atomic number 79 in the periodic table, known as one of noble metals. The density of gold is 19.3 g/cm3 and exhibits FCC structure[110]. An electrical resistivity of approximately 2.2×10^{-6} Ωcm makes it suitable for electrode application in devices[110]. Gold is also important for technological applications and hence research, because of its noble nature, chemical inertness, large atomic weight, good conductivity and suitable optical properties for different applications[151]. Gold thin films are generally used as IR reflectors, heater/ de-icing windows and transparent electrodes[71].

3.2 Methods of Preparation of TCO

3.2.1 RF-DC Sputtering

Among various physical vapor deposition methods, DC sputtering is mainly used to for deposition of metals, while RF sputtering technique has been mostly used for the growth of oxides or insulators[61]. In this technique, ion source aimed towards the target collects the sputtered particles on a substrate, enabling deposition of the thin film. The experimental arrangement has cathode and anode positioned opposite to each other in a vacuum chamber, which when pumped to the desired base pressure, has a noble gas (usually argon) introduced in its chambers. After that, a high voltage is applied between cathode and anode, and a glow discharge is ignited. The ions are bombarded from target to be deposited onto the substrate leading to formation of high-quality thin film on the desired substrate[152]. The thickness of deposited film depends on the deposition rate of the materials used for sputtering and deposition time[153].

3.2.2 E-beam/ Thermal Evaporation

It is one of most common techniques of all physical vapor deposition techniques for thin to thick film deposition. Thermal evaporation is generally used for metallic layer deposition, while e-beam for dielectric or semiconducting materials. In thermal evaporation technique, the element is heated by resistive heating up to a certain temperature so that the target material melts and evaporates towards the substrate due to vacuum. Generally, vacuum during deposition is kept 1×10^{-6} mbar to enable maximum mean path of evaporated material. This evaporation technique uses low voltage and high current, while in e-beam, high voltage and low current is required. In e-beam technique the target element is impacted by highly energetic dense electron

beam creating very high temperature locally. Due to this high-energy transfer, the target material evaporates and is deposited on the substrate[154].

After depositing thin films of desired thickness, the multilayer structures were exposed to energetic ion beams to check the stability of the grown multilayer TCO structure in radiation environment. For this, the effect of low energy as well as swift heavy ions on the stability of the devices were studied.

3.3 Post Treatment Methods

3.3.1 Swift Heavy Ions Irradiation

Ions exhibiting the energy between tens of MeV to few GeV are termed as swift heavy ions (SHI). SHI has been used extensively to tune various properties of material. The alteration in the properties of material is mediated by the interaction between target and incident ions which is primarily dependent on the choice of energetic ions, energy and total dose given to the target[133]. When an energetic ion traverse through material, it loses energy in two ways (i) elastic collision with target nuclei termed as nuclear energy loss (S_n) and (ii) through inelastic collision by electrons in the target which is termed as electronic energy loss (S_e). The electronic energy loss dominates over nuclear energy loss in the high-energy regime and it creates the changes though the path of the ions traversing though material. These changes include creation of defects and rapid annealing along the track of ion through material.

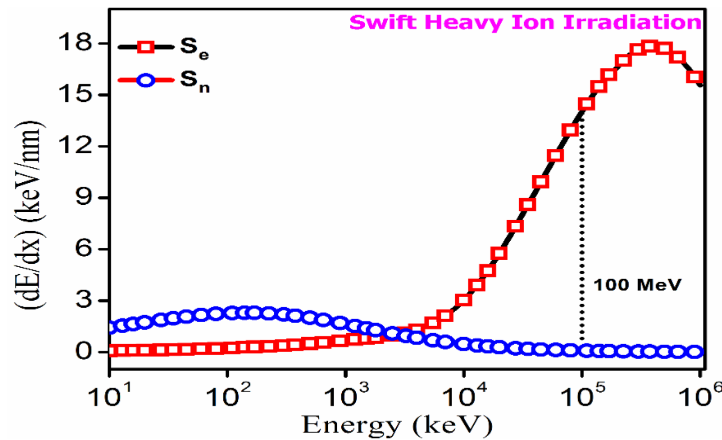

Figure 3.2 3.2 Energy Loss distribution in the 100 MeV swift heavy ion in the target material.

3.3.1.1 Pelletron Accelerator

In the present study, “15 UD Pelletron accelerator” available at Inter University Accelerator Centre (IUAC), New Delhi, India was used. This is a tandem Van de graaf type electrostatic accelerator that can produce ions having energy ranging from few tens to hundreds of MeV. The source of negative ions by cesium sputtering (SNICS), is being routinely used as ion source for accelerators and ion implanters. These sources can produce negative ions with currents ranging from a few μA to several mA.

In the accelerator, SNICS works as shown in Fig. 3.3. Cesium (Cs) vapor is formed by electrical heating of Cs ion source which falls on the area enclosed between cathode (which is kept cooled) to heat the surface of the ionizing material. Cool cathode condenses some of the cesium on the front and some Cs ionizes to Cs^+ ion because of hot surface. Cs^+ ions are accelerated by applying suitable voltage across the ionizer and the cathode. The Cs^+ ions impinge on the target and sputter the target atoms. The sputtered material may consist of neutral atoms or positively and negatively charged ions. Neutral or positively charged atoms will take up electron/s on passing through the condensed layer of cesium and thus produce negatively charged ions. These ions are

then repelled by the cathode voltage towards the ionizer and then are made to pass through a hole to the ground potential of the extraction electrode.

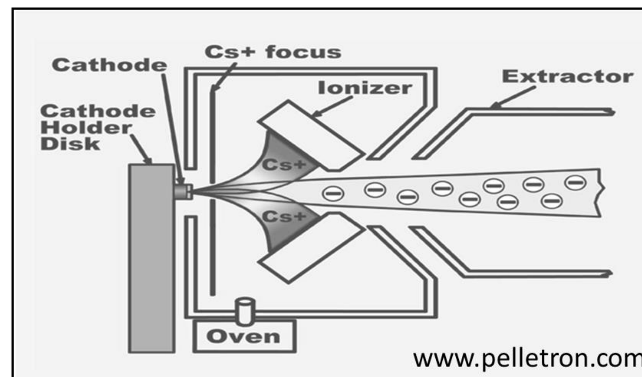

Figure 3.3 Schematic diagram of source of negative ions by Cesium Sputtering (SNICS)

3.3.1.2 Material Sciences Beam Line

The SHI Irradiation of stacked multi-layered thin films are performed in a high vacuum (10^{-6} torr) chamber. The fluence of rastering ions is counted by number of counts using Faradey cup by using the following formula:

$$number\ of\ counts = \frac{fluence \times q \times 1.6 \times 10^{-19}}{pulse\ height}$$

Where, q is ionic charge state and fluence is given in ions/cm^2. Using this formula, counts and time required for particular fluence in irradiation is calculated. In swift heavy ion irradiation, high energetic ions are incident on the target materials, they transfer a large amount of energy during passing the target. This produces high density of electronic excitation along the ion path in the narrow cylindrical zone. High amount of deposited energy leads to the large density of defects in the target material due to the localised heating effect along the ion path. These defects and a large amount of energy in the target material are responsible for the structural, electrical and optical modifications by SHI irradiation.

3.3.2 Low Energy Ion Implantation

Implantation of materials with beam of energetic particle is a standard tool for modifying the material properties. In this process, foreign atoms can be introduced in the host material. Implantation creates local amorphous region or recrystallizes the lattice depending upon the type of the host material. Ion implantation technique has been successfully demonstrated its usage in modification/tuning of materials' properties. The control over the desired material parameter with this technique is superior compared to any other physical/chemical technique. This process make use of variety of ion beams generated from an ECR source and mass analyzed by a dipole magnet. The primary loss of energy in ion implantation is through nuclear energy losses and when an ion enters the material, it transfers the energy to the host lattice thereby creating a collision cascade which is responsible for production of lattice defects. This creation of defects depends on energy/mass of incoming ion, fluence, implantation angle, temperature of target and radiation hardness of material. After a series of inelastic electronic collisions, the atom losses its entire energy and gets implanted.

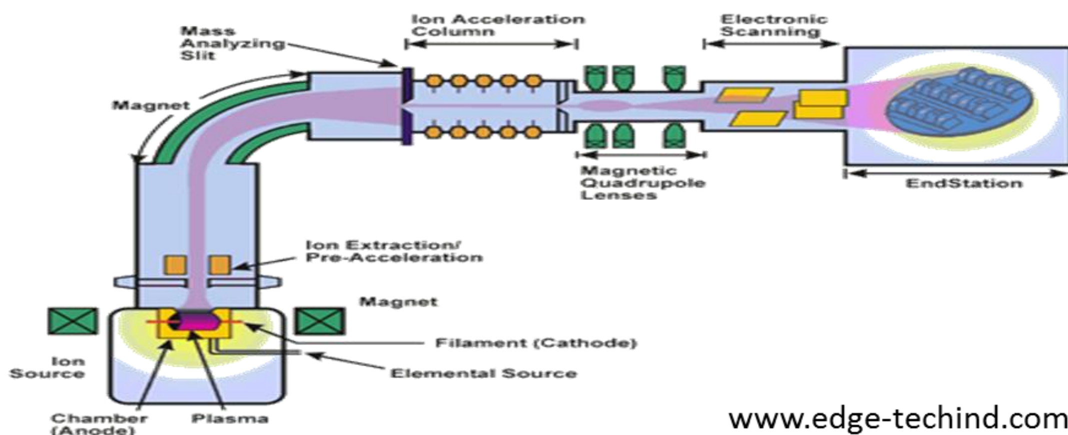

Figure 3.4 Schematic diagram of low energy ion beam implanter at Inter University Accelerator Centre, New Delhi.

3.3.3 Gamma Irradiation

In addition to the SHI and ion implantation, Gamma irradiation has also been selected as a tool to simulate the high radiation environment for testing TCO films for space application. For this purpose, the Gamma irradiation facility of Inter-University Accelerator Centre, New Delhi is used which employs radioactive material (cobalt-60) housed inside a Gamma Chamber (GC-1200). This chamber is designed to withstand gamma irradiation generated by a maximum activity of 185 TBq (5000Ci) of Cobalt-60 source. It offers various doses viz. 1Gy to 200Gy with an equivalent fluence of 1 x 10^{14} gamma/cm^2 to 1 x 10^{17} gamma/cm^2.

3.4 Characterization Techniques

3.4.1 X-ray Diffraction (XRD)

Figure 3.5 X-pert pro Panalytical model at MRC, MNITJ.

Crystal structure of a thin film can be determined by X-ray diffraction (XRD)[155]. XRD is a very useful technique for determining the orientation and crystallinity of grown films. The working mechanism of XRD is based on scattering of X-rays by atoms or planes through atomic points in the crystal lattice. XRD can be used to study the structures and crystallite size of the material. It can also be used for:

- Measurement of average spacing between layers or rows of atoms. The orientation of single crystal planes or grains.
- Determination of lattice constant.
- Measurement of shape, size and internal stress of small crystalline regions, by determination of lattice mismatches between films and substrates.
- Determination of dislocation density and quality of film by rocking curve measurements.

3.4.2 Rutherford Backscattering Spectrometry (RBS)

Rutherford backscattering spectrometry (RBS) is best technique to determine the thickness of thin and elemental composition[156]. This technique is based on scattering of α-particles from the nuclei in the target material. Transfer of energy between nucleus and alpha particles takes place during interaction and the particles are back scattered. This back scattered ion energy depends on the atomic number of target atom. On this basis, one can identify the elements present in the target. This scattering is independent of the stoichiometry and bonding of target material. The energy of α-particle is near about 1.5 to 3 MeV. RBS can be also used to determine the diffusion at the interface for multilayer.

3.4.3 X-ray Photoelectron Spectroscopy (XPS)

Photoelectron Spectroscopy is based on collection of photoelectrons emitted upon illumination of either ultraviolet or X-rays onto the samples. The number of electrons ejected from the sample surface and detected by the analyzer are plotted with respect to the binding energy of the electrons. The spectrum hence obtained provides information on the electronic structure as well as the chemical bonding and composition of the molecules[157].

XPS is surface sensitive technique and is used to analyze the surface chemistry the material being studied. Depth profiling can be done to expose deeper layers of the material by etching the sample with ions. Spatial distribution information is obtained by scanning focused X-ray beam across the sample surface. Peaks in the graph plotted between binding energy and intensity depict photoelectrons ejected without energy loss and the background is formed by photoelectrons with energy loss. Identification of the element present and its quantitative and chemical analysis is provided by the intensity and binding energy of the photoelectron peaks. The layers of thin film and its composition play an important role in the determination of the composition of elements. Quantitative analysis by XPS is found to be more accurate in comparison to other techniques. Detailed working of XPS is shown in the figure below.

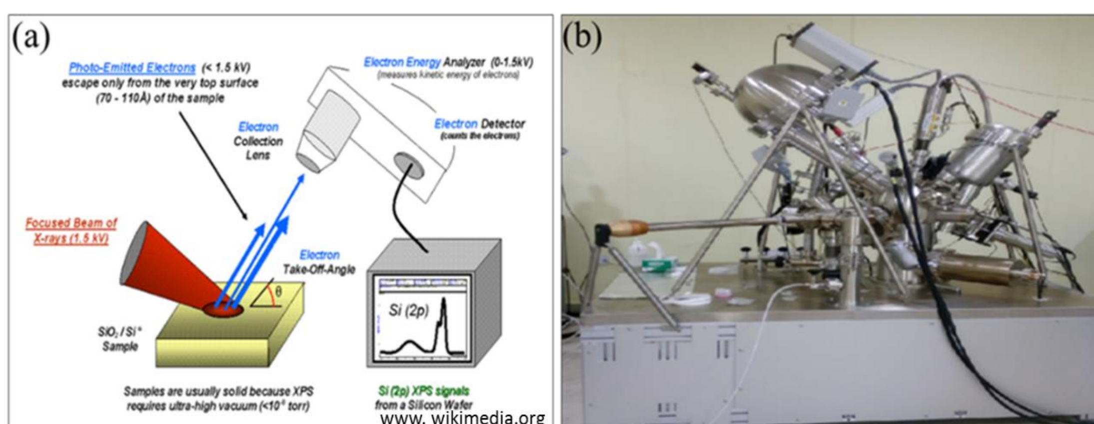

Figure 3.6 3.6 (a) Schematic representation of the working of XPS (b) XPS instrument (Omicron ESCA) at MRC, MNITJ.

3.4.4 Atomic Force Microscopy (AFM)

AFM gives the topographic images of samples under study by sensing the atomic (van der Waal) forces between a sharp tip and the sample. A schematic diagram of how AFM works is shown in Fig. 3.7(a). Here, the tip is mounted onto a cantilever. The head of the tip is coated with a reflecting material like gold and it is illuminated by a laser light. The reflected light is then collected on a quadrant photodiode. Any

deflection in the tip due to its interaction with the sample is monitored by measuring a distribution of light intensity in the photodiode. The tip is often made of silicon or silicon nitride with a width of ~10 nm. There are three main modes for AFM image acquisition; contact mode, non-contact mode and tapping or intermittent mode. The tapping mode has been used for most of the results acquired in this work. In tapping mode, the cantilever is set in resonant vibration, which is affected by the van der Waals forces between the tip and the surface as it approaches the sample surface. A topography image is acquired by scanning the tip over the surface while monitoring the resonant frequency. The technique is very suitable for obtaining direct information of topographical attributes such as surface roughness and crystallite features[158].

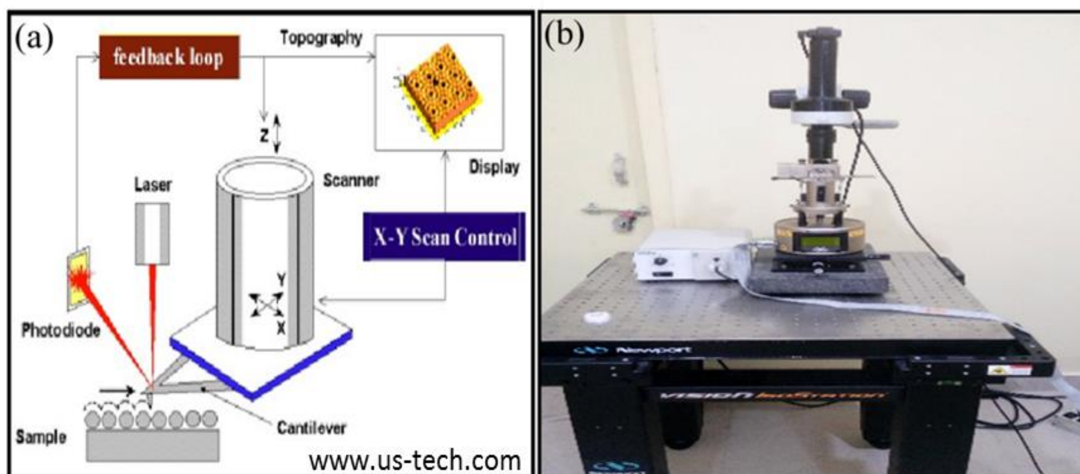

Figure 3.7 (a) Block diagram of Atomic Force Microscopy (b) Multimode Scanning Probe Microscope AFM at MRC, MNITJ.

3.4.5 Field Emission Scanning Electron Microscopy (FESEM)

In FESEM, a focused beam of electrons generated using a high electric field scan the surface of the sample and the signals produced in the form of secondary electrons, back scattered electrons and characteristic X rays are collected to create an image of the surface. Schematic diagram of working principle of FESEM is shown in Fig.3.8 Field emission (FE) is the emission of electrons from the surface of a conductor

caused by application of strong electric field. An extremely thin and sharp tungsten needle (tip diameter ~100 nm) is employed as a cathode. The acceleration voltage between cathode and anode is commonly ~ 0.5 kV to 30 kV. The apparatus requires an extreme vacuum (~ 10^{-9} Torr) in the column of the microscope. Because the size of electron beam produced by the FE source is about 1000 times smaller than that in a standard microscope with a thermal electron gun, the image quality is markedly improved.

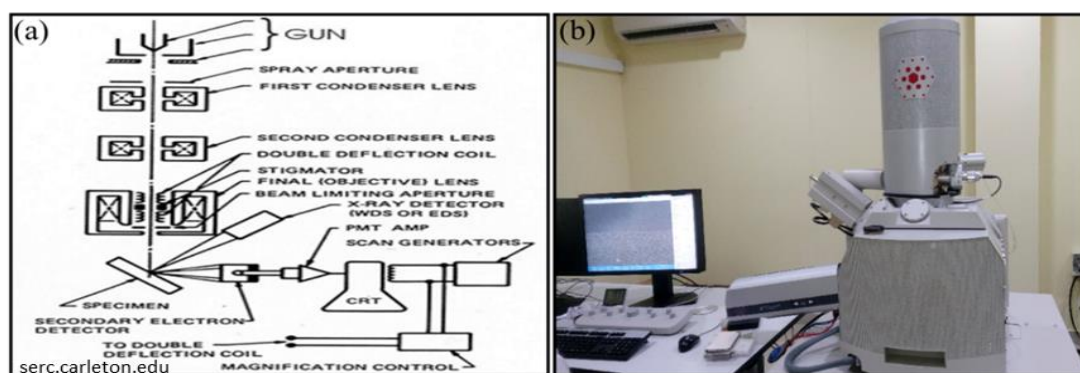

Figure 3.8 3.1 (a) Schematic diagram of components of Scanning electron microscope (b) Nova Nano FE-SEM 450 (FEI) at MRC, MNIT Jaipur.

FESEM is a very useful tool for high resolution imaging of surfaces. It is used to provide high resolution images giving information about surface topography, crystalline structure, composition, and electrical behavior of a specimen surface. It is essential to have the top surface of the sample as conducting. Non conductive or less conducting specimen are coated by a thin metallic or carbon coating to prevent accumulation of charge on the surface which degrades the image to be obtained[159].

3.4.6 Transmission Electron Microscopy (TEM) with EDS

Transmission electron microscopy (TEM) is a well-known technique and a powerful tool to obtain microstructural information viz. crystallinity and other internal features from a very thin sample. In TEM, electron beam emitted by an electron gun in

high vacuum environment is made to transmit through the specimen. Electrons are released from cathode on application of accelerating voltage with a small emission current. These electrons are accelerated by the presence of anode creating a positive attraction. The beam of electrons is controlled using electromagnetic lenses (wrapped copper wires) to focus it on the specimen. Apertures are used to adjust the contrast to enhance the quality of the image. Electron beams exiting the sample are made to fall on a phosphorescent screen or a CCD through projector lens.

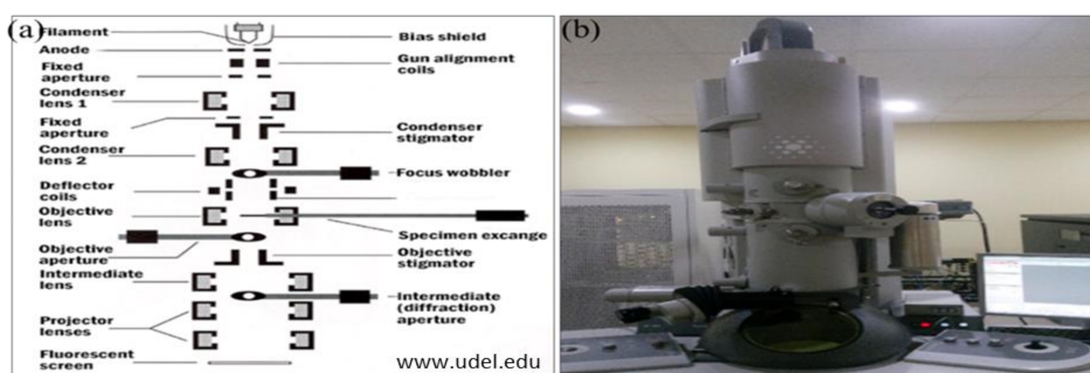

Figure 3.9 (a) Schematic representation of components of transmission electron microscope (TEM) (b) Tecnai G2 20(FEI) HR-TEM at MRC, MNITJ.

HR-TEM is capable of providing nanoscale information of the crystalline/polycystalline material by creating specimen image through interference between transmitted and scattered electrons. The bright field mode is the most commonly used mode for contrast formation. The image is formed by direct occlusion and absorption of the electrons by specimen. In dark field imaging the main electron beam is blocked by the aperture and the diffracted beam is used to generate the specimen image. Dark field mode is useful for thin film imaging. Point and area mapping through EDS gives the elemental analysis of a sample in that particular region. Area mapping is more useful in the sense that it provides more terms of element distribution and density[160].

3.4.7 UV–Vis Spectroscopy

As described earlier, light falls on to a material can either be reflected, transmitted or absorbed. The way a material interacts with light at varying wavelengths can give us useful information about the material. The principle of absorption spectroscopy is based on Beer's and Lambert law; it states that fraction of incident radiation absorbed is proportional to the number of absorbing molecules in its path. More is the absorption of light; higher is the peak intensity of absorption spectrum. In the present study, UV-Vis-IR light has been used for finding the transmittance of samples under investigation. By using UV-VIS-NIR spectroscopy on TCO materials, it is possible to determine the optical band gap of the material by Tauc's plot using fundamental absorption edge in the UV region. Absorption in the visible range can indicate impurities while the absorption/reflection in the near infra-red region gives an indication of the carrier concentration. This is an important feature if the material is to be used as front contact on a solar cell that utilizes NIR radiation[161].

Figure 3.10 UV/Vis/NIR Lambda 750 (Perkin Elmer) Spectrometer at MRC, MNITJ

3.4.8 Hall Measurement

Hall effect is one of the most common and comprehensive measurement for understanding transport properties of material by finding out charge carrier mobility (μ), concentration (n), type of conductivity (N or P) and sheet resistance. Sheet

resistance (given in ohms (Ω) per square) parameter is one of the important parameters used for evaluating the electrical performance of transparent conducting film. behavior of free charge carriers in a semiconductor under the effect of transverse electric and magnetic field. When a current carrying, semiconductor is subjected to a magnetic field, voltage is produced across the specimen transverse to both current and magnetic field. The voltage so produced is called as Hall voltage. The direction of Hall voltage reflects the direction of induced Lorentz force and sign of the charge carrier.

The Van der Pauw method is a technique commonly used to measure the resistivity and the Hall coefficient of a sample. It gives quite accurate results and can be used for any arbitrary shaped but two-dimensional sample. The sample should be solid and uniform with no holes. The van der Pauw method employ four-point probes placed around the perimeter of the sample which allows measurement of average resistivity, whereas a linear array would provide resistivity in the sensing direction only.[162]

Figure 3.11 (a) Sample holder used for the Van der Pauw measurements for Hall effect (b) Pictorial representation of the different components of Hall measurement apparatus.

Chapter-4

Fabrication and Characterization of SnO_2-Ag-SnO_2 Multilayer Thin Films and Their Ion Beam Effects

4.1 Introduction

This chapter reports the synthesis (SnO_2-Ag-SnO_2) samples using RF-DC sputtering technique and optimization of thickness of the sandwiched Ag layer keeping thickness of SnO_2 layers constant. Earlier studies have shown that SnO_2 thickness in the range of 25-45 nm[99] gives maximum transmittance for visible light[96] while Ag layer gives the best result in terms of electrical conductivity and optical transparency below 15 nm when it is a continuous layer[101]. It is known that the structural, morphological and optical and electrical properties of oxide-metal-oxide structure are modified due to metal layer formation and thickness[79]. In view of this, effect of Ag layer thickness sandwiched between two SnO_2 layers on the above properties of SnO_2-Ag-SnO_2 multilayer was investigated. Transmittance, absorbance and reflectance of the multilayer vary with thickness and hence the calculated values of reflective index and extinction coefficient also show a change. Furthermore, increase in Ag thickness improves the electrical conductivity at the cost of reduction in transparency. Therefore, optimization of sandwiched metal (Ag) layer is a prime requirement not only to get best optoelectronic properties but is also important for other commercial applications.

4.2 Experimental Study

The SnO_2-Ag-SnO_2 multilayer structure was deposited by RF-DC sputtering technique using standard commercial targets of SnO_2 and Ag. The oxide layers of SnO_2 (35 nm) were deposited on quartz substrates at room temperature. Ag layers with

different thickness were then deposited on SnO_2 dielectric layer by DC sputtering using 99.99% Ag target. Finally, SnO_2 (35 nm) top layer was deposited on the Ag/SnO_2/quartz structure again by RF magnetron sputtering technique. The base pressure of the chamber was maintained at 5×10^{-6} mbar and working pressure was 1×10^{-3} mbar during SnO_2 deposition and 1.5×10^{-2} mbar for Ag deposition. The power was 100 W for RF and 15 watt for DC sputtering. The flow of argon (Ar) was kept 15 sccm for both processes and deposition rate obtained for SnO_2 and Ag films were 2 Å/ sec. and 6 Å/ sec, respectively. The target to substrate distance was 10 cm and the deposition was carried out at room temperature (300 K i.e without substrate heating). Crystalline properties of SnO_2-Ag-SnO_2 (SAS) multilayer were observed using XRD with CuK_α radiation. Thickness of the films was calculated using Rutherford backscattering (RBS) with 2 MeV He^+ ion beams at IUAC, New Delhi (India). The surface morphology of SAS multilayer films was observed by FE-SEM and AFM measurements. The optical transmittance of SAS multilayer was measured using UV−Vis spectrophotometer with bare quartz substrate as reference in the spectral range of 400−800 nm at room temperature. The electrical properties of SAS multilayer were then investigated using ECOPIA-3000 room temperature Hall Measurement system with 0.55 Tesla magnet.

In the first part, SAS structure with Ag thickness from 8 nm to 30 nm was deposited to optimize the Ag thickness range making the structure suitable for electrode applications in optoelectronics.

4.3 Results and Discussion

4.3.1 X-ray Diffraction

XRD patterns of SAS multilayer films with varying Ag layer thickness are shown in Fig. 4.1. The elimination of preferred orientations for all samples occurs due to the amorphous state of SnO_2 in the multilayer since it is a room temperature deposition on an amorphous substratre[137]. The absence of preferred orientations is also due to small thickness of tin oxide[163]. The amorphous nature of SnO_2 for room temperature deposition and such lower thicknesses have been observed by several other researchers in recent past[52]. The peak corresponding to (111) plane of Ag is observed for thicknesses other than 4 nm and the intensity increases with Ag thickness. An additional peak at 2θ value of ~ 44.23° corresponding to (200) planes of Ag is also observed for higher thickness (20 and 30 nm). The increase in peak intensity of (111) and (200) peaks with thickness of Ag indicates an improvement in the crystalline nature of sandwiched Ag layer.

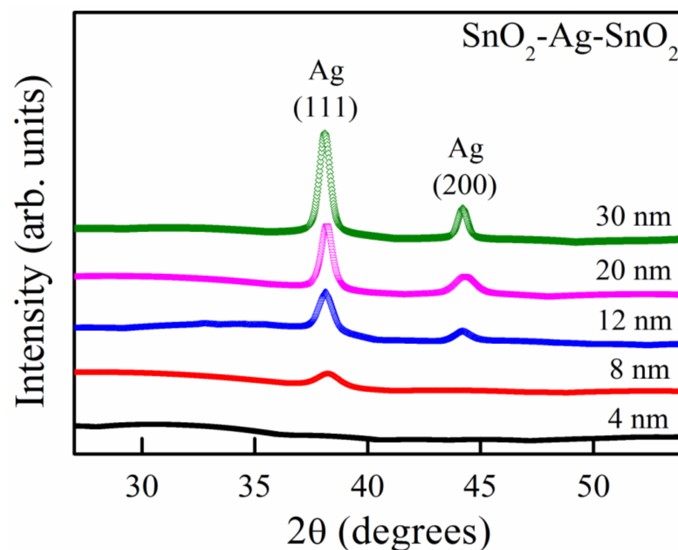

Figure 4.1: XRD pattern of SnO_2-Ag-SnO_2 with different Ag thickness (4-30 nm).

4.3.2 Rutherford Back Scattering Spectrometry

In order to determine the film thickness and composition of the SAS in the multilayer structure, RBS measurements were carried out and fitting was done using the X-RUMP simulation[164] for the SAS structure of 8 nm Ag thickness is shown in Fig. 4.2. The elemental peaks corresponding to Sn, O and Ag appear in RBS spectrum. The thickness of individual layers was measured from the fitted curve and obtained as SnO_2 (40±5 nm)/Ag (8±1nm)/ SnO_2 (40±5 nm). The ratio of Sn and O in top and bottom layer is ~30:70. Results indicated the formation of SnO_2 with metallic Ag. It indicates the deposition of SnO_2 layer with pure Ag interlayer with some spreading of Ag atoms into the SnO_2 layer at the interface.

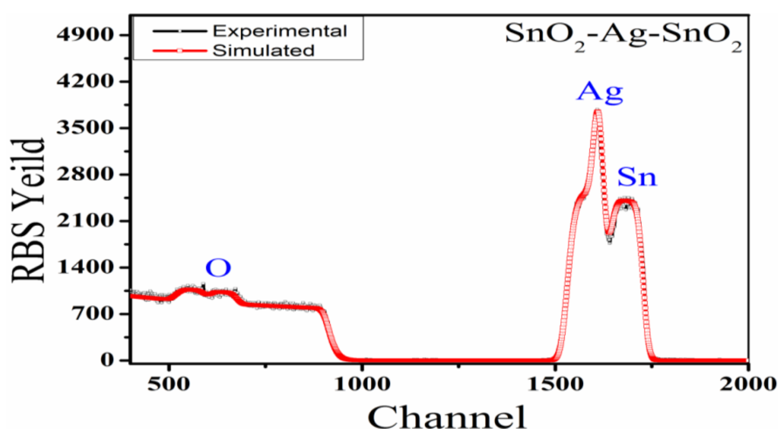

Figure 4.2: RUMP fitted RBS spectra of SnO_2-Ag-SnO_2 with Ag thickness of 8 nm.

4.3.3 Scanning Electron Microscope

The surface morphology of SAS films samples with different Ag thicknesses was characterized by FE-SEM and images are shown in Fig. 4.3 (a-e). SEM images show the presence of the round shape particles grown on the surface. Particle size calculated using SEM images and its variation with Ag layer thickness is shown in Fig. 4.3 (f)[165]. Particle size is seen to be changing with thickness of Ag layer and shows an increase, 12 nm for 4 nm thick layer and ~17 nm for Ag layer thickness of 12 nm. Further an increase in thickness gives a smaller particle size. Small islands of Ag join

together to make a continuous film as thickness increases[100]. It can be clearly seen from SEM images that there is no morphological change of top surface with Ag thickness variation.

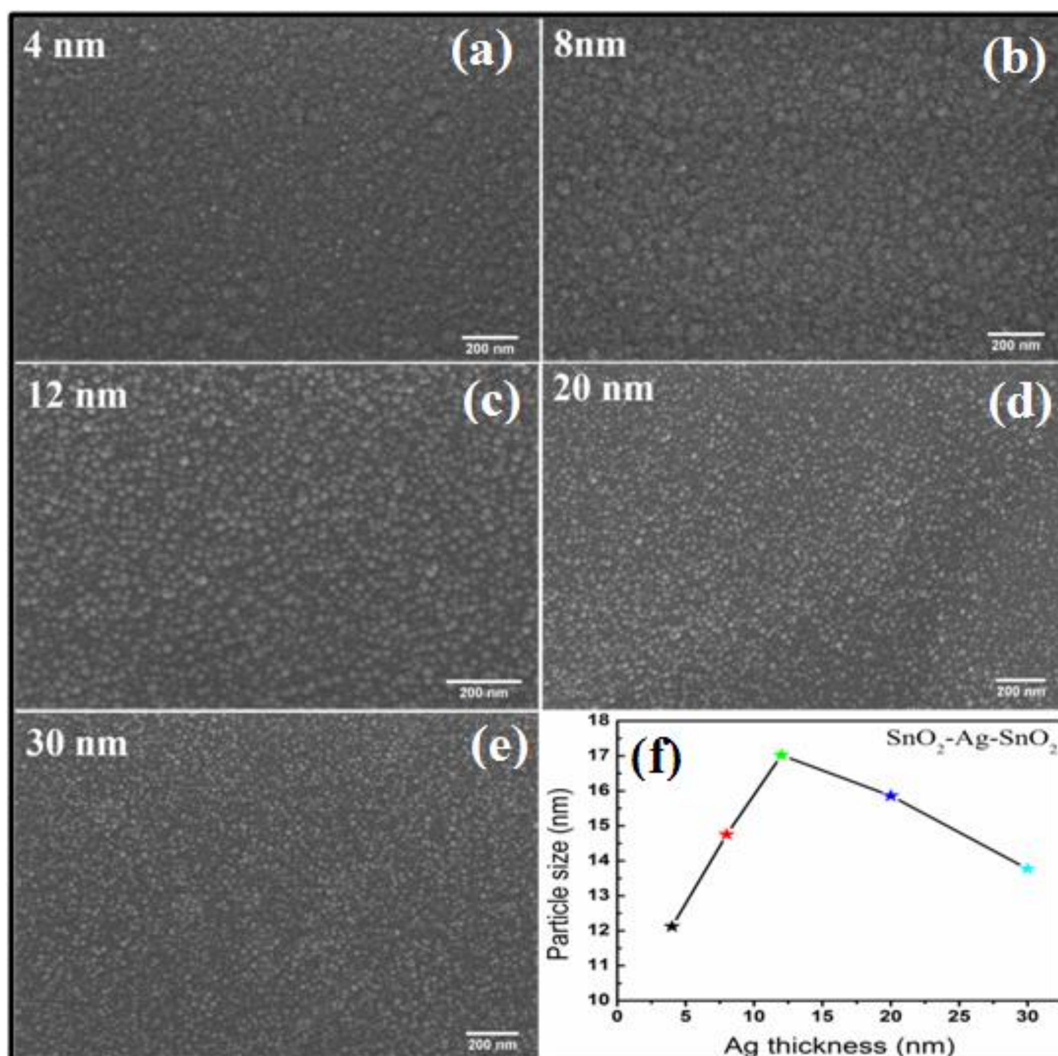

Figure 4.3: SEM micrographs of SnO_2-Ag-SnO_2 with different Ag thickness (4-30 nm) (a-e) and variation in particle size of top SnO_2 layer shown in (f).

4.3.4 Atomic Force Microscope

Fig. 4.4 (a-e) show AFM images[158] of SAS multilayer structure for different Ag thickness. AFM images show upper layer of SnO_2 as smooth and homogeneous[166]. The root mean square (RMS) surface roughness for the 4 nm Ag thick sample was observed to be ~ 0.72 nm. It increases and attains a maximum RMS value of ~ 1.1 nm

for 12 nm thick Ag layer. Further increase in Ag thickness leads to a slight reduction in RMS roughness to ~ 1.0 nm. Fig. 4.4 (f) shows the surface roughness variation curve with Ag layer thickness. The variation in RMS value is very low and the values are much below the acceptable value for device formation which is ≤ 3 nm, and is an important parameter for electrode application[2]. Low surface roughness is required for efficient operation of devices because higher roughness of electrode degrades the transmittance due to increased scattering from the surface[167].

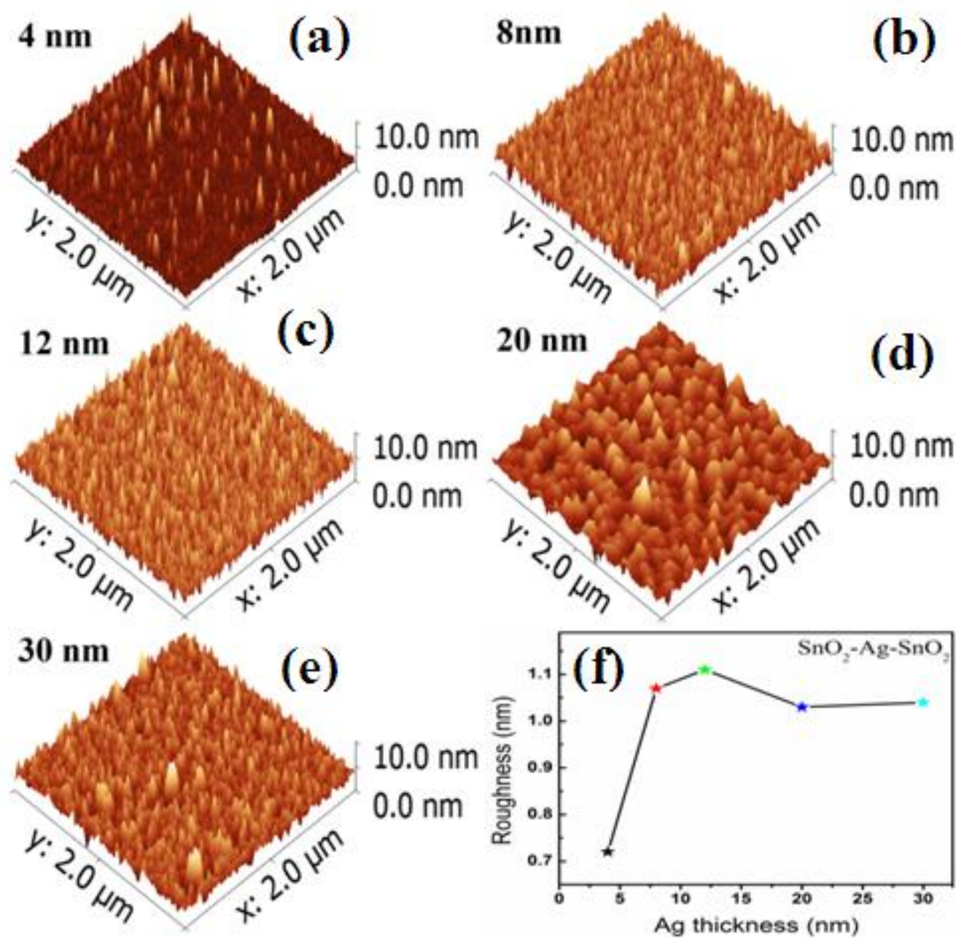

Figure 4.4: AFM images of SnO_2-Ag-SnO_2 with different Ag thickness (4-30 nm) (a-e) and variation in roughness curve shown in (f).

4.3.5 Transmission Electron Microscope

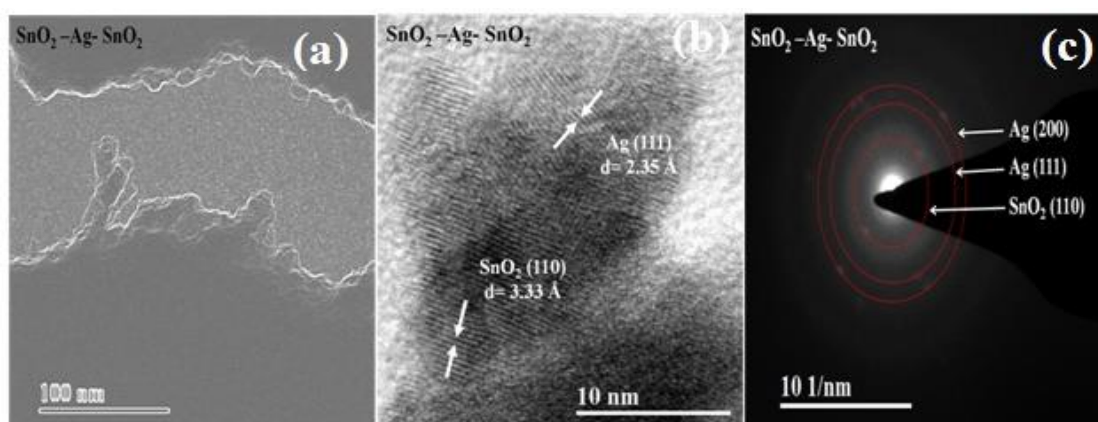

Figure 4.5: TEM micrographs of SnO_2-Ag-SnO_2 for 8 nm Ag thickness sample. (a) Image of stacked multilayer structure, (b) High resolution image of SAS structure and (c) Observed SAED pattern for SAS multilayer.

The microstructure of SAS multilayer films was characterized by TEM. TEM and selected area electron diffraction (SAED) investigation of the as-deposited SAS thin films gives further insight to understand the crystallinity behavior of SnO_2 and Ag. The SAS films were deposited on the TEM grid prior to analyzing with TEM. Fig. 4.5 shows the TEM results for SAS films. The overlap of the multilayer in the structure can be clearly seen from the Fig. 4.5 (a). The embedded stacked layers of silver[168] and tin oxide[169] are visible in between the torn parts of deposited film on the grid. Fig. 4.5 (b) exhibits the high-resolution images obtained from TEM. These images were analyzed by digital micrographs[170] to calculate the distance between two planes. The d-spacing for SnO_2 (110) and Ag (111) planes was found to be 3.33 Å and 2.35 Å, respectively. Fig. 4.5 (c) shows the SAED pattern for SAS films and consists of SnO_2 (110), Ag (111) and Ag (200) planes. TEM results indicate the polycrystalline nature of SnO_2 and Ag in the multilayer films.

4.3.6 UV-Vis Spectroscopic Study

Fig. 4.6 exhibits the transmittance and absorbance spectra of the SAS multilayer films for different Ag thickness. The average transmittance obtained is ~ 80 % for the least thickness (4 nm) of Ag layer and decreases to ~ 60 % for 30 nm thick Ag layer. Reflection increases with Ag thickness leading to decrease in transmittance. The optical properties of DMD multilayer are much affected by the thickness of Ag layer[41]. For 20 nm or greater thickness, the film acquires properties close to that of bulk metal, hence loss of optical band gap is observed. The optimized thickness of middle silver layer reported by various groups is found to be ~ 9 nm[99,96]. It has been observed that the electrical and optical properties of stacked multilayer structure are enhanced at the optimized thickness[171]. Further an increment in the Ag thickness causes degradation of both electrical as well as optical properties. Change in optical transmittance with Ag layer thickness provides an opportunity to tune properties as per requirement.

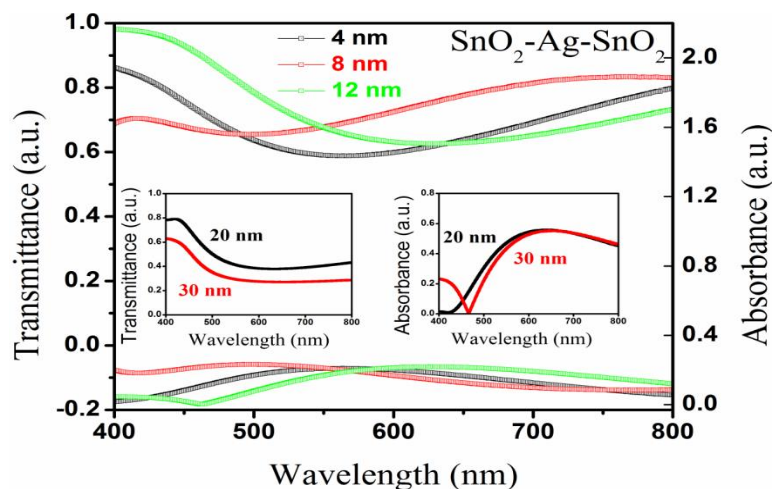

Figure 4.6: UV-Vis spectra of SnO_2-Ag-SnO_2 with different Ag thickness (4-12nm) and inset shows spectra for Ag thickness of 20 nm and 30 nm.

The best results in terms of transparency are obtained for 8 nm Ag layer as compared to that for 4 and 12 nm thick Ag layer. This is because a continuous film is formed at ~ 8 nm giving less scattering from its surface and lesser reflectance and

absorbance. For higher values of Ag thickness, transmittance is reduced by increased reflection due to thicker metal layer.

The absorption coefficient, band gap, refractive index and extinction coefficient have been calculated for SAS films and results were found appropriate for their application as a transparent electrode[33]. The band gap of the SnO_2-Ag-SnO_2 multilayer structure was calculated using Tauc's relation[172]

$$\alpha h\nu = A(h\nu - E_g)^{1/2}$$

where hν is the photon energy, α is the absorption coefficient, E_g is optical band gap and A is a constant.

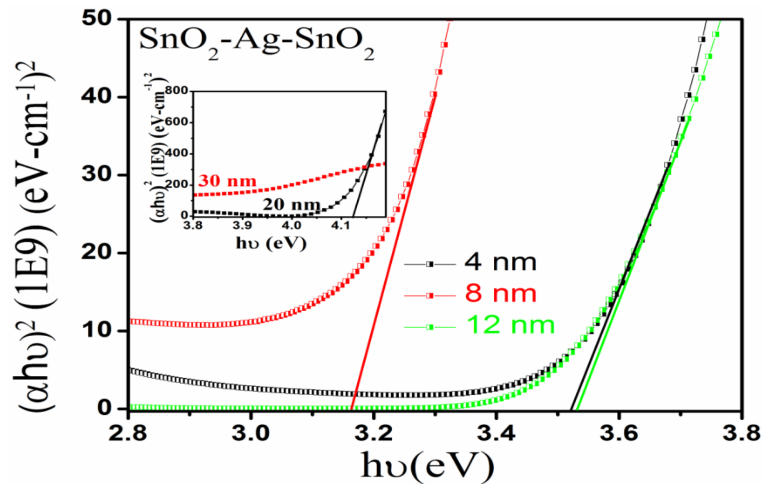

Figure 4.7: Tauc's plot for SnO_2-Ag-SnO_2 multilayer with varying Ag thickness (4-12 nm) and inset shows plot for Ag thickness of 20 nm and 30 nm.

The band gap increases from 3.5 eV to 4.1 eV as Ag thickness varies from 4 nm to 20 nm. The variation of band gap of the SAS films with different Ag thickness is shown in Fig. 4.7. The optical band gap of 4 nm silver layer was obtained 3.5 eV and it decreases to 3.18 eV for 8 nm thin Ag layer in stacked multilayer structure. Further, it increases to 3.5 eV and 4.1 eV for the 12 nm and 20 nm Ag layer respectively.

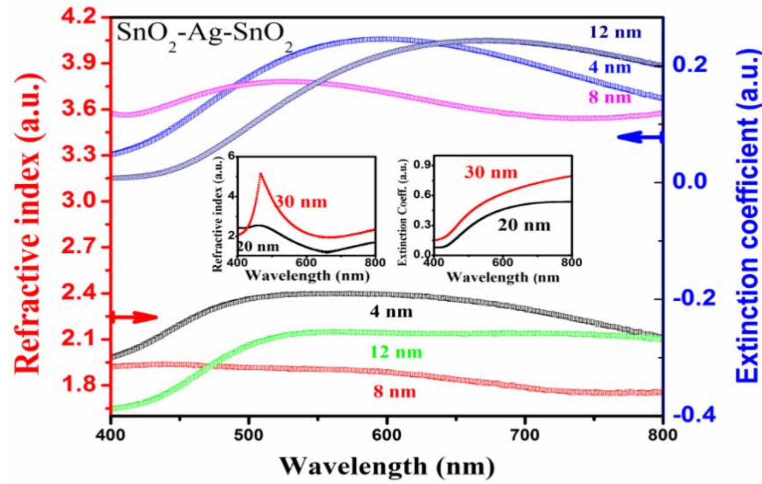

Figure 4.8: Refractive index (η) and extinction coefficient (κ) of SnO_2-Ag-SnO_2 with different Ag thickness (4-12 nm) and inset shows value of η and κ for Ag thickness of 20 nm and 30 nm.

4.3.7 Hall Measurements

Good electrical conductivity with optimum charge carriers and mobility is an essential parameter for the transparent electrode in optoelectronic devices application[142].

These SAS films are promising alternative option to ITO-based films, so it is a prime concern that these films have comparable electrical properties to the commercial ITO. To measure the carrier concentration, mobility, and electrical resistivity, Hall Effect measurements were carried out at room temperature. Fig. 4.9 shows the charge carrier concentration, mobility and sheet resistance of films for different thickness of Ag film. The charge carrier concentration was found to increase from 2.9×10^{19} cm^{-3} to 2.1×10^{22} cm^{-3} and Hall mobility changed from 7 cm^2 V^{-1}s^{-1} to 25 cm^2 v^{-1}s^{-1} as the Ag thickness increases. On the other hand, the sheet resistance decreases from 2.3×10^3 Ω/□ to 2 Ω/□ with an increase in Ag thickness from 4 nm to 30 nm. At 4 nm thickness, the Ag layer is not continuous hence a very high resistance. As soon as the Ag layer attains continuity, the conductivity of structure increases significantely[99,173]. It can be

explained from the fact that at 4nm thickness islands which are isolated from each other combine at thickness ~ 8nm forming channels for electrical conduction[174]. Free electrons available in the Ag layer can easily be introduced into the SnO_2 layer because of an ohmic contact at the interface[41].

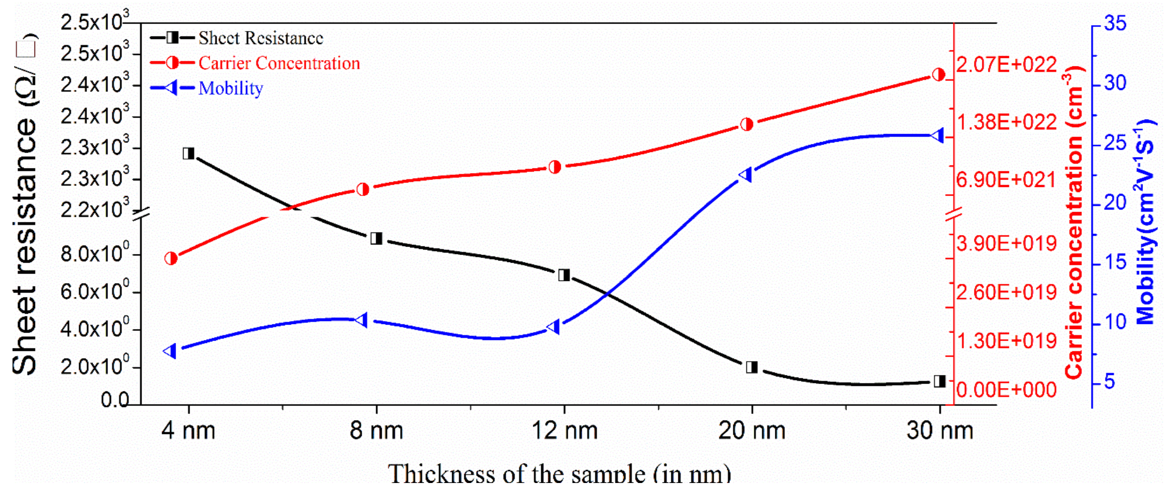

Figure 4.9: Hall measurements of SnO_2-Ag-SnO_2 with different Ag thickness (4-30 nm) indicating change in sheet resistance, mobility and carrier concentration.

4.4 Xe^+ Ion-beam (100 keV) Effect on SnO_2-Ag-SnO_2 Thin Films

Based on the results of an optimization study of sandwiched layer thickness, it is found that Ag layer thickness ~ 8-10 nm gives the best results among all thicknesses. Hence multilayers of SAS thin films deposited by RF-DC sputtering with 45 nm thickness for SnO_2 and 9 nm for Ag layer on quartz substrates were examined for the ion beam induced modifications[133] in the electrical and optical properties. Implantation and irradiation studies were performed on this multilayer structure. Ion implantation has been used to modify the structural[175], optical[127] and electrical[176] properties of tin oxide film[177]. The coming section and the section thereafter report the effect of Xe^+ ion beam of 100 keV energy of varying fluence and swift heavy ion irradiation on the electrical and optical properties of the films.

4.5 Result and Discussion

4.5.1 X-ray Diffraction

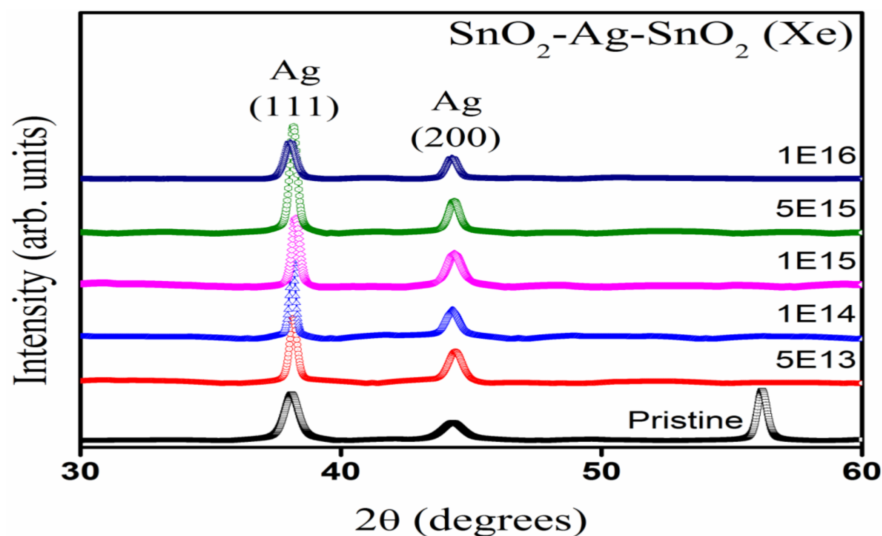

Figure 4.10: XRD pattern of pristine and Xe implanted SnO_2-Ag-SnO_2 films.

X-Ray diffraction patterns of pristine and implanted films with various fluences of Xe ion beam on SAS multilayer structure are shown in Fig. 4.10. The XRD pattern of pristine SAS structure has peaks corresponding to only Ag. There is no diffraction peak corresponding to SnO_2 which is amorphous because of its room temperature deposition[41]. The Ag peaks (111) and (200) are related to the face-centered cubic (FCC) JCPDS (04-0783)[175]. It can be clearly seen that Ag peak intensity increases up to the fluence of 5×10^{15} ions/cm^2 and then decreases for the highest fluence of 1×10^{16} ions/cm^2.

4.5.2 Rutherford Back Scattering

RBS spectrometry was performed in order to measure the thickness and composition of the multilayer thin films. The RBS spectra along with the RUMP fitted[164] pristine SAS multilayer structure for 9 nm thick Ag sample is shown in Fig. 4.11 (a). The elemental peaks of O, Sn, and Ag ions have been identified[169].

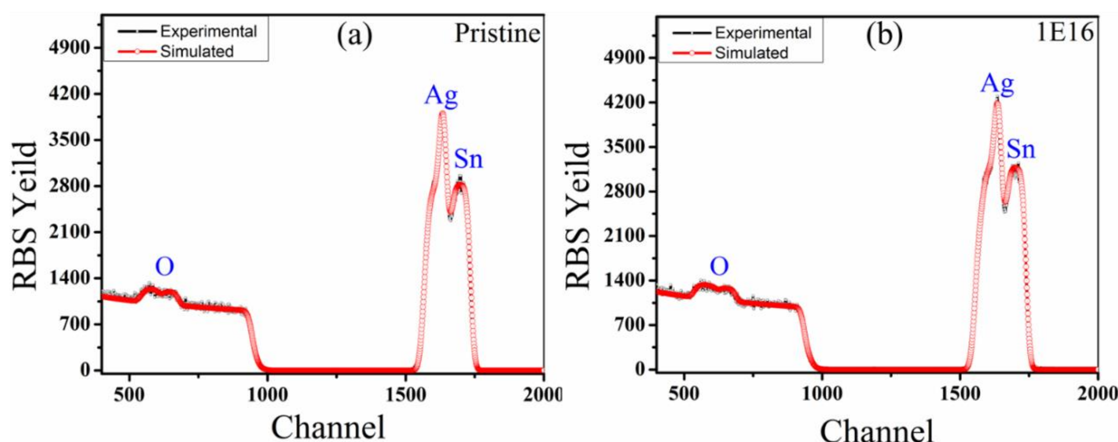

Figure 4.11: Experimental and Rump fitted RBS spectra of pristine (a) and 1E16 Xe implanted (b) SnO_2-Ag-SnO_2 films.

On analyzing the spectra with RUMP software, the thickness of the pristine SnO_2-Ag- SnO_2 multilayer structure is found to be ~ (45±5 nm) SnO_2/Ag (9±1nm)/ SnO_2 (45±5 nm). The analysis from RUMP shows formation of SnO_2 with pure Ag in the middle layer with small diffusion of Ag atoms into the SnO_2 layer at the interfaces. Implantation of Xe ions at the highest fluence of 1×10^{16} ions/cm^2 aggravates the diffusion of Ag ions into SnO_2 layers shown in Fig. 4.11 (b). The simulated thickness of Ag atoms in the SnO_2 layer is approximately 4 nm for both interfaces.

4.5.3 X-ray Photoelectron Spectroscopy

X-ray photoelectron spectroscopy[157] was used for elemental and chemical analysis of the SAS multilayer structure is shown in Fig. 4.12. Depth profiling was done using etching through Ar gas to find the chemical state of each individual layer of SAS structure. Figs. 4.12 (a-d) show XPS results of pristine and Xe ion implanted (at a fluence of 1×10^{16} ions/cm^2) SAS structure. Binding energy calibration is done by taking the C 1s peak at 284.6 eV. Fig. 4.12 (a) shows the survey spectrum of the SAS pristine and Xe implanted films.

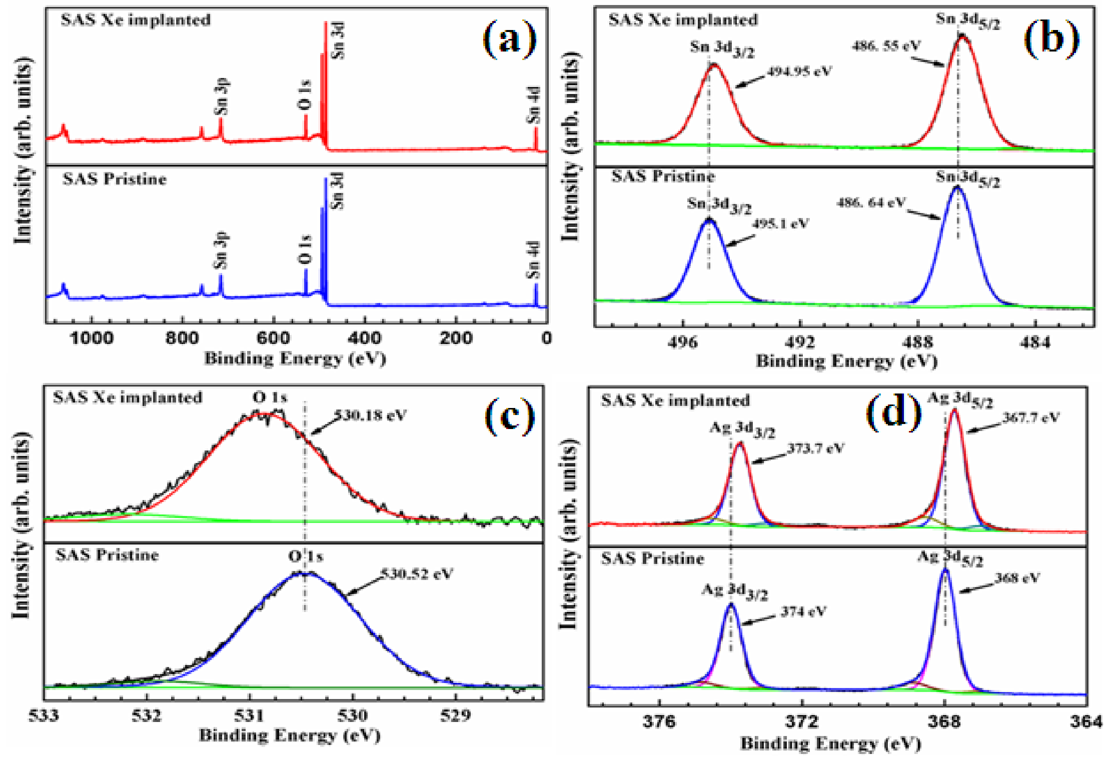

Figure 4.12. XPS spectra of pristine and Xe implanted SnO_2-Ag-SnO_2 films. (a) Survey scan for top layer SnO_2 layer, (b) Short scan for Sn, (c) Short scan for O and (d) Short scan for middle Ag layer in SAS structure.

The core spectrum of the Sn 3d is given in Fig. 4.12 (b)[166], Sn $3d_{3/2}$ and Sn $3d5_{/2}$ of the pristine film centered at 495.1 eV and 486.64 eV are shifted to lower binding energies of 494.95 eV and 486.55 eV, respectively mainly due to electron transfer from Ag to Sn oxide[177,178]. In the O 1s spectrum shown in Fig. 4.12 (c), the oxygen bound to tin for the pristine sample is seen at 530.6 eV[179] and shifts to lower binding energy 530.5 eV after Xe implantation. The observed shift in the O 1s peak is because of variation in oxygen vacancies on Xe ion implantation[180].

The core spectrum of Ag 3d is shown in Fig. 4.12 (d). The Ag $3d_{3/2}$ and Ag $3d_{5/2}$ peaks for pristine sample centered at 374 eV and 368 eV, are seen shifted to 373.7 eV and 367.7 eV, respectively after Xe implantation. Peaks for pristine films are shifted

towards lower binding energies than that for metallic Ag (Ag $3d_{3/2}$ at 374.2 eV; Ag$3d_{5/2}$ at 368.2 eV). This is because of electron transfer from metallic Ag to SnO_2 crystals[181,182]. Band bending occurs at the interface to match the Fermi levels of both materials[183]. Formation of SnO_2-Ag heterostructures takes place due to interaction of metal particles with the semiconductor oxide[6,11,36].

4.5.4 Scanning Electron Microscope

Surface morphology of pristine and Xe implanted SnO_2-Ag-SnO_2 multilayer thin films were investigated using SEM and AFM. SEM micrographs of pristine and implanted samples are shown in fig. 4.13. For all micrographs, well-defined crystals with sharp grain boundaries have been observed.

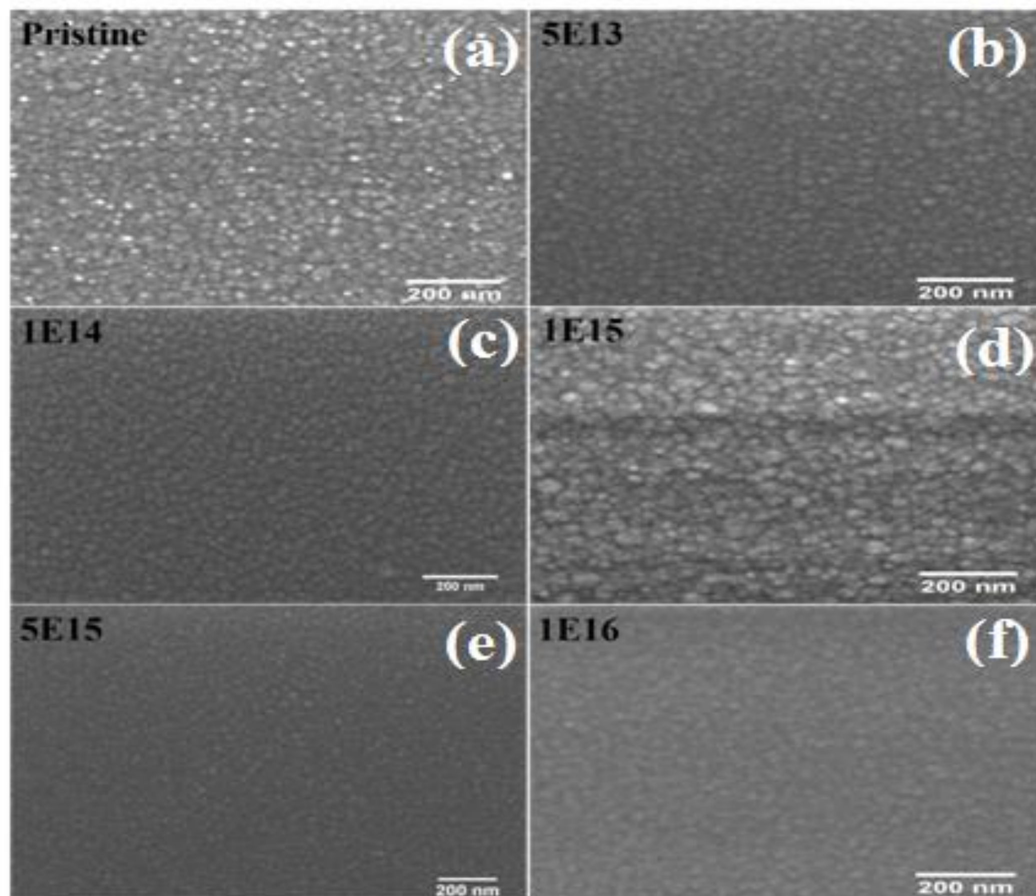

Figure 4.13: SEM images of pristine and Xe implanted SnO_2-Ag-SnO_2 films. (a) Pristine, (b-f) for fluence range 5E13 to 1E16 ions/cm^3.

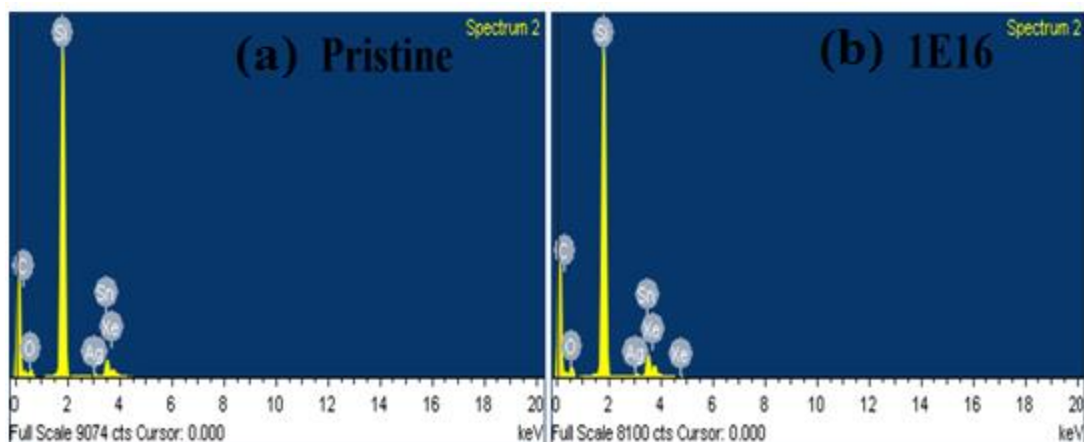

Figure 4.14: EDS of pristine (a) and Xe implanted (b) SnO_2-Ag-SnO_2 films.

Particle size and surface morphology of samples has significantly changed after implantation[175]. However, for the highest fluence films, some bigger size particles appear along with the continuous grains[41]. The particle size is found to vary in the range of 14–19 nm. EDS spectra of pristine and implanted films (for highest fluence 1E16) are shown in fig. 4.14. EDS spectra show the presence of Xe ions as shown in fig 4.14 (b).

4.5.5 Atomic Force Microscope

Roughness of the multilayer thin films was estimated with the help of AFM measurements and shown in Fig. 4.15. The images illustrate the growth of continuous and smooth surfaces for pristine as well as-implanted samples[184]. The surface roughness of pristine SAS sample is found to be ~ 1.81 nm. The AFM images demonstrate a slight change in the morphology and roughness after implantation. Variation in roughness with change in fluence is shown in Fig 4.16. The roughness decreases to 0.77 nm with increase in fluence up to 5E15. For the highest fluence, the roughness becomes 1.75 nm. Large roughness for highest fluence film is related to creation of large number of defects.

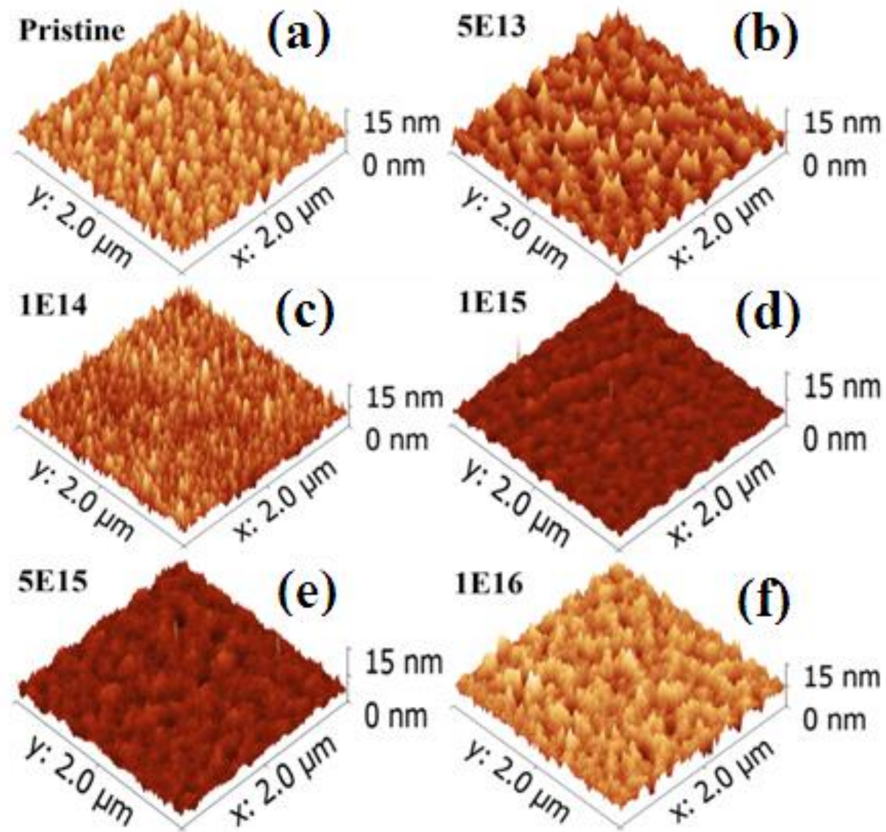

Figure 4.15: AFM images of pristine (a) and Xe implanted (b-f) SnO_2-Ag-SnO_2 films.

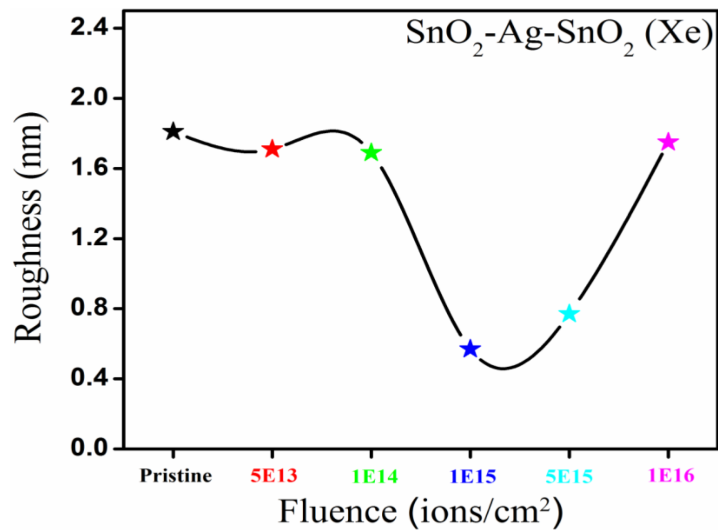

Figure 4.16: Variation in surface roughness of pristine and Xe implanted SnO_2-Ag-SnO_2 films.

This observation can be correlated with the SEM measurements where the presence of bigger particles can be clearly seen along with the well-defined grains for

highest fluence thin film. Implantation of large number of energetic ions may cause removal of grain boundaries between small grains and hence creation of bigger grains[175]. XRD results also suggest reduction in crystallinity for highest fluence thin film. Based on above it can be suggested that samples implanted with lower fluence (≤ 1E15 ions/cm^2) may be used for electrode applications while higher fluence damages the samples.

4.5.6 UV-Vis Spectroscopic Study

Optical properties of pristine and implanted multilayer thin films were examined with the help of UV-Vis spectroscopy. Fig. 4.17 shows the transmittance spectra of pristine and implanted multilayer thin films in the wavelength range 400–800 nm. The average transmittance for pristine and implanted thin films in the visible range is found in between ~ 65-80 %. The commercially available ITO slide (Sigma-Aldrich (Product Number: 703184, CAS Number: 50926-11-9) is reported to have a transparency of ~ 80 % (with R_s 30-60 Ω/sq and refractive index 1.517). The transparency in the present case is very much comparable to the commercial available transparent electrodes (ITO). Better performance of multilayer structure is seen compared to other reports of TCO ; N+ implanted FTO reported by Tuquabo *et al.*[127] and Sb doped SnO_2 by Rastomjee *et al.*[176] in terms of transmittance.

It has been found that there is a slight degradation in the transmittance for lower fluences (≤ 1E15) while there is an increment in the transmittance for higher fluences. Almost negligible variation in the transmittance for lower fluences is quite good for use of transparent conducting electrode in radiation environments. At highest fluence, there is an increase in transparency of the multilayer thin films. This is because of reduction in the grain boundary scattering from small grains as at highest fluence grains are large

with less grain boundary[175,185]. At lower fluences, defects created due to implantation of ions increases absorption which reduces transparency[127].

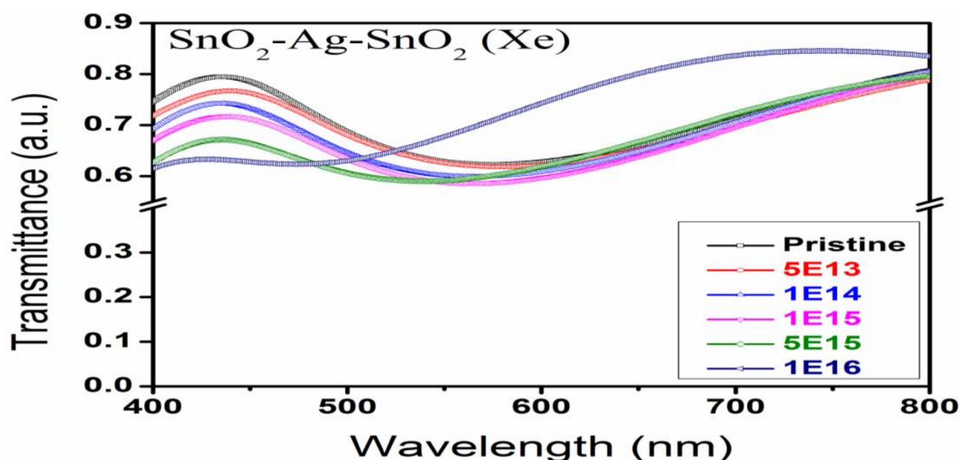

Figure 4.17: Transmittance spectra of pristine and Xe implanted SnO_2-Ag-SnO_2 films.

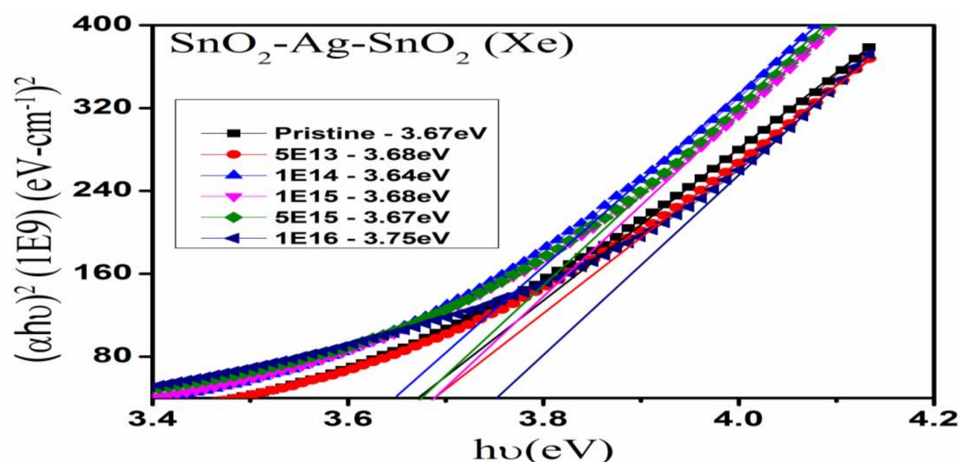

Figure 4.18: Tauc plot for pristine and Xe implanted SnO_2-Ag-SnO_2 films.

Tauc's plot[172] has been employed for the estimation of optical band gap as shown in Fig. 4.18. The band gap for the pristine multilayer was found to be ~ 3.67eV and is nearly close to the band gap of a thin film SnO_2[186]. There is negligible change in the band gap for lower fluence while a significant variation is observed for the highest fluence (1E16 ions/cm^2).

Other optical constants such as refractive index and extinction coefficient also have been calculated and shown in Fig. 4.19. These optical constants also exhibit similar behavior with different ion fluences as shown by transmittance and absorbance curves. Based on these observations, it can be concluded that multilayer structure possesses very good stability and only slight degradation in the transmittance with increasing fluence of Xe ions makes them appropriate for optoelectronic devices applications[187].

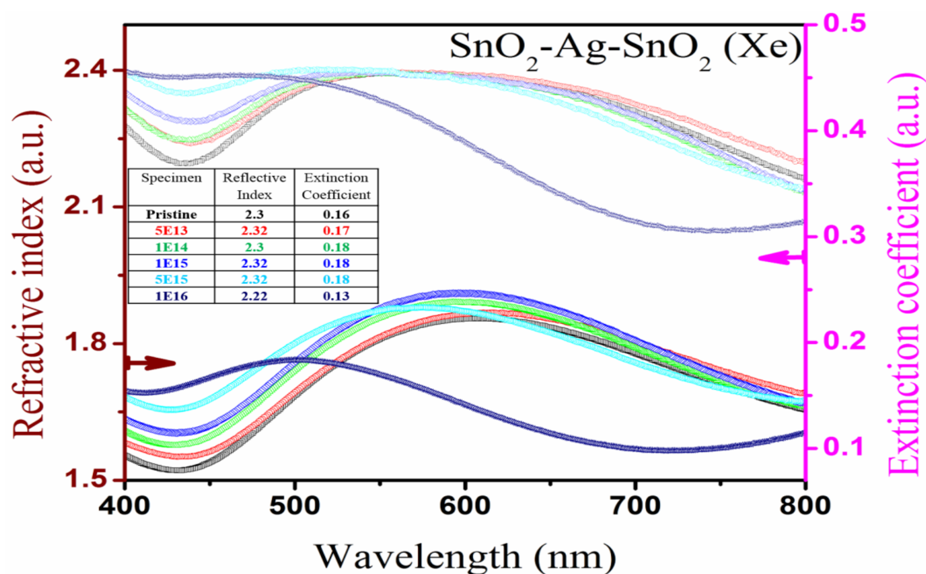

Specimen	Reflective Index	Extinction Coefficient
Pristine	2.3	0.16
5E13	2.32	0.17
1E14	2.3	0.18
1E15	2.32	0.18
5E15	2.32	0.18
1E16	2.22	0.13

Figure 4.19: Refractive index and extinction coefficient for pristine and Xe implanted SnO_2-Ag-SnO_2 films.

4.5.7 Hall Measurements

Variation in electrical properties of these multilayer films after Xe ion implantation of varying fluence is presented in Fig. 4.20. Hall measurements indicate that the electrical parameters like sheet resistance, mobility and concentration of charge carriers can be tuned by Xe ion implantation of different fluence. The curves indicate that the highest fluence 1E16 ions/cm^2 gives better results in terms of mobility and number of charge carriers along with required sheet resistance, especially for the organic photovoltaic application[186]. Charge carrier mobility for pristine film was found

to be ~4 cm^2/V-s which increases to ~11.8 cm^2/V-s for the fluence value 1E16 $ions/cm^2$. Both XRD and AFM confirm the grain growth with fluence resulting in a decrease in grain boundary scattering of charge carriers and improving the mobility[183]. Simultaneously charge carrier concentration increased from ~2×10^{21} cm^{-3} to ~6×10^{21} cm^{-3} as fluence increased to 1E16 $ions/cm^2$. The reason of initially increasing carrier concentration is mainly due to defects generated by the heavy Xe ions[127,176]. With higher fluence, SAS structure again regains its properties as compared to pristine samples leads to conclude the SAS structure stability in low energy environment. So here the most beneficially fluence is 1E16 $ions/cm^2$.

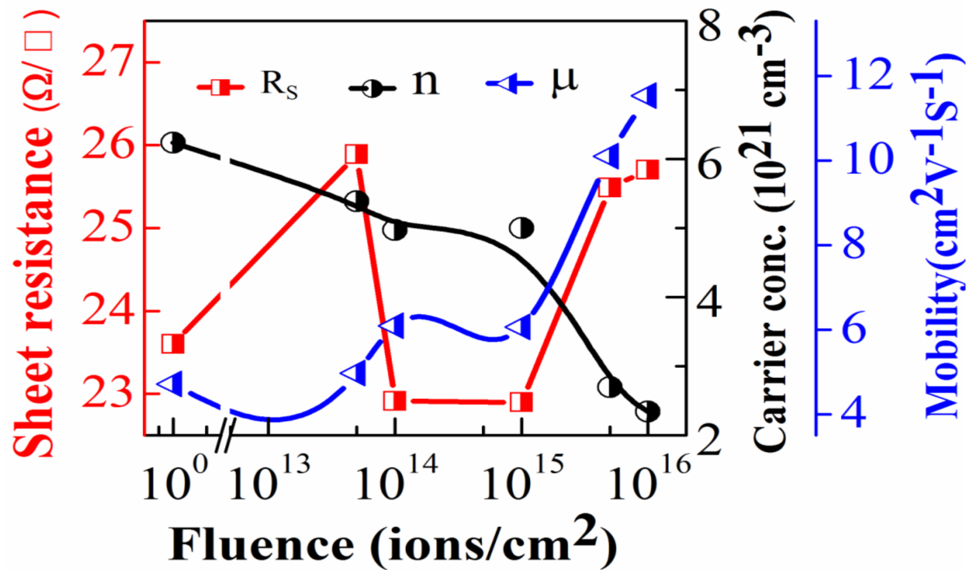

Figure 4.20: Carrier concentration, mobility and sheet resistance for pristine and Xe implanted SnO_2-Ag-SnO_2 films.

A slight increase in sheet resistance after implantation may be assigned to the surface roughness variation with increasing ion fluence. Moreover, the creation of defects and variation in oxygen concentration may be the possible reasons for increment in sheet resistance on Xe implantation[177]. As increase in defects affect the mobility negatively and conductivity depends upon on mobility and charge carrier. The band gap is also changing marginally and affects the electrical resistivity[127]. The

possible reason for this phenomenon may be due to other effects, such as the creation of trap states, which may cause sheet resistance enhancement. Similar behavior reported for AZO/Ag/AZO system for different annealing temperature and reason given for variation in sheet resistance was interface diffusion between metal-semiconductor[188].

4.6 O^{7+} Ion-Beam (100MeV) Effect on SnO_2-Ag-SnO_2 Thin Films

SnO_2-Ag-SnO_2 multilayer thin films were fabricated with a total thickness of ~ 65 nm on Si and glass substrates. E-beam evaporation was used to deposit the bottom and uppermost layers of SnO_2 using SnO_2 pellet and the deposition was done at room temperature[96]. The ~ 6 nm Ag middle layer was deposited by thermal evaporation using the Ag foil. The vacuum of 5.5×10^{-6} mbar was maintained during both depositions. After studying the role of ion beam implantation, Further investigation was carried out to understand the role of energetic swift heavy ions on the electrical and optical properties of these multilayer structures[189]. Energetic ion irradiation is carried out on these multilayers in order to check the radiation stability of such multilayers for their potential applications in radiation environments[133]. For this, the multilayer structure is exposed to the 100 MeV O^{7+} ions with two different fluence 1×10^{12} and 5×10^{12} ions/cm^2 using the pelletron facility at IUAC, New Delhi.

4.7 Results and Discussion

4.7.1 X-ray Diffraction

Fig. 4.21 shows the XRD patterns of the pristine and irradiated films. XRD patterns of both pristine and irradiated films exhibit amorphous nature. The amorphous nature of the diffraction pattern is attributed to very less thickness of the stacked

multilayer which reduces the number of diffraction planes in the path of the incoming collimated X-rays. Another possible reason for the amorphous nature of the films is related to the fact that deposition was carried out at room temperature. The less crystalline or nearly amorphous nature of the film is good for fabrication of these films on a plastic substrate[190].

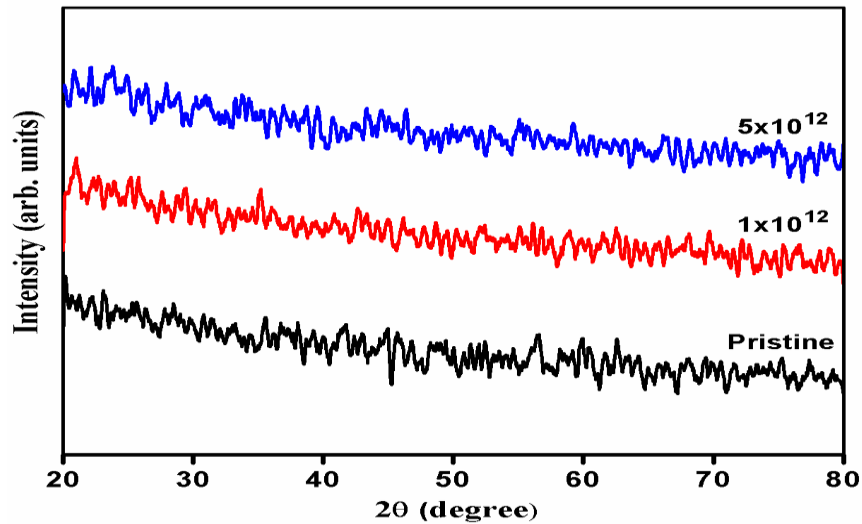

Figure 4.21: XRD pattern of SnO_2-Ag-SnO_2 pristine and irradiated films.

4.7.2 Rutherford Back Scattering

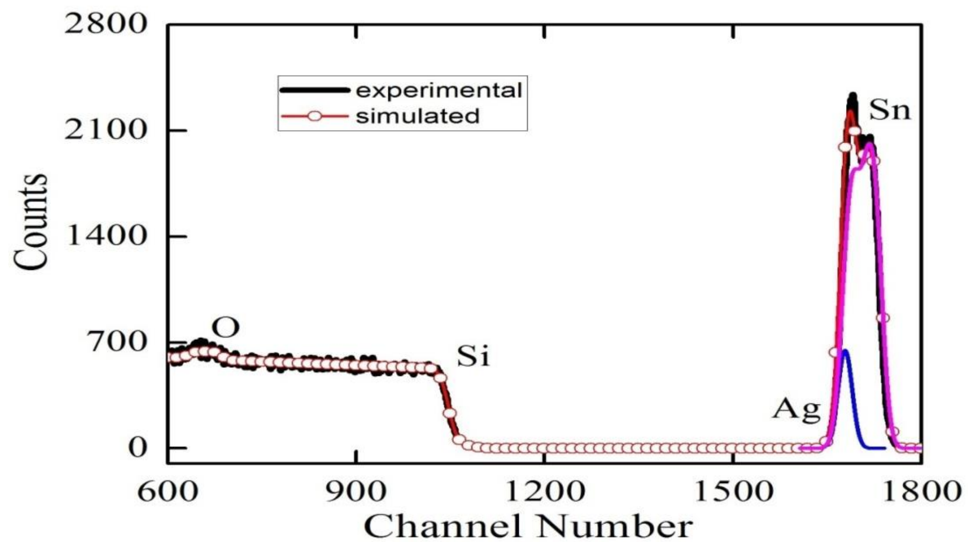

Figure 4.22: RBS spectrum of SnO_2-Ag-SnO_2 film with fitted profile.

RBS spectrum and SIMNRA-fitted[191] profile of the stacked multilayer SAS films are shown in Fig. 4.22. RBS spectra confirm the existence of the elements Sn, O, Ag and Si. The thickness of the film was estimated by fitting the data using SIMNRA software and found to be SnO_2 (30 nm)/Ag (6 nm)/SnO_2 (30 nm).

4.7.3 Raman Spectroscopy

In the bulk SnO_2, six-unit cell atoms generate different vibrational modes including IR active and Raman active. Fig. 4.23 shows the Raman spectra of pristine and SHI irradiated multilayer structure. The pristine and irradiated samples show one IR active mode at ~ 300 (e_u) cm^{-1} and two Raman active modes[192] at 425 and 620 (e_u) cm^{-1}. These IR and Raman modes show the growth of as-deposited and irradiated multilayer. The shift observed in these modes from their actual peak positions is attributed to the strain present in the multilayer structure. It is noticed that the intensity of the Raman peaks increases with the fluence[137].

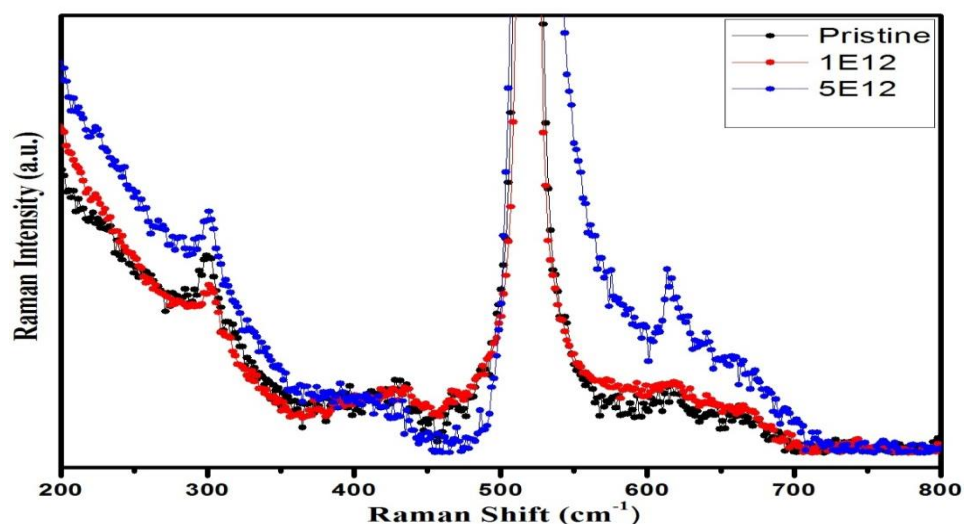

Figure 4.23: Raman spectra of SnO_2-Ag-SnO_2 pristine and irradiated films.

4.7.4 SEM and AFM Studies

Fig. 4.24 (a) shows FESEM images of the pristine and irradiated films. All films exhibit a uniform and smooth surface. Fig. 4.24 (b) shows the AFM images of SAS

films of the pristine and irradiated samples with 100 MeV O^{7+} ions at the fluence of 1×10^{12} ions/cm^2 and 5×10^{12} ions/cm^2. The scan area of the films was 2×2 µm^2. The effect of SHI irradiation on the surface roughness was investigated.

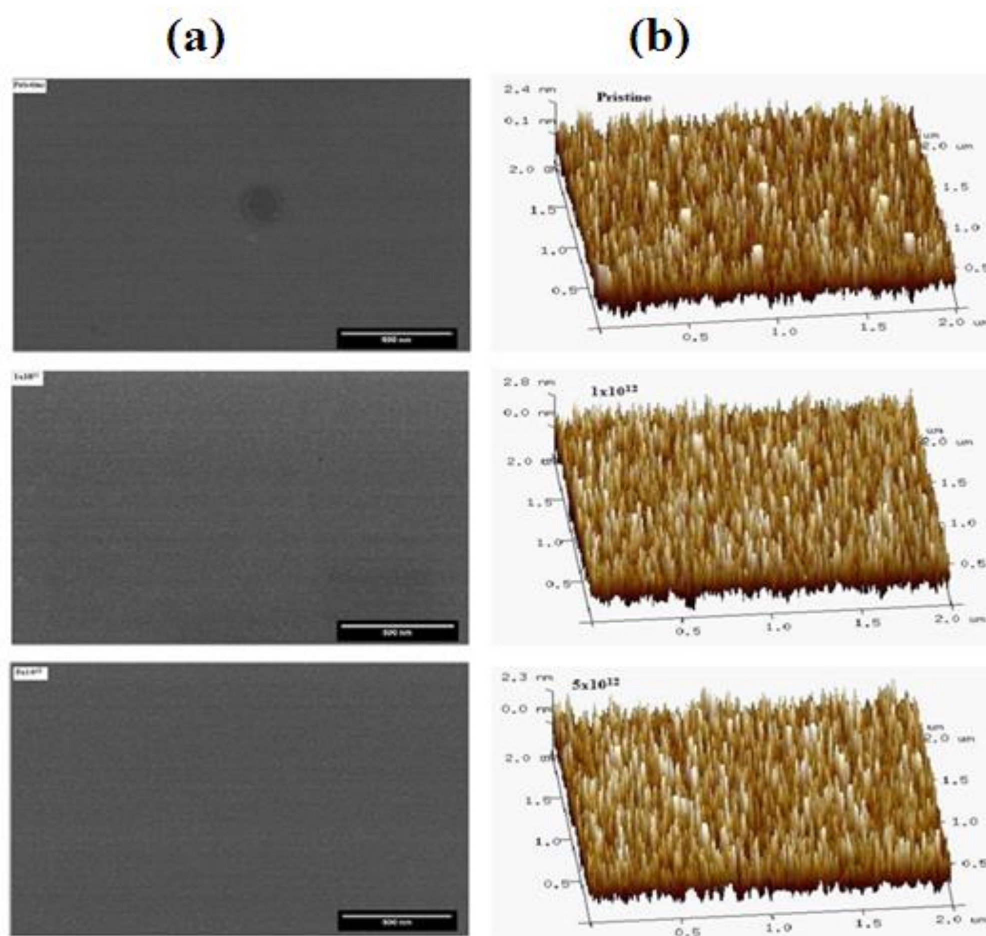

Figure 4.24: SEM (a) and AFM (b) images of the pristine and irradiated SnO_2-Ag-SnO_2 films.

The figures clearly depict the modification in the roughness of the films upon irradiation. The root mean square roughness of the pristine sample was ~ 1.6 nm which decreased to 0.68 nm for 1×10^{12} ions/cm^2 fluence. The 100 MeV O^{7+} ion irradiation causes erosion of surface microstructures and hence average height of the microstructures reduces. Further, it increases to 1.35 nm on increasing the fluence to 5×10^{12} ions/cm^2, but less than the RMS roughness value of the pristine sample. These results of surface roughness are in agreement with results reported by Aditya et al.[193]

for O ion irradiated SnO_2 thin film. However, Abhirami et al.[194] have reported different results for roughness of single layer tin oxide film using 120 MeV Ag^{9+} ions. The obtained roughness (R_q) is suitable for these thin films to be used as TCO in flat panel displays and touch screens[195].

4.7.5 UV-Vis Spectroscopic Study

Fig. 4.25 shows the transmittance and absorbance spectra of multilayer films in the wavelength range of 400–800 nm. The pristine sample was observed to have ~ 75% transmittance at 550 nm. The transmittance value exhibits a decreasing trend with an increase in wavelength. The highest average transmittance of > 80 % over the visible light spectrum is shown by the sample irradiated with the lower fluence of 1×10^{12} ion/cm^2. With further increase in the fluence (5×10^{12} ion/cm^2), the transmittance (excluding the substrate effect) of above 78% was observed as compared to pristine multilayer and transmittance increases with wavelength.

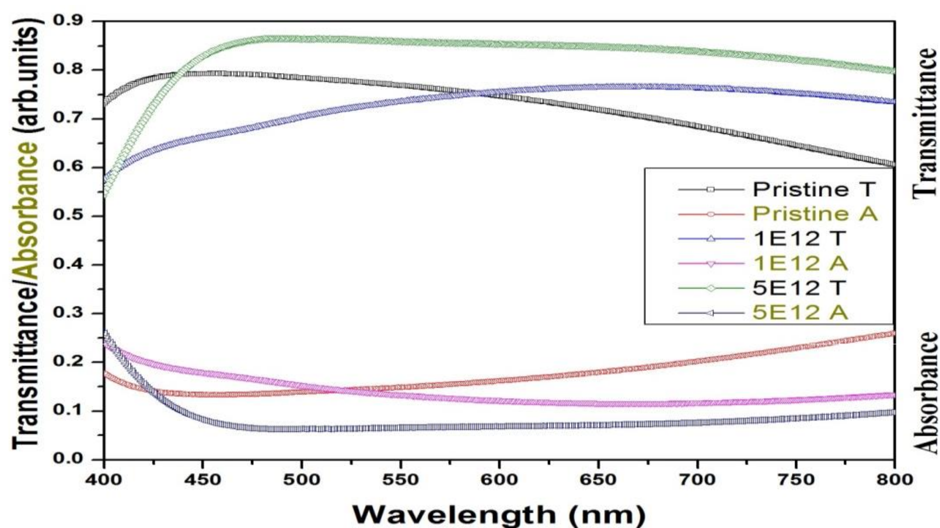

Figure 4.25: Transmittance and absorbance spectra of pristine and irradiated SnO_2-Ag-SnO_2 multilayer films.

The possible reason for the increase in transparency with irradiation could be the reduction of the surface roughness with irradiation leading to less absorption. There

is a possibility of formation of AgO in the ion tracks as O atoms released from metal oxide could combine with Ag atoms forming silver oxide (AgO). The reduction in transmittance at higher fluence may take place due to scattering from the metal atoms sputtered out of the metal layer and distributed in the oxide layer. These transmittance values also support the candidature of stacked multilayer films as an electrode in touch screen and flat panel display applications.

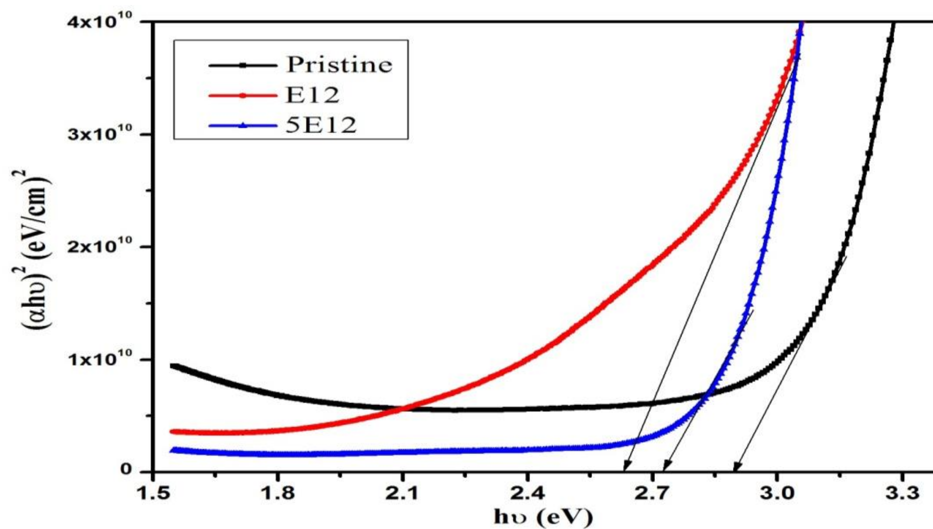

Figure 4.26: Tauc's plot of pristine and irradiated SnO_2-Ag-SnO_2 multilayer films.

The optical band gap of the trilayered structure was calculated using Tauc's equation by plotting $(ah\nu)^2$ v/s energy (hν) as shown in Fig. 4.26. The calculated bandgap energy of the multilayer was found to be ~ 2.91 eV for the pristine film which is lower than the band gap energy[143] of bulk or single layer SnO_2 but it is close to the reported value of SnO (2.5–3.0 eV)[196]. The calculated band gap is optical but the amorphous nature of thin film may not allow the proper estimation of band gap as the absorption edge is sharper (near to exact). There are few reports which claim SnO_2 have a direct bandgap of 4.0 eV and the indirect bandgap of 2.6 eV[197]. In a similar manner, these amorphous thin film exhibits lower band gap with respect to the standard value and shows high transparency because of its highly thin nature. Generally, this method,

which is, however, a crude one, is applicable for single layer but there have been reports about using the same method to determine the band gap for multilayers also[37]. The formation of oxide layer i.e. SnO_x (exhibiting the mixture of both SnO and SnO_2) is generally expected from e-beam deposition. Previous studies have shown the reduction in the band gap explained on the basis of X-ray absorption (XAS) and X-ray emission spectroscopy (XES) results[190]. Based on these results, it is inferred that the films contain proportionally more SnO compared to SnO_2. On SHI irradiation, the multilayer structure shows a red shift in absorption spectra which leads to decrease in the optical bandgap.

Formation of defects in SnO_2 layer due to irradiation may result in the decrease in optical band gap energy. High energy ion irradiation creates lattice distortion producing defect energy levels below the conduction band in the oxide. At higher fluence, the defect levels may be annealed out with the formation of narrow crystallites giving a higher band gap.

4.7.6 Hall Measurements

Resistivity, carrier concentration, and mobility of SAS thin films measured at room temperature are indicated in table 1. The Hall measurement result shows that these films have *n*-type behavior. The charge carrier concentration in these samples is quite high but mobility is limited. The sheet resistance of the pristine sample is 200 Ω/□ which becomes 787 Ω/□ for the highest fluence of 5E12. Such high sheet resistance value could be due to discontinuity induced in mid layer of Ag on irradiation. These electrical properties of SAS thin film justify the use of the multilayer as an electrode in flat panel display and touch-screen applications.

Table 1
Resistivity, carrier concentration, mobility and sheet resistance (R_{sh}) of 100 MeV O^{7+} irradiated SnO_2-Ag-SnO_2 multilayer thin film.

S. No	Fluence (ion/cm^2)	Resistivity (Ω.cm)	Carrier Concentration (/cm^3)	Mobility (cm^2/v.s)	R_{sh} (Ω/□)
1	Pristine	1.6×10^{-3}	4.6×10^{21}	0.85	200
2	1.0×10^{12}	4.1×10^{-3}	1.3×10^{21}	1.2	512.5
3	5.0×10^{12}	6.3×10^{-3}	6.3×10^{20}	1.6	787.5

4.8 Conclusion

Multi-layered SAS structure was deposited on glass and quartz substrates using RF-DC sputtering method. The Ag thickness was optimized for best optical and electrical properties. Results show that 8-12 nm Ag layer sandwiched between two SnO_2 layers of 35 nm each gives best results. The physical properties of SAS films having the optimized thickness were modified with 100 keV Xe ion implantation with fluence ranging from 5E13 to 1E16 ion/cm^2. The SAS films modified by ion beam of fluence 1E16 ions/cm^2 provides 75 % optical transparency in visible region and sheet resistance value 25 Ω/□ at room temperature. SAS films deposited by e beam and thermal evaporation were investigated for its morphological and structural stability as TCO under SHI ion irradiation. XRD studies show amorphous structure of the multilayer even after irradiation. An important observation to be highlighted here is that the films remain amorphized for irradiation conditions used in the current investigation. AFM and SEM studies show the top surface to have low roughness and smooth morphology which favor the growth of further layers for technological applications for

both pristine and irradiated samples. It is observed that electrical properties are changed drastically in terms of sheet resistance, mobility and carrier concentration. The results of the current investigation show that it is possible to tune the electronic and optical properties of these multilayers using ion irradiation. However, no drastic change is seen in the electrical and optical properties of the multilayer TCE under implantation. Hence, it is concluded that one can use such SnO_2-based hybrid thin films in low energetic environment for various optoelectronic applications.

Chapter-5

Fabrication and Characterization of SnO_x-Au-SnO_x Multilayer Thin Films and Their Irradiation Effects

5.1 Introduction

Various multilayers of metal oxide / metal / metal oxide or dielectric/metal/dielectric (DMD) have been investigated in recent past (e.g. SnO_2 /Ag /SnO_2[116], ZnO/Au / ZnO[103], ZnO /Ag/ ZnO[198], ZTO /Ag /ZTO[87], AZO /Au /AZO[62], GZO /Ag / GZO[85], GMZO /Ag /GMZO[88], etc.). SnO_2 /Au / SnO_2 has been a good choice among all these DMD's since a combination of SnO_2 with Au exhibits quite low electrical resistance with high optical transparency in the visible range.

5.2 Experimental Details

SnO_2 powder (Alfa-Aesar, 99.99% of purity, metal basis) was used as the starting material to make pellets for e-beam evaporation. SnO_2 powder was subjected to grinding and then pelletized. These pellets were then sintered at 500 °C for 3 hrs. This helps to get better structural stability for film deposition.

The quartz substrates of 1x1 cm^2 were cleaned using standard procedure and kept in isopropanol. These substrates were then given a heat treatment at 200 °C prior to deposition to remove any organic impurity on the surface. The stacked multilayer was then deposited on these quartz substrates using e-beam evaporation (for SnO_2 layer) and thermal evaporation (for Au layer) techniques at room temperature. SnO_2 films were deposited keeping the evaporation parameters as : source to substrate distance - 16 cm, base pressure 7×10^{-7} mbar, working pressure 1.4×10^{-5} mbar, rate of deposition 0.2 nm/sec, voltage 200 V and current 10 mA. The Au layer was deposited

using thermal evaporation unit with base pressure 8×10^{-7} mbar, working pressure 1.4×10^{-6} mbar, voltage 1 V, current 280 A and deposition rate of 0.1 nm/sec to deposit a thickness of 5 nm. The process of SnO_2 film deposition is then repeated to deposit the 35-nm thick uppermost layer making the total thickness of the multilayered structure as 75 nm.

The resultant SnO_x/Au/SnO_x stacked multilayer was annealed in open air furnace at various temperatures (30 - 150 °C) to test the thermal stability of the multilayered structure. These thin films annealed at different temperatures were then checked by X-ray diffraction. All other measurements were carried out on the as-deposited SnO_x/Au/SnO_x stacked multilayer at room temperature.

X-ray diffraction (XRD) measurement of the films was carried out using Bruker D8 Advance X-ray diffractometer. The field-emission scanning electron microscopy (FE-SEM) and atomic force microscopy (AFM) images were collected using Nova Nano FESEM 450 (FEI) and Nanoscope IIIa, respectively. UV-Vis spectrum of the sample was obtained using LAMBDA 750 (Perkin Elmer) UV-Vis-NIR spectrophotometer. Raman spectrum of the specimen was taken using Renishaw Raman spectrometer with Ar ion laser with 514.5 nm wavelength and 50 mW power. The low-temperature Hall measurements were performed using a variable temperature Hall set up (model HMS 5500) from Ecopia Co., Korea. The current-voltage characteristics were measured using a custom-built setup consisting of a cryostat controlled with Lakeshore 325 temperature controller and Keithley 2400 SMU.

The film thickness of stacked multilayer was estimated employing Rutherford backscattering (RBS) spectrometer using 2 MeV He^+ ion beams configured in Cornell geometry for optimum depth efficiency at Inter-University Accelerator Centre, New Delhi (India). Measurement of O *K*-edge and Sn *M*-edge XAS and XES were performed

at Resonant Elastic and Inelastic scattering (REIXS) beamline of Canadian Light Source (CLS), Canada. XAS spectra were obtained in both surface sensitive total electron yield (TEY) and bulk-sensitive total fluorescence yield (TFY) modes. Non-resonant XES measurements of the O *K*-edge were collected by exciting above the absorption edge at 560 eV. The interface study of the pristine and irradiated specimen was carried out with X-ray photoelectron spectroscopy (Omicron ESCA) using monochromatic *Al-Kα* X-ray source of 1486.7 *eV* with mean radius 124 mm and monochromatic X-ray resolution of 0.6 eV operating at a pressure 1×10^{-10} mbar.

5.3 Investigation on $SnO_x/Au/SnO_x$

5.3.1 X-ray Diffraction Study

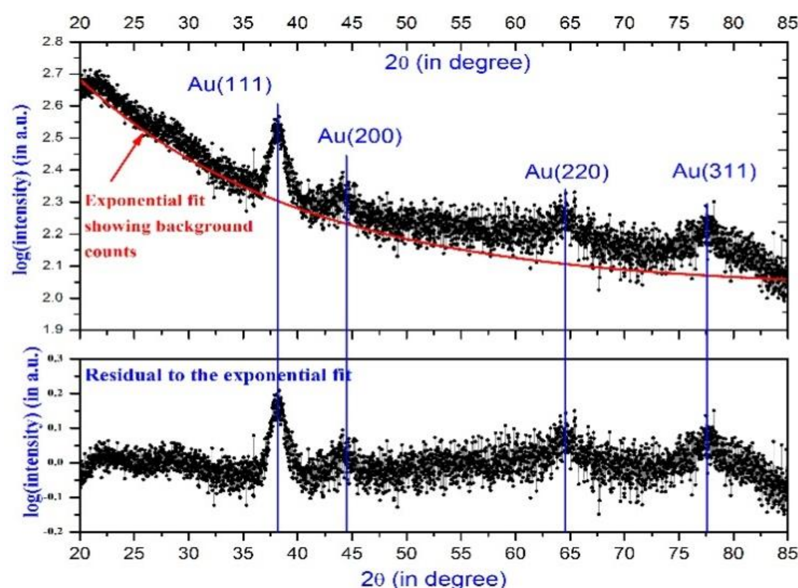

Figure 5. 1(a) X-ray diffraction pattern of as-deposited $SnO_x/Au/SnO_x$ stacked multilayer.

The glancing angle X-ray diffraction pattern of $SnO_x/Au/SnO_x$ stacked multilayer specimen (shown in Fig 5. 1a) indicates the formation of amorphous metal oxide with multiple peaks at 38.18°, 44.39°, 64.57° and 77.54° corresponding to Au cubic crystal planes of 111, 200, 220 and 311, respectively (JCPDS-card no. 00-004-0784). The high-intensity background counts in the top curve of Fig 5. 1a (shown with

exponential fit) is due to amorphous nature of SnO_x and SiO_2 (substrate) layer. The bottom curve of Fig 5. 1a shows the residue of the fit after subtracting the exponential fit data from the obtained spectrum.

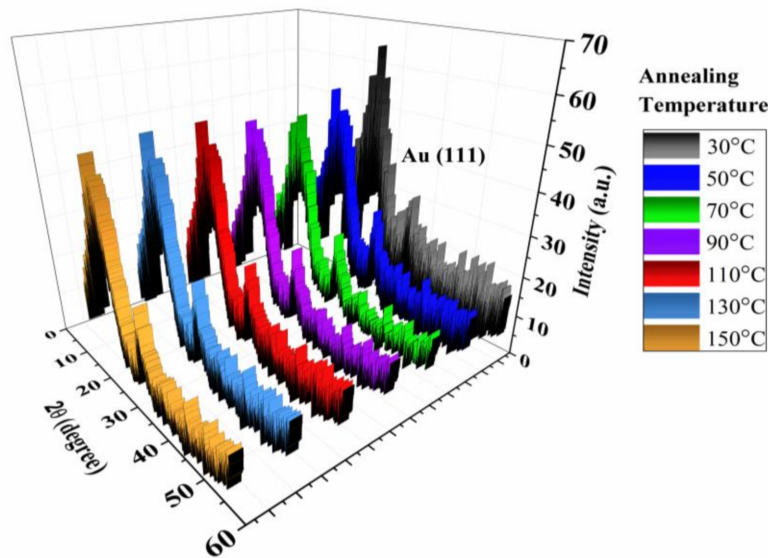

Figure 5.1 (b) X-ray diffraction pattern showing amorphous nature of stacked multilayers with annealing temperatures.

The diffraction patterns were also recorded for the stacked layers annealed at various temperatures and are shown in Fig 5. 1 b which indicates the formation of an amorphous phase except for an intense peak at $2\theta \approx 38.04°$ corresponding to Au (111) plane. There is no change in the intensity and the peak position with annealing temperatures. This confirms the stability of multilayer structure in the temperature range of photovoltaic and optoelectronic device operation, i.e., room temperature to 150 °C.

Such amorphous film is advantageous for the growth of various films due to the absence of lattice mismatch between the hetero-layers. A similar result of amorphous metal oxide film with crystalline metal as sandwich layer has been reported by Lee *et al.*[84]

5.3.2 Morphological Studies

Surface morphology of the stacked multilayer was investigated by FE-SEM and AFM, and the results are presented in Fig 5.2 (a-b). Both images suggest the formation of relatively flat films with randomly distributed islands with a typical dimension of nm. The size distribution of islands from FE-SEM image was analyzed using particle fitting tool of ImageJ[165] (assuming the circular shape of islands on the surface) and the radius of islands was determined to be in a range from 5 nm to 60 nm with an average radius of about 20 nm.

Fig 5. 2(b-c) shows the AFM image of multilayer (Fig 5. 2b) and the depth-distribution curve (Fig 5. 2c) which exhibits a maximum depth of around 7.5 nm and a maximum height of 11.64 nm when analyzed with Nanoscope™ version- 5.31R1. The average particle size distribution was also employed on 2D AFM scan assuming spherical particles on the film surface. This analysis show that these particles have a radius from 5 nm to 60 nm with a mean radius of about 28 nm which is consistent with results from FE-SEM analysis[165].

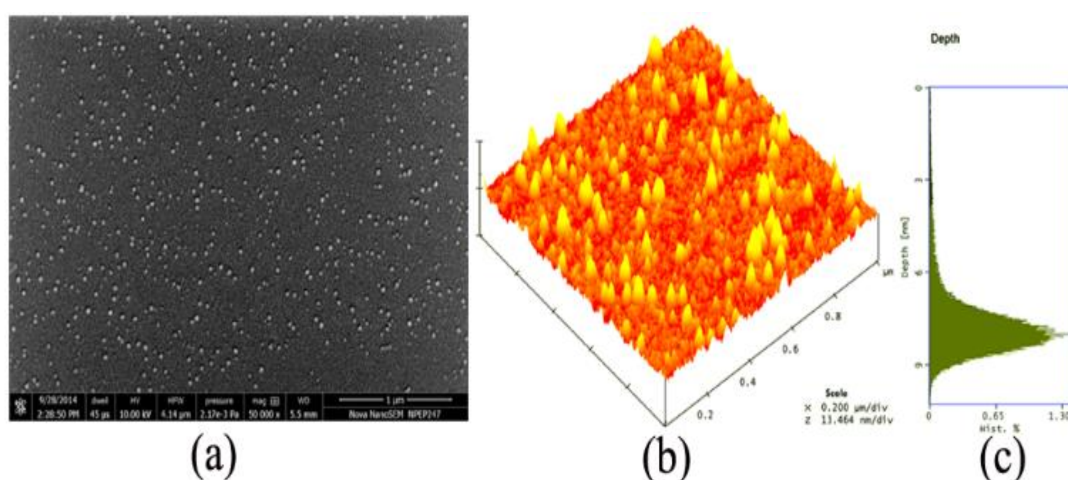

Figure 5.2 (a) SEM image exhibiting a flat topology of stacked multilayer **(b)** AFM image showing the surface topology of the sandwich layer along with (c) depth histogram.

The root-mean-square roughness of the stacked multilayer has been also calculated and found to be 1.184 nm. The small roughness is a necessary requirement for such stacked multilayered film for their use as substrate for optoelectronic applications[195].

Estimation of Au has also been performed using energy dispersive x-ray spectroscopy (EDS). Since the oxygen content cannot be quantified with the EDS (both substrate –SiO_2 and specimen layer SnO_2 contain oxygen), therefore a correct estimation of Au is not concluded using EDS.

5.3.3 XAS and XES Studies

The O *K*-edge XAS spectra of the stacked TCO multilayer were measured in both surface-sensitive TEY and bulk-sensitive TFY modes. Comparison of their characteristic features to those of SnO and SnO_2 powder reference samples (Fig 5. 3a) shows the surface region to be SnO, with additional spectral features evident from the TFY. This is further verified by the Sn M_{45}-edge TEY spectra (Fig 5. 3b) which are consistent with the O *K*-edge spectra showing a SnO-rich phase at the surface. Spectral features observed in the low energy regions of the O *K*–edge XAS in Fig 5. 3a are generated due to excitation from the O 1*s* core level into primarily O 2*p*-Sn 5*s* hybridized states[199], which form the bottom of the conduction band. The second region at higher energies is composed mainly of O 2*p*-Sn 5*p* hybridized states in SnO and SnO_2[200,201].The spectral peaks in the TFY spectrum of the TCO multilayer can be compared to XAS results of SnO_2 films deposited by atomic layer deposition (ALD)from Choi *et al.*[200] The line shape of the O 2*p*-Sn 5*s* peak at 534.5 eV and the energy splitting between this peak and the first peak in the O 2*p*-Sn 5*p* series (~2 eV), agrees with XAS of ALD films exhibiting an amorphous SnO_2 crystal structure[200].

The peak at 534.5 eV in the TCO multilayer also indicates SnO_2 by its energy location. Similarly, the first two sharper peaks *a* and *b* have similar energy splitting to the corresponding peaks in the SnO_2 reference sample (~1.2 eV). These details together indicate a dominant phase of SnO with a small amount of SnO_2 below the surface that is amorphous in nature. The TCO multilayer structure including Au in a sandwich structure may also promote overlap between O-2*p* and Au-5*d*6*s* orbitals and increase the density of conduction band states. This overlap may contribute to the increased intensity of higher energy features in the range of 535-540 eV[202].

A low energy shoulder feature under the bottom of the conduction band at 531.5 eV in TEY and TFY labeled as O_V is not typical of SnO or SnO_2 thin films or powders[199,196], and may be due to the presence of oxygen vacancies[200,201]. In the SnO/SnO_2 lattice of the TCO multilayer, oxygen vacancies introduced during the fabrication process could contribute to increased charge carrier transport and therefore conductivity by providing additional electronic states near the conduction band edge.

Non-resonant X-ray emission was also taken at the O *K*-edge to probe the density of valence band states, shown in Fig 5. 3c. Open blue circles show the raw XES spectrum overlaid with a smoothed line using 10 point FFT smoothing, which is used for the second derivative. From McLeod *et al.*[199], the contribution of Sn 5*d* states to the top valence band is much greater for the $5s^0$ oxides (SnO_2) than the $5s^2$ oxides (SnO). In $5s^0$ oxides the top of the valence band is dominated by a sharp distribution of O 2*p* states strongly hybridized with these Sn 5*d* states, extending ~2.5 eV into the valence band from the Fermi level[199]. In $5s^2$ oxides, specifically SnO, a hybridization occurs between O 2*p* and Sn 5*s* states at the valence band edge, while the top and middle of the valence band are largely dominated by O 2*p* states. By contrast to SnO_2, the top of the valence band of SnO exhibits a much broader distribution of states extending across

~5 eV[199]. The XES of the TCO multilayer shows a broad distribution of states near the top of the valence band (region *c* in Fig 5. 3d), indicating a SnO structure. From further comparison to experimental measurements, near the middle of the valence band in the region labeled *e* an additional peak may be resolved in pure SnO that arises from O2*p*-Sn 5*s* states. The broadening of this feature such that it cannot be resolved as in the case of the TCO multilayer shows disorder in the SnO lattice due to the amorphous SnO/SnO_2 phase. A similar smearing of valence band features *d* and *e* has been observed for SnO_2 thin films below 220 nm in thickness and was attributed to oxygen vacancies in that films[201].

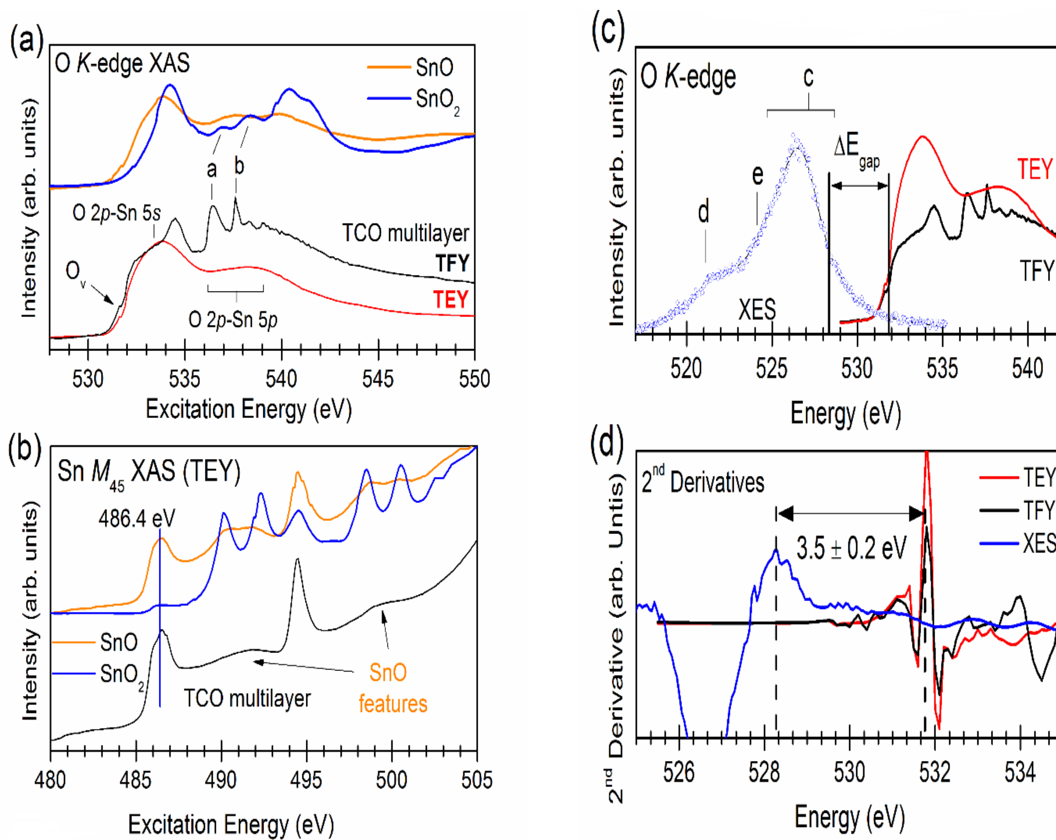

Figure 5.3 (a) O *K*-edge X-ray absorption spectra of SnO and SnO_2 reference samples along with the stacked TCO multilayer measured in TEY/TFY modes. **(b)** Sn *M*-edge spectra for the TCO multilayer compared to references, and **(c)** XES and XAS of the O *K*-edges where XES display a valence band line shape indicating SnO. **(d)** The magnitude of the band gap energy is determined using second derivatives to be 3.5 ± 0.2 eV.

The band gap in SnO/SnO_2 can be determined from O *K*-edge measurements plotted on a common energy scale as in Fig 5. 3c[199,200]. When the second derivative is plotted the distance between the highest-energy peak of the XES derivative and the lowest-energy peak of the XAS derivative provides the band gap energy splitting. This method provides a quantitative measurement of band gap energy without the use of line fitting to the valence and conduction band edges. The second derivatives for O *K*-edge XES and XAS of the TCO multilayer are shown in Fig 5. 3d, and find the TCO multilayer band gap to be 3.5 eV ± 0.2 eV, which is larger than the reported band gap range of 2.5-3.0 eV for SnO[196,203]. This result is significant because it indicates that even though the films contain proportionally more SnO compared to SnO_2, the band gap matches more closely to that of SnO_2 (3.6 eV). The SnO band structure and band gap energy are altered by the presence of a mixed phase with amorphous $SnO_2$and oxygen vacancies in a way that may be advantageous for device applications. A large band gap energy commonly results in higher transmittance in the visible range, while a metal-rich SnO/SnO_2 phase may serve to show lower resistivity of the TCO multilayer compared to pure metal oxide films.

5.3.4 Rutherford Back Scattering

Fig 5. 4 shows the RBS spectrum and RUMP-fitted[204] profile of the stacked multilayer. This spectrum indicates the distinct elemental peaks associated with Sn, O, Au and Si. The thickness of the structure is calculated with the help of this fitted profile. The estimated values are SnO_x (35 nm) / Au (5.2 nm) / SnO_x (35 nm) with composition of SnO_x layer as: 0.575 of O and 0.425 of Sn. This suggests the formation of SnO (which is consistent with results from the XAS investigations) with pure Au in the sandwich layer.

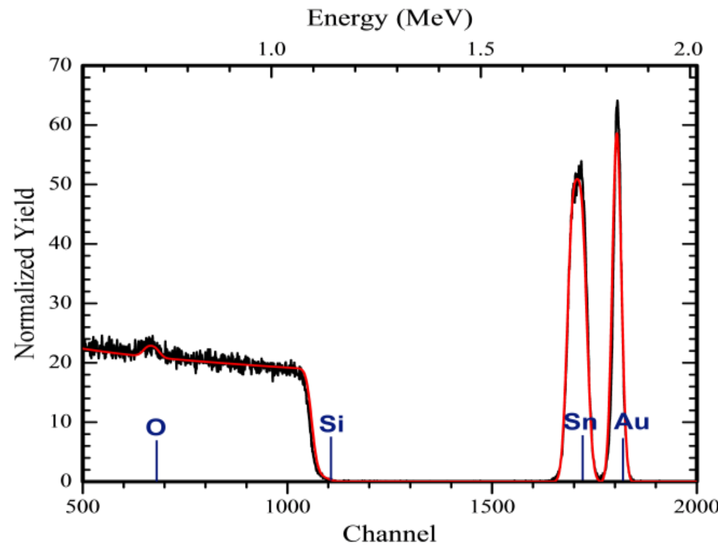

Figure 5.4 RBS spectrum along with a fitted profile of the stacked multilayer.

5.3.5 UV-Vis and Raman Spectroscopy

The optical properties of the stacked multilayer recorded from a UV-Vis spectrophotometer are presented in Fig 5. 5 exhibiting nearly the constant values for transmittance, absorbance, and reflectance beyond 475 nm of incoming radiation (0.83, 0.08 and 0.09, respectively). The typical value of transparency for a commercially available ITO slide from Sigma-Aldrich (Product Number: 703184, CAS Number: 50926-11-9) is 0.84 (surface resistivity 30-60 Ω/*sq* and refractive index 1.517) which is quite near to the value obtained from this stacked multilayer. This transmittance value is better as compared to other reports for SnO on quartz substrates by Liang *et al.*[205], The ITO, ITO / Au / ITO and ITO / Cu / ITO on polycarbonate substrates reported by Lee *et al.*[84] and Au-embedded F-doped SnO_2 on glass substrates reported by Chew *et al.*[206] Higher transmittance and lower absorbance/reflectance are desirable properties for prospective use of these stacked multilayers as TCOs. Coating the metal film with a dielectric layer of higher refractive index is known to increase the transmittance of the metal film with the dielectric layer acting as an antireflection film. A thin layer of polymer nanocomposites coated on metal as dielectric has been used to minimize the

reflection of Au film increasing the optical properties of the system[207]. Hence, the enhanced optical properties of proposed dielectric metal dielectric (DMD) structure in the entire visible region are due to the metal oxide layers on both sides of Au metal layer.

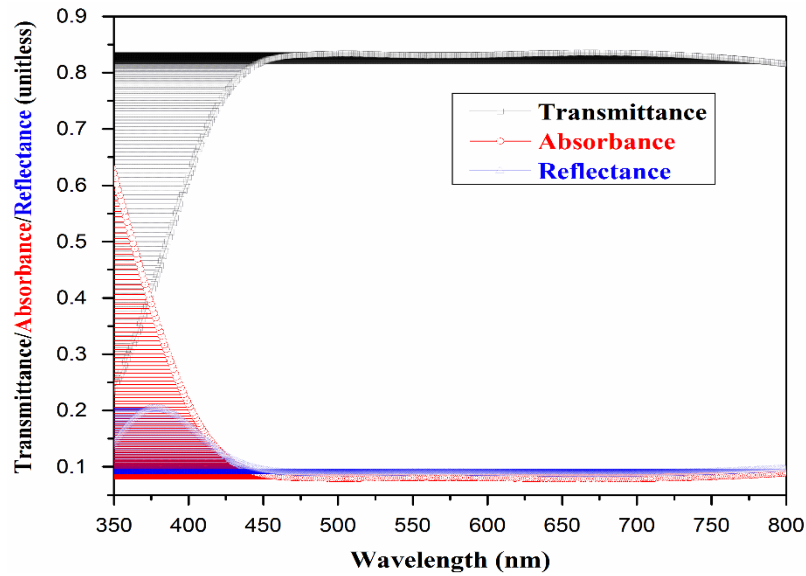

Figure 5.5 UV-Vis curve showing transmittance, absorbance and reflectance for stacked multilayer.

The Raman spectrum corresponding to stacked multilayer is shown in Fig 5. 6 (bold grey line) which includes multiple peaks deconvoluted from the Raman spectrum showing the contribution from the transitions corresponding to vibrational levels. SnO_2 unit cell exhibits a total of 18 branches for the vibrational modes in first Brillouin zone which results in four Raman active modes (A_{1g}, B_{1g}, B_{2g} and E_g)[208]. The bottom curve in Fig 5.6 shows the residue to the fit. The peak structure is broad which is indicative of the formation of crystallites of very small size. The Raman shifts at 437 and 787 cm^{-1} (refer peaks *b* and *e* in Fig 5. 6) pertain to the characteristics E_g and B_{2g} modes of SnO_2[66]. All the other peaks (*a*, *c*, *d* and *f*) belong to the characteristic peaks of SiO_2 originating due to the quartz substrate[209]. The major contribution in the Raman

spectrum is from the quartz substrate which is due to small thickness and high transparency of the film.

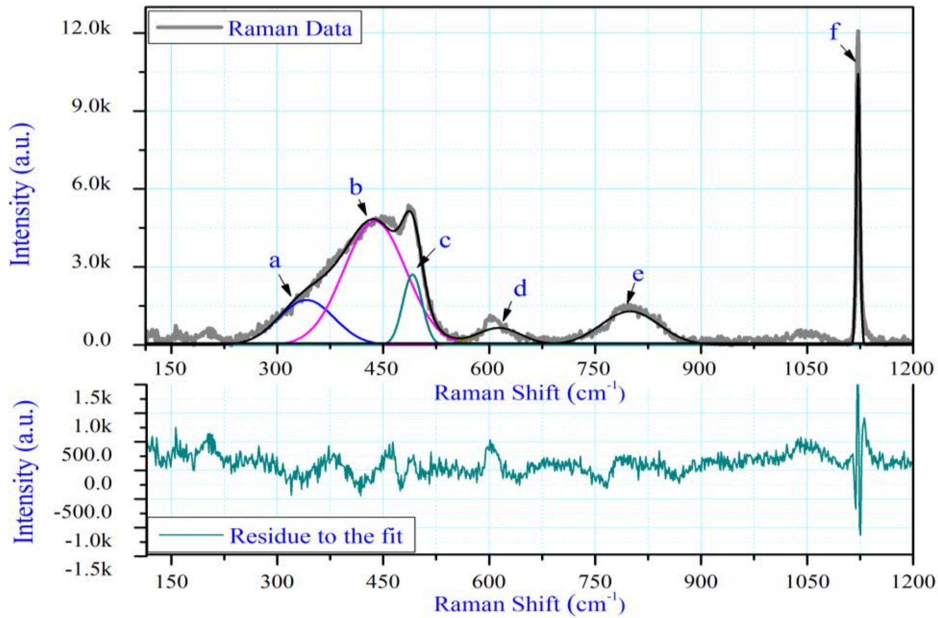

Figure 5.6 Raman spectrum of stacked multilayer. It also includes multiple peaks deconvoluted to show the contribution from the transitions corresponding to vibrational levels.

5.3.6 Low-Temperature Hall Study

Low-temperature Hall effect and electrical resistivity measurements were carried out using Van der Pauw configuration. The variation of resistivity and sheet resistance for the temperature range of 80 -340 K is presented in Fig 5. 7. The room temperature resistivity and sheet resistance for this stacked multilayer were 3.9×10^{-4} Ω·cm and 52 Ω/*sq*., respectively. The value of sheet resistance, 30-60 Ω/*sq*, is comparable to the commercial ITO slide from Sigma-Aldrich (Product Number: 703184, CAS Number: 50926-11-9). The resistivity values for SnO_x / Au / SnO_x specimen are lower than that for ITO films (31.2×10^{-4} Ω·cm) reported by Lee *et el.*[84] and slightly higher to ITO / Au / ITO and ITO / Cu / ITO structures showing resistivity of 0.56×10^{-4} Ω·cm and 1.51×10^{-4} Ω·cm, respectively[84].

The conduction mechanisms of these stacked structures may be explained by considering a thin continuous layer of metal (Au) embedded between two oxide layers thereby forming a DMD structure. The total resistance of this coplanar configuration is generally given by $1 / R_{total} = 1 / R_{metal} + 2 / R_{oxide}$ with $R_{oxide} \approx 1000R_{metal}$, so the $R_{total} \approx R_{metal}$. Therefore, the conductivity is primarily due to embedded metal film and solely responsible for exhibiting such low values of resistivity as compared to single layer TCO. Moreover, a critical thickness of the film is required to provide a continuous path for conduction of electron[81]. The room temperature resistivity and sheet resistance values for the stacked multi-layered structure are indicating a continuous metal interlayer[92].

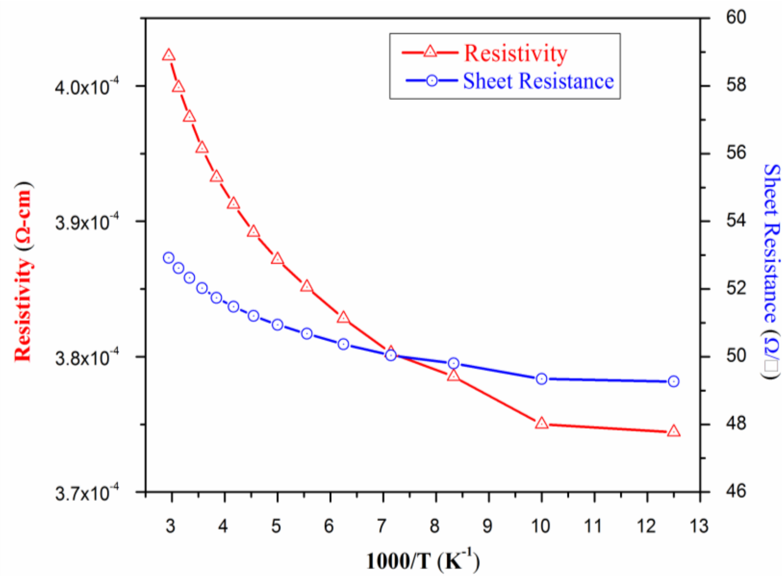

Figure 5.7 Electrical resistivity and sheet resistance as a function of reciprocal temperature.

Furthermore, the increase of both resistivity and sheet resistance with temperature is a typical characteristic of a degenerate semiconductor. This behavior is resultant of increased concentration of metallic dopant which translates the semiconducting nature into metallic. There are numerous reports that support this

argument in the literature e.g. Kim *et al.*[140] for ITO films, *n*-type ZnO doped with Ga[210], Sb-doped *p*-type ZnO[211], highly B-doped ZnO[212] films. In the present system, increased resistivity and sheet resistance with increasing temperature can be attributed to the effect of self-doping. The conclusions from XAS / XES and RBS investigations are indicative of the formation of metal-rich phase which would have produced the degenerate states thereby exhibiting a metal-like behavior.

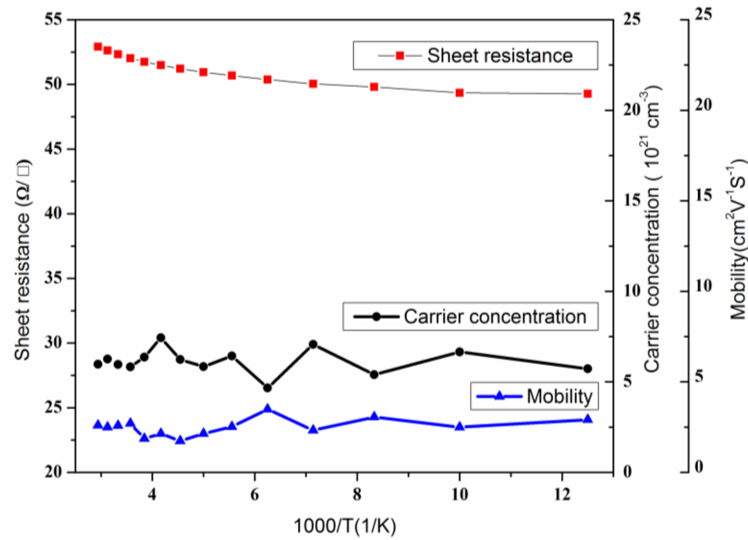

Figure 5.8 Sheet resistance, carrier concentration and mobility as a function of reciprocal temperature.

In addition to this, it is interesting to observe a very high conductivity and low sheet resistance even at very low temperature. The stacked multilayer was shown to exhibit the values for resistivity and sheet resistance as 3.7×10^{-4} Ωcm and 49 Ω. at 80 K, respectively with a very small variation in both of these quantities up to 340 K ($\delta\rho = 0.2\times10^{-4}$ Ω·cm and $\delta R_S = 2.7$ Ω.).

5.4 Irradiation Studies of Multi-layered SnO_x / Au / SnO_x TCO Thin Films for 100 *MeV* O^{7+} Ion Irradiation

5.4.1 Introduction

The ion beam related modification in optical, electrical and structural properties has been in focus in recent years to test the stability of these stacked multilayers towards the cosmic radiation since these radiations may cause soft errors to advanced commercial electronic components and systems which may result in high failure rates in support mechanism in space technology[213]. When a highly energetic ion beam traverses through the stacked multi-layered structure (MeO / M / MeO) it may result in intermixing due to diffusion of atoms at the interface of metal/metal oxide. Further, the highly energetic ion beam induces lattice defects which can alter the electronic and optical properties of stacked multilayer[133].

The stacked multilayer films were deposited to form a tri-layered structure SnO_x / Au / SnO_x by using e-beam evaporation for Au layer and RF-magnetron sputtering for SnO_2 layer to form a total thickness of ~ 75 nm. These stacked multilayer films were irradiated with 100 MeV O^{7+} ions of variable fluences from 5×10^{11} ions / cm^2 to 5×10^{12} ions / cm^2 at Inter-University Accelerator Centre, New Delhi, India using a 15UD Pelletron accelerator.

5.5 Result and Discussion

5.5.1 X-ray Diffraction Study

The pristine and irradiated films were analyzed by X-ray diffraction and the resultant spectra are shown in Fig 5.9. The spectrum is suggestive of diffraction mostly from Au lattice planes proving the amorphous nature of pristine SnO_2 and irradiated

layer. The FWHM of the diffraction peak from Au (111) plane indicates the decrease in grain size (calculated from Scherrer's formula) of Au from 44.4 nm for the pristine to 12.8 nm for initial irradiation dose of 5×10^{11} ions/cm^2. With further increase in irradiation fluence, the grain size increases slightly to 17.0 nm for irradiation fluence of 5×10^{12}ions/cm^2. The initial reduction in grain size upon irradiation may be ascribed to the internal strain induced by the ion bombardment. Similar results have been being reported by Abhirami et al.[194] with 120 MeV Ag^{9+} ions.

The swift heavy ions deposit their energy in the SnO_2 grains due to the femtosecond annealing effect induced by collision by highly energetic ions. This induces the growth in grain size of the base material. However, defragmentation of grains takes place on further increase in fluence due to higher energy deposition.

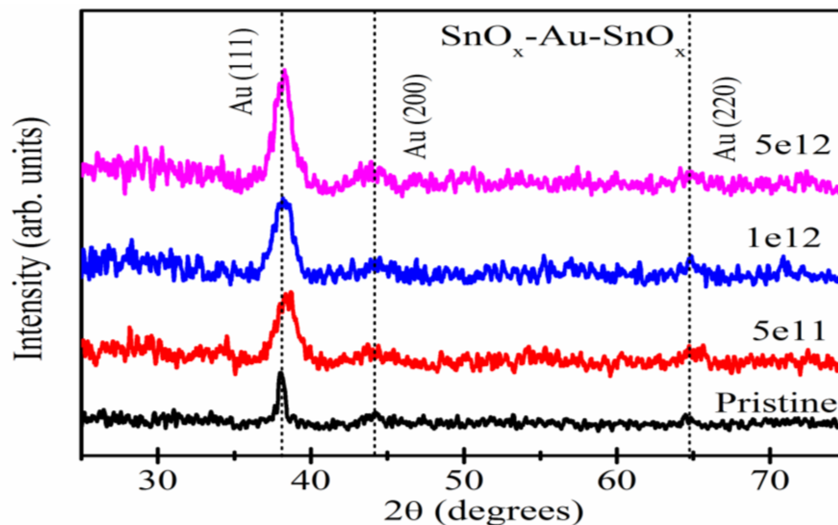

Figure 5.9 X-ray Diffraction spectra corresponding to pristine and 100 MeV O^{7+} irradiated stacked multilayer thin films.

5.5.2 RBS study

The RBS spectra fitted using RUMP simulation[204] software is shown in fig. 5.10 and fig 5.11 for pristine specimen and specimen irradiated with a fluence of 5×10^{12}

100 MeV O^{7+} ions/cm^2, respectively. The fitted profile confirms the formation of SnO_x / Au / SnO_x stacked multilayers with the thickness of SnO_x (35 nm) / Au (5.2 nm) / SnO_x (35 nm). The thickness of the middle Au layer changes post irradiation due to the diffusion of Au in the top and buried SnO_x layer.

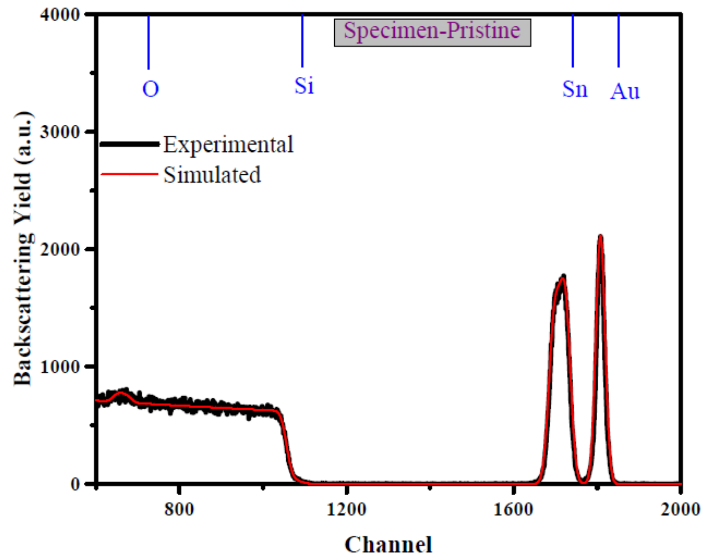

Figure 5.10 RBS spectra showing experimental and simulated data corresponding to the pristine SnO_x/Au/SnO_x thin film.

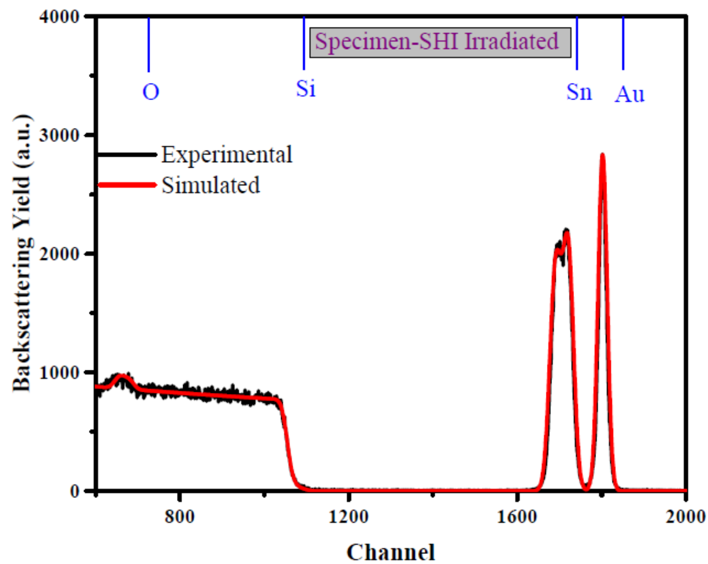

Figure 5.11 RBS spectra showing experimental and simulated data corresponding to the SnO_x /Au/SnO_x thin film irradiated with fluence of 5×10^{12} ions / cm^2

The simulated profile of RBS data of irradiated thin film indicates the thickness of layers as (28 nm SnO_x / 7 nm SnO_xAu / 5 nm Au / 4 nm SnO_xAu / 31 nm SnO_x). from this, one observes that the diffusion of Au occurs in a top layer up to 7 nm and 4 nm for bottom oxide layer from the interface. This is consistent with other reports mentioning the SHI induced diffusion of Au in the multi-layered thin film[214]. From these analysis, it is observed that the oxygen concentration in top layer has reduced after irradiation. The diffusion is more towards the top layer as compared to buried layer in the irradiated film.

5.5.3 Morphological Studies

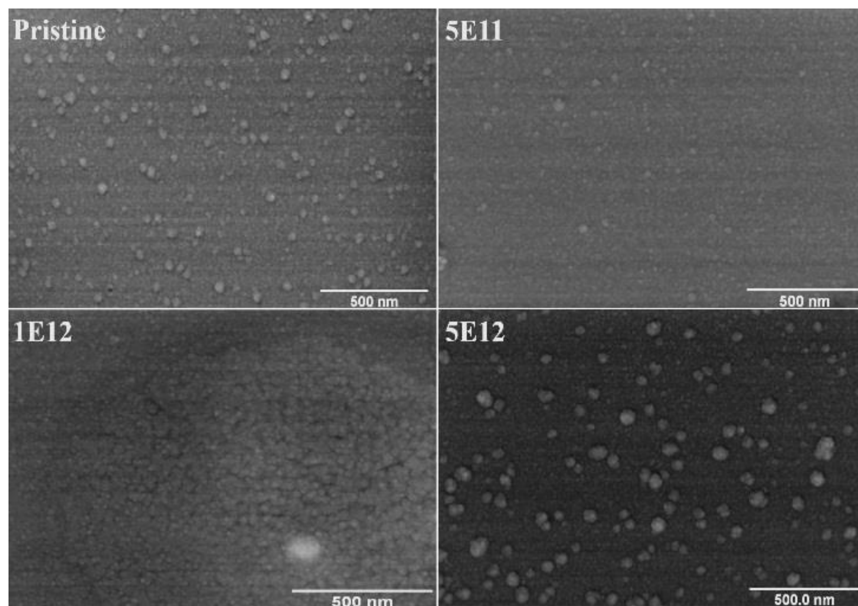

Figure 5.12 SEM micrographs for pristine (a), irradiated stacked multilayers with fluences 5×10^{11} ions / cm^2 (b), 1×10^{12} ions / cm^2 (c), and 5×10^{12} ions / cm^2 (d).

The SEM micrographs of pristine and 100 MeV O^{7+} ion irradiated stacked multilayers are shown in the Fig 5.12. The SEM micrograph of pristine SnO_x / Au / SnO_x is suggests the formation of a film of uniform morphology which is preserved even in the irradiated films.

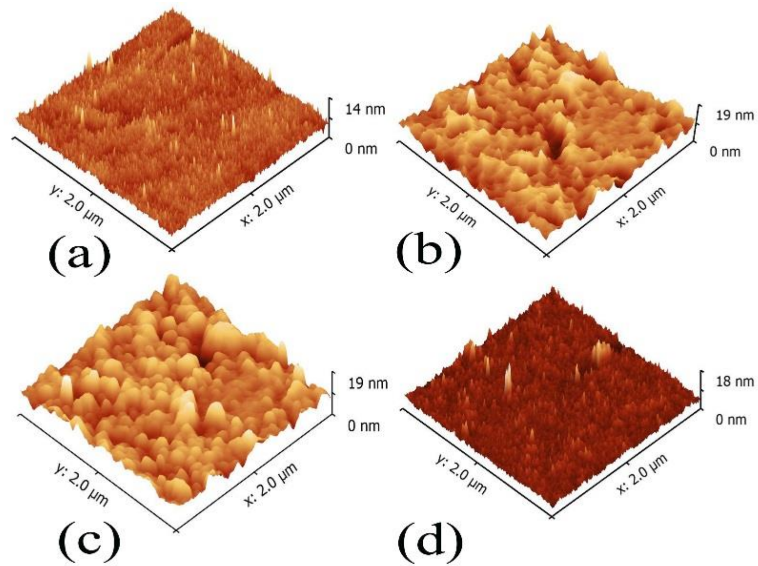

Figure 5. 13 AFM micrographs for pristine (a), irradiated stacked multilayers with fluence 5×10^{11} ions / cm^2 (b), 1×10^{12} ions / cm^2 (c), and 5×10^{12} ions / cm^2 (d).

The AFM micrographs for the pristine and irradiated SnO_x / Au / SnO_x thin films are given in the Fig 5.13 which are indicative of formation of films with small roughness. The surface of the specimen show agglomerated grains and grain growth in the irradiated sample till the ion fluence of 1×10^{12}ions / cm^2, which shows a decrease for a fluence of 1×10^{12}ions / cm^2. This is due to amorphization of the top layer (SnO_2) as a result of a high dose of irradiating ions. These features on the surface are suggestive of the alteration of the optical and electrical properties of the irradiated specimen[175].

5.5.4 UV-Vis and Raman Study

Fig 5.14 shows the variation of transmittance and absorption as a function of wavelength in the visible region. Transmittance and absorbance are seen to be almost constant in the visible region of the wavelength for the pristine specimen while with the irradiation fluence, there is a non-uniformity in the values of transmittance and absorption.

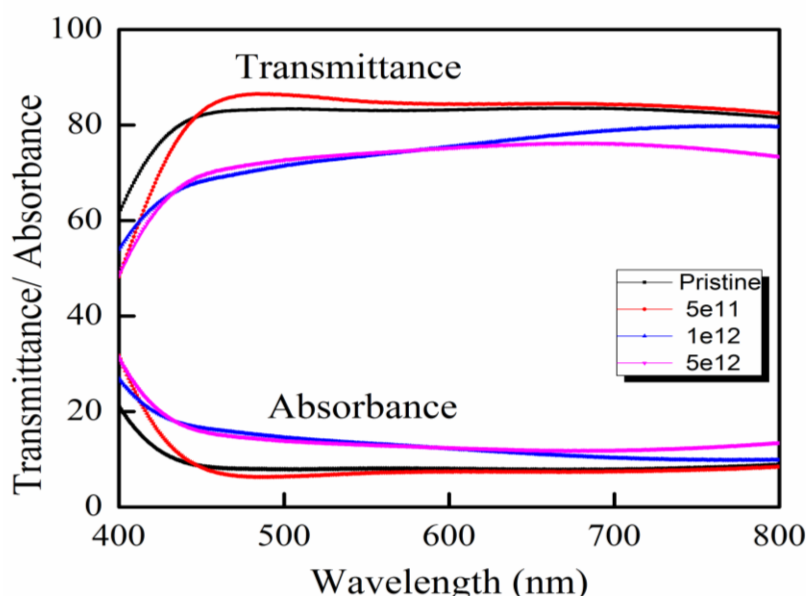

Figure 5.14 UV-Vis spectra for pristine (a), irradiated stacked multilayers with fluence 5×10^{11} ions / cm^2, 1×10^{12} ions / cm^2, and 5×10^{12} ions / cm^2

Initially, on irradiation for a fluence of 5×10^{11} ions / cm^2, the transmittance slightly improves showing highest transmittance ~ 86 at 491 nm and an average transmittance of 82 in the visible wavelength region. With further increase in the fluence, transmittance is deteriorated. A maximum of 79% at 795 nm and an average value of 74 is observed in the extended visible region of 400 nm to 800 nm at irradiation fluence of 1×10^{12} ions / cm^2. The transmittance further decreases and shows maximum value of 76 at 680 nm and an average value of 72 for the highest dose of irradiation at fluence 5×10^{12} ions / cm^2. This behaviour can be understood on the basis of diffusion of Au in the buried layer of SnO_2 causing scattering centres for the incoming photons and thereby increasing the reflectance from the sample[214]. The amount of these scattering centres increases with the increased dose which explains the decrease in transmittance and increase in absorbance.

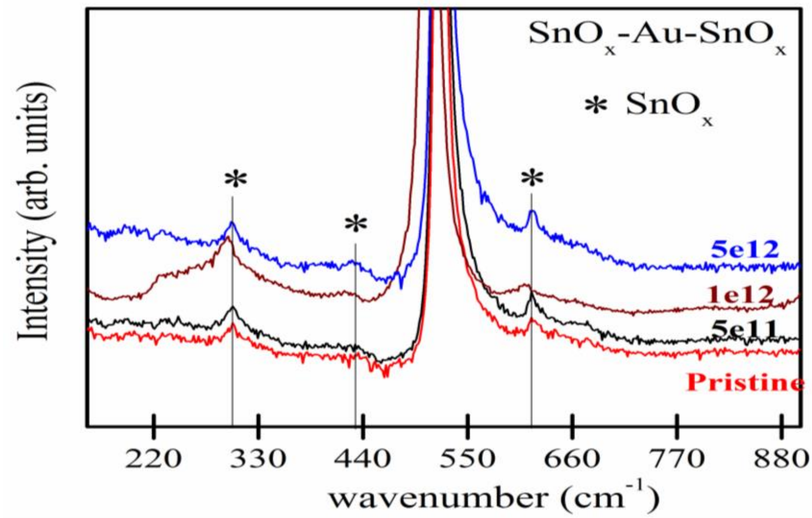

Figure 5.15 Raman spectra for pristine and irradiated stacked multilayer.

The Raman spectra collected with 514 nm line of Ar ion laser for the pristine and irradiated stacked multilayers are given in the Fig 5.15 which show high-intensity peaks primarily due to the SiO_2 lattice[209] at 301 and 617.6 cm^{-1}. These Raman peaks are due to the E_u Raman mode corresponding to the vibration of Sn and O atoms in a plane perpendicular to the c-axis suggesting the formation of SnO_2 [66]. Small intensity of peaks in pristine and irradiated specimen is due to lack of crystallinity among these stacked multilayers. Further, a relatively higher intensity peaks in the stacked multilayer irradiated with a fluence of 1×10^{12} ions / cm^2 are indicative of better crystallinity of the sample for this dose as compared to the pristine and specimen irradiated with a fluence of 5×10^{12} ions / cm^2. These results corroborate the X-ray diffraction results given above enunciating the betterment of crystallinity in the sample with initial fluence and further amorphization with the increased fluence[136].

5.5.5 Low Temperature Hall Studies

The variation of sheet resistance and resistivity with irradiation fluence is shown in the Fig 5.16 which evidences a decreasing trend in sheet resistance and resistivity with increase of fluences. The decreased sheet resistance may be understood on the

basis of ion beam mixing at the second interface (refer fig 5.17) of the multilayer specimen due to diffusion of Au into buried SnO_2 layer which provides better electrical conductivity between layers[135].

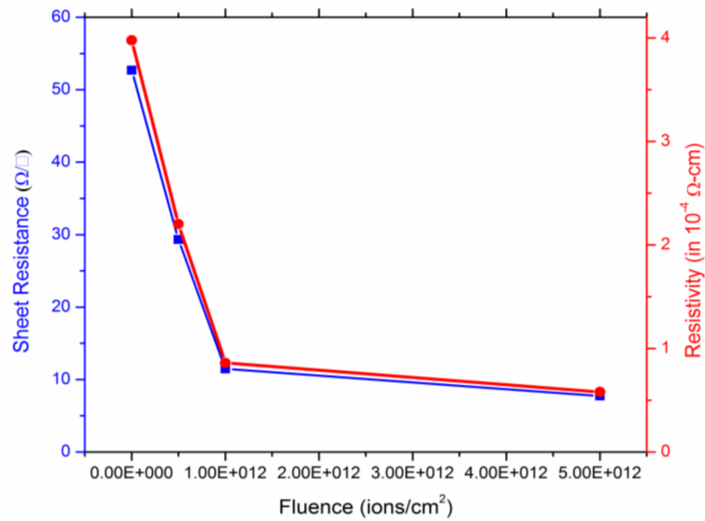

Figure 5. 16 Variation of sheet resistance and resistivity of pristine and 100 MeV O^{7+} irradiated stacked multilayers.

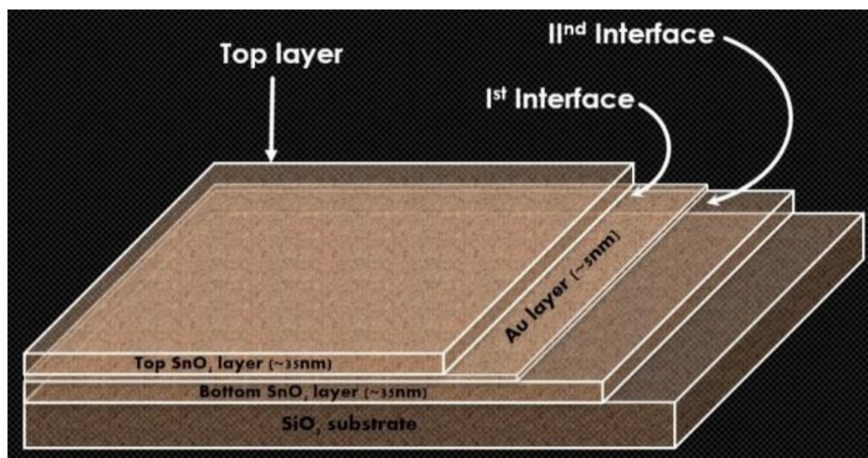

Figure 5.17 Schematic showing the interface of stacked multi-layered structure.

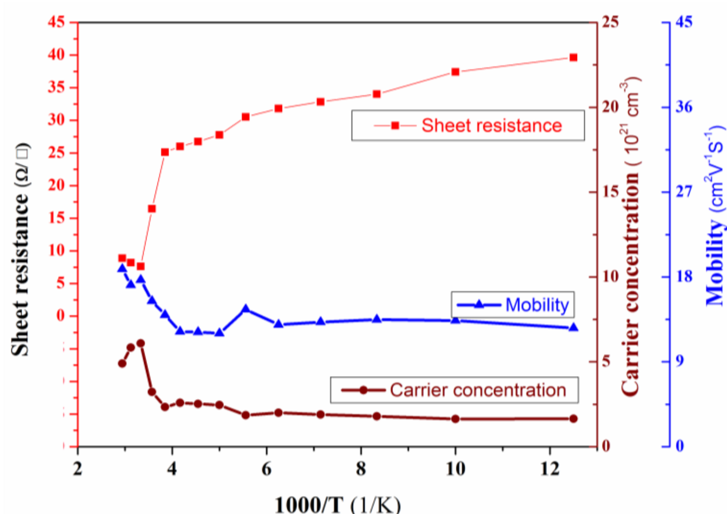

Figure 5.18 Variation of sheet resistance, carrier concentration and mobility with reciprocal of temperature corresponding to the $SnO_x/Au/SnO_x$ thin film irradiated with fluence of 5×10^{12} ions / cm^2.

The variation of sheet resistance, carrier concentration and mobility with temperature is shown in the fig 5.18 which is of same nature as shown by pristine specimen (refer fig 5.18).

5.5.6 XPS Study

The pristine and irradiated (with highest fluence of 5×10^{12} 100 MeV O^{7+} ions / cm^2) multi-layered SnO_x /Au/SnO_x thin film were analysed with XPS and the survey scan of the layers is shown in fig 5.19. The survey spectra are indicative of the presence of the Sn, O and C elements in the top layer[157]. The carbon in the top layer is atmospheric carbon left on the specimen and is not seen at Ist and IInd interface. Further, the Au element peak is seen only in the survey spectra taken at Ist and IInd interface. The intensity of the C 1speak is more in the irradiated specimen which may be due to deposition of C during irradiation of the specimen due to vacuum components.

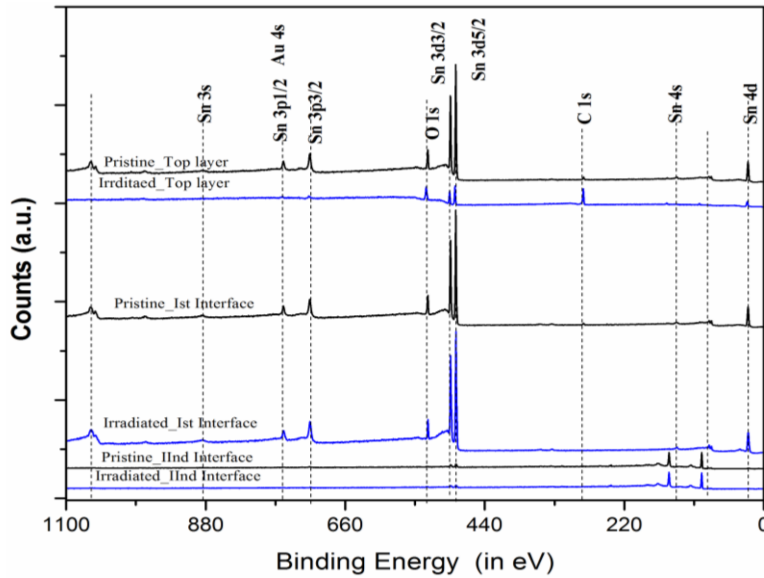

Figure 5.19 XPS survey scan of pristine and irradiated (with the highest fluence of 5 × 10^{12} ions / cm^2) multi-layered SnO_x /Au/SnO_x thin film.

The high-resolution spectra for individual peaks were collected and deconvoluted. The O-1s spectrum is shown to be produced by the contribution of chemisorbed oxygen (O_{chem}) at ~532 eV, O-Sn^{4+} bonding at ~530.5 eV and O-Sn^{2+} bonding at ~529.8 eV[215]. Similarly, the XPS spectra of Sn-3d5/2 is also shown to be constructed from three peaks originating due to the Sn metal (~485.2 eV), SnO bonding (~486.0 eV) and SnO_2 bonding (~486.6 eV)[177,169]. These deconvoluted spectra are shown as fig 5.20-5.22 for the top layer, Ist interface and IInd interface (refer fig 5.17 for the nomenclature of the layer and interfaces).

The XPS spectrum of the top layer of pristine and irradiated stacked multilayer shown in the fig. 5.20 is indicative of a very small amount of chemisorbed oxygen. The large area peak corresponding to the O-Sn^{2+} bonding compared to the peak area corresponding to O-Sn^{4+} bonding in O-1s XPS spectrum and large area under peak corresponding to the Sn^{2+} state compared to that corresponding to the Sn^{4+} state in XPS spectrum of Sn-$3d_{5/2}$ in top layer indicates formation of a mixed phase of SnO/SnO2 which is rich in SnO[205].

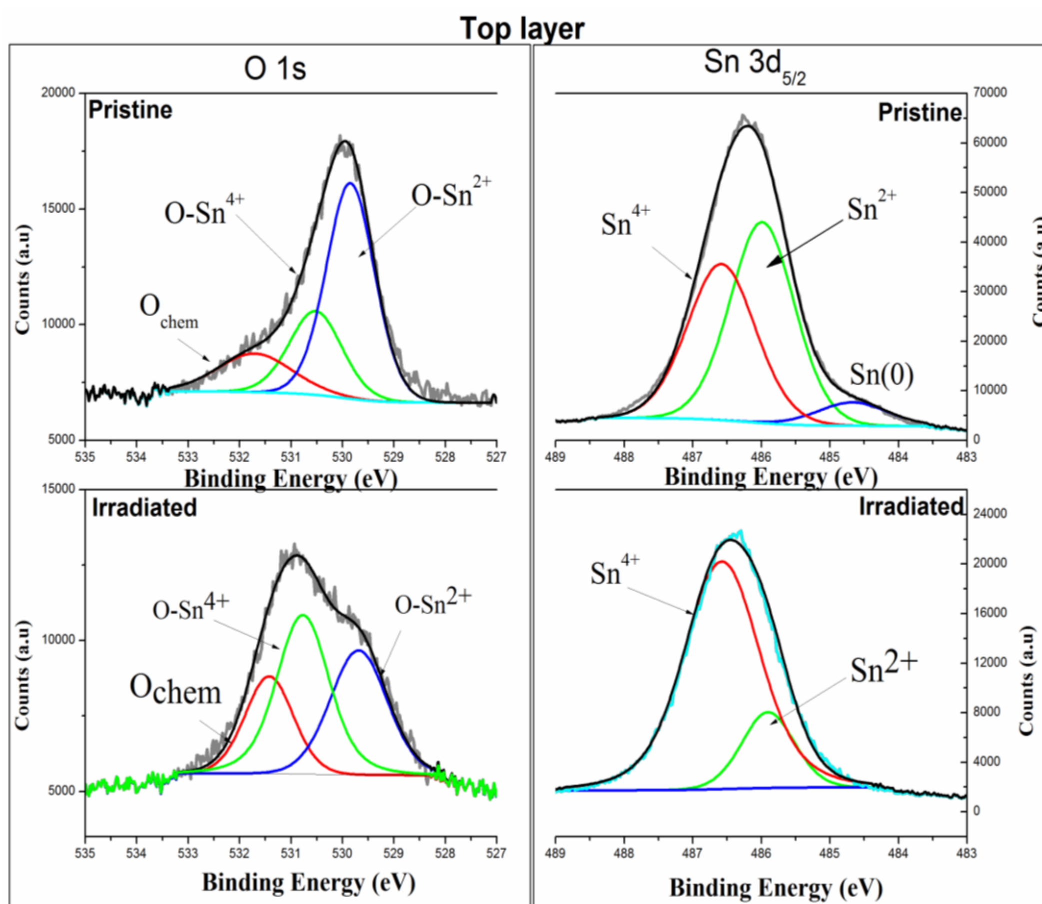

Figure 5.20 XPS spectra of O-1s and Sn $3d_{5/2}$ from top layer of pristine and irradiated (with highest fluence of 5×10^{12} ions / cm^2) multi-layered SnO_x /Au/SnO_x thin film.

XPS spectra of the irradiated stacked multilayer shows increase in area corresponding to the O-Sn^{4+} bonding compared to the area corresponding to O-Sn^{2+} in O-1s XPS spectrum and a larger area for peak corresponding to the Sn^{4+} state compared to the area for peak corresponding to the Sn^{2+} state in XPS spectrum of Sn-$3d_{5/2}$. It shows growth of SnO_2 over SnO making the layer richer in SnO_2 phase as compared to the SnO phase on irradiation[177].

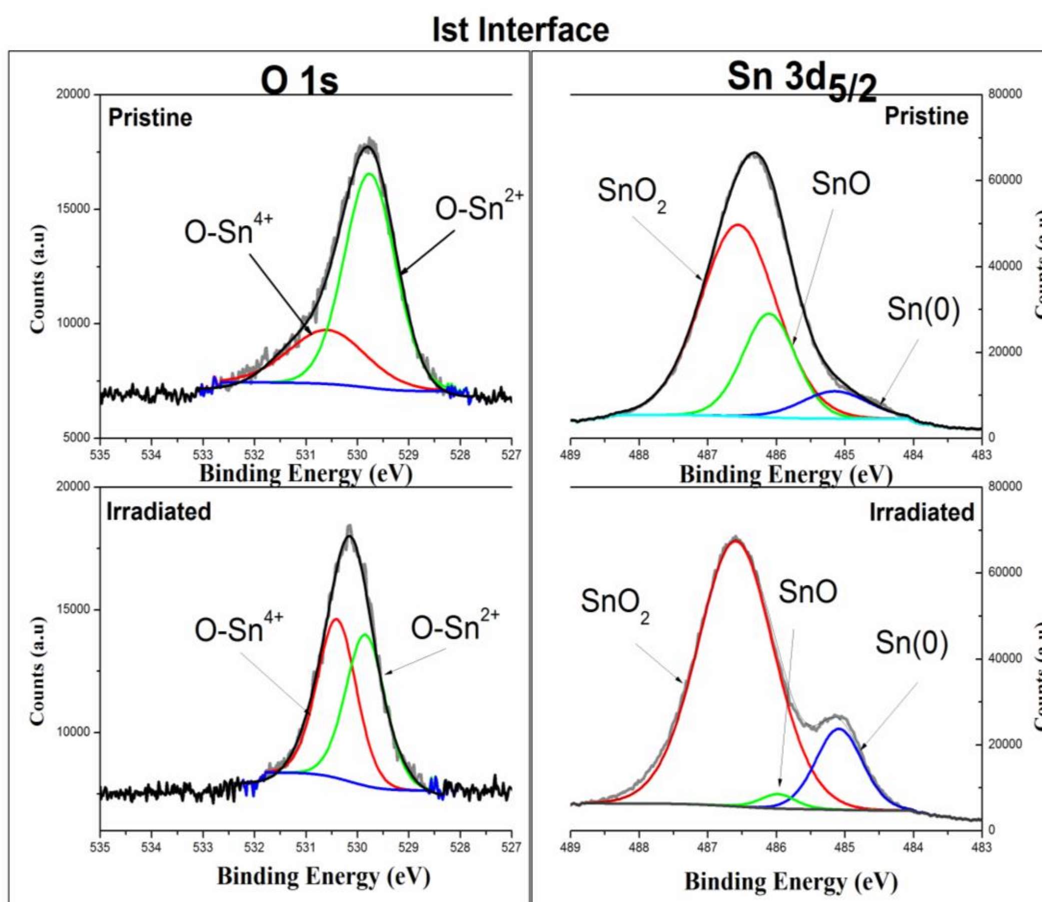

Figure 5.21 XPS spectra of O-1s and Sn $3d_{5/2}$ from Ist interface of pristine and irradiated (with highest fluence of 5×10^{12} ions / cm^2) multi-layered SnO_x /Au/SnO_x thin film.

The XPS spectra of Ist interface of pristine and irradiated stacked multilayer are shown in the fig. 5.21 which shows the formation of a layer of a mixed phase of Sn/SnO/SnO_2 dominated by SnO phase similar to the top layer. Post irradiation, this mixed phase composition changes to phase containing SnO/SnO_2 with no evidence of metallic Sn.

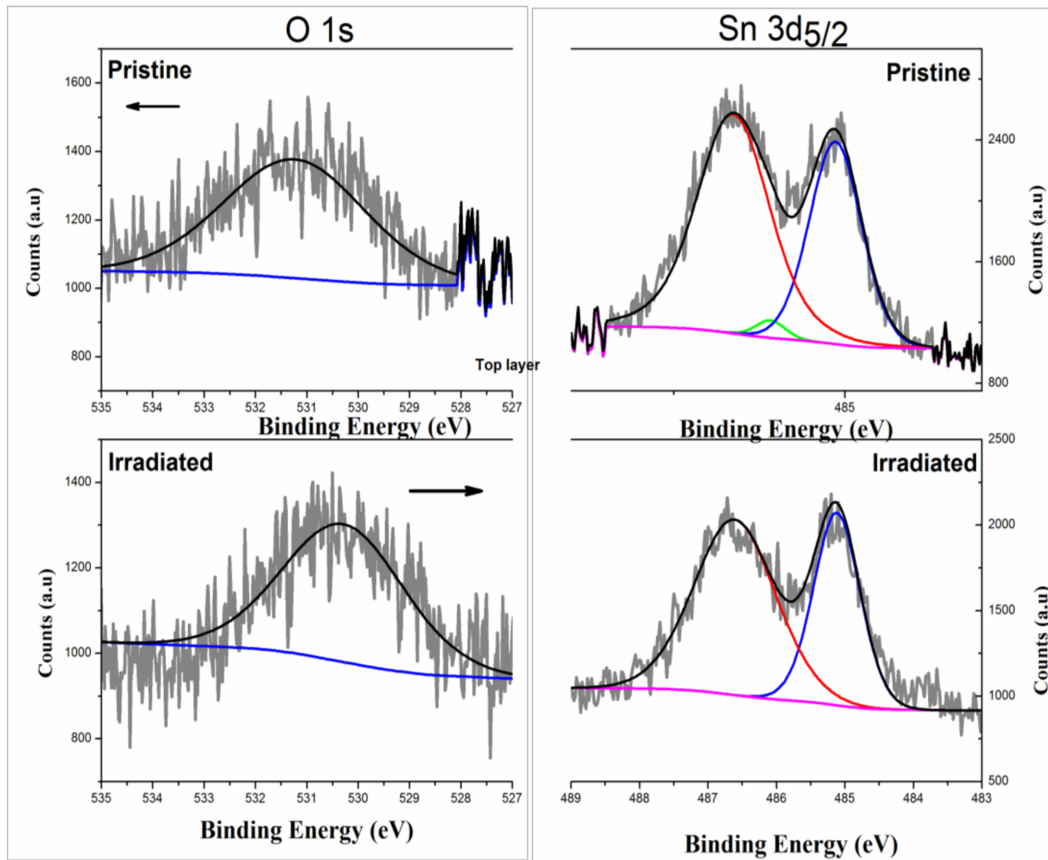

Figure 5.22 XPS spectra of O-1s and Sn $3d_{5/2}$ from IInd interface of pristine and irradiated (with the highest fluence of 5×10^{12} ions / cm^2) multi-layered SnO_x /Au/SnO_x thin film.

The XPS spectra of IInd interface (refer fig 5.22) of pristine and irradiated stacked multilayer are similar to the top layer with no evidence of metallic Sn and chemisorbed oxygen. The irradiation induced a small growth of SnO_2 phase over SnO.

5.6 Gamma Irradiation Study of Stacked Multi-layered SnO_x / Au / SnO_x Thin Films

5.6.1 Introduction

Owing to the increasing applicability of TCO in space applications (solar panels of spacecraft/satellites), food industry (for higher storage duration of fruits and vegetables) and medical radiotherapy application (cancer treatment), it is desired to test the stability of TCO for high energy γ-radiation[216]. The TCO may be exposed to high energetic particles which may lead to the permanent alteration in the structural, morphological, optical as well as electrical properties of TCO[119]. This study summarizes the effect of high energy γ-radiation (dose: 5kGy to100kGy) on the structural/ morphological/ optical/ electrical properties of stacked multi-layered SnO_x / Au / SnO_x thin films. The γ-radiation dose was delivered to the films using the radiation 60Co γ-ray source (dose rate - 0.99 kGy/hr) at room temperature housed at Inter University Accelerator Centre, New Delhi.

5.7 Result and Discussion

5.7.1 X-ray Diffraction Study

The X-ray spectra are shown in the fig. 5.23 exhibiting characteristic peaks corresponding to the Au lattice planes (111), (200) and (220). Apart from the standard Au peaks, the thin films did not produce any other diffraction peak which indicates the amorphous nature of the SnO_2 layer. Further, the intensity of the Au-peak from all three lattice planes (111), (200) and (220) increased on γ-irradiation for 5kGy γ-irradiation indicating the increased crystallinity of the Au layer. Further increase in dose of γ-irradiation (10-100 kGy) depressed the crystallinity and hence diffraction peaks due the

Au layer. At the highest dose of 100 kGy of γ-irradiation, the stacked multilayered thin film exhibits amorphous nature[217].

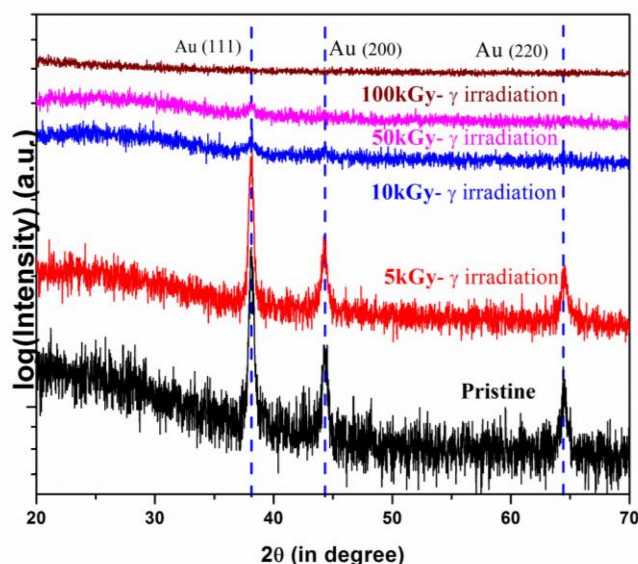

Figure 5.23 X-ray diffraction spectra corresponding to the pristine and γ-irradiated stacked multi-layered SnO_x / Au / SnO_x thin films at different doses (5kGy to 100 kGy).

5.7.2 AFM Study

The AFM micrographs corresponding to the pristine and γ-irradiated stacked multi-layered SnO_x / Au / SnO_x thin films at different doses (5kGy to 100 kGy) are shown as fig. 5.24. The fig 5.24 shows the surface of the top layer (SnO_x) which undergoes changes in morphology when exposed to the γ-radiation. The feature size on the AFM micrograph increased initially with γ-dose (5kGy) which is related to the growth of SnO/SnO_2 grains due to interaction with highly energetic photons. However, this interaction does not change the bulk effectively to produce any significant change in the X-ray diffraction pattern shown in fig. 5.23. With further increase in the dose of γ-radiation, surface smoothening takes place which is a result of the high rate of creation and annihilation of point defects at a higher dose of γ-radiation[216]. Initially roughness

of 10 kGy dose is around 3.5 nm high as compared to pristine (1.2 nm). With high dose 50 kGy it again reduced to 1.8 nm confirming the smoothing of surface.

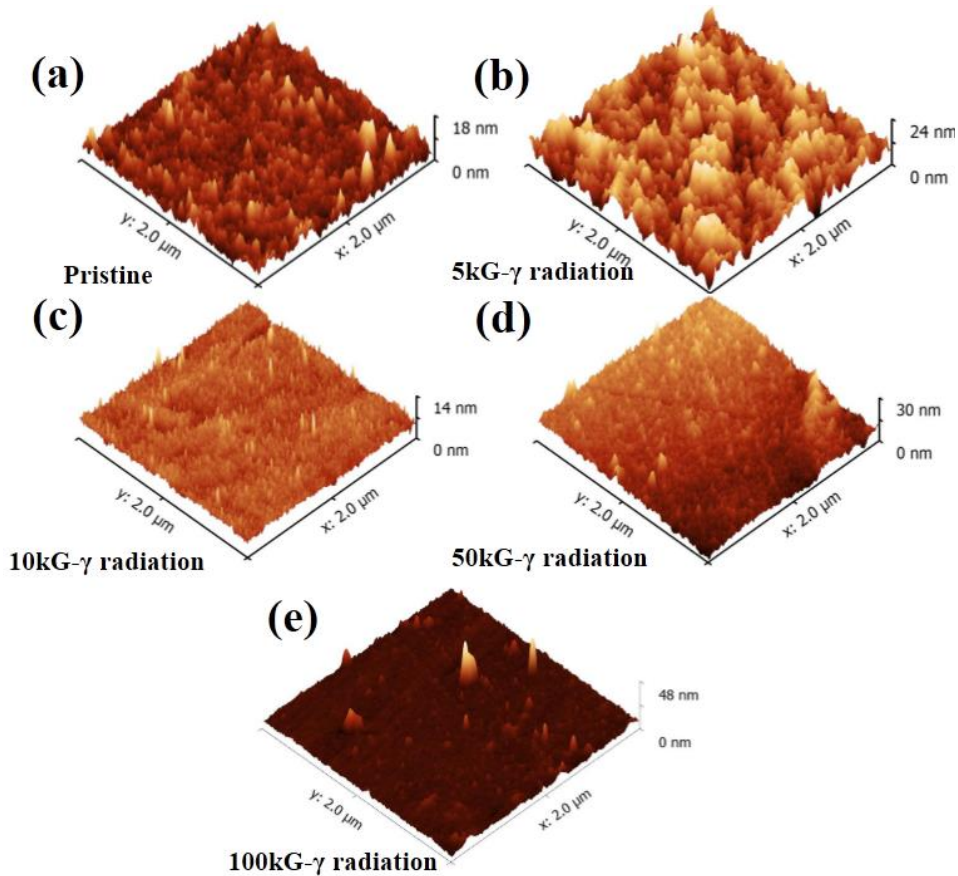

Figure 5.24 AFM micrograph showing the topography of the SnO_2 layer in pristine and γ-irradiated stacked multi-layered SnO_x / Au / SnO_x thin films at different doses (5kGy to 100 kGy).

5.7.3 UV-Vis Study

The UV-Vis spectra are given in fig 5.25 giving the absorbance and transmittance behavior with wavelength for pristine and γ-irradiated stacked multi-layered SnO_x / Au / SnO_x thin films for different doses (5kGy to 100 kGy). The spectra are indicative of a decrease in average transmittance (82.19 for pristine to 75.71 for highest dose) value in the visible region (400 nm to 800 nm*)* which is the preamble of deterioration of the optical properties for TCO applications[119]. Further, at the highest

fluence the transmittance does not remain constant throughout the visible region which raises a question on the stability of the TCO against gamma irradiation.

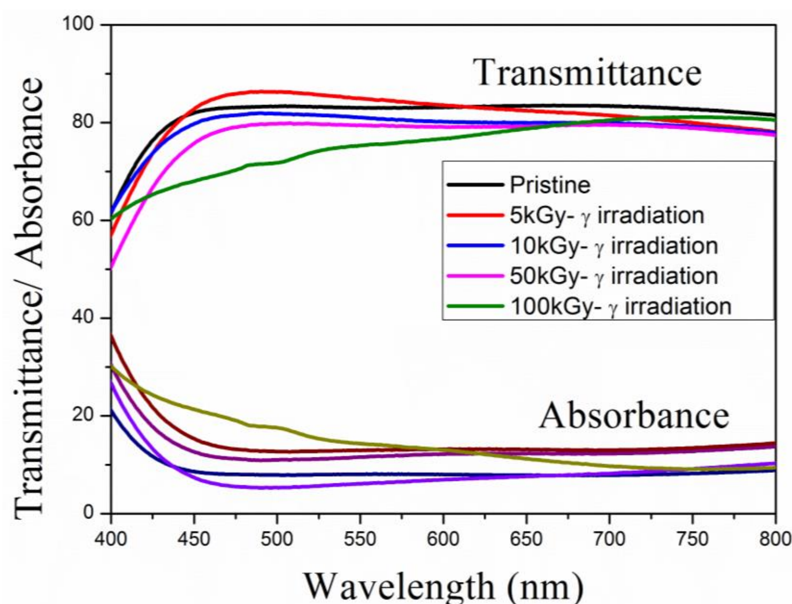

Figure 5.25 Absorbance and transmittance in the visible region for pristine and γ-irradiated stacked multi-layered SnO_x / Au / SnO_x thin films at different doses (5 kGy to 100 kGy).

5.7.4 RBS Study

The RBS spectra corresponding to the pristine and γ-irradiated stacked multi-layered SnO_x / Au / SnO_x thin films at 100 kGy with its fit using RUMP simulation[164] software are shown in fig. 5.26 and 5.27 respectively. The fitted profile confirms the formation of SnO_x / Au / SnO_x stacked multilayers with thickness of SnO_x (35 nm) / Au (5.2 nm) / SnO_x (35 nm). The thickness of the middle Au layer changes post irradiation due to the diffusion of Au in the top and buried SnO_x layer. The simulated profile of RBS data of irradiated thin film indicates the thickness of layers as (28 nm SnO_x / 7.5 nm SnO_xAu / 4.5 nm Au / 7 nm SnO_xAu / 30 nm SnO_x). After gamma irradiation, the oxygen concentration of top oxide layer decreases and shift of composition towards the metallic side. The diffusion layer thickness towards the top layer is around 7.5 nm and 7 nm towards the buried SnO_x layer.

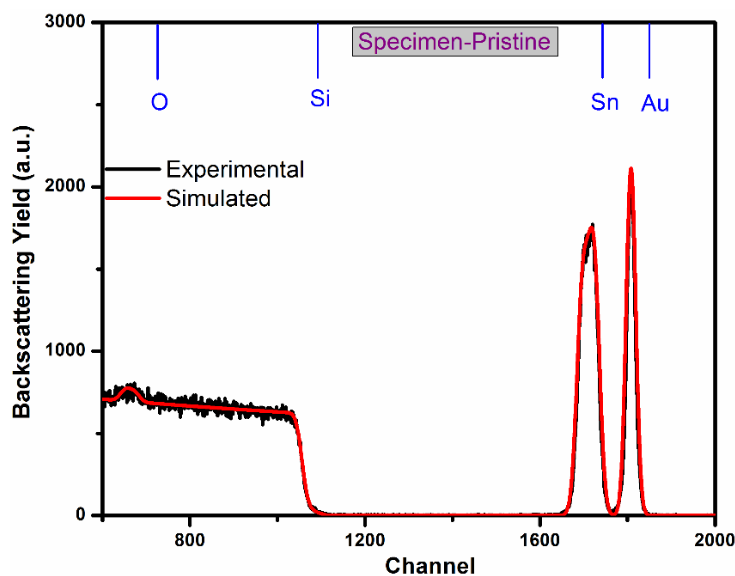

Figure 5.26 The RBS spectrum and its fit for pristine stacked multi-layered SnO_x / Au / SnO_x thin films.

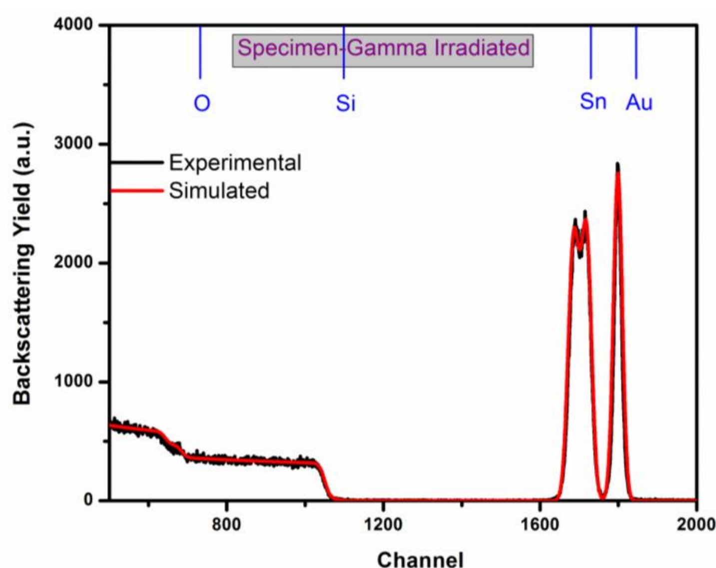

Figure 5.27 The RBS spectrum and its fit for stacked multi-layered SnO_x / Au / SnO_x thin films irradiated with γ-radiation at a dose of 100 kGy.

5.7.5 XPS Study

The high-resolution XPS spectra corresponding to the O-1s and Sn 3d $_{5/2}$ region are shown in the fig 5.28 for the top layer and the I^{st} interface between SnO_x and Au layer. The top layer post irradiation with *γ*-dose of 100 kGy shows some of the chemisorbed oxygen along with a peak indicating the formation of a mixed phase of

$Sn/SnO/SnO_2$. When compared to the pristine spectra given in fig. 5.20, it is concluded that the irradiation induces the growth of SnO_2 over SnO. Similar pattern is seen in the high-resolution spectra of Ist interface exhibits dominant SnO_2 phase over SnO phase[218].

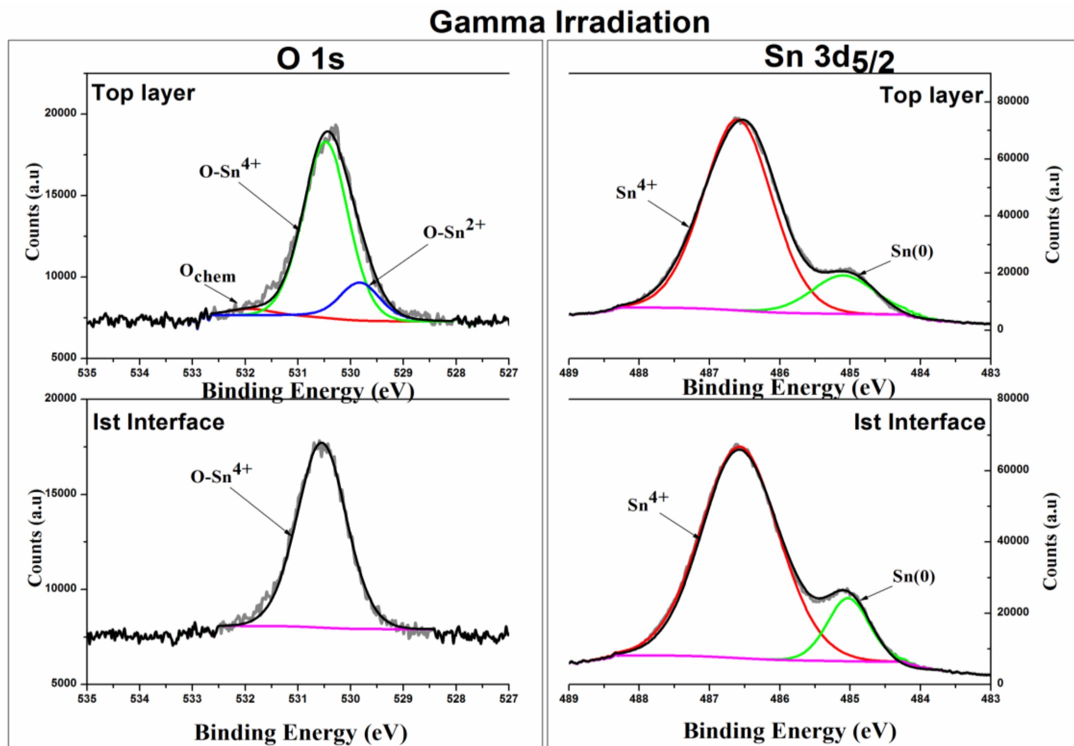

Figure 5.28 The high-resolution XPS spectra of top layer and Ist interface post γ-radiation at a dose of 100 kGy showing O-1s and Sn $3d_{5/2}$ region.

5.7.6 Hall Studies

The variation of resistivity and sheet resistance of samples for different doses of γ-radiation is shown in the fig 5.29. Both resistivity and sheet resistance increase on gamma irradiation showing deterioration of TCO structure post irradiation[119].

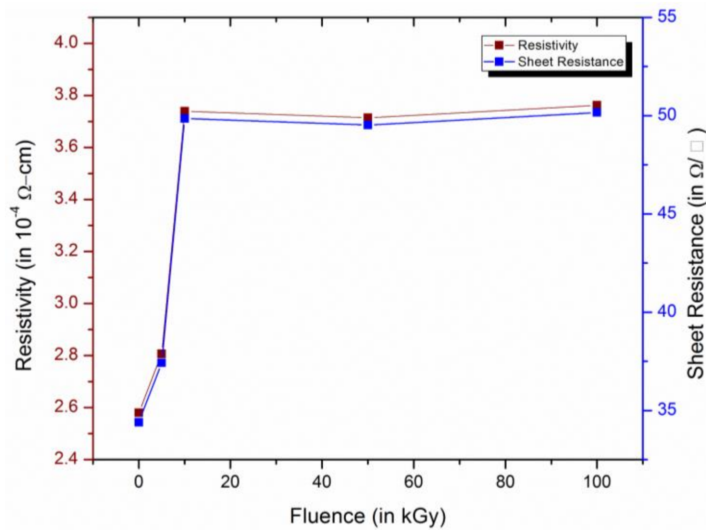

Figure 5.29 Variation of resistivity and sheet resistivity with the dose of γ-radiation.

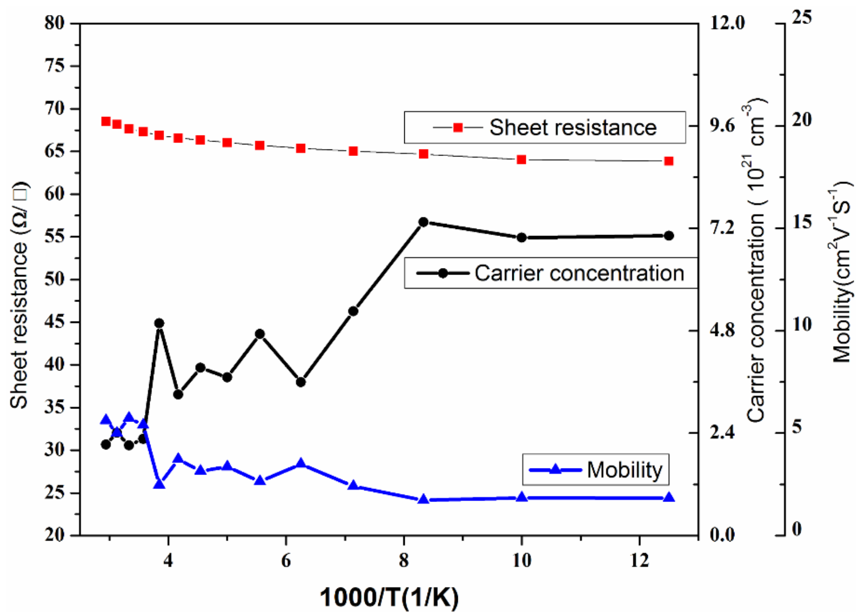

Figure 5.30 The temperature dependence of sheet resistance, carrier concentration and mobility in stacked multilayers of SnO_x/Au/SnO_x post γ-radiation of 100 kGy.

Fig 5.30 shows temperature dependence of sheet resistance, carrier concentration, and mobility in stacked multilayers of SnO_x/Au/SnO_x post γ-radiation of 100kGy showing a very small variation with change in temperature. It proves the stability of the irradiated film and absence of any metastable phase.

5.8 Conclusion

The stacked multilayered $SnO_x/Au/SnO_x$ structure was deposited on a quartz substrate using e-beam evaporation method for SnO_x and thermal evaporation method for *Au* layer to investigate its application as TCO. The XRD studies show an amorphous structure of the multilayer with AFM and SEM suggesting low roughness and flat morphology, respectively favoring the growth of further layers for technological applications. Both RBS and XAS investigations suggest the formation of primarily SnO with evidence of a mixed phase containing SnO_2. Analysis of the spectral features in XAS and XES measurements confirms the presence of a mixed SnO/SnO_2 phase. Amorphous SnO_2 within the SnO layer disrupts the SnO lattice and alters the electronic band structure. Combining XAS and XES measurements reveals a wide band gap energy (3.5 ± 0.2 eV), suitable for applications requiring high transparency in the visible range. Oxygen deficiency in SnO_x is indicated by RBS, and XAS confirms the presence of oxygen vacancies that can contribute to lower resistivity. The TCO characteristics resulting from the stacked multilayer were exhibiting high transparency (83% beyond 475 *nm*), lower sheet resistance ($52\Omega/sq.$) and lower resistivity ($3.9\times10^{-4}\Omega\cdot cm$) which are comparable to that of standard ITO substrates. The increase in room temperature resistivity and sheet resistance with temperature is also suggesting metallic behavior which is attributed to the metal-rich nature of the stacked multilayer. Such a multilayered structure with enhanced optical and electrical properties is proposed as a better replacement of the standard ITO substrates for optoelectronic applications.

The 100 MeV O^{7+} and gamma (10 kGy-100 kGy) irradiation was carried out on the stacked multilayer of $SnO_x/Au/SnO_x$ to test these multilayers for space applications.

The structural study (using XRD) concluded a very slight change in structure of the films post irradiation which is further corroborated by surface study by AFM. However, the slight change in the structure was evidenced as the phase change (indicated by XPS) which was responsible for the change in optical and electrical properties of these films. The SHI/gamma irradiation is thus concluded to change the performance parameters of these stacked multilayer structure and hence not suggested for space application presenting such type of radiation exposure. However, a possibility of tuning the properties was also observed by employing SHI irradiation which may be explored for general applications.

Chapter-6

Fabrication and Characterization of ZnO-Ag-ZnO Multilayer Thin Films and Their Ion Beam Effects

6.1 Introduction

Transparent conducting films (TCF) are key components in a variety of optoelectronic devices and systems, including organic and inorganic solar cells, light-emitting diodes (LEDs) and flat panel or liquid crystal displays[219]. ZnO is a prime candidate due to its wide band gap, good conductivity and high transparency in the visible wavelength region[220]. A continuous ultrathin Ag layer shows good electrical conductivity (at room temperature) and small optical losses (i.e. less reflection and absorption of visible wavelength region in thin film form) in visible range[221].

This chapter reports the synthesis of ZnO-Ag-ZnO (ZAZ) samples using RF-DC sputtering techniques. The thickness of Ag layer has been optimized by keeping ZnO layer thickness constant. Previous studies showed that the ZnO film gives maximum transmittance for visible light for 30-50 nm thickness[222]. The Ag layer gives best results in terms of electrical conductivity and transparency for thickness below 10 nm but with a requirement that the film has to be a continuous film[72]. It has been observed that the structural, morphological and optical properties of the oxide-metal-oxide structure are altered due to the embedded metal layer formation and its thickness[40]. In view of this, the effect of thickness of Ag layer embedded in two ZnO layers on the structural, morphological and optical properties of ZAZ multilayer has been investigated. Furthermore, electrical properties are also altered with variation in thickness of Ag. The optical properties of this multilayer which include transmittance,

absorbance and reflectance show variation with thickness. Optical parameters such as refractive index, extinction coefficient have also been calculated to observe how these changes with thickness. The increase in thickness of Ag enhances conductivity but simultaneously reduces transparency and hence, an optimization was done to improve opto electronic properties of the multilayer using different thickness of Ag layer. Results indicate that the multilayer shows the best result for the optimized thickness and the electrical and optical properties degrade for other values of thicknesses.

6.2 Experimental Study

ZnO-Ag-ZnO multilayer structure was deposited by RF-DC sputtering techniques using standard commercial targets. The dielectric layer of ZnO (40 nm) was deposited on glass substrate at room temperature by radio frequency (RF) magnetron sputtering using 99.99 % pure target. The Ag layer was then deposited on top of ZnO dielectric layer by DC sputtering using 99.99 % Ag target. Finally, last ZnO (40 nm) top layer was deposited on the Ag/ZnO/glass structure again by RF magnetron sputtering technique. The base pressure of the chamber was $5x10^{-6}$ mbar and working pressure was 1×10^{-3} mbar during ZnO deposition and 1.5×10^{-2} mbar for Ag layer deposition. The power was 100 W and 15 W for RF and DC sputtering respectively. The flow of Ar was kept as 15 sccm for both processes. Deposition rate obtained under mentioned conditions was 4 Å/ sec for ZnO and 6 Å/ sec for Ag film. The target to substrate distance was 10 cm and deposition temperature was kept 300 K. Crystalline properties of ZAZ multilayers were observed using X-pert Pro Pan Analytical X-ray diffraction (XRD) with CuKα radiation. Thickness of layers was calculated using Rutherford Back Scattering (RBS) using 2 MeV He^{+} ion beams at Inter University Accelerator Centre, New Delhi (India). The surface morphology of pristine and SHI

irradiated ZAZ multilayer films was observed by field emission scanning electron microscopy (FE-SEM) and atomic force microscopy (AFM) using Nova Nano FESEM 450 (FEI) and Nanoscope IIIa, respectively. Optical transmittance of ZAZ multilayers was measured using UV−Vis spectrophotometer LAMBDA 750 (Perkin Elmer) with bare glass substrate as a reference in the spectral range of 400−800 nm at room temperature. Electrical properties of ZAZ multilayers were then investigated using ECOPIA-3000 for room temperature, ECOPIA-5000 for LN2 to 350 K Hall Measurement system with 0.55 T magnets.

6.3 Results and Discussion

6.3.1 X-ray Diffraction

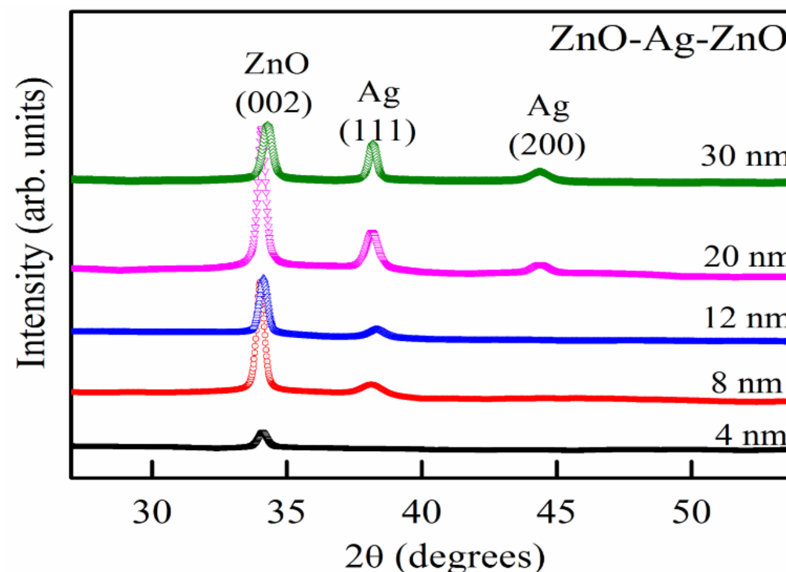

Figure 6.1: XRD pattern of ZAZ multilayer with different Ag layer thickness (4-30 nm).

Figure 6.1 shows the XRD pattern of ZAZ multilayer films grown with varying Ag layer thickness. The (002) diffraction plane corresponding to hexagonal wurtzite structure of ZnO (JCPDS Card no. 36-1451) is observed for all samples. The occurrence of preferred orientation (002) for all samples is due to the most energetic stable crystal

plane of ZnO. No additional diffraction peak corresponding to other phases are observed for these multilayers. The peak corresponding to Ag is not observed for multilayer structure having thickness 4 nm due to a very small thickness of sandwiched metal layer but observed for all other thicknesses greater than 4 nm. The intensity of the peak increases with Ag thickness. An additional peak at 2θ value ~ 44.2° corresponding to (200) planes of Ag is observed for higher thickness values (20 and 30 nm).

The lattice parameters and crystallite sizes for both ZnO and Ag are estimated. The *c*-axis lattice parameters for hexagonal ZnO (for 002 planes) is calculated using the relation $c = \lambda/sin\theta$where λ is the wavelength and θ is Bragg's angle. Lattice constant for cubic Ag (for 111 plane) is found using the relation, $d = a/\sqrt{h^2 + k^2 + l^2}$. Furthermore, the average crystallite size (D) of these samples is estimated from X-ray data using Scherer's formula D = 0.89 λ /βcosθ, where λ is the wavelength of x-rays used, β is FWHM and θ is Bragg's angle). The variation in these parameters (i.e. lattice parameter and crystallite size) for both ZnO and Ag is shown in Table 6.1. It has been found that crystallite size for Ag increases continuously with thickness with a small variation in the lattice parameter.

Table 6.1: Physical parameters calculated from XRD pattern for different Ag thickness.

Samples Details (Ag Thickness)	ZnO Parameters		Ag Parameters	
	Crystallite size (nm)	Lattice Parameter (Å)	Crystallite size (nm)	Lattice Parameter (Å)
4 nm	19.857	5.250	-------	-------
8 nm	26.733	5.264	16.989	4.040
12 nm	22.934	5.247	18.144	4.019
20 nm	27.031	5.257	21.517	4.035
30 nm	22.086	5.225	27.977	4.032

6.3.2 Rutherford Back Scattering

To confirm the film thickness and stoichiometry, the RBS measurements were performed on the samples. Figure 6.2 shows the RBS spectrum and RUMP simulated[204] ZAZ multilayer structure for 8 nm thick Ag sample. Distinct elemental peaks associated with Zn, O and Ag are observed. The thickness of layers calculated with the help of the fitted curve is found to be ZnO (40±5 nm)/Ag (8±1nm)/ZnO (40±5 nm). This suggests formation of ZnO with pure Ag in the sandwich layer including some spreading of Ag atoms into the ZnO layer.

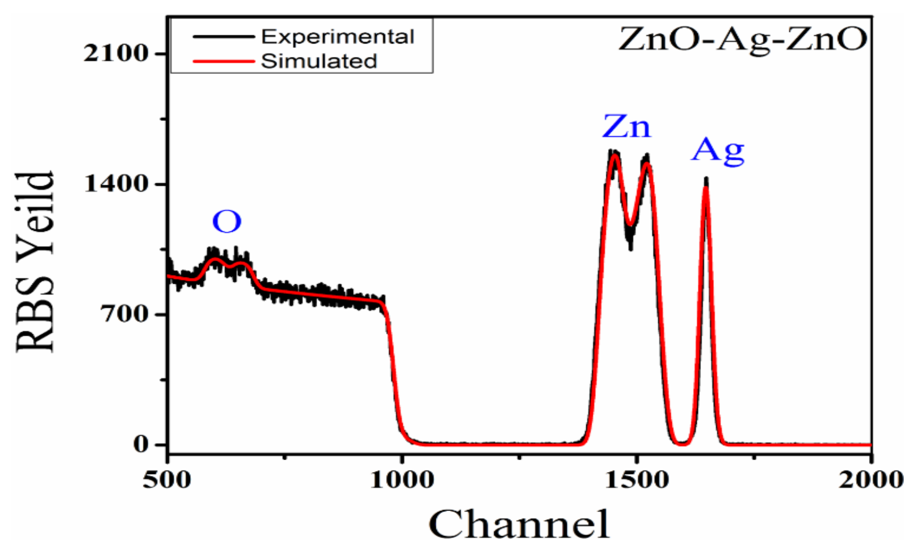

Figure 6.2: RBS pattern of ZAZ with Ag thickness 8 nm.

6.3.3 Scanning Electron Microscope

The morphology of the ZAZ multilayer thin films having different Ag thickness have been analyzed using FESEM measurements and are shown in fig. 6.3. The analysis of particle size and morphology suggests that there is not much change in the particle size but significant change in the morphology is observed on varying the thickness of sandwiched metal layer[153]. The variation in particle size is shown in fig. 6.3(f) and the average particle size is found to be in the range of ~ 12-16 nm. It has been found that well-defined crystals of zinc oxide from top layer of ZAZ are formed for the multilayer

thin film having Ag thickness of 8 nm. For other values of Ag layer thickness, either irregular particles or voids are seen. Based on this, it is concluded that sandwiched metal layer with 8 nm thickness gives best-optimized multilayer from a morphological point of view.

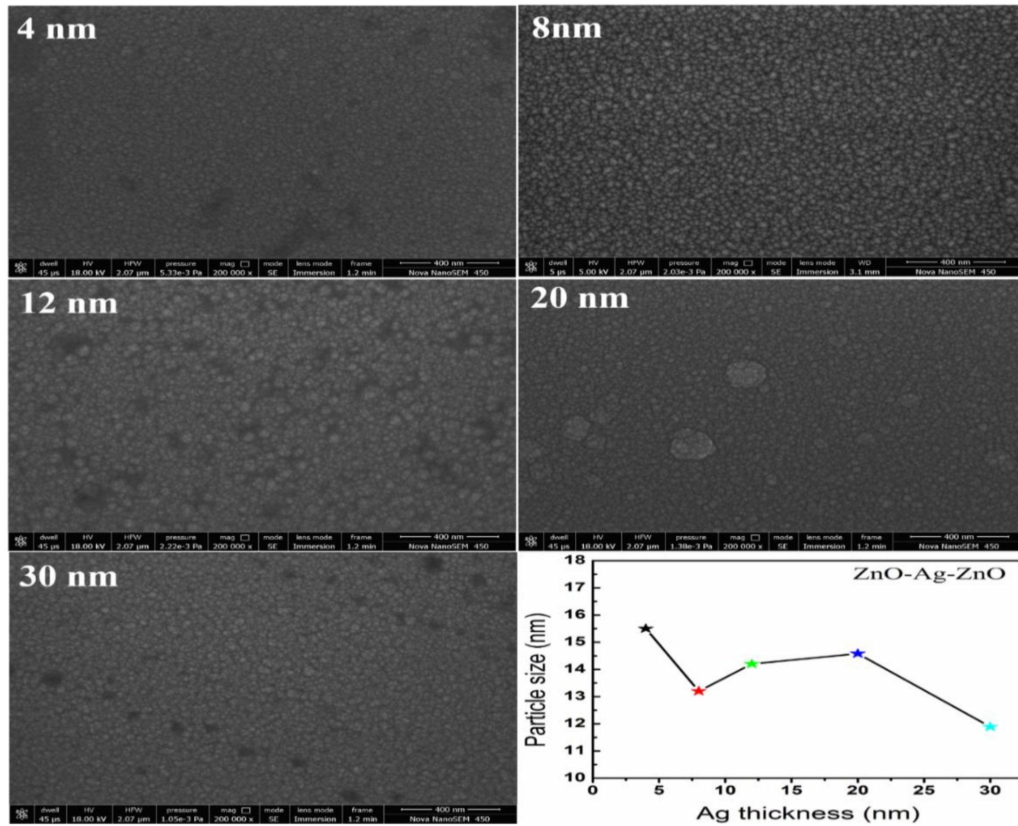

Figure 6.3: SEM micrographs of ZAZ with different Ag thickness (4-30 nm).

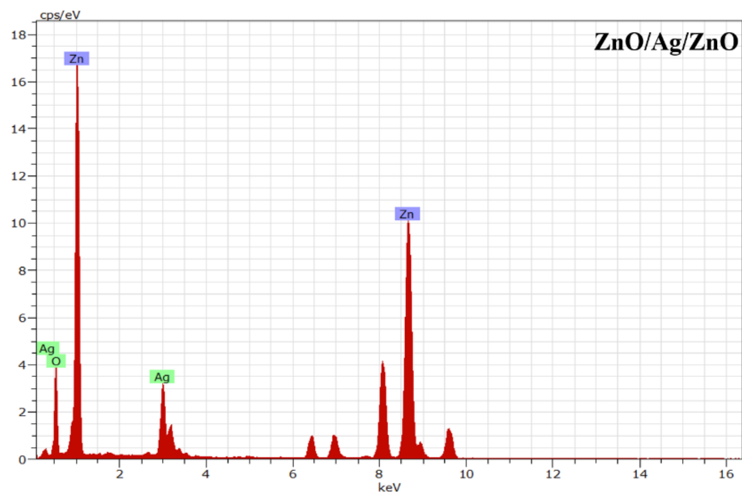

Figure 6.4: EDX micrograph of ZAZ with 8 nm thickness.

Furthermore, EDX measurements were performed to analyze the presence of elements and their compositions. The multilayer structure is seen to have Ag, Zn, and O ions. C and Ar ions are also seen due to their abundance in nature. The spectrum shows higher Zn content as a result of relatively large thickness of ZnO compared with Ag in the multilayer structure.

6.3.4 Atomic Force Microscope

Figure 6.5 illustrates AFM images for all multilayer thin films of ZAZ structure. The images confirm formation of a continuous and smooth surface for all samples. Different morphologies are seen for different Ag thickness demonstrating that the thickness of the inner Ag layer has an important role in determining the properties of the multilayer[86].

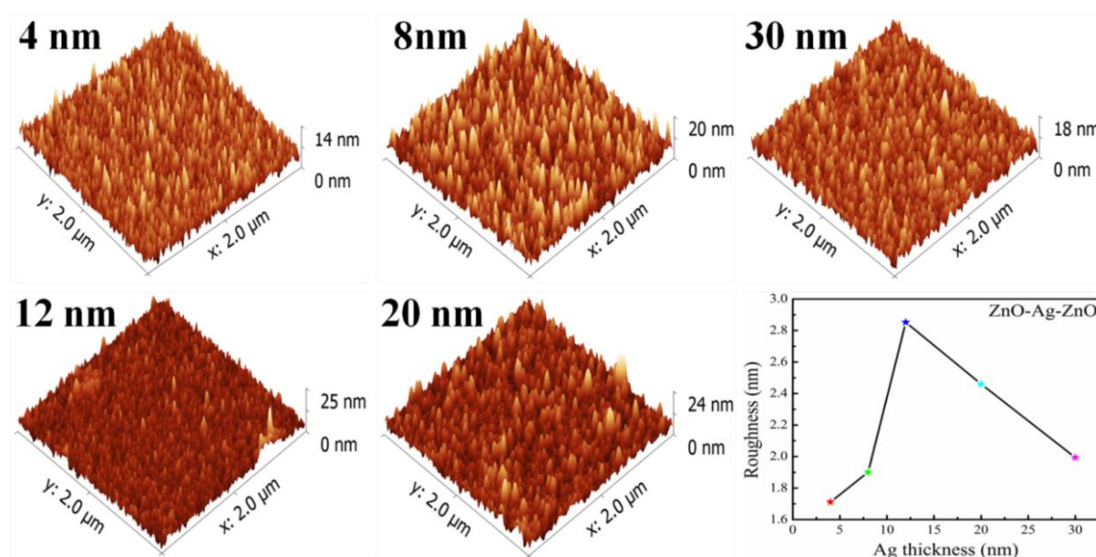

Figure 6.5: AFM images of ZAZ with Ag different thickness (4-30 nm).

The calculated roughness of ZAZ sample with 4 nm Ag layer is ~ 1.7 nm and takes a maximum value of ~ 2.88 nm for Ag thickness of 12 nm. Further, an increase in the Ag layer thickness causes a reduction in the roughness and it becomes ~ 2.0 nm for 30 nm thick Ag layer. The variation in the roughness is shown in Fig 6.5. The change

in the overall roughness is within the acceptable limit (< 3nm) for any device formation which is one of the required main parameters for electrode fabrication[167].

6.3.5 Transmission Electron Microscope

The as prepared multilayer ZAZ films were deposited on TEM grids to analyze the microstructure. The trilayer structure and its thickness do not allow getting all features from the multilayer. The images show layered depositions with different size particles. The high-resolution images from TEM were analyzed by digital micrograph software[170] to find out the crystallographic planes of top ZnO layer.

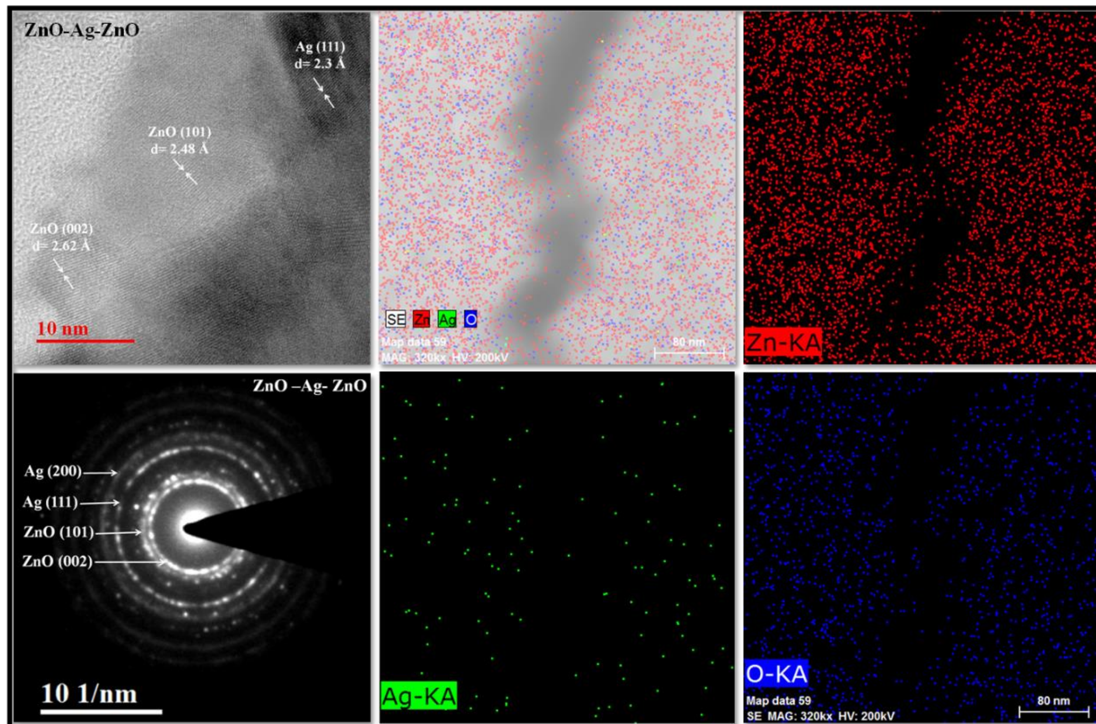

Figure 6.6: TEM micrographs of ZAZ with 8 nm Ag thickness.

The confirmed planes are (002) and (101) planes for ZnO as indicated in Fig. 6.6 (a). The SAED pattern exhibits the different diffraction planes of ZnO and Ag reflected as rings with different diameters. It confirms the polycrystalline structure of ZnO and Ag in the multilayer structure[141]. Elemental mapping shown in Fig.6.6 shows uniform distribution of elements Zn, Ag, and O in the films. It indicates uniformity in

the layers of the multilayer structure which is an essential feature for transparent electrode application.

6.3.6 UV-Vis Spectroscopic Study

It is well known that properties of DMD structure are very much influenced by the thickness of sandwiched layer. The threshold thickness for the sandwiched metal layer has been optimized by various groups and found to be around 10 nm[108]. It has been found that both transmittance and conductivity increase up to this percolation threshold. However, a further increase in the metal layer thickness leads to a reduction in both, transmittance as well as conductivity. In the present work, the optical properties of ZAZ stacked multilayer are measured using UV-Vis spectrophotometer over the wavelength range 400 to 800 nm and are presented in fig. 6.7. It can be seen that transmittance of the ZAZ multilayer can be precisely tailored just by the sandwiched layer thickness.

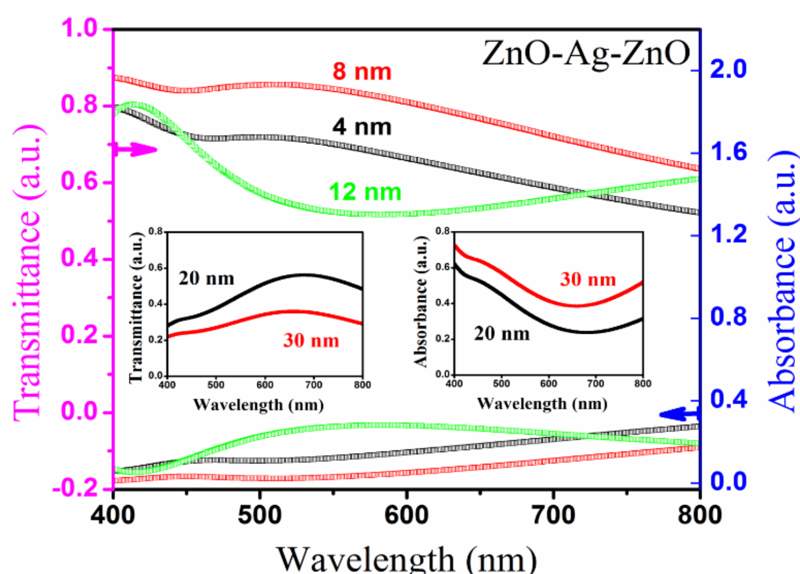

Figure 6.7: UV-VIS spectra of ZAZ with different Ag thickness (4-30 nm).

The average transmittance of ZAZ electrode climbs initially for smaller values of thickness (up to 8 nm thickness) of the metal layer. The multilayer structure exhibits an average transmittance of ~ 70-80 % for silver layer thickness 4 - 12 nm. However,

maximum transparency is obtained for ZnO-Ag-ZnO sample with 8 nm thick silver layer. This is due to the fact that surface scattering of incident light is very less for thin continuous metal Ag layer. After the threshold thickness of 8 nm, the transmittance drops drastically. For higher Ag thickness, the visible light is blocked by metallic layer by absorption, reflectance and surface interaction leading to lesser transmittance[90].

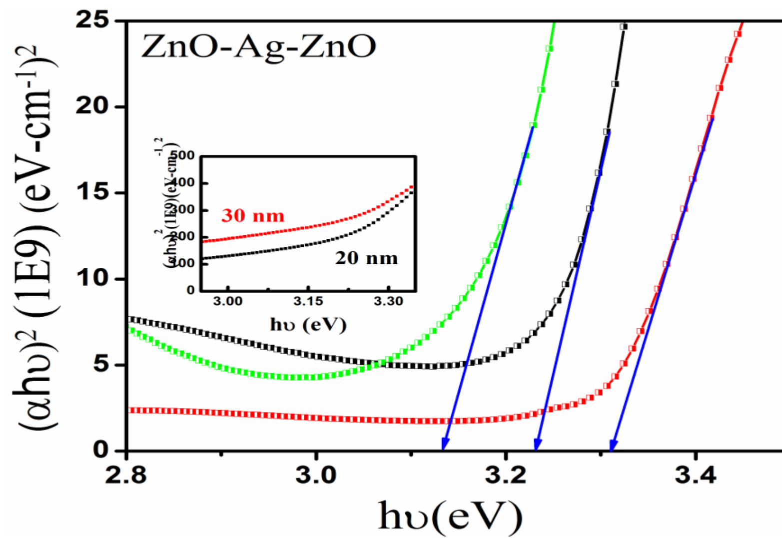

Figure 6.8: Tauc's plot for ZAZ multilayers with varying Ag thickness (4-30 nm).

Band gap, refractive index, and absorption coefficient have been calculated to check the suitability of ZAZ structure as a transparent electrode[33]. The bandgap of the ZAZ multilayer structure can be calculated using Tauc's relation $\alpha h\nu = A(h\nu - E_g)^{1/2}$. Here, α is the absorption coefficient, hν is the photon energy, A is a constant and E_g is the optical band gap[172]. From Tauc's plot (Figure 6.8), the optical bandgap for 4 nm thin Ag in the layered structure is found to be 3.22 eV. There is a slight enhancement in the optical bandgap (3.25 eV) of the films having 8 nm thin Ag layer. However, a further increase in the Ag layer thickness leads to a reduction in the bandgap. The reduction in the optical band gap is mainly due to the increased carrier concentration[223]. This has been discussed in the next section. Previous reports indicate that increased carrier concentration in ZAZ multilayer reduces the band gap when free charge carrier densities are above the Mott critical density[37].

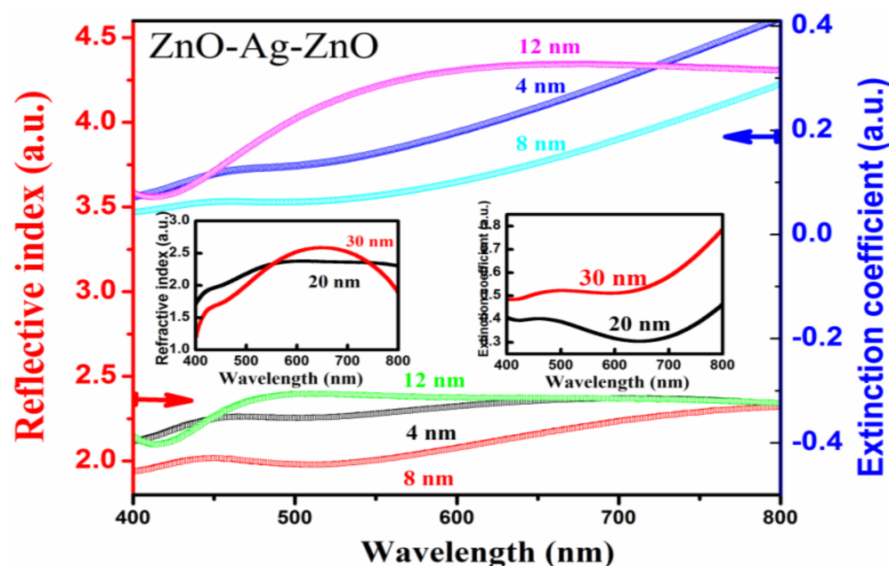

Figure 6.9: Refractive index and extinction coefficient for ZAZ multilayer with varying Ag thickness (4-30 nm).

6.3.7 Hall Measurements

One of the main requirements of the transparent electrode for optoelectronic devices is high electrical conductivity with adequate charge carrier number and mobility[33]. While developing the alternative transparent electrode, it is a prime concern to reach the electrical properties and stability of these properties making the TE comparable to the commercially available ITO electrode.

Room temperature Hall effect and electrical resistivity measurements were carried out using Van der Pauw configuration[162]. The variation of sheet resistance, carrier concentration, and mobility as a function of the Ag thickness at room temperature (300 K) is presented in Fig. 6.10. It is showing that the resistivity is very high with 4 nm Ag layer thickness. The growth of Ag layer is an island type growth where three-dimensional islands are formed initially. Coalescence of smaller islands leads to formation of larger ones and a continuous layer is formed after a critical stage[174]. It is proven by previous report that below 6 nm the Ag layer is not continuous[108]. So, at 4 nm the silver layer is a disconnected network structure leading to breaking of path for

charge carriers. Best electrical results are obtained when the thickness is increased to ~ 8 nm. Resistivity comes around 9.7×10^{-5} Ω cm with mobility ~ 6.6 $cm^2V^{-1}S^{-1}$ and charges carrier concentration 9.5×10^{21} cm^{-3}.

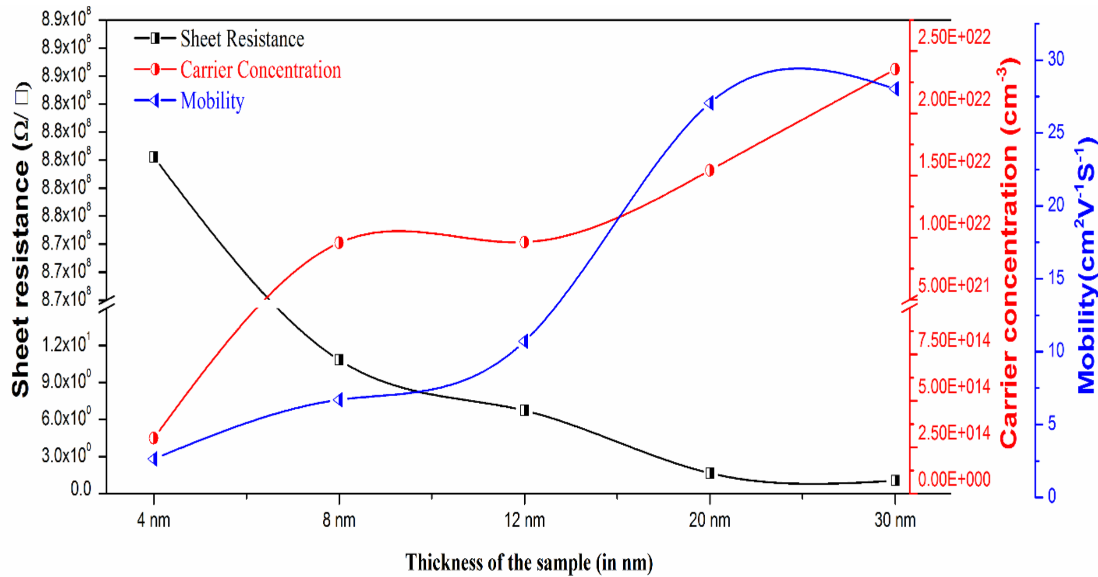

Figure 6.10: Hall measurements of ZAZ with different thickness (4-30 nm).

These set of values complete all electrical requirements for the transparent electrode. The results show that up to 12 nm Ag thickness the ZAZ structure gives nearly similar results. Further increase in Ag layer thickness improves electrical properties of the multilayer which then behaves like a pure metallic film, but the optical properties are reduced simultaneously. The Haacke's figure of merit (FOM) has been calculated for these samples to evaluate their performance[51].

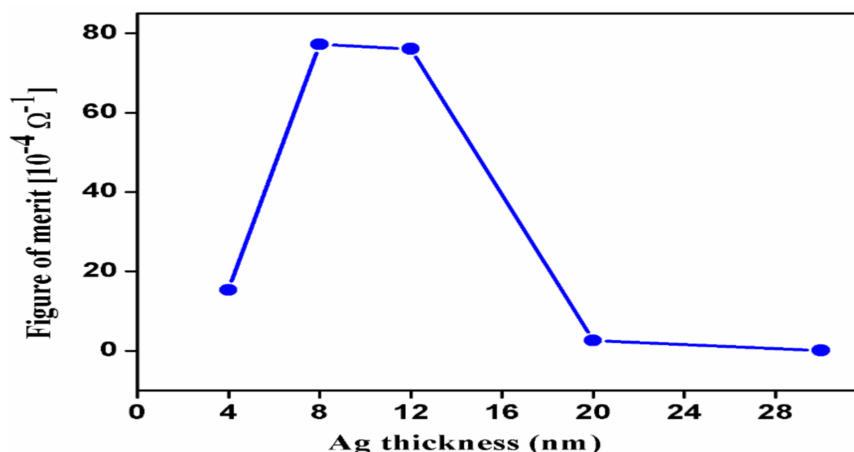

Figure 6.11: Haacke's FOM of ZAZ with different Ag thickness (4-30 nm).

Results show that FOM is very low for 4 nm Ag thickness and still lower values are obtained for higher thickness 20 nm and 30 nm. The stacked multilayer structure exhibits highest values of FOM for 8-12 nm Ag layer thickness and hence it can be inferred that the ZAZ structure gives best optical and electrical results for this thickness for transparent conducting electrode application.

6.4 Xe^{+} Ion-Beam (100keV) Effect on ZnO-Ag-ZnO Thin Films

Based on the results of the optimization study of the thickness of middle metal layer of ZAZ structure for transparent electrode application one can that 8-12 nm thin Ag layer is giving best results among all values of thickness studied. The multilayer ZAZ thin films were deposited by RF-DC sputtering technique over a quartz substrate with Ag layer (9nm) and each ZnO layer 40 nm. After optimizing the thickness of the sandwiched layer, ion implantation and irradiation studies to investigate the effect of ion beam induced modifications in the electrical and optical properties of the ZAZ multilayer with optimized Ag metal layer thickness were carried out. The Xe^{+} ion beam with 100 keV energy of varying fluence has been used to understand the role of ion

implantation as a tool to tune the properties of ZAZ[135]. In the next section reports the investigation on the effect of swift heavy ion irradiation on the electrical and optical properties.

6.5 Results and Discussion

6.5.1 X-ray Diffraction

XRD patterns of pristine and implanted ZAZ multilayer structure are shown in Fig. 6.11. XRD pattern of pristine ZAZ structure consists of peaks corresponding to ZnO and Ag layers. The peak corresponding to the hexagonal crystal structure of ZnO can be well matched with JCPDS (36-1451) while Ag peaks correspond to the face-centered cubic (FCC) JCPDS (04-0783). It can be clearly seen that intensity of both ZnO and Ag peaks reduce on implantation up to the fluence of 1×10^{15} ions/cm^2 and then increases with ion fluences. It is well known that change in peak intensity is related to change in crystallite size which can be estimated with the help of Scherer's formula ($0.89\lambda/\beta\cos\theta$). The crystallize size for ZnO and Ag were found to be ~ 11.1 nm and 24.4 nm respectively for pristine multilayer structure. The analysis of crystallite size shows that it decreases for both ZnO and Ag up to fluence value of 1×10^{15} ions/cm^2 as shown in Table 1 and a further increase in fluence value leads to an improvement in crystallite size. The reduction in crystallite size is related to the creation of defects when low energy ions pass through the host lattice[130]. At higher fluences, large numbers of incoming ions impart energy releasing strain among grains that cause improvement in crystallinity. The shift in (002) peak of ZnO on implantation is seen. The corresponding change in lattice parameter is estimated using the formula $c=\lambda/\sin\theta$ where c is the lattice parameter and θ is the Bragg's angle and given in Table 6.2. No systematic change in lattice parameter of ZnO is observed[129].

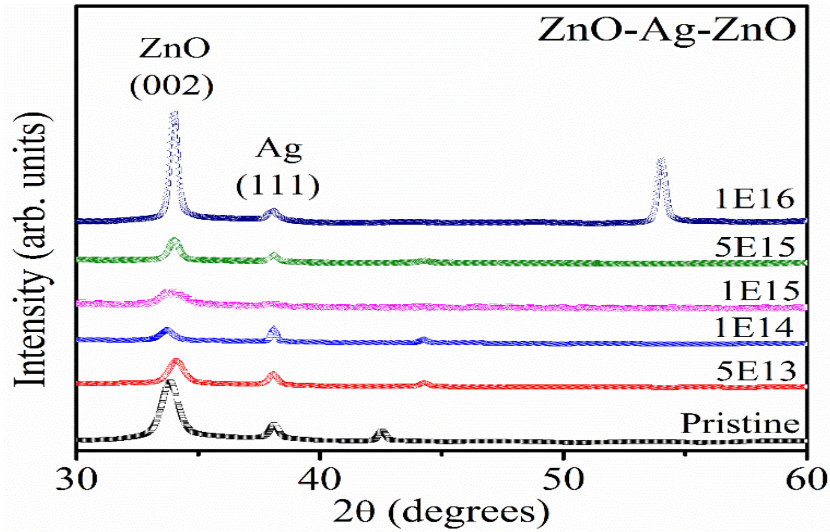

Figure 6.12: XRD pattern of pristine and Xe ion irradiated ZAZ multilayer thin films.

Table 6.2: Various physical parameters calculated from XRD and AFM measurements for implanted ZAZ multilayers

Samples Details (Fluence values)	ZnO Parameters		Ag Parameters		Roughness from AFM (nm)
	Crystallite size (nm)	Lattice Parameter (Å)	Crystallite size (nm)	Lattice Parameter (Å)	
Pristine	11.1	5.29	24.4	4.04	2.1
5E13	12.2	5.25	25.4	4.04	2.0
1E14	11.8	5.31	33.2	4.04	2.4
1E15	9.5	5.27	13.8	4.05	2.4
5E15	17.8	5.26	33.5	4.04	3.5
1E16	24.3	5.26	26.7	4.05	3.7

6.5.2 Rutherford Back Scattering

RBS measurements were performed to check the thickness and stoichiometry of the multilayer films. RBS spectra of pristine and implanted films along with RUMP fitting164 for 8 nm thick Ag layer is shown in fig. 6.13. Different elemental peaks corresponding to O, Zn, and Ag ions are seen. On analyzing the spectrum using RUMP,

the thickness of pristine ZAZ multilayer structure is found to be ~ (40±5 nm)/Ag (9±1nm)/ZnO (40±5 nm).

Figure 6.13: RBS spectra of ZAZ multilayer thin films (a) pristine and (b) Xe ion

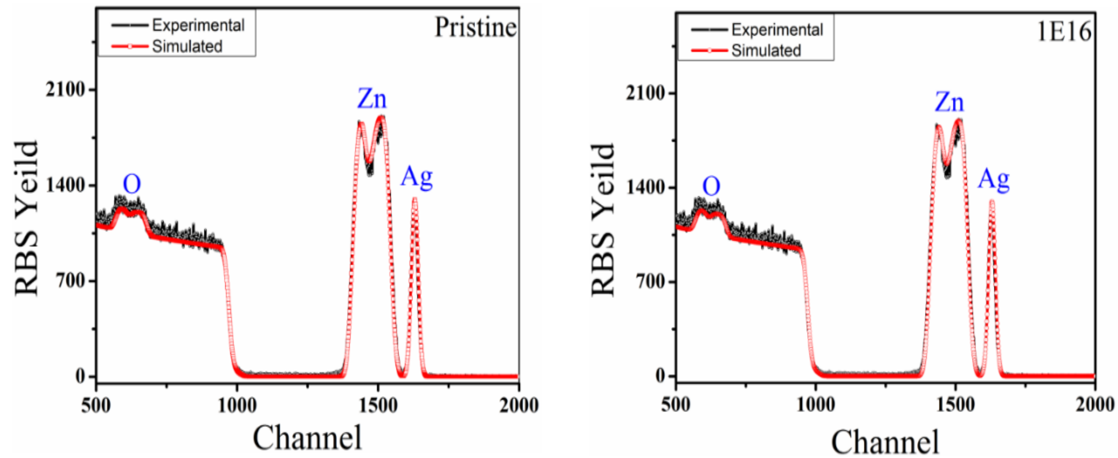

irradiated at a fluence of 1×10^{16} ions/cm^2.

This suggests formation of ZnO in top and bottom layers with pure Ag in the middle layer. Diffusion of Ag atoms into the ZnO layer is also observed. It can be clearly seen that the implantation of Xe ions at the fluence of 1×10^{16} ions/cm^2 increases the diffusion of Ag ions into ZnO layers. The simulated thickness of Ag atoms diffused in the ZnO layer is approximate 5 nm for both sides. The top layer diffusion is mainly due to sputtering of the Ag atom from middle metal layer and diffusion in bottom layer mainly due to energetic ions[127].

6.5.3 X-ray Photoelectron Spectroscopy

XPS measurements were employed to find out the chemical composition and analyze the chemical states of the multilayer structure for both pristine and Xe implanted films[157]. Multilayer analysis was done using etching via Ar gas to get information about the layers. Fig. 6.14 (a-d) presents the results from pristine and Xe ion implanted (at a fluence of 1×10^{16} ions/cm^2) ZAZ multilayer thin films. The binding energy scale in XPS was calibrated by considering C 1s peak at 284.6 eV. XPS results

infer the presence of Zn, O, and Ag as shown in the survey scan for both pristine as well as implanted multilayer thin films[178]. The survey scans of the top layer for the pristine and implanted samples are shown in fig. 6.14 (a). It consists of peaks corresponding to Zn and O ions. These peaks are retained after implantation which shows that trilayer maintains its structure and elemental composition even after implantation. The detailed analysis of the stability of structure composition is carried out by the elemental analysis.

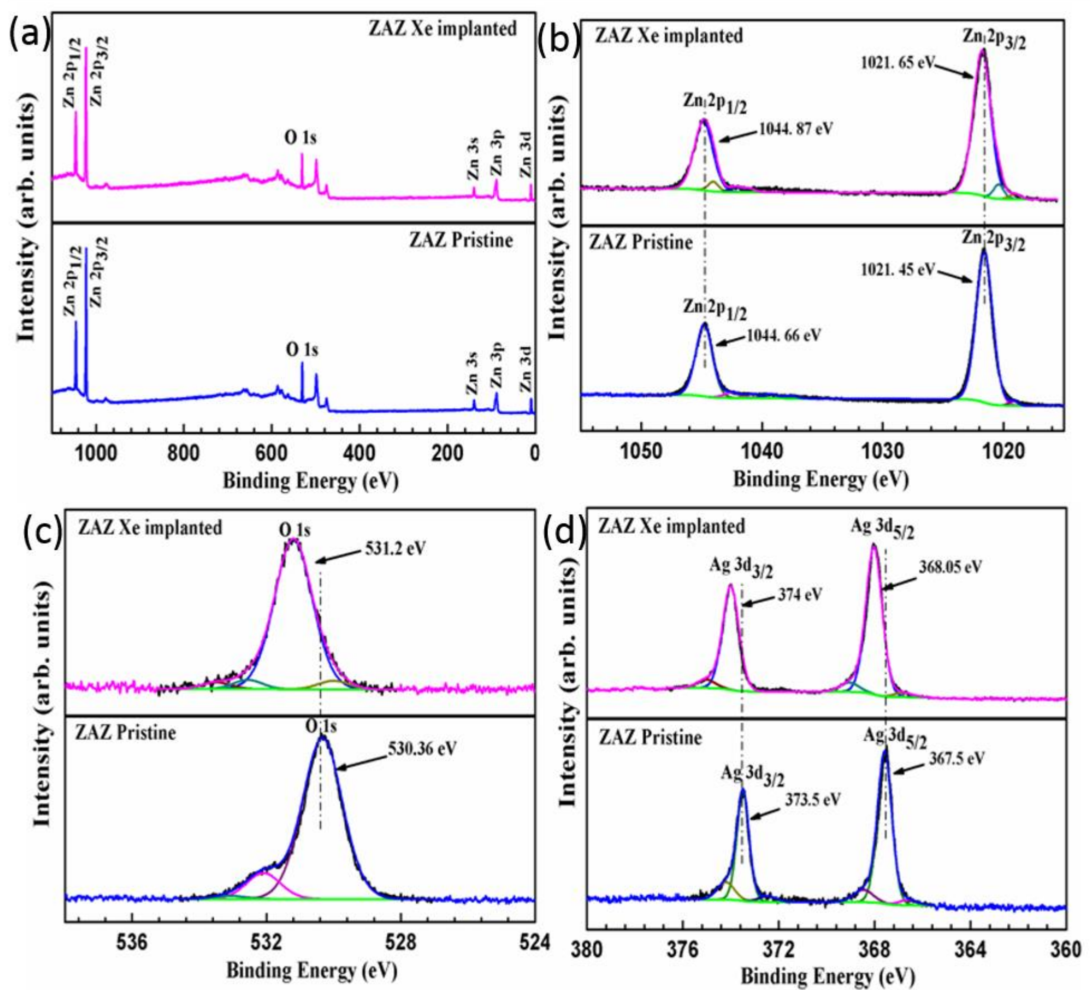

Figure 6.14: XPS spectra of pristine and Xe ion implanted at a fluence of 1×10^{16} ions/cm^2 ZAZ multilayer thin films (a) survey scan (b) Zn 2p-edge (c) O 1s-edge (d) Ag 3d-edge.

Elemental scan for Zn 2p, O 1s, and Ag 3d edges was performed on the top surface of multilayer and shown in fig. 6.14 (b-d). The peaks related to Zn $2p_{3/2}$ and Zn $2p_{1/2}$ are present at ~ 1021.45 eV, and 1044.66 respectively for pristine sample as can be seen from fig. 6.14 (b). The peak positions and the binding energy differences are in good agreement with the reported value of Zn in ZnO structure[65]. It suggests that Zn ions are present in +2 chemical state on the top surface of the multilayer. There is almost negligible change in the peak positions after implantation. This suggests that chemical state of the Zn ions in the multilayer structure is maintained[224].

Fig. 6.14 (c) shows the shape and position of the peak corresponding to O 1s in pristine and implanted thin films at the top surface. The pristine thin film O 1s profile is symmetric in nature and fitted into three symmetrical peaks (located at 530.36, 532.1eV and 533.15 eV, respectively). This indicates that there are three different kinds of O species present in this film[218]. The peak at low binding energy side (O 1s peak) on the spectrum at 530.36 eV is attributed to O^{2-} ions on the wurtzite structure of a hexagonal Zn^{2-} ion array, surrounded by Zn atoms with their full complement of nearest neighbour O^{2-} ions[225]. In other words, the intensity of this component is a measure of the number of oxygen atoms in a fully oxidised stoichiometric surrounding. The binding energy component centred at 532.8 eV is associated with O^{2-} ions that are in O deficient regions with in the matrix of ZnO or Zn-OH groups. The peak at 533.15 eV is due to chemisorbed water, H-O-H covalent bonds at ZnO surface[53]. An extra peak is observed at 530.1 eV after implantation, due to the formation of Ag_2O[53]. The fraction amount of this peak is very less representing that there is small oxidation may be at interface of metal / semiconductor. There is a shift in the peak representing O^{2-} ions on the wurtzite structure of a hexagonal Zn^{2-} ion array is due to oxygen defects created during implantation.

The spectra for the embedded Ag layer were obtained after etching of top ZnO layer and shown in Fig. 6.14 (d). Two main peaks centered at 367.5 and 373.5 eV were observed in the spectra attributed to Ag $3d_{5/2}$andAg $3d_{3/2}$, respectively in the pristine sample[224]. Thin film of Ag shows shift in peak positions of Ag 3d towards the lower binding energies as compared to bulk Ag (Ag $3d_{5/2}$ at 368.2 eV; Ag $3d_{3/2}$ at 374.2 eV). In the multilayer structure when there is a metal-semiconductor interface (Ag-ZnO) the electron transfer from Ag to ZnO layer to achieve equilibrium and fermi level matching causing shift in binding energy[141]. The peak corresponding to Ag_2O, representing the Ag+2 state is also present in the specimen[226]. With Xe ion implantation the Ag 3d peaks shifted towards the higher binding energy as compared to pristine because of more ionic form of Ag. Corresponding shifts of the Ag 3d peaks by 0.5–0.8 eV to higher binding energy were observed after exposing to an implantation, this clearly indicate the more metallic formation of Ag after implantation.

6.5.4 Scanning Electron Microscope

Morphological studies of Xe ion implanted ZAZ multilayer thin films were investigated using SEM and AFM measurements. SEM images for pristine and implanted samples are shown in fig. 6.15. Well-defined crystals with sharp grain boundaries have been observed for all samples. There is no significant change in both the particle size as well as morphology for implanted samples. However, for the highest fluence sample, there is the presence of some agglomeration of particles in addition to the continuous grains. The particle size of top ZnO is found to vary in the range of 17 – 20 nm and the variation is shown in figure 6.16.

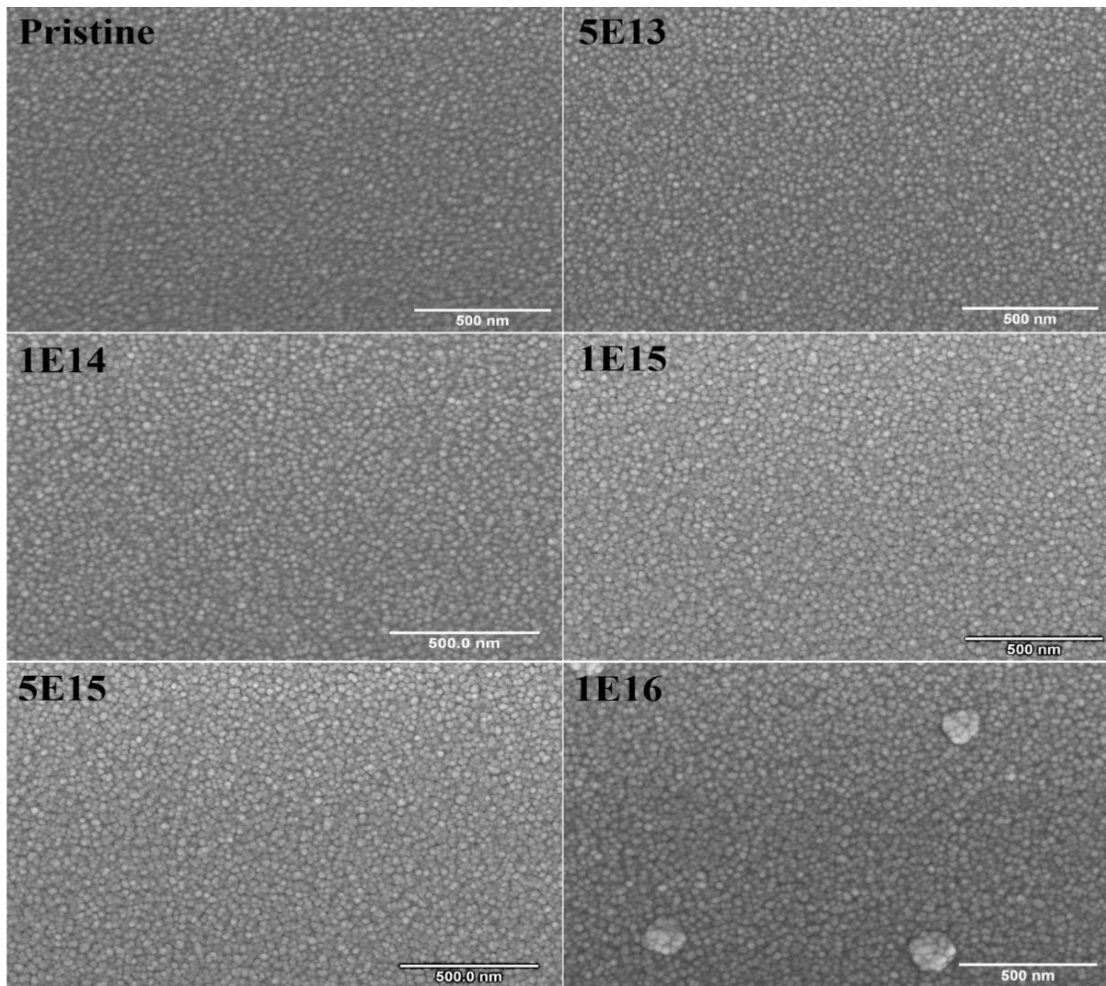

Figure 6.15: SEM micrographs of pristine and Xe ion irradiated ZAZ multilayer thin films.

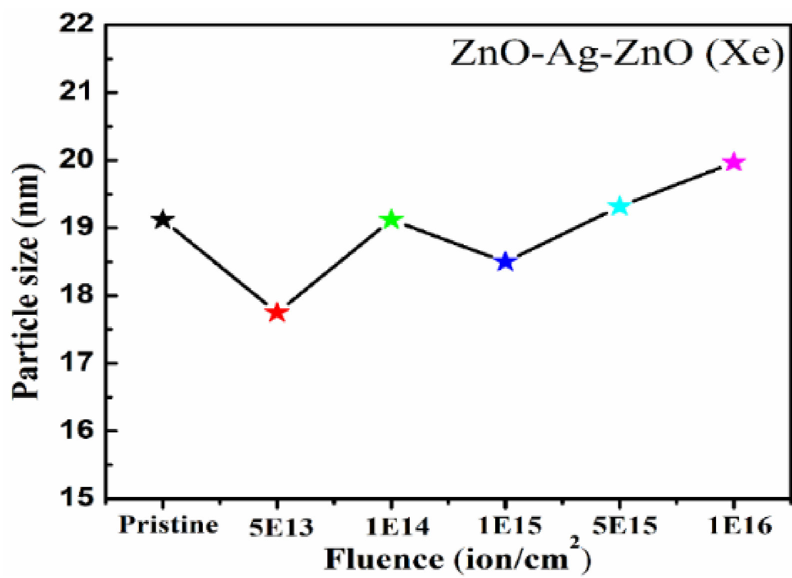

Figure 6.16: Variation of particle size from SEM micrographs of pristine and Xe ion irradiated ZAZ multilayer thin films.

6.5.5 Atomic Force Microscope

The surface morphology and roughness of the multilayer thin films were observed with the help of AFM measurements and shown in Fig. 6.17. The images illustrate growth of continuous and smooth surfaces for pristine as well as-implanted samples. The surface roughness of pristine ZAZ sample is found to be ~ 2.09 nm. The AFM images demonstrate a slight change in the morphology and roughness of films on implantation[122]. The variation in the surface roughness is shown in Table 6.2. The roughness remains almost constant for lower fluence samples and shows an increase for fluence 5E15 (3.5 nm) and 1E16 (3.7 nm). Large roughness at higher fluence is related to the creation of more number of defects. This can be correlated with the SEM measurements where the presence of agglomerated particles can be clearly seen along with the well-defined grains. The change in the roughness for these fluences is also exceeding the acceptable limit (≤ 3 nm) for electrode fabrication. Based on the morphological analysis, it is evident that samples with lower fluence (≤ 1E15 ions/cm^2) are suitable for electrode fabrication but that with higher fluence can degrade the device properties.

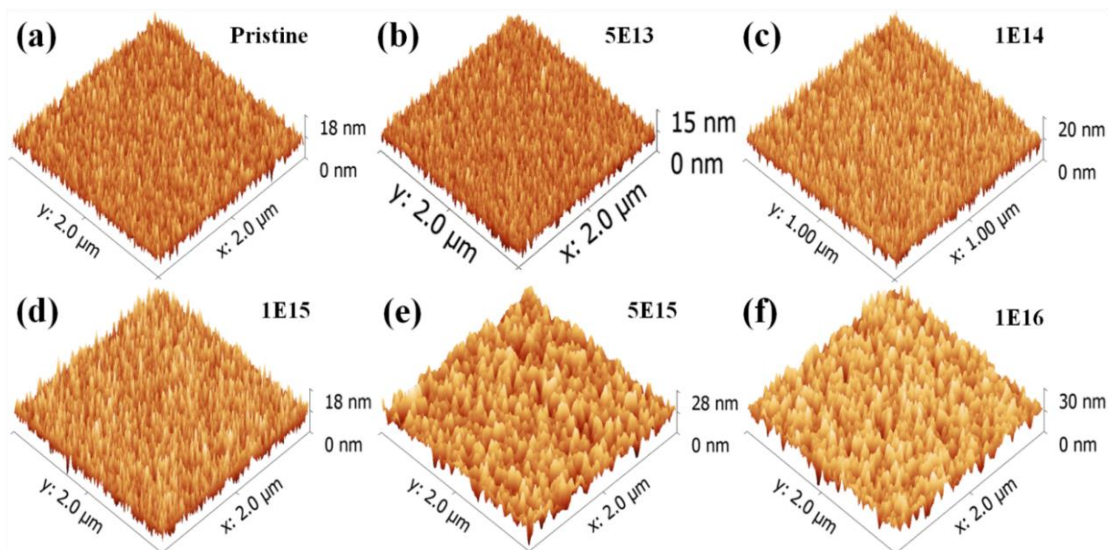

Figure 6.17: AFM micrographs of pristine and Xe ion implanted ZAZ multilayer thin films.

6.5.6 Transmission Electron Microscope

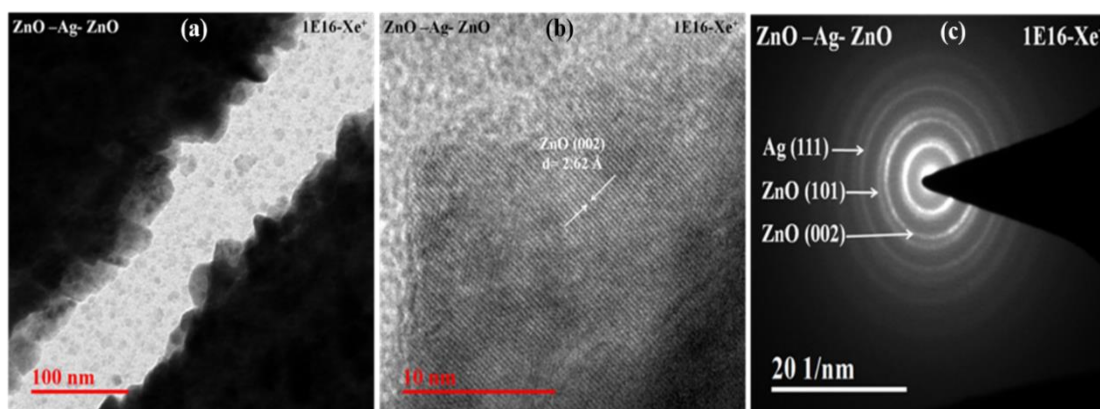

Figure 6.18: TEM images of Xe ion implanted ZAZ multilayer thin films.

Xe ion implanted multilayer ZAZ films (deposited on TEM grids) were analyzed for the microstructure through TEM. It is not possible to get all internal features of the trilayer film due to its structure and high thickness. The first image shows layered depositions of the multilayer structure. The high-resolution images from TEM were analyzed by digital micrograph software to identify crystallographic planes of top ZnO layer which are found (002) as indicated in Fig. 6.18. The SAED pattern exhibits different diffraction planes of ZnO and Ag reflected as concentric rings confirming the polycrystalline structure of ZnO and Ag in the multilayer structure[141].

6.5.7 UV-Vis Spectroscopic Study

Optical properties of pristine and implanted multilayers were examined with the help of UV-Vis spectroscopy. Fig. 6.19 shows the transmittance spectra of pristine and implanted multilayer thin films in the wavelength range of 300 – 800 nm. The average transmittance for all samples in the visible range is found in between ~ 70-80 %. The obtained value of transparency in the present case is very much comparable to that of commercial available transparent electrodes (ITO)[33]. Also, the multilayer structure

under investigation has shown improved performance as compared to other reports for metal-metal oxide hybrid structures viz. TCO; ITO, ITO/Au/ITO and ITO/Cu/ITO by Lee *et al.*[34] and Sb-doped Ag/SnO_2 by Yu *et al.*[171] in terms of transmittance.

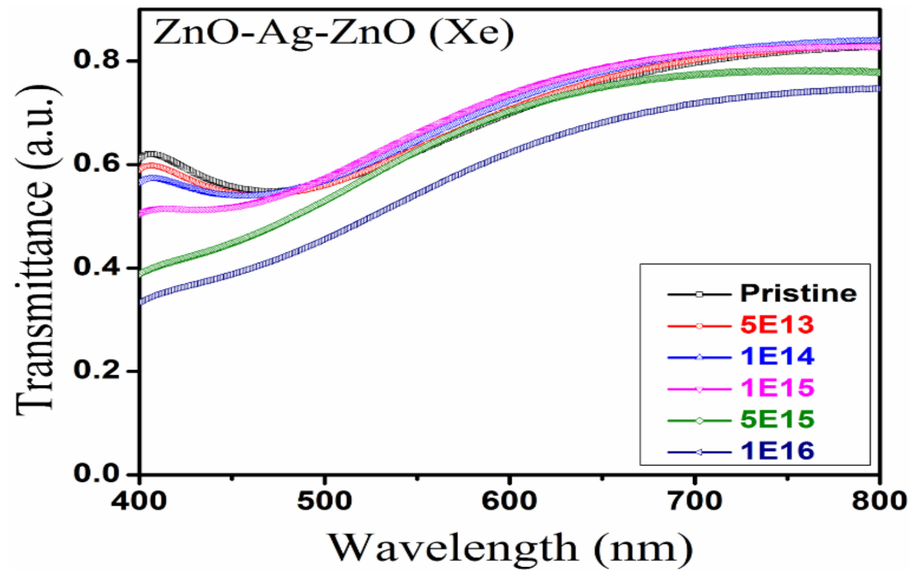

Figure 6.19: Transmittance spectra of pristine and Xe ion irradiated ZAZ multilayer thin films in the visible region.

It is shown that there is negligible variation in the transmittance for lower fluences (≤ 1E15) while there is degradation in the transmittance for higher fluence. Almost negligible variation in the transmittance for lower fluence is quite useful for the application of transparent conducting electrode in radiation environments. At the highest fluence, there is a reduction in transparency of the multilayer thin films. Defects created in the oxide layer for a higher dose of implantation increase absorption resulting in reduced transparency19. Another, important factor that might be responsible for this reduction could be increased surface roughness leading to less transmittance115.

Tauc's plot have been employed for the estimation of optical band gap by plotting $(\alpha h\nu)^2$ v/s energy (hν) as shown in fig. 6.20. The band gap for the pristine multilayer was found to be ~ 3.24 eV which is lower than the band gap of bulk or single

layer ZnO. Negligible change in the bandgap is observed for lower fluence and does not show a regular behavior for higher fluence (5E15 and 1E16 ions/cm^2).

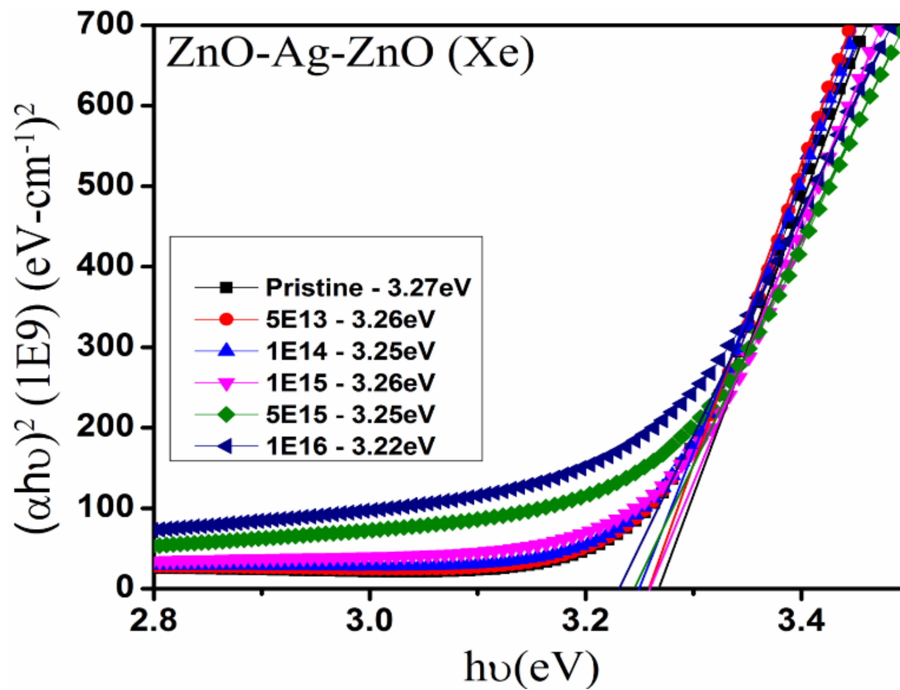

Figure 6.20: Bandgap plot of pristine and Xe ion irradiated ZAZ multilayer thin films.

Other optical constants such as refractive index and extinction coefficient have been calculated[227]. These optical constants also exhibit a trend similar to transparency behavior as shown in figure 6.21. Based on these observations, it can be concluded that multilayer structure possesses very good stability under implantation of ions showing a slight degradation in the transmittance at a very high fluence of Xe ions.

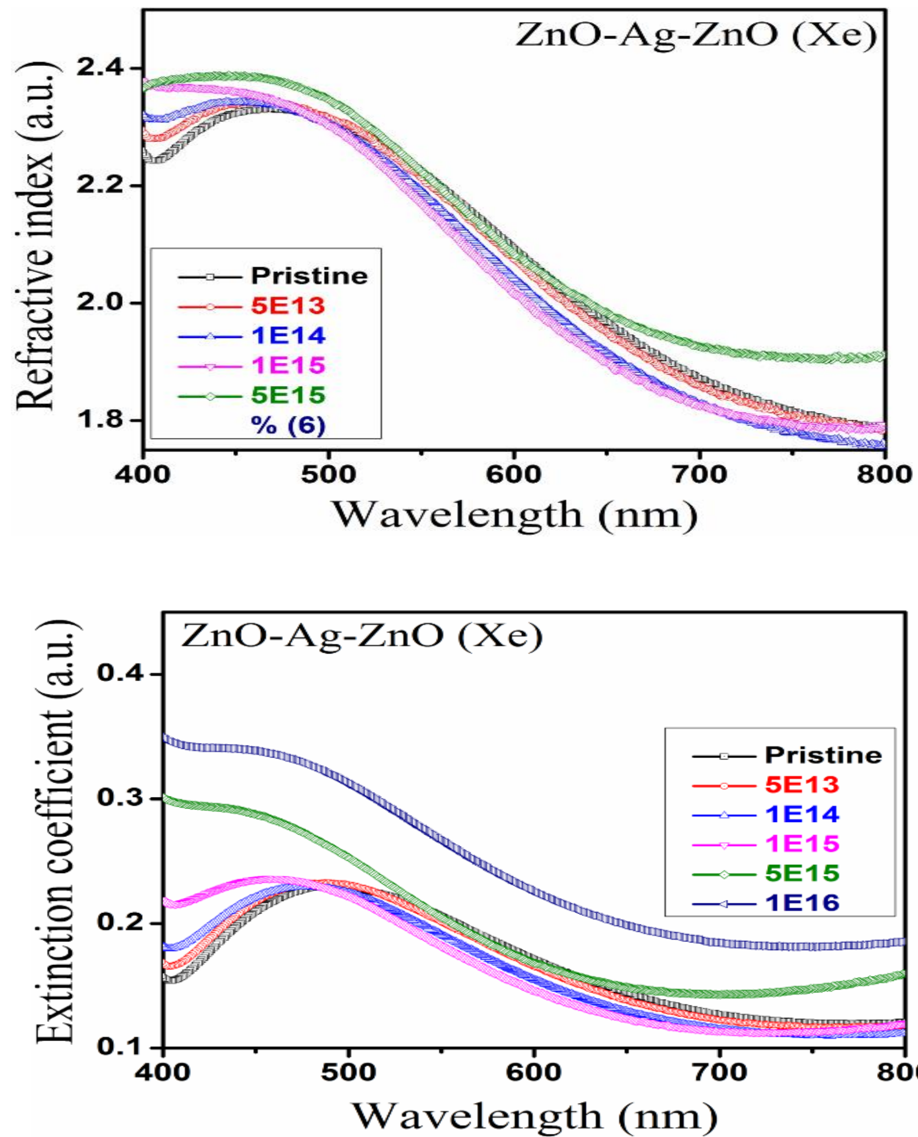

Figure 6.21: Calculated refractive index and extinction coefficient spectra of pristine and Xe ion irradiated ZAZ multilayer thin films in the visible region.

6.5.8 Hall Measurements

The variation in the electrical properties for different fluence of Xe ion implantation is presented in the figure 6.22. The Hall measurements indicate that electrical parameters like sheet resistance, mobility, and a number of charge carriers can be tuned using Xe ion implantation with different fluence. The curve indicates that initially with low fluence range 5E13 and 1E14 ions/cm^2 gives better results in terms of mobilities and charge carrier with required sheet resistance, especially for the organic

photovoltaic application[5]. The reason for increasing the mobility initially is mainly due to defects generated by the heavy Xe ions[98]. Increase in the crystallite size reduced the grain boundaries, leads to decrease in grain boundary scattering and increase in mobility[225]. With higher fluence, ZAZ structure again regains its properties as compare to pristine samples leads to conclude the ZAZ structure stability in low energy environment. So here the most beneficially fluence is 5E13 and 1E14 ions/cm^2.

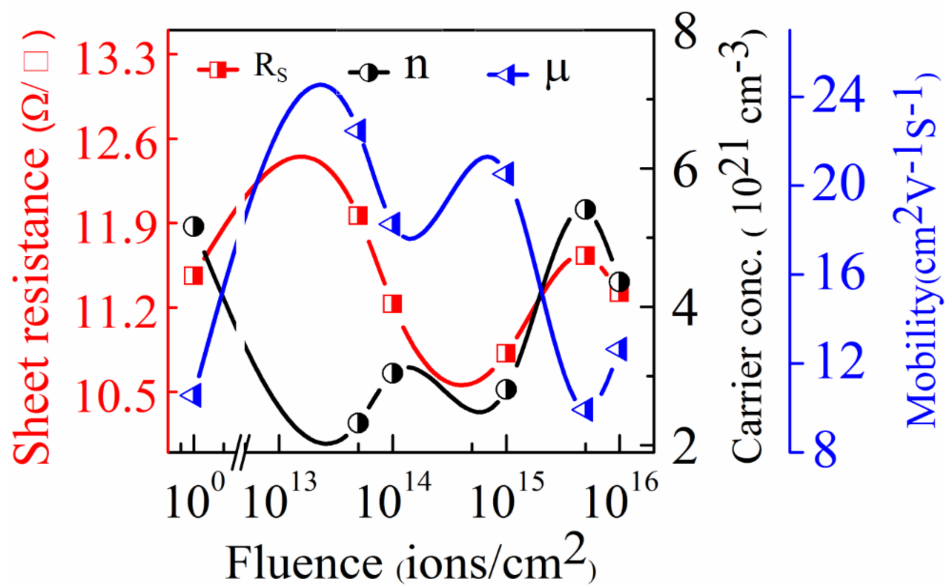

Figure 6.22: Hall measurement of pristine and Xe ion irradiated ZAZ multilayer thin films for different fluences.

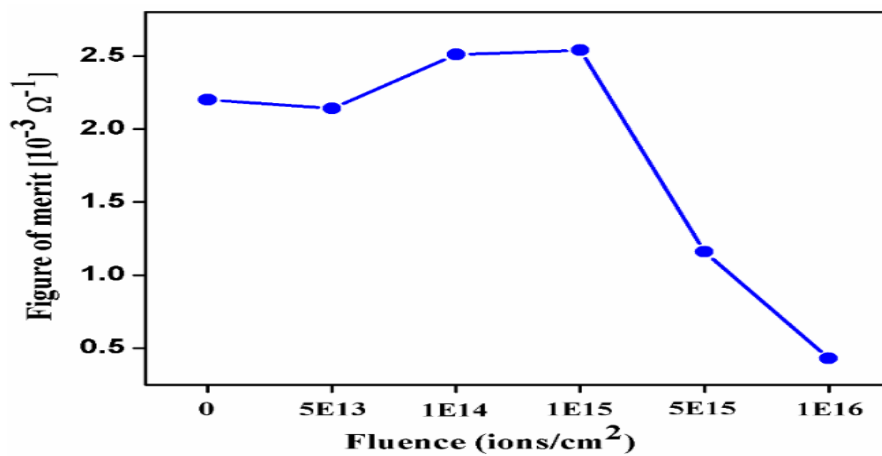

Figure 6.23: Calculated Haacke FOM for pristine and Xe ion irradiated ZAZ multilayer thin films.

The calculated figure of merit is $2.5\times10^{-3}\Omega^{-1}$ for 1E14 and $2.6\times10^{-3}\Omega^{-1}$ for 1E15 ion/cm^2. The calculated FOM using Haacke's formula is a combination of optical transparency and sheet resistance of the specimen and is a unique way to compare optical and electrical properties for electrode application.

6.6 Ag^{7+} Ion-Beam (100MeV) Effect on ZnO-Ag-ZnO Thin Films

After investigation of optimization of metal layer thickness (8-12 nm) and the implantation (Xe^{+} 100 keV) study to modifications in the electrical and optical properties, we perform the swift heavy ion irradiation study on the ZAZ specimen. In this section, Ag^{+7} ion beam with 100 MeV energy by varying the fluences have been used for the study. The specimen dielectric/metal/dielectric multilayer of ZnO (40 nm)/ Ag (9 nm)/ ZnO (40 nm) was deposited on glass substrates at room temperature by RF-DC sputtering. In the next section, we have investigated the role of swift heavy ions on the electrical and optical properties and also check the stability of ZAZ structure in the extreme condition.

6.7 Results and Discussion

6.7.1 X-ray Diffraction

Fig. 6.24 shows XRD patterns of pristine and SHI irradiated ZAZ multilayer structure. It is evident that the pristine layered structure consists of only (002) diffraction peak corresponding to the hexagonal crystal structure of ZnO (JCPDS (36-1451). The crystallize size was calculated using Scherer's formula ($0.89\lambda/\beta\text{Cos}\theta$) which is ~ 7.2 nm for pristine multilayer structure. XRD patterns of 100 MeV Ag^{7+}irradiated layered structure with ion fluence (5E11 to 5E12 ions/cm^2) consist of two peaks; one

corresponding to hexagonal ZnO while the other peak is related to the face-centered cubic (FCC) Ag (111) corresponding to JCPDS (04-0783). The crystallite size is showing an increase for ZnO and Ag up to fluence value of 1E12 ions/cm^2 (see Table 6.3). The increase in the crystallite size for both ZnO and Ag is attributed to the annealing effect induced by the ion beam irradiation and understood on the basis of thermal spike model[228]. According to this model[138], a large amount of heat energy transfer by the projectile ions into the electronic systems takes place when energetic ions pass through the material. This energy is distributed among the electrons and consequently to lattice atoms through the electron-lattice coupling. Deposition of such high energy raises the lattice temperature appreciably along the ion tracks within a very short duration of time ($\sim 10^{-14}$ s) and quenches rapidly. The rise and fall of temperature within a short interval of time generate pressure waves which in turn modifies the crystal structure. At lower fluence, the energy of incoming ions imparted to the system releases strain among the grains that cause improvement in crystallinity. On the other hand, the overlap of ion tracks causes disorder in the lattice among large grains at higher fluences. SHI irradiation induced modifications in crystallinity have been reported by various groups earlier[138].

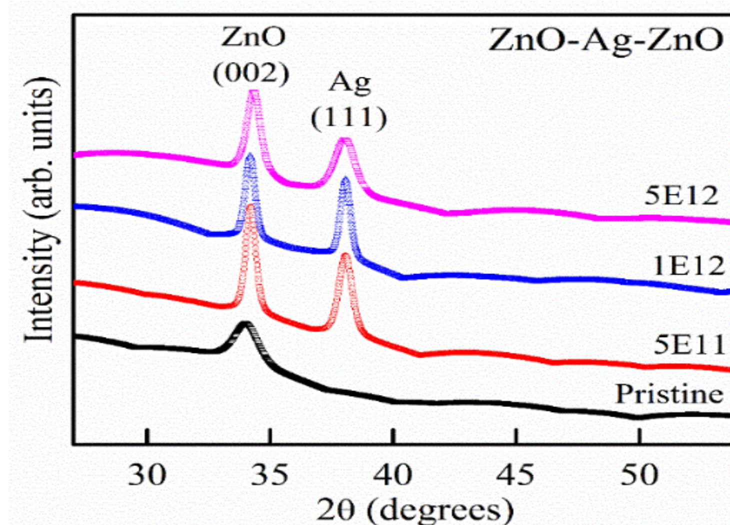

Figure 6.24. XRD pattern of pristine and SHI irradiated ZAZ multilayer structure.

Table: 6.3. Various Parameters calculated for ZnO and Ag from XRD pattern for 100 MeV Ag^{7+} irradiated ZnO/Ag/ZnO multilayer thin films

Samples Details	ZnO Parameters			Ag Parameters	
	Crystallite size (nm)	Lattice Parameter (Å)	Stress (N/m^2)	Crystallite size (nm)	Lattice Parameter (Å)
Pristine	7.2	5.261	-4.792	--	--
5E11	15.4	5.235	-2.483	12.32	4.049
1E12	16.5	5.234	-2.475	16.48	4.049
5E12	12.9	5.217	-0.9414	9.19	4.051

Furthermore, it is also observed that peak corresponding to ZnO (002) shifts systematically towards lower angles. The shift in diffraction peaks leads to decrease in lattice parameter, estimated using the relation $c=\lambda/\sin\theta$. When highly energetic ions pass through the material, a large number of defects are generated due to the dominance of electronic energy loss. These defects, in turn, induce stress in the system and might be responsible for the decrease in lattice constant.

6.7.2 Rutherford Back Scattering

Fig. 6.25 shows the RBS spectra and RUMP simulated profiles of ZAZ multilayer structure for pristine and SHI irradiated films[164]. Distinct elemental peaks associated with Zn, O and Ag ions are observed. Thicknesses of various layers were calculated with the help of the fitted curves and found to be ZnO (40±5 nm)/Ag (9±1 nm)/ZnO (40±5 nm). This suggests the formation of ZnO with pure Ag in the sandwich layer with diffusion occurring at the interfaces. During the sputtering process, deposition of high energetic atoms leads to diffusion of few Ag atoms in ZnO layers. Through RBS, it is seen that SHI irradiation causes an increase in diffusion layer. This

indicates that high energetic ions transfer their energy to the host multilayer leading to an increase in mixing or diffusion in multilayer[150].

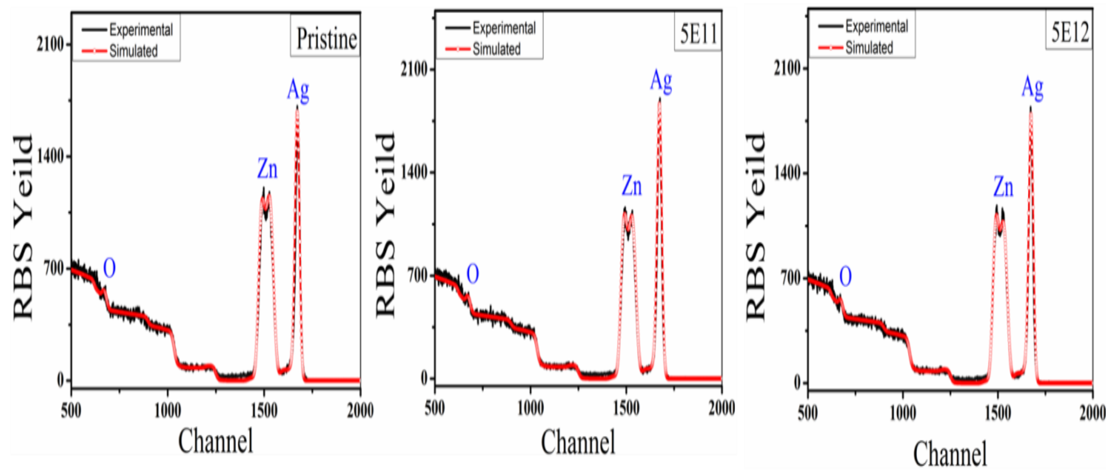

Figure 6.25. RBS spectra of pristine and SHI irradiated ZAZ multilayer structure.

6.7.3 X-ray photoelectron spectroscopy

XPS measurements were carried on ZAZ multilayer structure to analyze the chemical states of the elements. Depth profiling using etching was done for analysis of the three layers. XPS results confirm the presence of Zn, O and Ag ions at respective layer positions and the effect of SHI irradiation. Fig. 26(a) represents the survey scan of the top layer of the multilayer after cleaning by Ar sputtering. It consists of peaks corresponding to Zn, O and surface C. The binding energy scale was calibrated by considering C 1s peak at 284.6 eV[157]. The curve shows that the trilayer maintains its stability even after SHI irradiation as there is no Ag metal on the top from the middle layer. The smooth and homogenous dielectric layer is retained over the continuous mid metal layer ensuring the stability of the multilayer structure.

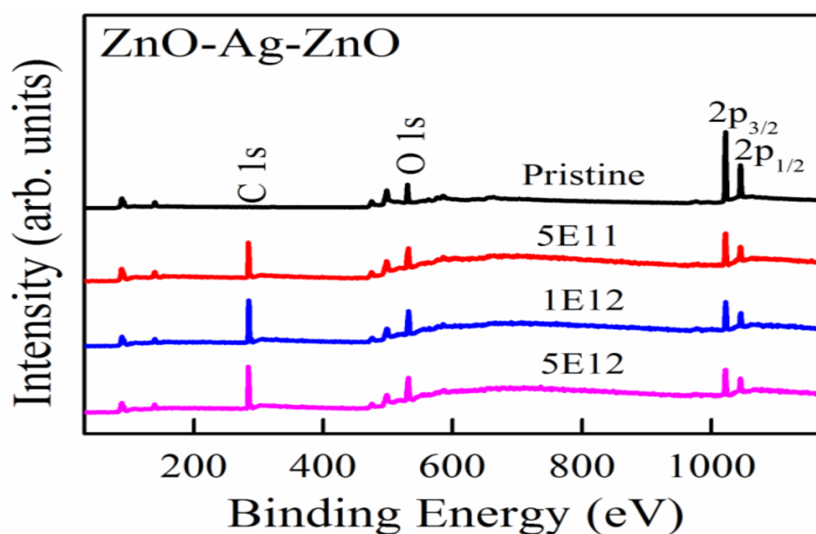

Figure 6.26(a). XPS result of pristine and irradiated ZAZ multilayer structure at the top surface (survey scan).

Elemental analysis for Zn 2p, O 1s edges performed on the top surface of multilayer are shown as short scan in Fig. 26 (b-c). The peaks corresponding to Zn $2p_{3/2}$ and Zn $2p_{1/2}$ shown in Fig. 26(b), are present at ~ 1022.1 eV, and 1045.2 eV respectively[229]. The binding energy difference of Zn $2p_{3/2}$ and Zn $2p_{1/2}$ is found to be ~ 23.1 eV which is in accordance with the standard reference value reported for binding energy of Zn in ZnO[230]. It can be inferred from the peak positions and their difference values that Zn ions are present in Zn^{2+} chemical state on the top surface of the multilayer. A very small shift occurs in the two Zn peak positions after SHI irradiation, exhibiting stability of Zn chemical state.

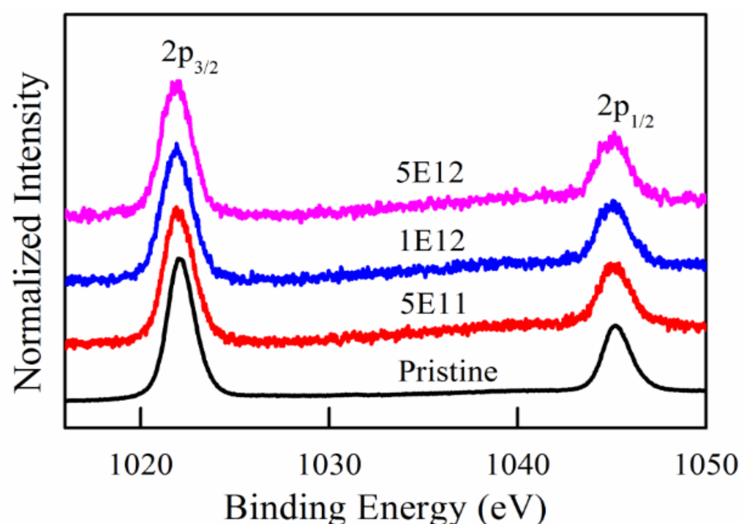

Figure 6.26 (b). XPS results of pristine and irradiated ZAZ multilayer structure of the top surface (short scan for Zn).

Fig. 6.26 (c) shows the shape and position of the peak corresponding to O 1s XPS in pristine and irradiated thin films at the top surface. The pristine thin film O 1s XPS profile is asymmetric in nature and fitted into two symmetrical peaks (located at 530.0 and 531.7eV, respectively). This indicates that there are two different kinds of O species present in this film. The peak at low binding energy side (O1s peak) on the spectrum at 530 eV is attributed to O^{2-} ions on the wurtzite structure of a hexagonal Zn^{2-} ion array[231], surrounded by Zn atoms with their full complement of nearest neighbour O^{2-} ions[225]. In other words, the intensity of this component is a measure of the number of O atoms in a fully oxidized stoichiometric surrounding. The binding energy component centered at 531.7 eV is associated with O^{2-} ions that are in oxygen deficient regions with in the matrix of ZnO or Zn-OH groups. An extra peak is observed at 529.0 eV after irradiation, due to formation of Ag_2O[53]. The intensity of Ag_2O peak is decreased with increased ion fluence due to the mixing of Ag in ZnO sandwich layer. Furthermore, the intensity of peak towards higher binding energy side decreases with SHI irradiation as compared to pure multilayer structure. This indicates that

chemisorbed oxygen of the surface hydroxyls which in turn is responsible for the modification in optical properties changes as the ion fluence increases[232,233].

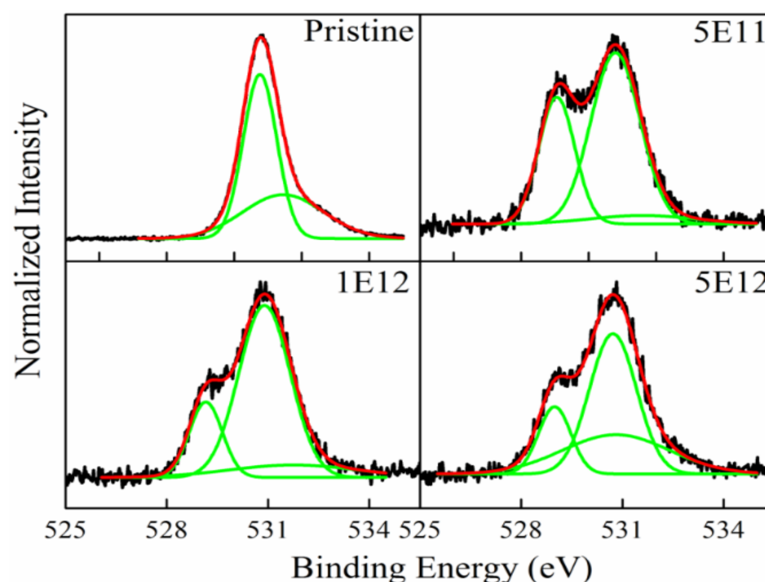

Figure 6.26 (c). XPS results of pristine and irradiated ZAZ multilayer structure at the top surface (short scan for O).

The spectra for the embedded Ag layer were obtained after etching of top ZnO layer and shown in Fig. 26(d). Two peaks centered at 367 and 372.9 eV were observed in the spectra attributed to Ag $3d_{5/2}$ and Ag $3d_{3/2}$, respectively. A remarkable shift in peak positions of Ag 3d towards the lower binding energies as compared to bulk Ag (Ag$3d_{5/2}$ at 368.2 eV; Ag $3d_{3/2}$ at 374.2 eV) is observed for thin film. The shift in the binding energy of Ag is mainly due to electron transfer from metallic Ag to ZnO crystals (i.e., the formation of monovalent Ag). Transfer of electrons takes place due to band bending at the interface to match the Fermi levels. The metal atoms come into contact with the semiconductor oxide at the interface to form ZnO-Ag hetero structures[234]. When Ag layer (work function = 4.26 eV) comes in contact with ZnO layer (work function = 5.3 eV), electron transfer takes place from Ag to ZnO at the interface of ZnO-Ag. This transfer of electrons results in producing higher charge in

Ag[235]. The monovalent Ag has lower binding energy as compared to zero-valent Ag leading to a shift in binding energies of Ag $3d_{5/2}$ and Ag $3d_{3/2}$[236].

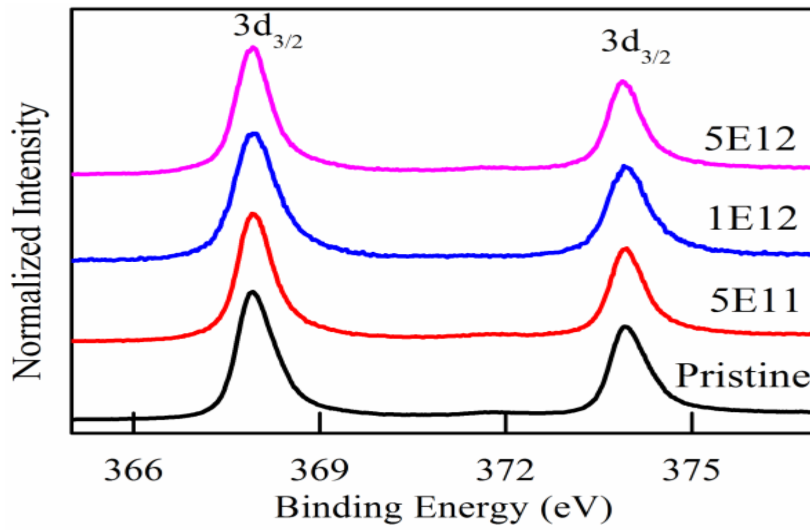

Figure 6.26 (d). XPS spectra of pristine and irradiated ZAZ multilayer structure at middle layer (short scan for Ag).

6.7.4 Scanning Electron Microscope

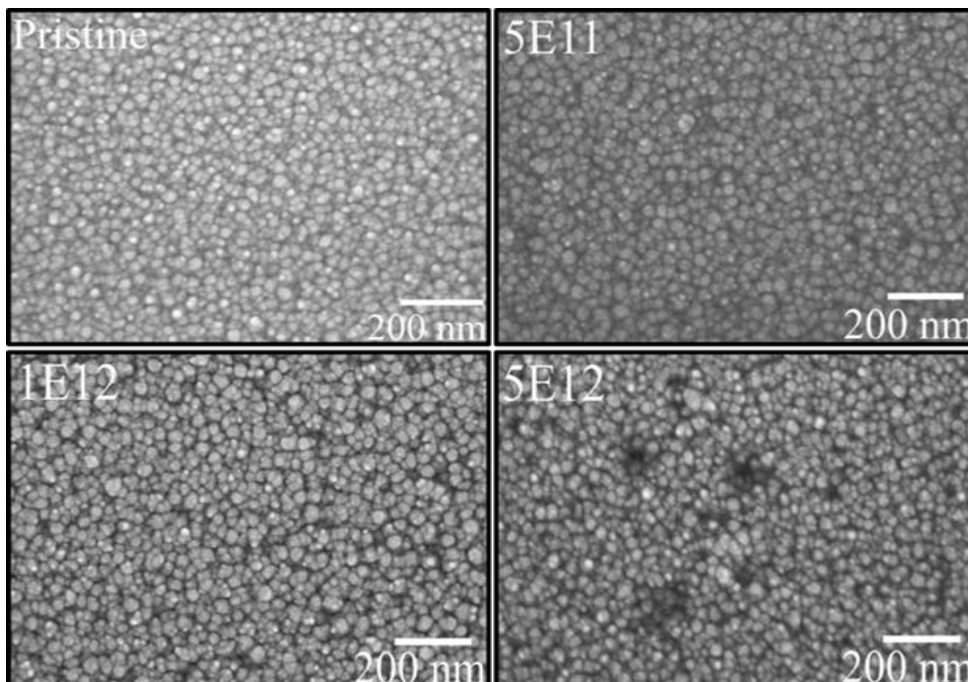

Figure 6.27. SEM images of pristine and SHI irradiated ZAZ multilayer structure with different ion fluences.

Fig. 6.27 illustrates FESEM images of pristine and SHI irradiated ZAZ multilayer structure and show well-arranged particles with circular shape. The pristine layered structure (Fig. 6.27-a) consists of well-defined continuous particles of nearly equal size completely covering the surface which is smooth in nature. On irradiation, these well-defined continuous particles rearrange themselves and exhibit a change in morphology. XRD measurements confirm grain growth for lower fluence values[237]. Narrow voids are seen to be created by the passage of ions along the path of the ion beam for the highest fluence as shown by SEM image. It can be argued on the basis of existing literature that two different mechanisms either surface diffusion or sputtering occur on irradiation[238]. When the energy of incident ions is not sufficient to excite the atoms from the surface, then the atoms diffuse causing surface diffusion. On the other hand, electronic sputtering takes place (atoms can leave the surface) for irradiation by energetic ion possessing higher energy than surface binding energy and usually occurs at higher fluences. Due to sputtering, atoms are knocked out from the surface resulting in the decrease in size (at 5E12 ions/cm^2). At higher fluence value, the overlap of ion tracks promotes disorder in the lattice.

6.7.5 Atomic Force Microscope

Fig. 6.28 illustrates AFM images for pristine and irradiated multilayer thin films. The images confirm the formation of continuous and smooth surface for all samples. These images of films for different fluences demonstrate nearly same morphology of grains. The calculated roughness of pristine is ~ 2.97 nm, which continuously decreases with ion fluences and reaches a minimum value of ~ 2.48 nm for the highest fluence. The high-energy ions with heavy mass act as a cutting tool for the hikes and irregularities at the surface of the deposited thin film and hence irradiation

leads to reduction in surface roughness with ion fluences. The height and size of grains present on the top surface of layered structure continuously change with irradiation. All images show that there is no large or continuous cluster formation at the surface of top ZnO layer deposited on the Ag layer. Formation of smooth films with root mean square roughness (RMS) value of ≈ 2.5 nm, (close to ITO films ≈ 2-3 nm) is quite important for TCEs because high surface roughness of an electrode allows direct current to flow between cathode and anode[239]. This evolution of morphology (with very small roughness and continuous growth) of a multilayer structure with SHI irradiation favours the use of the present layered structure as a transparent electrode in optoelectronic devices in radiation environment[82].

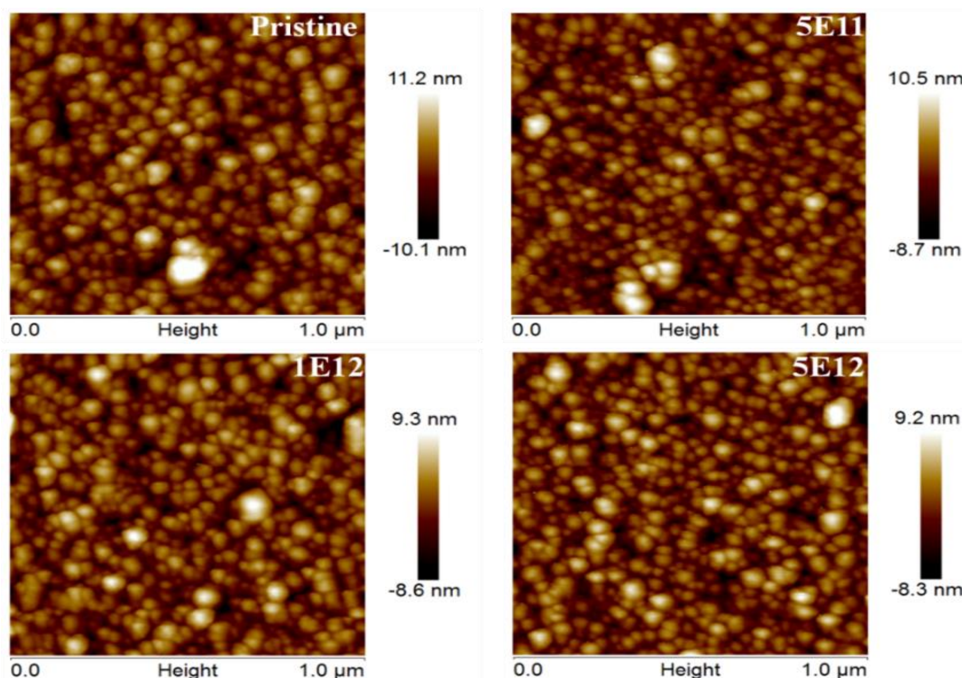

Figure 6.28. AFM images of pristine and SHI irradiated ZAZ multilayer structure.

6.7.6 UV-Vis Spectroscopic Study

The optical measurements of pristine and irradiated stacked multilayer done using UV-Vis spectrophotometer are presented in Fig. 6.29 (a) and exhibit average transmittance between ~ 70-80 % for all the films in the visible spectral range.

Commercially available ITO slide (Sigma-Aldrich (Product Number: 703184, CAS Number: 50926-11-9) has a typical value of transparency of ~ 80 % (with R_s 30-60 Ω/sq and refractive index 1.517). Hence these films show comparable results of ITO films. This performance of the multilayer in terms of variation in transmittance value is better as compared to other reports for TCO; ITO, ITO/Au/ITO, and ITO/Cu/ITO reported by Lee *et al.*[34] and Au-embedded F-doped SnO_2 reported by Chew *et al.*[240] A small variation in transmittance and lower absorbance / reflectance is desirable for use of these multilayers as electrodes in a radiation environment.

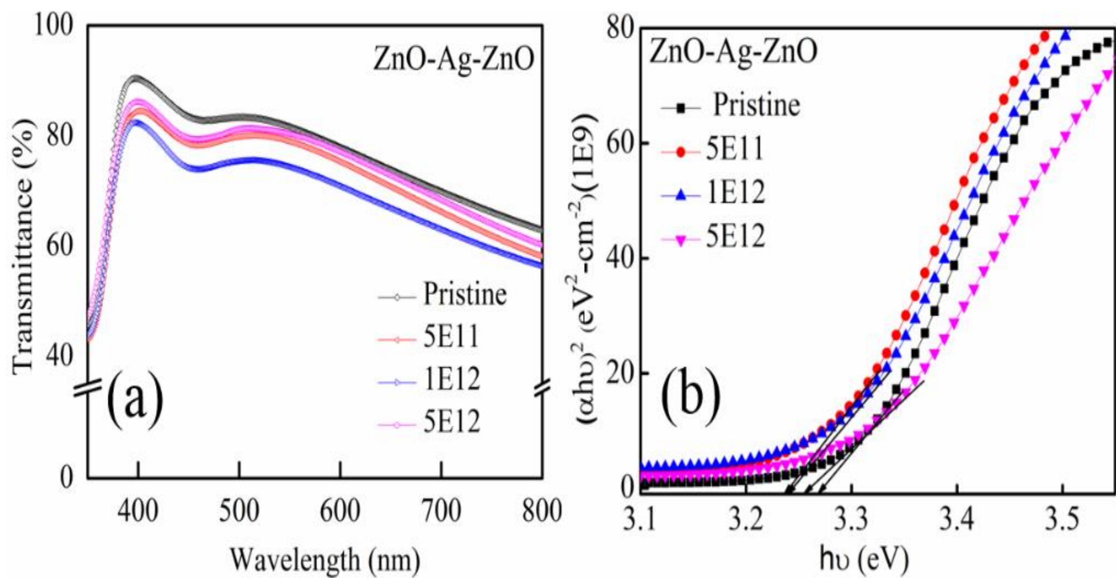

Figure 6.29. Pristine and SHI irradiated ZAZ multilayer structure (a) Transmittance spectra and (b) optical band gap from Tauc's plot.

Fig. 6.29 (a) shows the transmittance spectra of pristine and irradiated films in the wavelength range of 300–800 nm. The pristine ZAZ film was observed to have transparency of ~ 90% and the transmittance value exhibits a decreasing trend with an increase in wavelength. The multilayer sample irradiated with fluence ranging from 5E11 to 5E12 ion/cm^2 shows a lower value of transmittance (excluding the substrate effect) as compared to pristine multilayer. The maximum transmittance of ~ 80% over the visible light spectrum is shown by the irradiated samples. Initially with irradiation,

the transmittance decreases due to scattering from the metal atoms sputtered from the metal layer and distributed in the oxide layer. The defects created in the oxide layer by ion irradiation are also increasing the absorption that results in the reduction of transparency. At highest fluence, the transparency again recovers and becomes ~82 %. One factor responsible for this increase in transparency at highest fluence could be the least value of surface roughness giving a highly smooth surface leading to less absorption[213].

Optical band gap of multilayer structure was calculated using Tauc's equation by plotting $(\alpha h\nu)^2$ v/s energy ($h\nu$) as shown in Figure 7 (b). The calculated band gap value of pristine multilayer was found to be ~ 3.27 eV which is lower than the bandgap of bulk or single layer ZnO. A very small change is observed in the band gap of the multilayer on irradiation. Normally irradiation leads to decrease in band gap improving the electrical properties of the TCE. The bandgap determined using Tauc's plot is found to vary from 3.27 to 3.24 eV on irradiation up to 1E12 ion/cm^2 fluence due to the increase in grain size. While at highest ion fluence, the band gap exhibits reverse trend. The band gap increases to 3.28 eV for 5E12 ion/cm^2 irradiated multilayer structure. Such behavior is understood on the basis of the fact that for lower fluences, the annealing takes place (based on thermal spike model) while more of sputtering occurs for higher fluences which may produce more defect states. It is to be noted that variation in the bandgap is not significant. Other optical constants such as reflective index and extinction coefficient have been calculated.

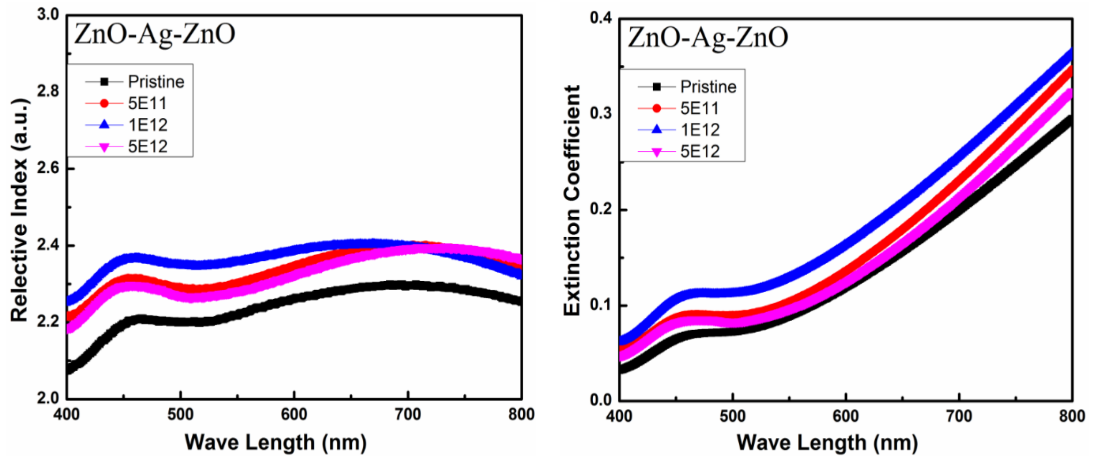

Figure 6.30. Refractive Index and Extinction coefficient variation spectra of pristine and SHI irradiated ZAZ multilayer structure.

These optical constants also show a similar trend (Figure 6.30). It can be concluded that the multilayer shows a very good stability and a limited degradation in the radiation environment thus enhancing the suitability[241] and applicability in optoelectronic devices which are most likely to bear such conditions[242].

The photoluminescence (PL) spectra for all sample was recorded and shown in the figure 6.31 consisting the characteristic peak of ZnO at wavelength 380 nm. The PL spectra consist of an intense peak in the UV range and the broad peak ~ 525 nm in the visible range[118].

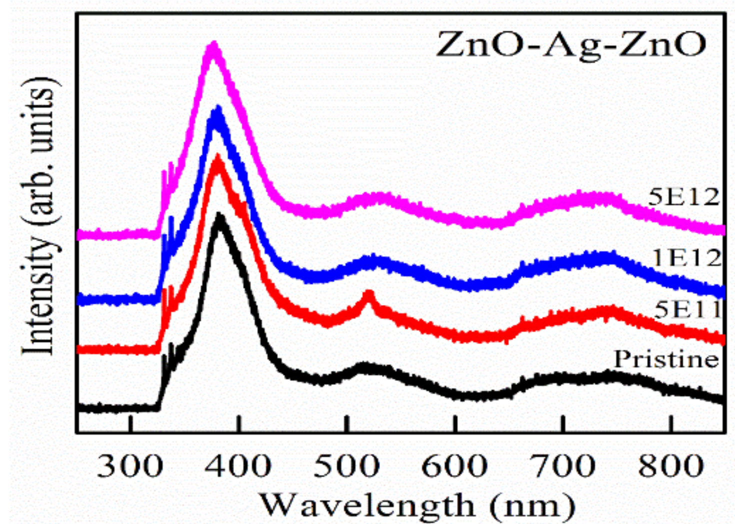

Figure 6.31. Photoluminescence spectra of pristine and SHI irradiated ZAZ multilayer structure.

6.7.7 Hall Measurements

One of the main requirements for a transparent electrode for optoelectronic devices is high electrical conductivity with adequate charge carrier number and mobility. In the quest for development of an alternative transparent electrode, it is a prime concern to get the electrical properties comparable to the commercially available ITO electrode. The complete optoelectronic device must be stable under application in a wide temperature range and harsh radiation conditions.

For this, Hall effect and electrical resistivity measurements were carried out using Van der Pauw configuration. The variation of sheet resistance, carrier concentration, and mobility as a function of the temperature (80 -350 K) is presented in Fig. 6.32 (a-d). Room temperature resistivity and sheet resistance obtained for the pristine multilayer were 2.1×10^{-4} Ω ·cm and 24 Ω/sq., respectively. The value of sheet resistance, 25-35 Ω/sq, is comparable to the commercial ITO slide from Sigma-Aldrich (Product Number: 703184, CAS Number: 50926-11-9) and reported by Sahu et al. The resistivity values for ZAZ pristine sample are lower than that for ITO films (31.2×10^{-4} Ω·cm) by Lee *et al*[243].

The conduction mechanism in these stacked structures is explained by considering a thin continuous layer of metal (Ag) embedded between two oxide layers thereby forming a DMD structure. The total resistance of this coplanar configuration is generally given by a parallel combination of resistance as: $1 / R_{total} = 1 / R_{metal} + 2 / R_{oxide}$ with $R_{oxide} > 1000R_{metal}$, so the $R_{total} \approx R_{metal}$[82]. Therefore, the conductivity is primarily due to embedded metal film and solely responsible for exhibiting such low values of resistivity as compared to single layer TCO. A critical thickness of the metal film is required to provide a continuous path for conduction of electron. The room

temperature resistivity and sheet resistance values for stacked layered structures are indicating a continuous metal inter layer for these multilayers.

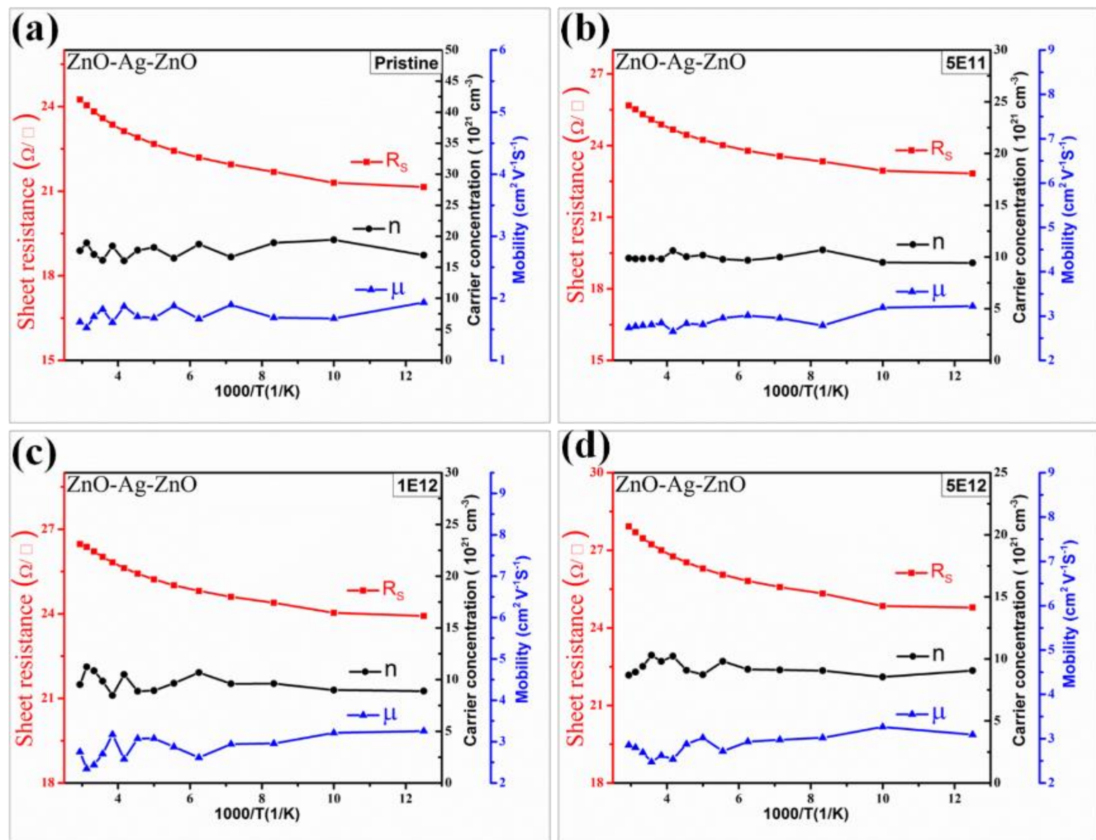

Figure 6.32. Electrical properties of pristine and SHI irradiated ZAZ multilayer structure with a variation in temperature.

In degenerate semiconductors both the resistivity and sheet resistance increase with the temperature. Increased concentration of metallic dopant induces metallic behavior in the semiconductor. Numerous studies have reported the similar behavior of degenerate semiconductors e.g. n-type ZnO doped with Ga[244], B-doped ZnO films[245], Sb-doped p-type ZnO[246]. In the present study, the behavior of variation of sheet resistance with temperature is due to self-doping effect (Ag atoms into ZnO).

Fig. 6.33 (a) shows variation in electrical properties of ZAZ samples for different fluences of SHI irradiation. There is an increase in the sheet resistance and decrease in carrier concentration with increase in fluence. Mobility is also found to

increase on irradiation and increases for higher fluences. Irradiation creates point and complex defects sites in the ZnO lattice which act as charge trap center. Decrease in number of charge carriers due to ion beam irradiation might increase resistance. Further, the decrease in a total number of charge carriers might decrease the effective collision time resulting in increased drift velocity and hence mobility. The difference in room temperature sheet resistance (δRs ≈ 3 Ω/sq.) between pristine and sample irradiated with highest fluence is still very less and negligible compared to variation in other wide band gap material irradiated with similar ion fluences[247].

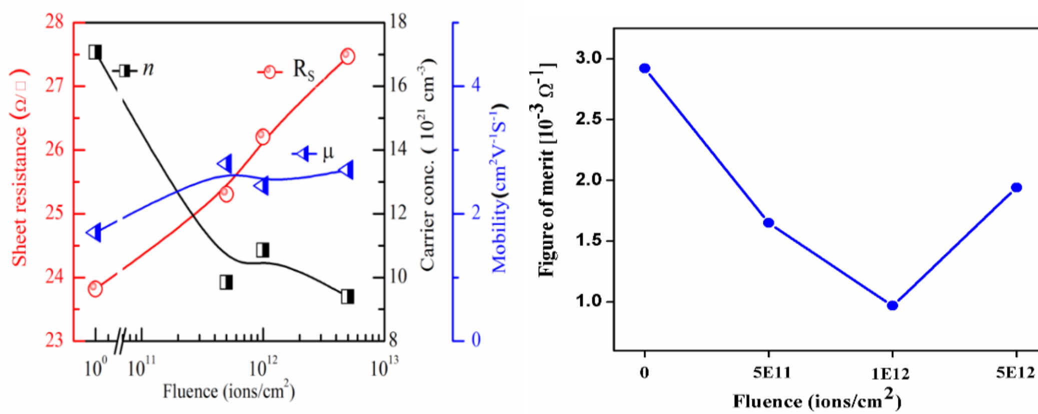

Figure 6.33 (a) Electrical properties of pristine and SHI irradiated ZAZ multilayer structure at room temperature. (b) FOM for pristine and SHI irradiated ZAZ structure at room temperature.

Fluence	Resistivity (Ω ·cm)	Sheet Resistance (Ω/□)	Carrier Concentration (1E21) (cm^{-3})	Mobility (cm2/v.s)
0	2.14373E-4	23.82	17.07	1.71
5E11	2.27764E-4	25.31	9.84	2.79
1E12	2.35856E-4	26.21	10.85	2.44
5E12	2.47192E-4	27.47	9.39	2.69

Table 6.4 - Variation in electrical properties with fluence at room temperature for 100 MeV Ag^{7+} irradiated ZnO/Ag/ZnO multilayer thin films.

The calculated Haacke FOM is $2.95\times10^{-3}\Omega^{-1}$ for pristine and $2.0\times10^{-3}\Omega^{-1}$ for 5E12 ion/cm^2 fluence which is comparatively better than that for other fluence. It clearly shows the stability of these multilayer structure for the high energetic environment.

6.8 Conclusion

Multi-layered ZnO/Ag/ZnO structure was deposited on glass and quartz substrates using RF-DC sputtering method. The Ag thickness was optimized for superior optical and electrical properties. It is seen that 8-12 nm Ag layer sandwiched between 40 nm each of two ZnO layer shows the best results. The properties of ZAZ films were then modified with 100 keV Xe ion implantation with fluence range 5E13 to 1E16 ion/cm^2. The fluence 1E15 provides best results in terms of conductivity and transparency represented by FOM ($2.56 \times 10^{-3}\Omega^{-1}$). These ZAZ films were investigated for their morphological and chemical stability as TCO under SHI ion irradiation. XRD studies show the multilayer retains their crystalline structure even after irradiation. It may be highlighted here that the films are not amorphized for irradiation conditions used in the current investigation. As deposited and irradiated films are smooth and have low roughness as exhibited by AFM and SEM studies. Such films favor growth of further layers for technological applications. XPS study indicates metallic Ag layer and irradiation generated defects embedded in metal oxide layer after SHI irradiation. It is observed that electrical properties do not change much in the temperature range (80 to 350 K) in terms of sheet resistance, mobility and carrier concentration. The results of the current investigation show that it is possible to tune the electronic and optical properties of these multilayers using irradiation. However, as no drastic change is seen

in the electrical and optical properties of the multilayer TCE under irradiation, it may be concluded that use of such ZnO-based hybrid thin films is possible in radiation harsh environment for various optoelectronic applications.

Chapter-7

Conclusion and Future Work

7.1 Conclusion

The thesis summarizes the investigation carried out on the stacked trilayer thin films (DMD structure) for TCO applications. The following conclusions are made from the study:

1. Synthesis of stacked multi-layered SnO_2-Ag-SnO_2 structure was done on glass and quartz substrates using RF-DC sputtering method in which SnO_2 layer exhibited amorphous nature.

2. The optimization of TCO parameters was carried out by varying the thickness of Ag layer. Results indicated that 8-12 nm Ag sandwiched layer between 35 nm each SnO_2 layer was best for TCO applications.

3. The optical and electrical properties of stacked multi-layered SnO_2-Ag-SnO_2 structure were demonstrated to be tunable by making use of 100 keV Xe ion implantation and 100MeV O^{7+} SHI irradiation.

4. The structure of the films remained unaffected on ion implantation as evidenced by XRD patterns while the morphology suggested the growth of surface features pointing toward grain growth. However, the SHI irradiation introduced ion beam mixing of layers and it resulted in the diffusion of Ag layer into bottom SnO_2 layer.

5. The variation of electrical properties viz. sheet resistance, mobility and carrier concentration was observed on post irradiation which was shown to be stable for low temperature operation of these films. However, the exposure to the high fluence led to the deterioration of the stacked multi-layered SnO_2-Ag-SnO_2 structure and it puts up a limit for its use for space application.

6. The synthesis of stacked multilayered SnO_x-Au-SnO_x structure was demonstrated on a quartz substrate using e-beam evaporation method for SnO_x and thermal evaporation method for Au layer for TCO application. The XRD

pattern indicated the amorphous nature of SnO_x layer while the surface roughness was ideal for TCO application.

7. The stacked multilayered SnO_x-Au-SnO_x exhibited higher transparency (83% beyond 475 nm), lower sheet resistance ($52\Omega/sq.$) and lower resistivity ($3.9\times10^{-4}\Omega\cdot cm$) which are comparable to that of standard ITO substrates.

8. The RBS and XAS/XES investigations indicated the formation of mixed phases of SnO/SnO_2 which provided a wide band gap energy (3.5 ± 0.2 eV), suitable for TCE applications.

9. The SHI irradiation of the stacked multilayer of SnOx-Au-SnO_x by using 100 *MeV* O^{7+} irradiation indicated insignificant change in structure and surface morphology. However, the optical transmittance and conductivity were degraded post irradiation.

10. The gamma radiation (10-100kGy) also indicated degradation of TCO properties for TCE applications.

11. The phase change (SnO_2-SnO) in both top and bottom layers was concluded to be responsible for this degradation. However, it can be considered as a method for tuning the electrical and optical properties of staked multilayer thin films. These films are also stable in terms of electrical properties post irradiation for a large range of temperature.

12. The multi-layered ZnO-Ag-ZnO structure was deposited and optimized in terms of Ag layer thickness for better TCE properties using RF-DC sputtering method. The optimized structure contained 8-12 nm of Ag layer sandwiched between ~40 nm thick ZnO layer exhibiting a preferred c-axis orientation.

13. The film properties were tested for modification in structural, optical and electrical properties with 100 keV Xe ion implantation and 100MeV Ag7+ SHI irradiation which indicated negligible change in the structure of the film. This is due to the radiation hardness of ZnO layer.

14. The optical and electrical parameters complimented the structural study showing no significant changes. This indicates the possibility of use of multi-layered ZnO-Ag-ZnO structure as TCE for space application.

15. The stacked multilayered SnO_x-Au-SnO_x structure was concluded to be the best among all structures discussed under the scope of the presented thesis. It exhibited constant transmittance in visible region with lower sheet resistance. The values are comparable to commercially available ITO films.

16. The structural, morphological, optical and electrical properties of stacked multilayered structures can be tuned by making use of ion implantation and gamma/SHI irradiation. However, high fluence could degrade them for TCE applications.

17. The multi-layered ZnO-Ag-ZnO structure was found most suitable for space applications due to its radiation hardness among other structures.

7.2 Scope of Future Work

1. It is proposed to test these stacked multilayered structures replacing ITO for the opto-electronic devices including organic solar cell, liquid crystal display and perovskites solar cell.
2. It is also required to test the stacked multilayered structure in high temperature range for different applications.
3. Fabrication of oxide/metal/oxide stacked multilayer structure on flexible substrates to be done for flexible electronic applications.
4. High bandgap oxides may be used in oxide/metal/oxide structure for near UV range devices in different environment.
5. It may also be useful to fabricate and investigate organic electrode by substituting the oxide layer by polymer and generate organic/metal/organic structure for an all organic optoelectronic device.

References

[1] K. Ellmer, Nat. Photonics **6**, 809 (2012).

[2] B.G. Lewis, MRS Bull. **25**, 22 (2000).

[3] S. Lany and A. Zunger, Phys. Rev. Lett. **98**, 45501 (2007).

[4] T.C. Yeh, Q. Zhu, D.B. Buchholz, A.B. Martinson, R.P.H. Chang, and T.O. Mason, Appl. Surf. Sci. **330**, 405 (2015).

[5] R.G. Gordon, MRS Bull. **25**, 52 (2000).

[6] M.T. Greiner and Z.-H. Lu, NPG Asia Mater. **5**, e55 (2013).

[7] M.T.J. FACCHETTI, ANTONIO, *Transparent Electronics: From Synthesis to Applications - Google Books*, First (Wiley, 2010).

[8] C.J.M. Emmott, A. Urbina, and J. Nelson, Sol. Energy Mater. Sol. Cells **97**, 14 (2012).

[9] G.U. Kulkarni, S. Kiruthika, R. Gupta, and K. Rao, Curr. Opin. Chem. Eng. **8**, 60 (2015).

[10] G.J. Exarhos and X. Zhou, **515**, 7025 (2007).

[11] B. Bissig, T. Jäger, L. Ding, A.N. Tiwari, and Y.E. Romanyuk, APL Mater. **3**, (2015).

[12] S. Chuang, C. Tsung, C. Chen, L. Ou, R. Horng, C. Lin, D. Wuu, S. Chuang, C. Tsung, C. Chen, S. Ou, and R. Horng, (2015).

[13] S. Chen, S. Wang, S. Chen, and S. Wang, **223304**, (2014).

[14] D.-J. Kim, H.-J. Kim, K.-W. Seo, K.-H. Kim, T.-W. Kim, and H.-K. Kim, Sci Rep **5**, (2015).

[15] Y. (Michael) Yang, Q. Chen, Y.-T. Hsieh, T.-B. Song, N. De Marco, H. Zhou, and Y. Yang, ACS Nano **9**, 7714 (2015).

[16] X. Chen and S.S. Mao, Chem. Rev. **107**, 2891 (2007).

[17] A. Stadler, Materials (Basel). **5**, 661 (2012).

[18] I. Hamberg and C.G. Granqvist, J. Appl. Phys. **60**, R123 (1986).

[19] K. Ravichandran, R. Anandhi, K. Karthika, P. V. Rajkumar, N. Dineshbabu, and C. Ravidhas, Superlattices Microstruct. **83**, 121 (2015).

[20] A.H. Ali, A. Shuhaimi, and Z. Hassan, Appl. Surf. Sci. **288**, 599 (2014).

[21] Q. Nian, M. Callahan, D. Look, H. Efstathiadis, J. Bailey, and G.J. Cheng, APL Mater. **3**, (2015).

[22] J.N. Namik K. Temizer, Sudhakar Nori, J. Appl. Phys. **23705**, (2014).

[23] H.J. Kim, K.W. Seo, Y.J. Noh, S.I. Na, A. Sohn, D.W. Kim, and H.K. Kim, Sol. Energy Mater. Sol. Cells **141**, 194 (2015).

[24] M. Aleksandrova, N. Kurtev, V. Videkov, S. Tzanova, and S. Schintke, Microelectron. Eng. **145**, 112 (2015).

[25] A. Kumar and C. Zhou, ACS Nano **4**, 11 (2010).

[26] H. Peelaers, E. Kioupakis, C.G. Van De Walle, H. Peelaers, E. Kioupakis, and C.G. Van De Walle, **11914**, 210 (2012).

[27] D.S. Hecht, L. Hu, and G. Irvin, Adv. Mater. **23**, 1482 (2011).

[28] J. Zou, H.L. Yip, S.K. Hau, and A.K.Y. Jen, Appl. Phys. Lett. **96**, (2010).

[29] J.-Y. Lee, S.T. Connor, Y. Cui, and P. Peumans, Nano Lett. **8**, 689 (2008).

[30] C. Guillén and J. Herrero, Thin Solid Films **520**, 1 (2011).

[31] Z. Xue, X. Liu, N. Zhang, H. Chen, X. Zheng, H. Wang, and X. Guo, ACS Appl. Mater. Interfaces **6**, 16403 (2014).

[32] Y.-Y. Choi, K.-H. Choi, H. Lee, H. Lee, J.-W. Kang, and H.-K. Kim, Sol. Energy Mater. Sol. Cells **95**, 1615 (2011).

[33] M. Girtan, Sol. Energy Mater. Sol. Cells **100**, 153 (2012).

[34] J.Y. Lee, J.W. Yang, J.H. Chae, J.H. Park, J.I. Choi, H.J. Park, and D. Kim, Opt. Commun. **282**, 2362 (2009).

[35] L. Zhang, R. Persaud, and T.E. Madey, Phys. Rev. B **56**, 10549 (1997).

[36] A. Indluru and T.L. Alford, J. Appl. Phys. **123528**,

(2009).

[37] H.J. Lee, J.W. Kang, S.H. Hong, S.H. Song, and S.J. Park, ACS Appl. Mater. Interfaces **8**, 1565 (2016).

[38] X. Guo et al., Sci. Rep. **5**, 10569 (2015).

[39] Z. Wang, C. Zhang, R. Gao, D. Chen, S. Tang, J. Zhang, D. Wang, X. Lu, and Y. Hao, Sol. Energy Mater. Sol. Cells **127**, 193 (2014).

[40] J. Zou, C.Z. Li, C.Y. Chang, H.L. Yip, and A.K.Y. Jen, Adv. Mater. **26**, 3618 (2014).

[41] L. Liu, S. Ma, H. Wu, B. Zhu, H. Yang, J. Tang, and X. Zhao, Mater. Lett. **149**, 43 (2015).

[42] D.R. Sahu, S.-Y. Lin, and J.-L. Huang, Appl. Surf. Sci. **252**, 7509 (2006).

[43] A. Dhar and T.L. Alford, **12102**, (2013).

[44] S.W. Liu, T.H. Su, P.C. Chang, T.H. Yeh, Y.Z. Li, L.J. Huang, Y.H. Chen, and C.F. Lin, Org. Electron. Physics, Mater. Appl. **31**, 240 (2016).

[45] C. Lee, R. Pandey, B. Wang, W. Choi, D. Choi, and Y. Oh, Sol. Energy Mater. Sol. Cells **132**, 80 (2015).

[46] M. Kim, C. Lim, D. Jeong, H.S. Nam, J. Kim, and J. Lee, Org. Electron. Physics, Mater. Appl. **36**, 61 (2016).

[47] K. Badeker, Ann Phys. **22**, 749 (1907).

[48] H. Kim, A. Piqué, J.S. Horwitz, H. Mattoussi, H. Murata, Z.H. Kafafi, D.B. Chrisey, J.S. Horwitz, H. Mattoussi, H. Murata, and Z.H. Kafafi, Appl. Phys. Lett. **3444**, 9 (2002).

[49] L. Holland and G. Siddall, Vacuum **3**, 375 (1953).

[50] J.L. Vossen, J. Vac. Sci. Technol. **13**, 116 (1976).

[51] G. Haacke, J. Appl. Phys. **47**, 4086 (1976).

[52] K.L. Chopra, S. Major, and D.K. Pandya, Thin Solid Films **102**, 1 (1983).

[53] M.N. Islam, T.B. Ghosh, K.L. Chopra, and H.N. Acharya, Thin Solid Films **280**, 20 (1996).

[54] T. Minami, Semicond. Sci. Technol. **20**, S35 (2005).

[55]UK Pat. (1952).

[56]Phil. Tech. Rev. **29**, 47 (1968).

[57] D.L. White and M. Feldman, Electron. Lett. **6**, 837 (1970).

[58] E. Ando, S. Suzuki, N. Aomine, M. Miyazaki, and M. Tada, Vacuum **59**, 792 (2000).

[59] C.G. Granqvist, in *Handb. Transparent Conduct.* (Springer US, Boston, MA, 2011), pp. 353–423.

[60] D.S. (David S.. Ginley, *Handbook of Transparent Conductors* (Springer, 2010).

[61] S. Swann, Phys. Technol. **19**, 67 (1988).

[62] C.H. Chu, H.W. Wu, and J.L. Huang, Thin Solid Films **605**, 121 (2016).

[63] a. Sudha, S.L. Sharma, and T.K. Maity, Mater. Lett. **157**, 19 (2015).

[64] S.H. Lee, D.M. Ho, A.J. Jacobson, and T.R. Lee, Chem. Mater. **25**, 4697 (2013).

[65] S. Chen, M.E.A. Warwick, and R. Binions, Sol. Energy Mater. Sol. Cells **137**, 202 (2015).

[66] Q.-H. Wu, J. Song, and J. Li, Surf. Interface Anal. **40**, 1488 (2008).

[67] M.T.J. FACCHETTI, ANTONIO, *Transparent Electronics: From Synthesis to Applications*, First (Wiley, 2010).

[68] S. Chen, M.E.A. Warwick, and R. Binions, Sol. Energy Mater. Sol. Cells **137**, 202 (2015).

[69] R. Soltanmoradi, S.A. Dyakov, Q. Wang, M. Qiu, and M. Yan, Appl. Phys. Lett. **61110**, 101 (2014).

[70] G. Zhao, W. Wang, T.-S. Bae, S.-G. Lee, C. Mun, S. Lee, H. Yu, G.-H. Lee, M. Song, and J. Yun, Nat. Commun. **6**, (2015).

[71] E.J. Gillham, J.S. Preston, and B.E. Williams, London, Edinburgh, Dublin Philos. Mag. J. Sci. **46**, 1051 (1955).

[72] C. Zhang, D. Zhao, D. Gu, H. Kim, T. Ling, Y.K.R. Wu, and L.J. Guo, Adv. Mater. **26**, 5696 (2014).

[73] M. Kracker, C. Worsch, C. Bocker, and C. Rüssel, Thin Solid Films **539**, 47 (2013).

[74] D.C. Olson and D.S. Ginley, in *Handb. Transparent Conduct.* (Springer US, Boston, MA, 2011), pp. 425–457.

[75] P.P. Edwards et al., Dalt. Trans. **60**, 2995 (2004).

[76] H. Hosono, J. Non. Cryst. Solids **352**, 851 (2006).

[77] W.J. Li, C.Y. Kong, H.B. Ruan, G.P. Qin, G.J. Huang, T.Y. Yang, W.W. Liang, Y.H. Zhao, X.D. Meng, P. Yu, Y.T. Cui, and L. Fang, Solid State Commun. **152**, 147 (2012).

[78] M. Chen, et al. J. Phys. D. Appl. Phys. **33**, 2538 (2000).

[79] C. Guillén and J. Herrero, Thin Solid Films **520**, 1 (2011).

[80] H. Han, N.D. Theodore, and T.L. Alford, J. Appl. Phys. **103**, 13708 (2008).

[81] Z. Xue, X. Liu, N. Zhang, H. Chen, X. Zheng, H. Wang, and X. Guo, ACS Appl. Mater. Interfaces **6**, 16403 (2014).

[82] H.-J. Lee, J.-W. Kang, S.-H. Hong, S.-H. Song, and S.-J. Park, ACS Appl. Mater. Interfaces **8**, 1565 (2016).

[83] A. Indluru and T.L. Alford, J. Appl. Phys. **105**, 123528 (2009).

[84] J.Y. Lee, J.W. Yang, J.H. Chae, J.H. Park, J.I. Choi, H.J. Park, and D. Kim, Opt. Commun. **282**, 2362 (2009).

[85] H.-K. Park, J.-W. Kang, S.-I. Na, D.-Y. Kim, and H.-K. Kim, Sol. Energy Mater. Sol. Cells **93**, 1994 (2009).

[86] M. Girtan, Sol. Energy Mater. Sol. Cells **100**, 153 (2012).

[87] Y. Cho, N.S. Parmar, S. Nahm, and J.W. Choi, J. Alloys Compd. **694**, 217 (2017).

[88] W.-S. Liu, Y.-H. Liu, W.-K. Chen, and K.-P. Hsueh, J. Alloys Compd. **564**, 105 (2013).

[89] J. Yun, W. Wang, T.S. Bae, Y.H. Park, Y.-C. Kang, D.-H. Kim, S. Lee, G.-H. Lee, M. Song, and J.-W. Kang, ACS Appl. Mater. Interfaces **5**, 9933 (2013).

[90] I. Crupi, S. Boscarino, V. Strano, S. Mirabella, F. Simone, and A. Terrasi, Thin Solid Films **520**, 4432 (2012).

[91] W. Cao, Y. Zheng, Z. Li, E. Wrzesniewski, W.T. Hammond, and J. Xue, Org. Electron. **13**, 2221 (2012).

[92] K. Sivaramakrishnan, N.D. Theodore, J.F. Moulder, and T.L. Alford, J. Appl. Phys. **106**, 63510 (2009).

[93] T. Minami, Thin Solid Films **516**, 5822 (2008).

[94] T. Minami, Thin Solid Films **516**, 1314 (2008).

[95] A.R. Gentle, S.D. Yambem, P.L. Burn, P. Meredith, and G.B. Smith, J. Appl. Phys. **119**, (2016).

[96] A. Bou, P. Torchio, D. Barakel, F. Thierry, A. Sangar, P.-Y. Thoulon, and M. Ricci, J. Appl. Phys. **116**, 23105 (2014).

[97] P.K. Chiu, W.H. Cho, H.P. Chen, C.N. Hsiao, and J.R. Yang, Nanoscale Res. Lett. **7**, 304 (2012).

[98] I. Lorite, P. Díaz-Carrasco, M. Gabás, J.F. Fernández, and J.L. Costa-Krämer, Mater. Lett. **109**, 167 (2013).

[99] S. Yu, W. Zhang, L. Li, D. Xu, H. Dong, and Y. Jin, Thin Solid Films **552**, 150 (2014).

[100] S. Yu, L. Li, D. Xu, H. Dong, and Y. Jin, Thin Solid Films **562**, 501 (2014).

[101] S.H. Yu, C.H. Jia, H.W. Zheng, L.H. Ding, and W.F. Zhang, *High Quality Transparent Conductive SnO2/Ag/SnO2 Tri-Layer Films Deposited at Room Temperature by Magnetron Sputtering* (2012).

[102] A. Kim, Y. Won, K. Woo, C.H. Kim, and J. Moon, ACS Nano **7**, 1081 (2013).

[103] H.M. Lee, Y.J. Lee, I.S. Kim, M.S. Kang, S.B. Heo, Y.S. Kim, and D. Kim, Vacuum **86**, 1494 (2012).

[104] J. Ho Kim, Y.J. Moon, S.K. Kim, Y.Z. Yoo, and T.Y. Seong, Ceram. Int. **41**, 14805 (2015).

[105] S.-H. Chuang, C.-S. Tsung, C.-H. Chen, S.-L. Ou, R.-H. Horng, C.-Y. Lin, and D.-S. Wuu, ACS Appl. Mater. Interfaces **7**, 2546 (2015).

[106] S. Addanki, J. Jayachandiran, K. Pandian, and D. Nedumaran, Sensors Actuators, B Chem. **210**, 17 (2015).

[107] D. Kim, Appl. Surf. Sci. **256**, 1774 (2010).

[108] A. Indluru and T.L. Alford, J. Appl. Phys. **105**, 123528 (2009).

[109] H. Wei and H. Eilers, J. Phys. Chem. Solids **70**, 459 (2009).

[110] A. Kossoy, V. Merk, D. Simakov, K. Leosson, S. Kéna-Cohen, and S.A. Maier, Adv. Opt. Mater. **3**, 71 (2014).

[111] D.J. Kim, H.J. Kim, K.W. Seo, K.H. Kim, T.W. Kim, and H.K. Kim, Sci Rep **5**, 16838 (2015).

[112] M.L. Grilli, I. Di Sarcina, S. Bossi, A. Rinaldi, L. Pilloni, and A. Piegari, Thin Solid Films **594**, 261 (2015).

[113] W.T. Yen, Y.C. Lin, and J.H. Ke, Appl. Surf. Sci. **257**, 960 (2010).

[114] S.M.B. Ghorashi, A. Behjat, M. Neghabi, and G. Mirjalili, Appl. Surf. Sci. **257**, 1602 (2010).

[115] J.-A. Jeong, Y.-S. Park, and H.-K. Kim, J. Appl. Phys. **107**, 23111 (2010).

[116] S.J. Kim, E.A. Stach, and C.A. Handwerker, Thin Solid Films **520**, 6189 (2012).

[117] T.. Young, J.. Chang, and H.. Ueng, Thin Solid Films **322**, 319 (1998).

[118] J. Hong, K.-I. Katsumata, and N. Matsushita, Acta Mater. **103**, 844 (2016).

[119] A. Alyamani and N. Mustapha, Thin Solid Films **611**, 27 (2016).

[120] A. Indluru, K.E. Holbert, and T.L. Alford, Thin Solid Films **539**, 342 (2013).

[121] G. Zhao, S.M. Kim, S.G. Lee, T.S. Bae, C.W. Mun, S. Lee, H. Yu, G.H. Lee, H.S. Lee, M. Song, and J. Yun, Adv. Funct. Mater. **26**, 4180 (2016).

[122] J.F. Gibbons, Proc. IEEE **60**, 1062 (1972).

[123] N.E. Sosa, C. Chen, J. Liu, T.J. Marks, M.C. Hersam, N.E. Sosa, C. Chen, J. Liu, T.J. Marks, and M.C. Hersam, **22110**, 1 (2012).

[124] C.H. Hong, Y.J. Jo, H.A. Kim, I.-H. Lee, and J.S. Kwak, Thin Solid Films **519**, 6829 (2011).

[125] S. Keshri, A. Kumar, and D. Kabiraj, Thin Solid Films **526**, 50 (2012).

[126] R. Fromknecht, I. Khubeis, S. Massing, and O. Meyer, Nucl. Instruments Methods Phys. Res. Sect. B Beam Interact. with Mater. Atoms **147**, 191 (1999).

[127] T. Tesfamichael, G. Will, M. Colella, and J. Bell, Nucl. Instruments Methods Phys. Res. Sect. B Beam Interact. with Mater. Atoms **201**, 581 (2003).

[128] F. Bekisli, Lehigh Preserve Hydrogen in the Semiconducting Oxides SnO2 and TiO2 Studied by FTIR Spectroscopy, Lehigh University, 2013.

[129] T. Moe Børseth, F. Tuomisto, J.S. Christensen, E. V Monakhov, B.G. Svensson, and A. Yu Kuznetsov, Phys. Rev. B **77**, (2008).

[130] J.E. Stehr, X. Wang, S. Filippov, S.J. Pearton, I.G. Ivanov, W. Chen, I. Buyanova, J.E. Stehr, X.J. Wang, S. Filippov, I.G. Ivanov, W.M. Chen, and I.A. Buyanova, J. Appl. Phys. **113**, (2013).

[131] Y. Dong, F. Tuomisto, B.G. Svensson, A.Y. Kuznetsov, and L.J. Brillson, Phys. Rev. B **81**, 81201 (2010).

[132] J.K. Park et al., Sci. Rep. **6**, 23378 (2016).

[133] D.K. Avasthi and G.K. Mehta, *Swift Heavy Ions for Materials Engineering and Nanostructuring* (Springer Science & Business Media, 2011).

[134] G.H. Vineyard, Radiat. Eff. **29**, 245 (1976).

[135] H.K. Singh, D.K. Avasthi, and S. Aggarwal, Nucl. Inst. Methods Phys. Res. B **353**, 35 (2015).

[136] H. Thakur, K.K. Sharma, R. Kumar, P. Thakur, Y. Kumar, A.P. Singh, S. Gautam, and K.H. Chae, Condens. Matter Mater. Sci. (2011).

[137] R.S. Chauhan, V. Kumar, D.C. Agarwal, D. Pratap, I. Sulania, and A. Tripathi, Nucl. Instruments Methods Phys. Res. Sect. B Beam Interact. with Mater. Atoms **286**, 295 (2012).

[138] D.C. Agarwal, A. Kumar, S.A. Khan, D. Kabiraj, F. Singh, A. Tripathi, J.C. Pivin, R.S. Chauhan, and D.K. Avasthi, Nucl. Instruments Methods Phys. Res. Sect. B Beam Interact. with Mater. Atoms **244**, 136 (2006).

[139] N.G. Deshpande et al., J. Phys. D. Appl. Phys. **41**, 35308 (2008).

[140] H. Kim, C.M. Gilmore, A. Piqué, J.S. Horwitz, H. Mattoussi, H. Murata, Z.H. Kafafi, and D.B. Chrisey, J. Appl. Phys. **86**, (1999).

[141] R. Chen, C. Zou, J. Bian, A. Sandhu, and W. Gao, Nanotechnology **22**, 105706 (2011).

[142] H. Hosono, in *Handb. Transparent Conduct.* (Springer US, Boston, MA, 2011), pp. 459–487.

[143] S. Das and V. Jayaraman, Prog. Mater. Sci. **66**, 112

(2014).

[144] K.G. Godinho, A. Walsh, and G.W. Watson, J. Phys. Chem. C **113**, 439 (2009).

[145] Y.J. Kwon, S.Y. Kang, P. Wu, Y. Peng, S.S. Kim, and H.W. Kim, ACS Appl. Mater. Interfaces **8**, 13646 (2016).

[146] Ü. Özgür, Y.I. Alivov, C. Liu, A. Teke, M.A. Reshchikov, S. Doğan, V. Avrutin, S.J. Cho, and H. Morkọ, J. Appl. Phys. **98**, 1 (2005).

[147] O. Szabó, S. Kováčová, V. Tvarožek, I. Novotný, P. Šutta, M. Netrvalová, D. Rossberg, and P. Schaaf, Thin Solid Films **591**, 230 (2015).

[148] D.S. Ghosh, Q. Liu, P. Mantilla-Perez, T.L. Chen, V. Mkhitaryan, M. Huang, S. Garner, J. Martorell, and V. Pruneri, Adv. Funct. Mater. **25**, 7309 (2015).

[149] W. Wang, M. Song, T. Bae, Y.H. Park, Y. Kang, S. Lee, S. Kim, D.H. Kim, S. Lee, and G. Min, Adv. Funct. Mater. **24**, 1551 (2014).

[150] H. Han, N.D. Theodore, and T.L. Alford, J. Appl. Phys. **103**, 13708 (2008).

[151] F.L.M. Sam, C.A. Mills, L.J. Rozanski, and S.R.P. Silva, Laser Photon. Rev. **8**, 172 (2014).

[152] L. Holland and G. Siddall, Vacuum **3**, 245 (1953).

[153] Y.H. Kim, J.W. Lee, and R.I. Murakami, IEEE Trans. Nanotechnol. **12**, 991 (2013).

[154] S.M. Rossnagel, J. Vac. Sci. Technol. A Vacuum, Surfaces, Film. **21**, S74 (2003).

[155] B.D. Cullity, *Elements of X-Ray Diffraction* (2001).

[156] J. Perrière, Vacuum **37**, 429 (1987).

[157] J. Chastain, R.C. King, and J.F. Moulder, *Handbook of X-Ray Photoelectron Spectroscopy: A Reference Book of Standard Spectra for Identification and Interpretation of XPS Data* (Physical Electronics Eden Prairie, MN, 1995).

[158] G. Binnig, C.F. Quate, and C. Gerber, Phys. Rev. Lett. **56**, 930 (1986).

[159] H. Seiler, J. Appl. Phys. **54**, R1 (1983).

[160] D.B. Williams and C.B. Carter, in *Transm. Electron Microsc.* (Springer US, Boston, MA, 1996), pp. 3–17.

[161] A.B. Djuris, *UV-VIS and Photoluminescence Spectroscopy for Nanomaterials Characterization* (2013).

[162] W. Robert Thurber, (2010).

[163] F. Fang, Y. Zhang, X. Wu, Q. Shao, and Z. Xie, Mater. Res. Bull. **68**, 240 (2015).

[164] L.R. Doolittle, Nucl. Instruments Methods Phys. Res. Sect. B Beam Interact. with Mater. Atoms **9**, 344 (1985).

[165] C.A. Schneider, W.S. Rasband, and K.W. Eliceiri, Nat. Methods **9**, 671 (2012).

[166] F.A. Akgul, C. Gumus, A.O. Er, A.H. Farha, G. Akgul, Y. Ufuktepe, and Z. Liu, J. Alloys Compd. **579**, 50 (2013).

[167] Y.-H. Tak, K.-B. Kim, H.-G. Park, K.-H. Lee, and J.-R. Lee, Thin Solid Films **411**, 12 (2002).

[168] Y. Cai, H. Fan, M. Xu, and Q. Li, Colloids Surfaces A Physicochem. Eng. Asp. **436**, 787 (2013).

[169] J. Heo, A.S. Hock, and R.G. Gordon, 4964 (2010).

[170] D.R.G. Mitchell and B. Schaffer, Ultramicroscopy **103**, 319 (2005).

[171] S. Yu, W. Zhang, L. Li, D. Xu, H. Dong, and Y. Jin, Acta Mater. **61**, 5429 (2013).

[172] J. Tauc, in *Amorph. Liq. Semicond.* (Springer US, Boston, MA, 1974), pp. 159–220.

[173] C. Zhang, D. Zhao, D. Gu, H. Kim, T. Ling, Y.R. Wu, and L.J. Guo, Adv. Mater. **26**, 5696 (2014).

[174] R.S. Sennett and G.D. Scott, J. Opt. Soc. Am. **40**, 203 (1950).

[175] S.P. Kaye, H. Kheyrandish, and J.S. Colligon, Nucl. Instruments Methods Phys. Res. Sect. B Beam Interact. with Mater. Atoms **61**, 38 (1991).

[176] C.S. Rastomjee et al., J. Mater. Chem. **2**, 511 (1992).

[177] Z. Tao, H. Junda, and L. Hong, Appl. Surf. Sci. **161**, 459 (2000).

[178] S. Balachandran, K. Selvam, B. Babu, and M. Swaminathan, Dalton Trans. **42**, 16365 (2013).

[179] M. Kwoka, L. Ottaviano, P. Koscielniak, and J. Szuber, Nanoscale Res. Lett. **9**, 260 (2014).

[180] I.-S. Hwang, J.-K. Choi, H.-S. Woo, S.-J. Kim, S.-Y. Jung, T.-Y. Seong, I.-D. Kim, and J.-H. Lee, ACS Appl. Mater. Interfaces **3**, 3140 (2011).

[181] V.N. Singh, B.R. Mehta, R.K. Joshi, F.E. Kruis, and S.M. Shivaprasad, Sensors Actuators B Chem. **125**, 482 (2007).

[182] M. Mirzaee and A. Dolati, J. Nanoparticle Res. **16**, 2582 (2014).

[183] T. Sahm, A. Gurlo, N. Bârsan, and U. Weimar, Sensors Actuators, B Chem. **118**, 78 (2006).

[184] M. Marikkannan, V. Vishnukanthan, A. Vijayshankar, J. Mayandi, J.M. Pearce, M. Marikkannan, V. Vishnukanthan, A. Vijayshankar, and J. Mayandi, **27122**, 0 (2015).

[185] H. Peelaers, E. Kioupakis, and C.G. Van de Walle, Appl. Phys. Lett. **100**, 11914 (2012).

[186] P.M. Gorley, V.V. Khomyak, S.V. Bilichuk, I.G. Orletsky, P.P. Horley, and V.O. Grechko, Mater. Sci. Eng. B **118**, 160 (2005).

[187] K.W. Jo, S.W. Moon, and W.J. Cho, Appl. Phys. Lett. **106**, (2015).

[188] D.R. Sahu, S.-Y. Lin, and J.-L. Huang, Thin Solid Films **516**, 4728 (2008).

[189] R. Kelly and E. Giani, Nucl. Instruments Methods Phys. Res. **209**, 531 (1983).

[190] N. Zhou, D.B. Buchholz, G. Zhu, X. Yu, H. Lin, A. Facchetti, T.J. Marks, and R.P.H. Chang, Adv. Mater. **26**, 1098 (2014).

[191] M. Mayer, in *AIP Conf. Proc.* (AIP, 1999), pp. 541–544.

[192] A. Kar et al., Semicond. Sci. Technol. **25**, 24012 (2010).

[193] A. Sharma, K.D. Verma, M. Varshney, D. Singh, M. Singh, K. Asokan, and R. Kumar, Radiat. Eff. Defects Solids **165**, 930 (2010).

[194] K.M. Abhirami, P. Matheswaran, B. Gokul, R. Sathyamoorthy, D. Kanjilal, and K. Asokan, *Effect of SHI Irradiation on the Morphology of SnO2 Thin Film Prepared by Reactive Thermal Evaporation* (2013).

[195] Z.R. Li and H. Meng, *Organic Light-Emitting Materials and Devices* (CRC/Taylor & Francis, 2007).

[196] C. McGuinness, C.B. Stagarescu, P.J. Ryan, J.E. Downes, D. Fu, K.E. Smith, and R.G. Egdell, Phys. Rev. B **68**, 165104 (2003).

[197] R. Summitt, J.A. Marley, and N.F. Borrelli, J. Phys. Chem. Solids **25**, 1465 (1964).

[198] H. Han, N.D. Theodore, and T.L. Alford, J. Appl. Phys. **103**, 13708 (2008).

[199] J.A. McLeod, N.A. Skorikov, L.D. Finkelstein, E.Z. Kurmaev, and A. Moewes, J. Phys. Chem. C **116**, 24248 (2012).

[200] D. Choi, W.J. Maeng, and J. Park, Appl. Surf. Sci. **313**, 585 (2014).

[201] G.S. Chang, J. Forrest, E.Z. Kurmaev, A.N. Morozovska, M.D. Glinchuk, J.A. Mcleod, A. Moewes, T.P. Surkova, and N.H. Hong, Phys. Rev. B **165319**, 1 (2012).

[202] D.-Y. Cho, S.-I. Na, K.-B. Chung, and H.-K. Kim, Appl. Surf. Sci. **347**, 88 (2015).

[203] S. Das and V. Jayaraman, Prog. Mater. Sci. **67**, 161 (2015).

[204] L.R. Doolittle, Nucl. Instruments Methods Phys. Res. Sect. B Beam Interact. with Mater. Atoms **9**, 344 (1985).

[205] L.Y. Liang, Z.M. Liu, H.T. Cao, and X.Q. Pan, ACS Appl. Mater. Interfaces **2**, 1060 (2010).

[206] C.K.T. Chew, C. Salcianu, P. Bishop, J. Carmalt, and I.P. Parkin, J. Mater. Chem. C **0**, 1 (2014).

[207] M. Elbahri, M.K. Hedayati, V.S. Kiran Chakravadhanula, M. Jamali, T. Strunkus, V. Zaporojtchenko, and F. Faupel, Adv. Mater. **23**, 1993 (2011).

[208] A. Diéguez, A. Romano-Rodríguez, A. Vilà, and J.R. Morante, J. Appl. Phys. **90**, 1550 (2001).

[209] T.F. Cooney, E.R.D. Scott, A.N. Krot, S.K. Sharma, and A.A. Yamaguchi, Am. Mineral. **84**, 1569 (1999).

[210] M. Joseph, H. Tabata, H. Saeki, K. Ueda, and T. Kawai, Phys. B Condens. Matter **302**, 140 (2001).

[211] F.X. Xiu, Z. Yang, L.J. Mandalapu, D.T. Zhao, J.L. Liu, and W.P. Beyermann, Appl. Phys. Lett. **87**, 152101 (2005).

[212] S.Y. Myong, J. Steinhauser, R. Schlüchter, S. Faÿ, E. Vallat-Sauvain, A. Shah, C. Ballif, and A. Rüfenacht, Sol. Energy Mater. Sol. Cells **91**, 1269 (2007).

[213] S. Kumar, R. Kumar, and D.P. Singh, Appl. Surf. Sci. **255**, 8014 (2009).

[214] Y.K. Mishra, D.K. Avasthi, P.K. Kulriya, F. Singh, D. Kabiraj, A. Tripathi, J.C. Pivin, I.S. Bayer, and A. Biswas, (2007).

[215] L.Y. Liang, Z.M. Liu, H.T. Cao, and X.Q. Pan, ACS Appl. Mater. Interfaces **2**, 1060 (2010).

[216] A. Arshak, K. Arshak, O. Korostynska, and S. Zleetni, **51**, 78 (2004).

[217] A. Maged, L. Nada, and M. Amin, Phys. Sci. Int. J. **7**, 20 (2015).

[218] D. Craciun, G. Socol, S. Le Ca??r, L.M. Trinca, A.C. Galca, D. Pantelica, P. Ionescu, and V. Craciun, Thin Solid Films **614**, 2 (2016).

[219] J.F. Wager, Science (80-.). **300**, (2003).

[220] U. Özgür, Y.I. Alivov, C. Liu, A. Teke, M.A. Reshchikov, S. Doğan, V. Avrutin, S.-J. Cho, and H. Morkoç, J. Appl. Phys. **98**, 41301 (2005).

[221] B. O’Connor, C. Haughn, K.-H. An, K.P. Pipe, and M. Shtein, Appl. Phys. Lett. **93**, 223304 (2008).

[222] J.H. Kim, J.Y. Na, S.K. Kim, Y.Z. Yoo, and T.Y. Seong, J. Electron. Mater. **44**, 3967 (2015).

[223] H.R. An, S.T. Oh, C.Y. Kim, S.H. Baek, I.K. Park, and H.J. Ahn, J. Alloys Compd. **615**, 728 (2014).

[224] H.R. Liu, G.X. Shao, J.F. Zhao, Z.X. Zhang, Y. Zhang, J. Liang, X.G. Liu, H.S. Jia, and B.S. Xu, J. Phys. Chem. C **116**, 16182 (2012).

[225] V. Kumar, H.C. Swart, O.M. Ntwaeaborwa, R.E. Kroon, J.J. Terblans, S.K.K. Shaat, A. Yousif, and M.M. Duvenhage, Mater. Lett. **101**, 57 (2013).

[226] L. Duan, B. Lin, W. Zhang, S. Zhong, and Z. Fu, Appl. Phys. Lett. **88**, 3 (2006).

[227] S. Sharma, S. Vyas, C. Periasamy, and P. Chakrabarti, Superlattices Microstruct. **75**, 378 (2014).

[228] V. Kumar, F. Singh, O.M. Ntwaeaborwa, and H.C. Swart, Appl. Surf. Sci. **279**, 472 (2013).

[229] P. Kumar, H.K. Malik, and K. Asokan, EPL (Europhysics Lett. **110**, 67006 (2015).

[230] P. Kumar, V. Sharma, A. Sarwa, A. Kumar, R. Goyal, K. Sachdev, S. Annapoorni, K. Asokan, and D. Kanjilal, RSC Adv. **6**, 89242 (2016).

[231] V. Kumar, O.M. Ntwaeaborwa, and H.C. Swart, J. Colloid Interface Sci. **465**, 295 (2016).

[232] H.R. Liu, G.X. Shao, J.F. Zhao, Z.X. Zhang, Y. Zhang, J. Liang, X.G. Liu, H.S. Jia, and B.S. Xu, J. Phys. Chem. C **116**, 16182 (2012).

[233] K. Lim, K. Kim, S. Kim, S.Y. Park, H. Kim, and Y.S. Kim, Adv. Mater. **25**, 2994 (2013).

[234] V.K. Kaushik, J. Electron Spectros. Relat. Phenomena **56**, 273 (1991).

[235] D. Lin, H. Wu, R. Zhang, and W. Pan, Chem. Mater. **21**, 3479 (2009).

[236] R. Chen, C. Zou, J. Bian, A. Sandhu, and W. Gao, Nanotechnology **22**, 105706 (2011).

[237] D.C. Agarwal, R.S. Chauhan, D.K. Avasthi, S.A. Khan, D. Kabiraj, and I. Sulania, J. Appl. Phys. **104**, 24304 (2008).

[238] P. Mallick, R. Biswal, C. Rath, D.C. Agarwal, A. Tripathi, D.K. Avasthi, D. Kanjilal, P. V Satyam, and N.C. Mishra, Nucl. Instruments Methods Phys. Res. Sect. B Beam Interact. with Mater. Atoms **268**, 470 (2010).

[239] Y.-H. Tak, K.-B. Kim, H.-G. Park, K.-H. Lee, and J.-R. Lee, Thin Solid Films **411**, 12 (2002).

[240] C.K.T. Chew, C. Salcianu, P. Bishop, C.J. Carmalt, and I.P. Parkin, J. Mater. Chem. C **3**, 1118 (2015).

[241] X.-Y. Li, H.-J. Li, Z.-J. Wang, H. Xia, Z.-Y. Xiong, J.-X. Wang, and B.-C. Yang, Opt. Commun. **282**, 247 (2009).

[242] K. Nomura, H. Ohta, A. Takagi, T. Kamiya, M. Hirano, and H. Hosono, Nature **432**, 488 (2004).

[243] S. Lee, S. Bang, J. Park, S. Park, Y. Ko, and H. Jeon, Phys. Status Solidi **209**, 698 (2012).

[244] M. Joseph, H. Tabata, H. Saeki, K. Ueda, and T. Kawai, Phys. B Condens. Matter **302**, 140 (2001).

[245] S.Y. Myong, J. Steinhauser, R. Schlüchter, S. Faÿ, E. Vallat-Sauvain, A. Shah, C. Ballif, and A. Rüfenacht, Sol. Energy Mater. Sol. Cells **91**, 1269 (2007).

[246] F.X. Xiu, Z. Yang, L.J. Mandalapu, D.T. Zhao, J.L. Liu, and W.P. Beyermann, Appl. Phys. Lett. **87**, 152101 (2005).

[247] A. Kumar, A. Hähnel, D. Kanjilal, and R. Singh, Appl. Phys. Lett. **101**, 153508 (2012).

Bio-data

……………………………………………………………………………………

Name: Vikas Sharma

Address: Department of Physics,
Malaviya National Institute of Technology,
Jaipur-302017 (India)

Mobile: +91-9828618786, +91- 9351402045

Email: phyvikas@gmail.com

……………………………………………………………………………………

Career objective:

To engage in high end research activities focused on emerging technology requirements using the training and knowledge received in device fabrication, physics and technical communication as a doctoral student in applied science.

Educational qualifications:

Ph. D.: Thesis Title: "Stacked Multilayered Transparent Electrode"
(Physics- Materials Technology -Experimental)
Year of passing 2017, C.G.P.A – 8.75 /10.00
National Institute of Technology Jaipur (INDIA)

Master of science: Physics
Year of passing 2008, C.G.P.A – 7.96 /10.00
National Institute of Technology Jaipur (INDIA)

Bachelor of Science: Physics, Chemistry, Mathematics
Year of passing: 2006, Percentage: 68.89%
University of Rajasthan Jaipur (INDIA)

Research Interests:

Materials manipulation for desired applications, Nanotechnology, Transparent Electrode, Optoelectronics, Energy conversion devices.

Research positions

(a) **Research Scholar:** December 2011 to May 5, 2017

Research activity: Synthesis and characterization of metal/metal oxide based TCO.

Research Lab: Materials Research Center, NIT Jaipur (INDIA)

Research Fellowship: GATE Fellowship, MHRD, New Delhi (INDIA)

Responsibility: Fabrication and analysis of stacked multilayered thin films, Project co-coordinator in the research group for project work of M.Sc./M.Tech. Students

(b) Junior Research fellow: August 2010 to July 2011

Research Activity: Investigation of CNT doped liquid crystal for display application.

Research Lab: Liquid Crystal Lab, Department of Physics, BITS Pilani (INDIA)

Sponsored Agency: Institute Fellowship

Responsibility: Synthesis and analysis of CNT doped liquid crystal cell

(c) CSIR Project Associate: March 2009 to July 2010

Research Activity: Design & fabrication of MEMS based ISFET Bio sensors

Research Lab: MEMS & Micro sensors Group, CEERI Pilani (INDIA)

Sponsored Agency: Defense Research and Development Organization (DRDO)

Responsibilities: Fabrication and analysis of ISFET (Si_3N_4 based) to be used as sensor for pH measurement

Research projects:

1. Title: Swift heavy ion induced modifications on multilayer systems (53112 MS).

   Funding Institute: Inter University Accelerator Centre, New Delhi (INDIA)
2. Title: Effect of ion implantation on multi-layer for opto-electronics applications (58508).

   Funding Institute: Inter University Accelerator Centre, New Delhi (INDIA)

Experimental skills:

Synthesis: RF-DC Sputtering, E beam/Thermal Evaporation, Spin/Dip Coating

Software: Origin, ImageJ, SRIM, Gwyddion, Digital Micrograph, SIMNRA, CasaXPS.

Characterization: UV-Vis spectroscopy, Hall measurement, AFM, SEM, TEM, Raman Spectroscopy, Photoluminescence, X-ray diffraction, X-ray Photoelectron Spectroscopy, Rutherford Back Scattering.

Fellowships/Awards:

MHRD Fellowship for GATE-2010

Best Poster award at National Conference Thermo Physics (NCTP-2015)

Best Oral award at National Conference (ASHE-2016)

Professional Membership

Life member of Ion Beam Society of India.

Life member of Thermo Physical Society of India.

Student member of Soft Materials Society of India.

Organizing Responsibilities

- International conference on soft materials (ICSM)- 2014
- National conference on thermos physics (NCTP)- 2015
- International workshop on Surface Engineering- 2016

Research Summary

- International Journals: 10 — Conference proceedings: 08
- International Conference: 07 — National Conference: 08

A. *Journal Publication*

1. "High-Performance Radiation Stable ZnO/Ag/ZnO Multilayer Transparent Conductive Electrode", **Vikas Sharma**, P. Kumar, A. Kumar, Surbhi, K. Asokan and K. Sachdev, Solar Energy Materials and Solar Cell, 2017.
2. "Probing into highly transparent and conducting SnO_x/Au/SnO_x thin films for futuristic TCO applications" **Vikas Sharma**, Rishi Vyas, B. Paul, G. S. Chang, K. Asokan and K. Sachdev, *RSC Advances*, 2016, 6, 29135.
3. "Understanding the origin of ferromagnetism in Er doped ZnO system, Parmod Kumar, **Vikas Sharma**, Ankita Sarwa *et al.*, *RSC Advances*,2016,6, 89242.
4. "A study on 100 MeV O^{7+} irradiated SnO_2/Ag/SnO_2 multilayer as transparent electrode for flat panel display application" **Vikas Sharma**, Satyavir Singh, K. Asokan and K. Sachdev, *Nuclear Instruments and Methods in Physics Research B* 379 (2016) 141–145.
5. "Fabrication of Highly Efficient TiO_2/Ag/TiO_2 Multilayer Transparent Conducting Electrode with N Ion Implantation for Optoelectronic Applications", Satyavir Singh, **Vikas Sharma** *et al.*, *Ceramic International*, Press, 2017.

6. "Effect of High Energetic Ion Irradiation on SnO_x/Au/SnO_x Stacked Multilayer Structure, **Vikas Sharma**, R. Vyas, Surbhi, K. Asokan and K. Sachdev, APL, Communicated, 2017.
7. "Investigations on Multilayered TCO as Transparent Electrode in Organic Devices" **Vikas Sharma**, Pooja Meena, Amena Salim, Rishi Vyas, K.Sachdev, *Macromolecular Symposia*, 2015, 357, 124
8. "Structural, electrical and magnetic properties of dilutely Y doped $NiFe_2O_4$ nanoparticles" Parmod Kumar, Gaeta Rana, Gagan Dixit, Ashish Kumar, **Vikas Sharma**, Rajan Goyal, K. Sachdev, S. Annapoorni, K. Asokan, *Journal of Alloys and Compounds*, 685, 2016, 492.
9. "Investigation of phase segregation in yttrium doped zinc oxide" Parmod Kumar, Vikram Singh, **Vikas Sharma**, et. al., *Ceramics International*, 2015 41 (5), 6734-6739.
10. "Si_3N_4 Gate ISFET for Biomedical, Food and Environmental Applications, Based on Four Mask Layers using Standard MOSFET Technology" M. D. Prakash, **Vikas Sharma**, V. K. Khanna, *Int. J. Bio. Sci. Engg*., 2012, 03 (01).

B. *Conference Proceeding*

1. "Opto-electronic and morphological alteration in SnO_2/Au/SnO_2 thin film as a result of 120 MeV Ni^{7+} irradiation for TCE application, **Vikas Sharma**, Rishi Vyas, Surbhi Shekhawat, Satyavir Singh, K. Asokan and Kanupriya Sachdev., *IEEE Explore*,2016, accepted.
2. "Study of 120 Mev Ni^{7+} Ion Beam Irradiated SnO_2/Ag/SnO_2 Multilayer Thin Films" **Vikas Sharma**, Neeru Pathak, et. al., *AIP Conference Proceedings*, 2016, accepted.
3. "Investigation of ITO Free Transparent Conducting Polymer Based Electrode" **Vikas Sharma**, Sapna and Kanupriya Sachdev, *AIP Conference Proceedings*, 1731, 080053 (2016).
4. "Investigation of post annealing effects on Nb: TiO_2 transparent conducting thin films" Satyavir Singh, **Vikas Sharma** and K. Sachdev, *Advanced Science Letters*, accepted, 2016.
5. "Enhanced UV and suppressed defect related emission in yttrium doped zinc oxide" **Vikas Sharma**, Parmod Kumar, Geeta Rana, Rishi Vyas, K. Sachdev,

Hitendra K. Malik, and K. Asokan, *AIP Conference Proceedings*, 1591, 1491 (2014)

6. "Study of Oxide Etching for MOSFET - based MEMS Bio Sensor" **Vikas Sharma**, V. K. Khanna, K. Sachdev, *AIP Conference Proceedings*, 1512, 518-519 (2013).
7. "Synthesis and Characterization of Graphene Oxide (GO) and Reduced Graphene Oxide (rGO) for Gas Sensing Application" Neeru Sharma, **Vikas Sharma**, Mitlesh Kumari, Ragini Gupta, S.K. Sharma, K. Sachdev, *Macromolecular Symposia*, 2017.
8. "Investigation on Solution Processed Graphene Oxide Based Tri-layer Structure for Transparent Conducting Electrode" Garima Makhija, **Vikas Sharma**, Satyavir Singh, Neeru Sharma, Kanupriya Sachdev, *Macromolecular Symposia*, 2017.

Workshop/School attended

1 INUP Familiarization Workshop on "Nanofabrication Technology at MNITJ, 2016 & IITB 2015.

2 International workshop on Surface Engineering at MNITJ, 2016.

3 International School on Ion Beam modification at MNITJ, 2016.

4 DST-SERB School-2015 on Ion Interaction with Matter by DST-India and Rajkot University, March 03-21, 2015

5 National Workshop on "Condense Matter Physics" 2014 organized by Birla Institute of Technology and Science Pilani on 21 - 23 March 2014

6 National Workshop on "Ion beams in Materials Research" (IBMR-2013) organized by Malaviya National Institute of Technology Jaipur on 22 - 23 March 2013.

7 National Workshop on Nano- Structure Characterization, NIT Hamirpur, June 3-7, 2013.

8 National School on Thin Film fabrication, IUAC Delhi, Dec.11-13, 2012

9 Joint Academies Lecture Workshop on Frontier in Physics University of Delhi, Jan21-23, 2011.

10 DST-SERC School-2008 on Processing Plasmas organized by DST- India and BIT,

Mesra Dec. 15-27, 2008.

Short Term Course

1. Short Term Course on “Characterization Techniques” 17-21 June, 2013
2. Short Term Course on “Frontiers Materials” 12-17 August, 2013

Other achievements

- Qualified “Graduate Aptitude Eligibility Test (GATE – 2011).
- Qualified “Joint Entrance Screening Test (JEST- 2008).
- NCC “**A”** Certificate in Air wing
- Captain of Departmental Cricket team
- Attended NSS camps organized in the school as well as during college level.
- Traning attachment with Indian Naval Academy (INA) Ezhimala.
- Proud attachment with Indian Military Academy (IMA) Dehradun.

Declaration

I herewith declare that I have produced this thesis without the prohibited assistance of third parties and without making use of aids other than those specified; notions taken over directly or indirectly from other sources have been identified as such. This thesis has not previously been presented in identical or similar form to any other Indian or foreign examination board. The thesis work was conducted from July, 2011 to December, 2016 under the supervision of Dr. K. Sachdev at Department of Physics, Malaviya National Institute of Technology Jaipur.

JAIPUR Vikas Sharma

RSC Advances

PAPER

Cite this: *RSC Adv.*, 2016, **6**, 29135

Probing the highly transparent and conducting $SnO_x/Au/SnO_x$ structure for futuristic TCO applications†

V. Sharma,*[a] R. Vyas,[b] P. Bazylewski,[c] G. S. Chang,[d] K. Asokan[e] and K. Sachdev[af]

A $SnO_x/Au/SnO_x$ transparent conductive oxide (TCO) multilayered film was fabricated with a total thickness of 75 nm using both e-beam and thermal evaporation techniques. X-ray diffraction confirms the amorphous nature of SnO_x with a crystalline peak attributed to the presence of diffraction from the Au (111) plane. The morphological studies using atomic force microscopy (AFM) and scanning electron microscopy (SEM) revealed a smooth top layer of the sandwich structure. A Rutherford backscattering spectrum has been used to probe the thickness of individual TCO layers, and reveals an oxygen deficient structure in the SnO_x layer. X-ray absorption spectroscopy (XAS) and X-ray emission spectroscopy (XES) measurements confirm the formation an SnO-rich phase and the presence of oxygen vacancies. The specimen exhibited resistivity and sheet resistance of 3.9×10^{-4} Ω cm and 52 Ω sq.$^{-1}$, respectively, with an optical transparency of 83% beyond 475 nm. The superior parameters exhibited by this stacked multilayer are due to relatively lower oxygen concentration in the tin oxide layer, and it is therefore proposed as a necessary ingredient to increase the overall conductivity in metal oxide multilayer thin films.

Received 18th November 2015
Accepted 11th March 2016

DOI: 10.1039/c5ra24422f

www.rsc.org/advances

Introduction

There has been a growing need for transparent conducting oxides (TCOs) to support photovoltaic and optoelectronic applications. Various TCOs have been developed, scaling from very simplistic structures[1] to the most complicated heterostructures.[2–4] Such structures have already been discussed and later discarded for their complex counterparts offering high conductivity, transparency and stability, but at a cost of complex manufacturing procedures. The quest for research in TCOs has led to the development of a coating with (1) superior transparency in visible region, (2) excellent conducting properties and (3) better temperature and mechanical stability. The optimization of transparency and conductivity has always presented a roadblock for the development of efficient TCOs.

In recent years, the efficiency of transparent oxides has improved to some extent but requires more research.[4] The conductivity of these metal oxides is limited by the scattering due to coulomb interaction between ionized donor and free electrons.[5] This puts a limit to the TCO conductivity as 4×10^{-4} Ω cm.[6–8] Among various structures, stacked multilayer thin films have proved to be suitable candidate. It is well known that thickness of metal oxide and noble metal layer play an important role in tuning the electrical conductivity and optical properties of the stacked multilayer. The thickness of metal layer below 20 nm increases the transparency as well as charge transport.[9] It is reported that Au metal is more effective in increasing conductivity and transparency.[10] Due to the high cost (indium bar price 99.99% ≈ $1000 per 100 g) and relatively limited availability of indium in nature, the research for alternatives to ITO is in progress.

One of such alternatives is tin oxide which offers higher conductivity even at ultrathin thickness[11,12] which is necessary for it to be realized as a candidate for TCO applications. In this aspect, a tri-layered structure has been reported by Bou *et al.*[13] which describes the use of indium-tin-oxide (ITO) free $SnO_x/Au/SnO_x$ for organic photovoltaic application. It is reported that the sheet resistance is 6.7 Ω sq.$^{-1}$ with a transparency of 67%. These values are comparable to those of ITO films. Yu *et al.*[14] also reported such tri-layered structure with Ag as sandwich layer ($SnO_2/Ag/SnO_2$) offering sheet resistance of 9.61 Ω sq.$^{-1}$, resistivity of 4.8×10^{-5} Ω cm and transmittance of more than 83% in the visible region.

[a]Department of Physics, Malaviya National Institute of Technology, Jaipur-302017, India. E-mail: phyvikas@gmail.com

[b]Department of Physics, School of Basic Sciences, Jaipur National University, Jaipur-302017, India

[c]Department of Physics & Astronomy, University of Western, London-N6A 3K7, Ontario, Canada

[d]Department of Physics & Engineering Physics, University of Saskatchewan, Saskatoon-S7N 5E2, Canada

[e]Materials Science Division, Inter-University Accelerator Centre, New Delhi-110067, India

[f]Materials Research Centre, Malaviya National Institute of Technology, Jaipur-302017, India. E-mail: ksachdev.phy@mnit.ac.in

† Electronic supplementary information (ESI) available. See DOI: 10.1039/c5ra24422f

This journal is © The Royal Society of Chemistry 2016

In addition to the material and design of multilayer structure, the device performance is known to be dictated conclusively by the surface morphology of TCO especially for display[15,16] and energy conversion applications like OLED or OPV.[17] There have been reports on the role of surface roughness as one of the influencing factors in determining the efficiency of TCO electrodes.[15] Films with higher roughness are known to show less transparency as a result of scattering of light due to the rough surface.[16] In the case of organic electronic devices, control over surface roughness of the TCO is a serious concern. Two or more organic active layers are to be deposited on the TCO and poor interfacial adherence between the top surface and the next organic active layer is detrimental to the device performance.[17]

X-ray absorption spectroscopy (XAS) and X-ray emission spectroscopy (XES) have been used extensively in recent years for probing the electronic structure of materials.[18–21] In case of XAS, the absorption of X-ray by one of the core electrons results in the electron being excited to a higher energy unoccupied state or ejected from the atom thereby creating a core hole. XAS is useful in studying the local atomic environment and analyzing materials based on their characteristic X-ray absorption edge. In X-ray emission, the incident X-ray knocks out a core electron. The core hole is filled by a valence electron and a photon is emitted and can be detected to provide a measure of the valence band states, complimentary to XAS. XAS studies have been used to investigate the effect of Ag doping on the electronic structure of In_2O_3 films and have reported an increase in the density of conduction band states in the O K-edge spectrum.[20] This has been attributed to the orbital overlap between the O-2p and Ag-4d and Ag-5sp orbitals, which may result in increased electron carrier transport.[20] Kapilashrami *et al.*[21] have used the XAS and XES spectra to determine the band gap of $Zn_{1-x}Sn_xO$ thin films.

In the present manuscript, the focus is to revive the discussion on conventional process by designing a multilayer structure for better TCO properties. For this, e-beam evaporation was used to create a mixed phase of SnO/SnO_2 with reduced oxygen during deposition due to vacuum drag to increase the conductivity of metal oxide layer. This study also aims to increase the transmittance of multilayered films over the reported transmittance[13,14] using a high performing stacked multilayered structure of $SnO_x/Au/SnO_x$ for various technological applications.

Experimental details

Sample preparation

SnO_2 powder (Alfa-Aesar, 99.999% of purity, metal basis) is used as starting material for making pellet for e-beam evaporation. SnO_2 powder was subjected to grinding and then pelletized. These pellets were then sintered at 500 °C for 3 h to get better structural stability for film deposition.

The quartz substrates of 1×1 cm^2 were cleaned using standard cleaning processes and kept in iso-propanol. These substrates were then given a heat treatment at 200 °C prior to deposition to remove any organic impurity on the surface. The stacked multilayer was then deposited on these quartz substrates using e-beam evaporation (for SnO_2 layer) and thermal evaporation (for Au layer) techniques at room temperature. SnO_2 films were deposited keeping the evaporation parameters as: source to substrate distance – 16 cm, base pressure 7×10^{-7} mbar, working pressure 1.4×10^{-5} mbar, rate of deposition 0.2 nm s^{-1}, voltage 200 V and current 10 mA. The Au layer was deposited using thermal evaporation unit with base pressure 8×10^{-7} mbar, working pressure 1.4×10^{-6} mbar, voltage 1 V, current 280 A and deposition rate of 0.1 nm s^{-1} to deposit a thickness of 5 nm. The process of SnO_2 film deposition is then repeated to deposit the 35 nm thick uppermost layer making the total thickness of the multilayered structure as 75 nm.

The resultant $SnO_x/Au/SnO_x$ stacked multilayer was annealed in open air furnace at various temperatures (30–150 °C) to test the thermal stability of multilayered structure. These thin films annealed at different temperature were then checked by X-ray diffraction. All other measurements were carried out for the as deposited $SnO_x/Au/SnO_x$ stacked multilayer at room temperature.

Characterization

X-ray diffraction (XRD) measurement of the sample was carried out using a Bruker D8 Advance X-ray diffractometer. The field-emission scanning electron microscopy (FE-SEM) and atomic force microscopy (AFM) images were collected using Nova Nano FESEM 450 (FEI) and NanoscopeIIIa, respectively. UV-vis spectrum of the sample was obtained using LAMBDA 750 (Perkin Elmer) UV-vis NIR spectrophotometer. The Raman spectrum of specimen was taken using Renishaw Raman spectrometer with Ar ion laser with 514.5 nm wavelength and 50 mW power.

The low temperature Hall measurements were performed using a variable temperature Hall set up (model HMS 5500) from Ecopia Co., Korea. The current–voltage characteristics were measured using a custom built setup consisting of a cryostat controlled with Lakeshore 325 temperature controller and Keithley 2400 SMU.

The interface was investigated with Rutherford backscattering (RBS) spectrometry using 2 MeV He^+ ion beams at Inter-University Accelerator Centre, New Delhi (India). Measurement of O K-edge and Sn M-edge XAS and XES were performed at Resonant Elastic and Inelastic scattering (REIXS) beamline of Canadian Light Source (CLS), Canada. XAS spectra were obtained in both surface sensitive total electron yield (TEY) and bulk-sensitive total fluorescence yield (TFY) modes using linearly polarized X-rays at 45° angle of incidence. Non-resonant XES measurements of the O K-edge were collected by exciting above the absorption edge at 560 eV.

Results and discussion

X-ray diffraction study

The glancing angle X-ray diffraction curve for room temperature $SnO_x/Au/SnO_x$ staked multilayer specimen (shown in Fig. 1a) is suggestive of formation of amorphous metal oxide. Multiple peaks at 38.18°, 44.39°, 64.57° and 77.54° correspond to the Au

 This journal is © The Royal Society of Chemistry 2016

cubic crystal planes of 111, 200, 220 and 311, respectively (JCPDS-card no. 00-004-0784).

The high intensity background counts in the top curve of Fig. 1a (shown with exponential fit) is due to amorphous nature of SnO_x and SiO_2 (substrate) layer. The bottom curve of Fig. 1a shows the residue of the fit after subtracting the exponential fit data from the obtained spectrum.

The diffraction patterns were also recorded for the staked layer annealed at various temperatures and are shown in Fig. 1b which indicates the formation of an amorphous phase except an intense peak at $2\theta \approx 38.04°$ corresponding to Au (111) plane. We note that there is no change in the intensities and the peak positions with annealing temperatures. This confirms the stability of multilayer structure in the temperature range of photovoltaic and optoelectronic device operation, *i.e.*, room temperature to 150 °C.

Such amorphous film is advantageous for growth of various films due to absence of lattice mismatch between the hetero-layers. A similar result of amorphous metal oxide film with crystalline metal as sandwich layer has been reported by Lee *et al.*[10]

Morphological studies

Surface morphology of the stacked multilayer was investigated by FE-SEM and AFM, and the results are presented in Fig. 2a and b. Both images suggest the formation of relatively flat films with randomly distributed islands of typical nanometer dimension. The size distribution of islands from FE-SEM image was analyzed using particle fitting tool of ImageJ[22] (assuming circular shape of islands on the surface) and the radius of islands was determined to be in a range from 5 nm to 60 nm with an average radius of about 20 nm.

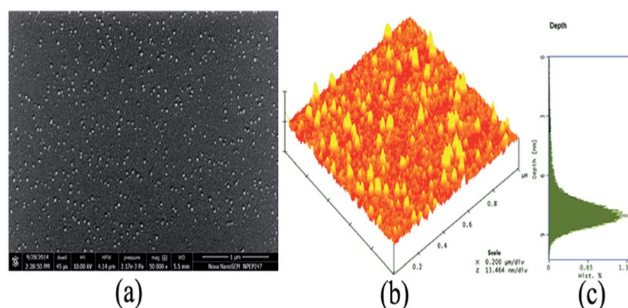

Fig. 2 (a) SEM image exhibiting a flat topology of stacked multilayer (b) AFM image showing the surface topology of sandwich layer along with (c) depth histogram.

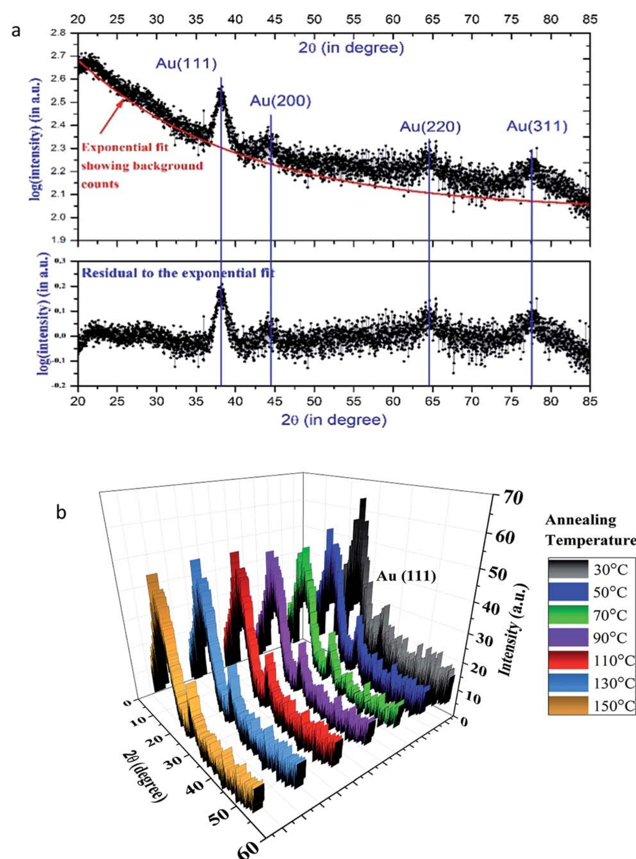

Fig. 1 (a) X-ray diffraction pattern of as-deposited SnO_x/Au/SnO_x staked multilayer. (b) X-ray diffraction pattern showing amorphous nature of stacked multilayers at different annealing temperatures.

Fig. 2b and c shows the AFM image of multilayer (Fig. 2b) and the depth–distribution curve (Fig. 2c) which exhibits a maximum depth of around 7.5 nm and a maximum height of 11.64 nm when analyzed with Nanoscope™ version-5.31R1. The average particle size distribution was also employed on 2D AFM scan assuming spherical particles on the film surface. This analysis showed that these particles have radius ranging from 5 nm to 60 nm with a mean radius of about 28 nm which is consistent with results from FE-SEM analysis.[22]

The root-mean-square roughness of the stacked multilayer has been also calculated and found to be 1.184 nm. The small roughness is a necessary requirement for such stacked multi-layered film for their use as substrate for optoelectronic applications.[15]

The estimation of Au has also been performed using energy dispersive X-ray spectroscopy (EDS) and is given under ESI (see Fig. S1† with Si and S2† after ignoring Si). The tables showing the relative contents of elements are also appended as Tables S1 and S2† which suggest the purity of the staked multilayer. Since the oxygen content cannot be quantified with the EDS (both substrate $-SiO_2$ and specimen layer SnO_2 contain oxygen), therefore a correct estimation of Au is not concluded using EDS.

XAS and XES studies

The O K-edge XAS spectra of the stacked TCO multilayer were measured in both surface-sensitive TEY and bulk-sensitive TFY modes. Comparison of their characteristic features to those of SnO and SnO_2 powder reference samples (Fig. 3a) shows the surface region to be SnO, with additional spectral features evident from the TFY. This is further verified by the Sn M_{45}-edge TEY spectra (Fig. 3b) which are consistent with the O K-edge spectra showing a SnO-rich phase at the surface. Spectral features observed in the low energy regions of the O K-edge XAS in Fig. 3a are generated due to excitation from the O 1s core level

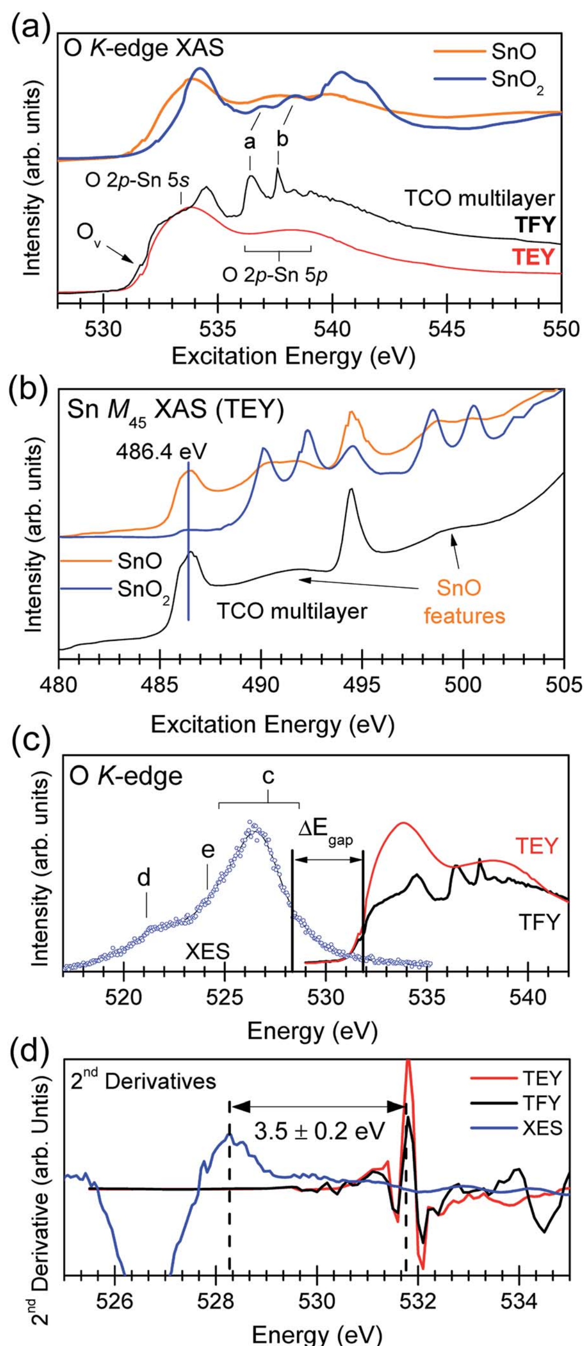

Fig. 3 (a) O K-edge X-ray absorption spectra of SnO and SnO_2 reference samples along with the stacked TCO multilayer measured in TEY/TFY modes. (b) Sn M-edge spectra for the TCO multilayer compared to references, and (c) XES and XAS of the O K-edge where XES displays a valence band line shape indicating SnO. (d) The magnitude of the band gap energy determined using second derivatives comes out to be 3.5 ± 0.2 eV.

into primarily O 2p-Sn 5s hybridized states,[24] which form the bottom of the conduction band. The second region at higher energies is composed mainly of O 2p-Sn 5p hybridized states in SnO and SnO_2.[24–26] The spectral peaks in the TFY spectrum of the TCO multilayer can be compared to XAS results of SnO_2 films deposited by atomic layer deposition (ALD) from Choi *et al.*[25] The line shape of the O 2p-Sn 5s peak at 534.5 eV and the energy splitting between this peak and the first peak in the O 2p-Sn 5p series (~2 eV), agrees with XAS of ALD films exhibiting an amorphous SnO_2 crystal structure.[25]

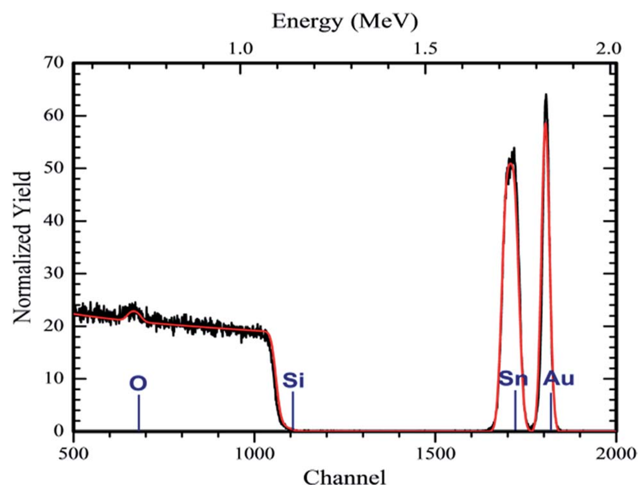

Fig. 4 RBS spectrum along with fitted profile of the stacked multilayer. The peaks assigned for Sn and Au are seen at higher channels and Si and O are seen at lower channels.

The peak at 534.5 eV in the TCO multilayer also indicates SnO_2 by its energy location. Similarly the first two sharper peaks a and b have similar energy splitting to the corresponding peaks in the SnO_2 reference sample (~1.2 eV). These details together indicate a dominant phase of SnO with small amount of SnO_2 below the surface that is amorphous in nature. The TCO multilayer structure including Au in a sandwich structure may also promote overlap between O-2p and Au-5d6s orbitals and increase the density of conduction band states. This overlap may contribute to the increased intensity of higher energy features in the range of 535–540 eV.[20]

A low energy shoulder feature under the bottom of the conduction band at 531.5 eV in TEY and TFY labeled as O_V is not typical of SnO or SnO_2 thin films or powders,[23–26] and may be due to the presence of oxygen vacancies. In the SnO/SnO_2 lattice of the TCO multilayer, oxygen vacancies introduced during the fabrication process could contribute to increased charge carrier transport and therefore conductivity by providing additional electronic states near the conduction band edge.

Non-resonant X-ray emission was also taken at the O K-edge to probe the density of valence band states, shown in Fig. 3c. Open blue circles show the raw XES spectrum overlaid with a smoothed line using 10 point FFT smoothing, which is used for the second derivative. From McLeod *et al.*,[24] the contribution of Sn 5d states to the top valence band is much greater for the $5s^0$ oxides (SnO_2) than the $5s^2$ oxides (SnO). In $5s^0$ oxides the top of the valence band is dominated by a sharp distribution of O 2p states strongly hybridized with these Sn 5d states, extending ~2.5 eV into the valence band from the Fermi level.[24] In $5s^2$ oxides, specifically SnO, a hybridization occurs between O 2p and Sn 5s states at the valence band edge, while the top and middle of the valence band are largely dominated by O 2p

 This journal is © The Royal Society of Chemistry 2016

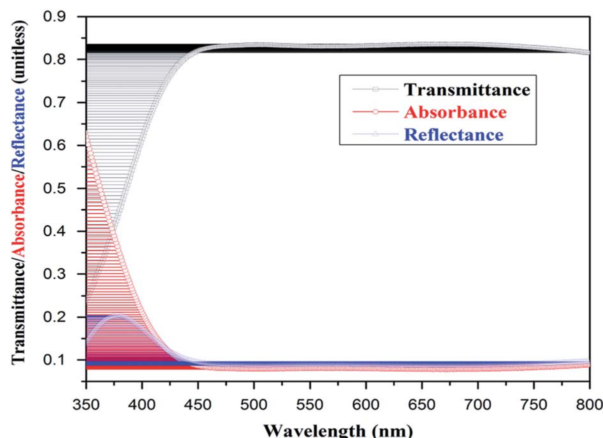

Fig. 5 UV-vis curve showing transmittance, absorbance and reflectance for stacked multilayer.

states. By contrast to SnO_2, the top of valence band of SnO exhibits a much broader distribution of states extending across ~5 eV.[24] The XES of the TCO multilayer shows a broad distribution of states near the top of the valence band (region c in Fig. 3d), indicating an SnO structure. From further comparison to experimental measurements in ref. 24, near the middle of the valence band in the region labeled e an additional peak may be resolved in pure SnO that arises from O 2p-Sn 5s states. The broadening of this feature such that it cannot be resolved as in the case of the TCO multilayer shows disorder in the SnO lattice due to the amorphous SnO/SnO_2 phase. A similar smearing of valence band features d and e has been observed for SnO_2 thin films below 220 nm in thickness, and was attributed to oxygen vacancies in that films.[26]

The band gap in SnO/SnO_2 can be determined from O K-edge measurements plotted on a common energy scale as in Fig. 3c.[24,25] When the second derivative is plotted the distance between the highest-energy peak of the XES derivative and the lowest-energy peak of the XAS derivative is taken to be the band gap energy splitting. This method provides a quantitative measurement of band gap energy without use of line fitting to the valence and conduction band edges. The second derivatives for O K-edge XES and XAS of the TCO multilayer are shown in Fig. 3d, and give the TCO multilayer band gap to be 3.5 eV ± 0.2 eV, which is larger than the reported band gap range of 2.5–3.0 eV for SnO.[23,27] This result is significant because it indicates that even though the films contain proportionally more SnO compared to SnO_2, the band gap matches more closely to that of SnO_2 (3.6 eV).[23] The SnO band structure and band gap energy are altered by the presence of a mixed phase with amorphous SnO_2 and oxygen vacancies in a way that may be advantageous for device applications. A large band gap energy commonly results in higher transmittance in the visible range, while a metal rich SnO/SnO_2 phase may serve to lower resistivity of the TCO multilayer compared to pure metal oxide films.

RBS study

Fig. 4 shows the RBS spectrum and RUMP-fitted profile of the stacked multilayer.[28] This spectrum indicates the distinct elemental peaks associated with Sn, O, Au and Si. The thickness of structure is calculated with the help of this fitted profile. The estimated values are SnO_x (35 nm)/Au (5.2 nm)/SnO_x (35 nm) with composition of SnO_x layer as: 0.575 of O and 0.425 of Sn. This suggests the formation of SnO (which is consistent with results from the XAS investigations) with pure Au in the sandwich layer.

UV-vis and Raman spectroscopy

The optical properties of the stacked multilayer recorded from a UV-vis spectrophotometer are presented in Fig. 5 exhibiting nearly constant values for transmittance, absorbance and reflectance beyond 475 nm of incoming radiation (0.83, 0.08 and 0.09, respectively). The typical value of transparency for a commercially available ITO slide from Sigma-Aldrich (Product Number: 703184, CAS Number: 50926-11-9) is 0.84 (surface resistivity 30–60 Ω $sq.^{-1}$ and refractive index 1.517) which is quite near to the value obtained from this stacked multilayer. This transmittance value is better as compared to other reports for SnO on quartz substrates by Liang *et al.*,[16] the ITO, ITO/Au/

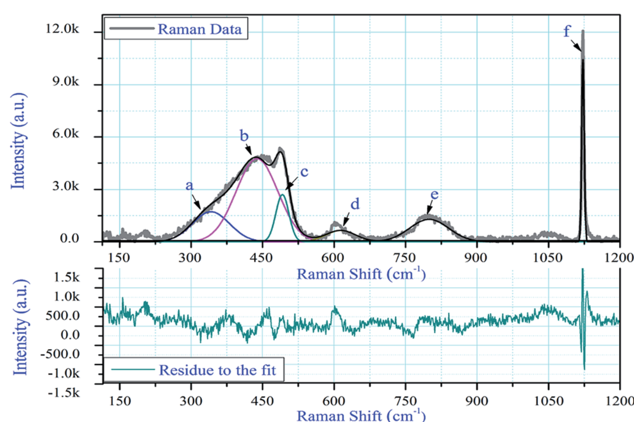

Fig. 6 Raman spectrum of stacked multilayer.

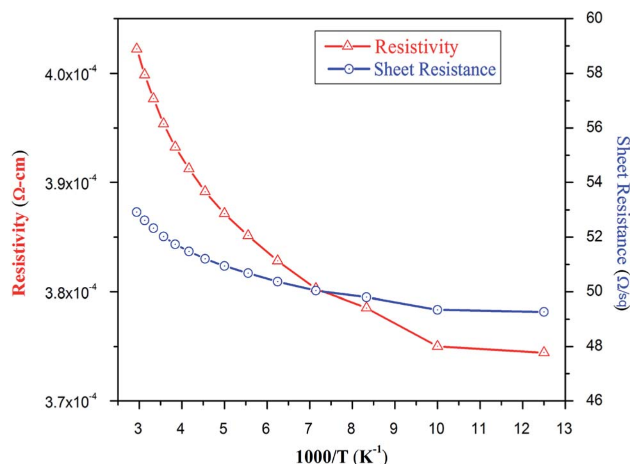

Fig. 7 Electrical resistivity and sheet resistance as a function of reciprocal temperature.

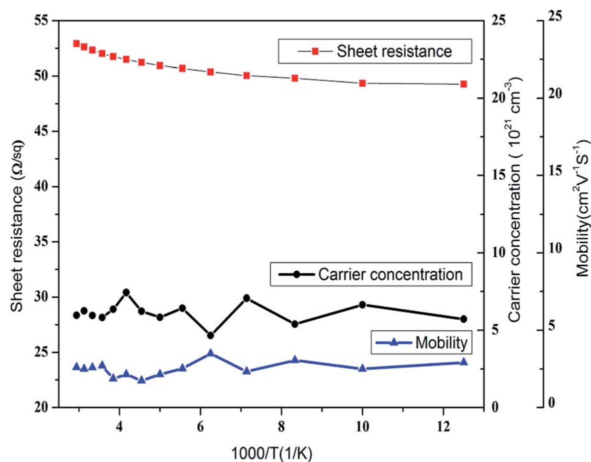

Fig. 8 Sheet resistance, carrier concentration and mobility as a function of reciprocal temperature.

ITO and ITO/Cu/ITO on polycarbonate substrates reported by Lee *et al.*[10] and Au-embedded F-doped SnO_2 on glass substrates reported by Chew *et al.*[29] Higher transmittance and lower absorbance/reflectance are desirable properties for prospective use of these stacked multilayers as TCOs. Coating the metal film with a dielectric layer of higher refractive index is known to increase transmittance of the metal film with the dielectric layer acting as an antireflection film. Thin layer of polymer nano composite coated on metal as dielectric has been used to minimize the reflection of gold film increasing the optical properties of the system.[30] Hence enhanced optical properties of proposed dielectric metal dielectric (DMD) structure in the entire visible region are a result of having metal oxide layers on both sides of Au metal layer.

The Raman spectrum corresponding to stacked multilayer is shown in Fig. 6 (bold grey line) which includes multiple peaks deconvoluted from the Raman spectrum showing contribution from the transitions corresponding to vibrational levels. SnO_2 unit cell exhibits a total of 18 branches for the vibrational modes in first brillouin zone which results in four Raman active modes (A_{1g}, B_{1g}, B_{2g} and E_g).[31] The bottom curve in Fig. 6 shows the residue to the fit. The peak structure is broad which is indicative of the formation of crystallites of very small size. The Raman shifts at 437 and 787 cm^{-1} (refer peaks b and e in Fig. 6) pertain to the characteristics E_g and B_{2g} modes of SnO_2.[32,33] All the other peaks (a, c, d and f) belong to the characteristic peaks of SiO_2 (ref. 34) originating due to quartz substrate. The major contribution in the Raman spectrum is from the quartz substrate which is due to small thickness and high transparency of the film.

Low temperature Hall study

Low temperature Hall effect and electrical resistivity measurements were carried out using van der Pauw configuration. The variation of resistivity and sheet resistance for the temperature range of 80–340 K is presented in Fig. 7.

The room temperature resistivity and sheet resistance for this stacked multilayer were 3.9×10^{-4} Ω cm and 52 Ω $sq.^{-1}$, respectively. This value of sheet resistance is comparable to that of commercial ITO slide from Sigma-Aldrich (Product Number: 703184, CAS Number: 50926-11-9). The resistivity values for $SnO_x/Au/SnO_x$ specimen are lower than that for ITO films (31.2×10^{-4} Ω cm) reported by Lee *et al.*[10] and slightly higher to ITO/Au/ITO and ITO/Cu/ITO structures showing resistivity of 0.56×10^{-4} Ω cm and 1.51×10^{-4} Ω cm, respectively.[10]

The conduction mechanisms of these stacked structures may be explained by considering a thin continuous layer of metal (Au) embedded between two oxide layers thereby forming a DMD structure. The total resistance of this coplanar configuration is generally given by: $1/R_{\text{total}} = 1/R_{\text{metal}} + 2/R_{\text{oxide}}$ with $R_{\text{oxide}} \approx 1000R_{\text{metal}}$, so the $R_{\text{total}} \approx R_{\text{metal}}$. Therefore the conductivity is primarily due to embedded metal film and solely responsible for exhibiting such low values of resistivity as compared to single layer TCO. Moreover a critical thickness of the film is required to provide a continuous path for conduction of electron.[10,35,36] The room temperature resistivity and sheet resistance values for the staked multi layered structure are indicating a continuous metal inter layer.

Furthermore, the increase of both resistivity and sheet resistance with temperature is a typical characteristic of a degenerate semiconductor.[37] This behavior is resultant of increased concentration of metallic dopant which translates the semiconducting nature into metallic. There are numerous reports that support this argument in the literature *e.g.* Kim *et al.* for ITO films,[37] n-type ZnO doped with Ga,[38] Sb-doped p-type ZnO,[39] highly B-doped ZnO films.[40] In the present system, increased resistivity and sheet resistance with increasing temperature can be attributed to effect of self-doping. The conclusions from XAS/XES and RBS investigations are indicative of formation of metal rich phase which would have produced the degenerate states thereby exhibiting a metal like behavior (Fig. 8).

In addition to this, it is interesting to observe very high conductivity and low sheet resistance even at very low temperature. The stacked multilayer was shown to exhibit the values for resistivity and sheet resistance as 3.7×10^{-4} Ω cm and 49 Ω $sq.^{-1}$ at 80 K, respectively with a very small variation in both of these quantities up to 340 K ($\delta\rho = 0.2 \times 10^{-4}$ Ω cm and $\delta R_S = 2.7$ Ω $sq.^{-1}$).

Conclusions

The stacked multilayered $SnO_x/Au/SnO_x$ structure was deposited on quartz substrate using e-beam evaporation method for SnO_x and thermal evaporation method for Au layer to investigate its application as TCO. The XRD studies show an amorphous structure of the multilayer with AFM and SEM suggesting low roughness and flat morphology, respectively favoring the growth of further layers for technological applications. Both RBS and XAS investigations suggest formation of primarily SnO with evidence of a mixed phase containing SnO_2. Analysis of the spectral features in XAS and XES measurements confirms the presence of a mixed SnO/SnO_2 phase. Amorphous SnO_2 within the SnO layer disrupts the SnO lattice and alters the electronic band structure. Combining XAS and XES measurements reveals a wide band gap energy (3.5 ± 0.2 eV), suitable for applications requiring high transparency in the visible range. Oxygen

 This journal is © The Royal Society of Chemistry 2016

deficiency in SnO_x is indicated by RBS, and XAS confirms the presence of oxygen vacancies that can contribute to lower resistivity. The TCO characteristics resulting from the stacked multilayer were exhibiting high transparency (83% beyond 475 nm), low sheet resistance (52 Ω sq.$^{-1}$) and low resistivity (3.9×10^{-4} Ω cm) which are comparable to that of standard ITO substrates. The increase in room temperature resistivity and sheet resistance with temperature is also suggesting metallic behavior which is attributed to the metal rich nature of the stacked multilayer. Such a multilayered structure with enhanced optical and electrical properties is proposed as a better replacement of the standard ITO substrates for opto-electronic applications.

Acknowledgements

The authors (V. S, R. V and K. S) are thankful for the research facilities provided by Inter University Accelerator Centre (IUAC), New Delhi (INDIA), Materials Research Centre (MRC) at MNIT Jaipur (INDIA), Wide Band Gap Semiconductor Lab at IIT-New Delhi and Canadian Light Source (CLS) at Saskatoon (CANADA). G. S. Chang acknowledges support from the Natural Sciences and Engineering Research Council of Canada (NSERC) and Canada Foundation for Innovation (CFI).

References

1 M. Nistor, E. Millon, C. Cachoncinlle, W. Seiler, N. Jedrecy, C. Hebert and J. Perrière, *J. Phys. D: Appl. Phys.*, 2015, **48**, 195103.
2 W. Cao, Y. Zheng, Z. Li, E. Wrzesniewski, W. T. Hammond and J. Xue, *Org. Electron.*, 2012, **13**, 2221–2228.
3 T. Qiu, B. Luo, M. Liang, J. Ning, B. Wang, X. Li and L. Zhi, *Carbon*, 2015, **81**, 232–238.
4 K. Zilberberg, F. Gasse, R. Pagui, A. Polywka, A. Behrendt, S. Trost, R. Heiderhoff, P. Görrn and T. Riedl, *Adv. Funct. Mater.*, 2014, **24**, 1671–1678.
5 H. Han, N. D. Theodore and T. L. Alford, *J. Appl. Phys.*, 2008, **103**, 013708.
6 J. Bellingham, W. Phillips and C. Adkins, *J. Mater. Sci. Lett.*, 1992, **11**, 263–265.
7 M. Chen, Z. Pei, X. Wang, Y. Yu, X. Liu, C. Sun and L. Wen, *J. Phys. D: Appl. Phys.*, 2000, **33**, 2538.
8 K. Ellmer, *Nat. Photonics*, 2012, **6**, 809–817.
9 A. Indluru and T. L. Alford, *J. Appl. Phys.*, 2009, **105**, 123528.
10 J. Y. Lee, J. W. Yang, J. H. Chae, J. H. Park, J. I. Choi, H. J. Park and D. Kim, *Opt. Commun.*, 2009, **282**, 2362–2366.
11 S. Bansal, D. K. Pandya and S. C. Kashyap, *Appl. Phys. Lett.*, 2014, **104**, 082108.
12 J. Dominguez, L. Fu and X. Pan, *Appl. Phys. Lett.*, 2001, **79**, 614–616.
13 A. Bou, P. Torchio, D. Barakel, F. Thierry, A. Sangar, P. Y. Thoulon and M. Ricci, *J. Appl. Phys.*, 2014, **116**, 023105.
14 S. Yu, C. Jia, H. Zheng, L. Ding and W. Zhang, *Mater. Lett.*, 2012, **85**, 68–70.
15 Z. R. Li and H. Meng, *Organic Light-Emitting Materials and Devices*, CRC, Boca Raton, 2007.
16 L. Y. Liang, Z. M. Liu, H. T. Cao and X. Q. Pan, *ACS Appl. Mater. Interfaces*, 2010, **2**, 1060–1065.
17 Y. H. Tak, K. B. Kim, H. G. Park, K. H. Lee and J. R. Lee, *Thin Solid Films*, 2002, **411**, 12–16.
18 C. X. Kronawitter, M. Kapilashrami, J. R. Bakke, S. F. Bent, C. H. Chuang, W. F. Pong, J. Guo, L. Vayssieres and S. S. Mao, *Phys. Rev. B: Condens. Matter Mater. Phys.*, 2012, **85**, 125109.
19 K. G. Godinho, A. Walsh and G. W. Watson, *J. Phys. Chem. C*, 2008, **113**, 439–448.
20 D. Y. Cho, S. I. Na, K. B. Chung and H. K. Kim, *Appl. Surf. Sci.*, 2015, **347**, 88–95.
21 M. Kapilashrami, C. X. Kronawitter, T. Törndahl, J. Lindahl, A. Hultqvist, W. C. Wang, C. L. Chang and S. S. Mao, *Phys. Chem. Chem. Phys.*, 2012, **14**, 10154–10159.
22 C. A. Schneider, W. S. Rasband and K. W. Eliceiri, *Nat. Methods*, 2012, **9**, 671–675.
23 C. McGuinness, C. B. Stagarescu, P. J. Ryan, J. E. Downes, D. Fu, K. E. Smith and R. G. Egdell, *Phys. Rev. B: Condens. Matter Mater. Phys.*, 2003, **68**, 165104.
24 J. A. McLeod, N. A. Skorikov, L. D. Finkelstein, E. Z. Kurmaev and A. Moewes, *J. Phys. Chem. C*, 2012, **116**, 24248–24254.
25 D. Choi, W. J. Maeng and J.-S. Park, *Appl. Surf. Sci.*, 2014, **313**, 585–590.
26 G. S. Chang, J. Forrest, E. Z. Kurmaev, A. N. Morozovska, M. D. Glinchuk, J. A. McLeod, A. Moewes, T. P. Surkova and N. H. Hong, *Phys. Rev. B: Condens. Matter Mater. Phys.*, 2012, **85**, 165319.
27 S. Das and V. Jayaraman, *Prog. Mater. Sci.*, 2014, **66**, 112–255.
28 L. R. Doolittle, *Nucl. Instrum. Methods Phys. Res., Sect. B*, 1985, **9**, 344–351.
29 C. K. Chew, C. Salcianu, P. Bishop, C. J. Carmalt and I. P. Parkin, *J. Mater. Chem. C*, 2015, **3**, 1118–1125.
30 M. Elbahri, M. K. Hedayati, V. S. K. Chakravadhanula, M. Jamali, T. Strunkus, V. Zaporojtchenko and F. Faupel, *Adv. Mater.*, 2011, **23**, 1993–1997.
31 A. Dieguez, A. Romano-Rodrıguez, A. Vila and J. R. Morante, *J. Appl. Phys.*, 2001, **90**, 1550–1557.
32 E. Fazio, F. Neri, S. Savasta, S. Spadaro and S. Trusso, *Phys. Rev. B*, 2012, **85**, 195423.
33 Q.-H. Wu, J. Song and J. Li, *Surf. Interface Anal.*, 2008, **40**, 1488–1492.
34 T. F. Cooney, E. R. D. Scott, A. N. Krot, S. K. Sharma and A. Yamaguchi, *Am. Mineral.*, 1999, **84**, 1569–1576.
35 Z. Xue, X. Liu, N. Zang, H. Chen, X. Zheng, H. Wang and X. Guo, *ACS Appl. Mater. Interfaces*, 2014, **6**, 16403–16408.
36 K. Sivaramakrishnan, N. D. Theodore, J. F. Moulder and T. L. Alford, *J. Appl. Phys.*, 2009, **106**(63510), 1–8.
37 H. Kim, C. M. Gilmore, A. Piquã̌, J. S. Horwitz, H. Mattoussi, H. Murata, Z. H. Kafafi and D. B. Chrisey, *J. Appl. Phys.*, 1999, **86**, 6451–6461.
38 M. Joseph, H. Tabata, H. Saeki, K. Ueda and T. Kawai, *Phys. B*, 2001, **302**, 140–148.
39 F. X. Xiu, Z. Yang, L. J. Mandalapu, D. T. Zhao, J. L. Liu and W. P. Beyermann, *Appl. Phys. Lett.*, 2005, **87**, 152101.
40 S. Y. Myong, J. Steinhauser, R. Schlüchter, S. Faÿ, E. Vallat-Sauvain, A. Shah, C. Ballif and A. Rüfenacht, *Sol. Energy Mater. Sol. Cells*, 2007, **91**, 1269–1274.

This journal is © The Royal Society of Chemistry 2016

Nuclear Instruments and Methods in Physics Research B 379 (2016) 141–145

Contents lists available at ScienceDirect

Nuclear Instruments and Methods in Physics Research B

journal homepage: www.elsevier.com/locate/nimb

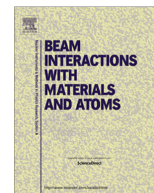

A study on 100 MeV O^{7+} irradiated SnO_2/Ag/SnO_2 multilayer as transparent electrode for flat panel display application

Vikas Sharma [a], Satyavir Singh [a,*], K. Asokan [c], Kanupriya Sachdev [a,b]

[a] *Department of Physics, Malaviya National Institute of Technology, Jaipur 302017, India*
[b] *Materials Research Centre, Malaviya National Institute of Technology, Jaipur 302017 India*
[c] *Inter-University Accelerator Centre, Aruna Asaf Ali Road, New Delhi 110067, India*

A R T I C L E I N F O

Article history:
Received 12 November 2015
Received in revised form 28 April 2016
Accepted 28 April 2016
Available online 4 May 2016

Keywords:
Transparent electrode
Irradiation
Multilayer

A B S T R A C T

The multilayer thin films of SnO_2/Ag/SnO_2 were deposited using electron-beam and thermal evaporation for flat panel display application. The as-prepared SnO_2/Ag/SnO_2 specimen was irradiated with 100 MeV O^{7+} ions by varying the fluences 1×10^{12} and 5×10^{12} ions/cm^2. The pristine and irradiated films were investigated using XRD, SEM, AFM and Raman to find out modification in the structure and surface morphology of the films. UV–Vis and Hall measurement techniques were used to investigate the optical and electrical properties respectively. It was observed that the roughness of the film after irradiation (for the fluence of 1×10^{12} ions/cm^2) decreased to 0.68 nm from 1.6 nm and showed an increase in roughness to 1.35 nm on increasing the fluence to 5×10^{12} ions/cm^2. This oxide/metal/oxide structure fulfills the basic requirements of a TCE, like high-transmittance >75% for pristine and >80% for the fluence of 1×10^{12} ions/cm^2 over a broad spectrum of visible light for practical applications. The multilayer structure shows change in the electrical resistivity from 1.6×10^{-3} Ω cm to 6.3×10^{-3} Ω cm after irradiation.
© 2016 Elsevier B.V. All rights reserved.

1. Introduction

Transparent electrode is one of the key components in organic photovoltaic (OPV), touch screen and flat panel display devices and hence significant work is being carried upon in this area globally [1]. ITO thin film coated glass is the most commonly used transparent electrode, but the scarcity of Indium (In) reflected in its price variation has resulted in a search for its alternatives for transparent conducting electrode (TCE) applications. Tin oxide is one of the prominent choices due to its wide band gap and ease of fabrication. Metals or metal nanowires are also some of the alternatives investigated for this purpose. Silver film due to its good conductivity can act as a TCE if its thickness is kept below a certain critical thickness to ensure moderate transparency [2]. In recent years a multilayer structure of oxide/metal/oxide has emerged as a prominent candidate for electrode applications in touch screen or flat panel devices [3] due to its distinct advantages. Such multilayer structures with different metal oxides and metals viz., TiO_2/Ag/TiO_2 [4], MgO/Ag/MgO [5], ZnO/Ag/ZnO [6] and AZO/Ag/AZO [7] have been synthesized and investigated for their application in energy conversion and display devices. These multilayer structures are more efficient as compared to single layer TCO [3]. A transparency of ∼80% in the visible region and a sheet resistance of 150–450 Ω/□ is sufficient for touch screen or flat panel display electrode applications.

Swift Heavy Ion (SHI) irradiation is a unique tool to investigate the interaction of heavy energetic ions with material and to introduce defects and modify the properties of the material. It can degrade or enhance the properties of the materials depending on type, mass and energy of ion and the interacting material state, structure and fabrication parameters [8]. When SHI interacts with material, the energy is dissipated through two ways (i) nuclear energy loss (S_n): the ion energy is directly transferred to the host atom, and (ii) electronic energy loss (S_e): electronic excitation of host atom by inelastic collisions. The deposition of localized energy is high within a confined volume, resulting in a non equilibrium state [9]. The ion passes through the thin film without being deposited because the range of SHI is few microns and these films are tens of nanometers thick.

TCE being a key component in flat panel device plays an important role in its efficiency. The optical and electrical properties of TCE have a significant effect on the working of device because light has to pass through the TCE [10,11]. However, there are very few studies on the SHI irradiation effect on TCE [12,13]. The energy loss of SHI irradiation is of the order of keV/nm, which occurs in several hundreds of picoseconds, localized in a cylinder of ∼10 nm diameter giving rise to very high ∼0.1 eV/atom excitation yield of

* Corresponding author.
E-mail address: satyavir84@gmail.com (S. Singh).

http://dx.doi.org/10.1016/j.nimb.2016.04.059
0168-583X/© 2016 Elsevier B.V. All rights reserved.

electrons [14]. These extreme conditions initiate non-equilibrium processes and may modify the crystal structures, thus modifying their structural, electrical and optical properties. SHI effects on thin film of tin oxide [15–19] and metal doped metal oxides [20,21] have been studied with different ions and energies. In the present work, the effect of SHI irradiation of 100 MeV O^{7+} ions on SnO_2/Ag/SnO_2 multilayer on glass substrate for its application as transparent electrode was investigated. To the best of our knowledge there is no study on the effect of SHI irradiation on a multilayer metal oxide/metal/metal oxide structure.

2. Experimental details

SnO_2/Ag/SnO_2 multilayer thin film was fabricated with a total thickness of 60 nm on Si and glass substrates. All these substrates were thoroughly cleaned by standard methods [22]. E-beam evaporation was used to deposit the bottom and uppermost layers of SnO_2 using SnO_2 pallet and the deposition was done at room temperature. The ~6 nm Ag middle layer was deposited by thermal evaporation using silver foil. Vacuum of 5.5×10^{-6} mbar was maintained during the depositions. The as deposited sample was irradiated with 100 MeV O^{7+} ions with two different fluences 1×10^{12} and 5×10^{12} ions/cm^2 using the pelletron facility at Inter University Accelerator Centre, New Delhi. X-ray diffraction (XRD) and Raman spectroscopy were used for structural investigations. The XRD of the structure is taken using solar slit in thin film mode (shown by grey color with high noise) on Panalytical X- Pert Pro. The morphology of the samples was studied by field emission scanning electron microscopy (FESEM) and atomic force microscopy (AFM). FESEM Nona Nano 450 was used to study the surface morphology of the SnO_2/Ag/SnO_2 multilayer thin film. The Raman spectra of stacked multilayer deposited on Si substrates were recorded with 532 nm laser from solid state laser. The transmission and absorbance spectra for the SnO_2/Ag/SnO_2 multilayer were taken using UV–Vis spectrophotometer (Perkin Elmer Lambda 750). Hall measurement setup HMS 3000 (Ecopia) was used to investigate the electrical properties of the samples.

3. Results and discussion

3.1. XRD measurements

Fig. 1 shows the XRD patterns of the pristine and irradiated films. The XRD patterns of both pristine and irradiated films exhibit amorphous nature. The amorphous nature of the diffraction pattern is attributed to very less thickness of the staked multilayer which reduces the number of diffraction planes in the path of the incoming collimated X-rays. Another possible reason for the amorphous nature of the films is related to the fact that deposition was carried out at room temperature. The less crystalline or nearly amorphous nature of the film is good for fabrication of these films on a plastic substrate [23].

3.2. RBS measurements

RBS spectrum and SIMNRA-fitted profile of the stacked multilayer SnO_2/Ag/SnO_2 film are shown in Fig. 2. RBS spectra confirms the existence of elements Sn, O, Ag and Si. Thickness of the film was estimated by fitting the data using SIMNRA software. The thickness values were found to be SnO_2 (30 nm)/Ag (6 nm)/SnO_2 (25 nm).

3.3. Raman spectroscopy

In the bulk SnO_2, six unit cell atoms generate different vibrational modes including IR active and Raman active. Fig. 3 shows the Raman spectra of pristine and SHI irradiated multilayer structure. The pristine and irradiated samples show one IR active mode at 300 (e_u) cm^{-1} and two Raman active modes at 425 and 620 (e_u) cm^{-1} [24]. These IR and Raman modes show the growth of as-deposited and irradiated multilayer. The shift observed in these modes from their actual peak positions is attributed to the strain present in the multilayer structure. It is noticed that the intensity of the Raman peaks increases with the fluence [25].

3.4. Surface characterization

Fig. 4(a) shows FESEM images of the pristine and irradiated films. These films exhibit a uniform and smooth surface. Fig. 4(b) shows the AFM images of SnO_2/Ag/SnO_2 pristine and irradiated films at the fluence of 1×10^{12} and 5×10^{12} ions/cm^2. The scan area of the films was kept 2×2 μm^2. The effect of SHI irradiation on the surface roughness was investigated. The figures clearly depict the modification in roughness of the films upon irradiation. The root mean square roughness of the pristine sample was 1.6 nm which decreased to 0.68 nm for 1×10^{12} ions/cm^2 fluence. The 100 MeV O^{7+} ion irradiation causes erosion of surface microstructures and hence average height of the microstructures reduced.

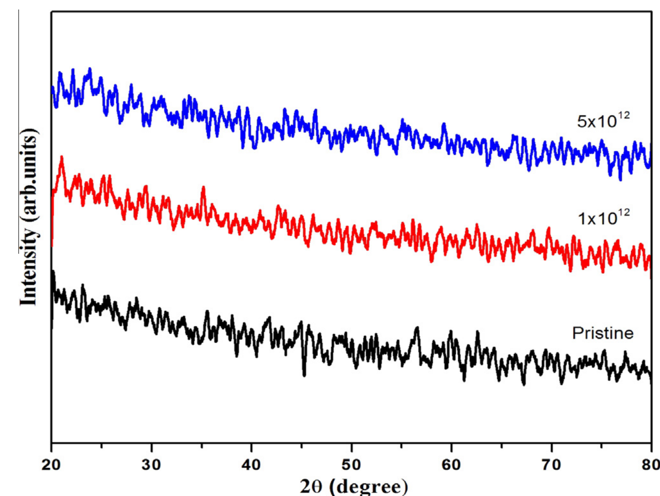

Fig. 1. XRD pattern of SnO_2/Ag/SnO_2 pristine and irradiated films.

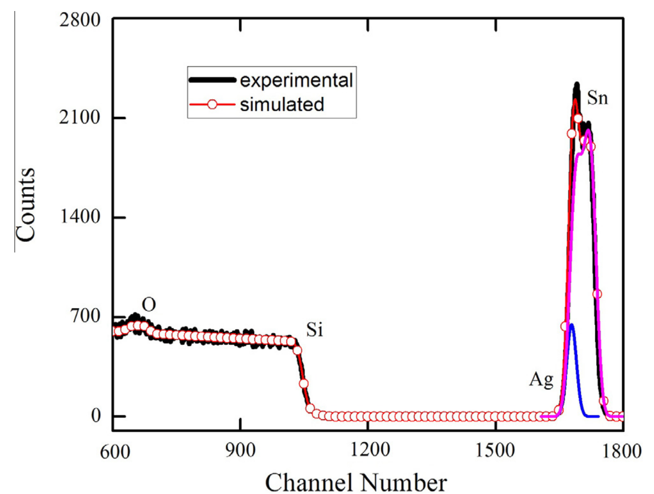

Fig. 2. RBS spectrum of SnO_2/Ag/SnO_2 film with fitted profile.

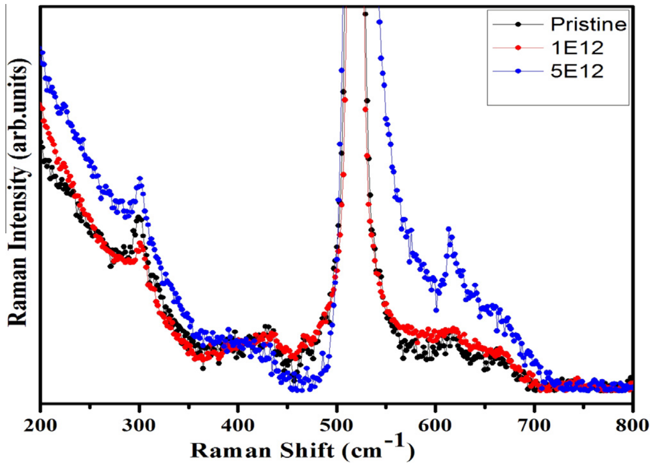

Fig. 3. Raman spectra of SnO_2/Ag/SnO_2 pristine and irradiated films.

Further it increased to 1.35 nm on increasing the fluence to 5×10^{12} ions/cm^2, which is below the RMS roughness value for the pristine sample. These results of surface roughness are in agreement with results reported by Aditya et al. [19] on O ion irradiated SnO_2 thin film. Abhirami et al. [15] have reported a different result for roughness for the single layer tin oxide film using 120 MeV Ag^{9+} ions. The obtained roughness (R_q) is suitable for these thin films to be used as TCO in flat panel display and touch screens [26].

3.5. UV–Visible spectroscopy

Fig. 5 shows the transmitance and absorbance spectra of these films in the wavelength range of 400–800 nm. The pristine sample was observed to have ~75% transmittance at 550 nm and the transmittance value exhibits a decreasing trend for increase in wavelength. The sample irradiated with fluence 5×10^{12} ion/cm^2 shows a transmittance (excluding the substrate effect) of above 78% as compared to pristine multilayer and transmittance increases with wavelength. Highest average transmittance of >80% over the visible light spectrum is shown by the sample irradiated with the lower fluence of 1×10^{12} ion/cm^2.

The possible reason for increase in transparency with irradiation could be reduction of the surface roughness with irradiation leading to less absorption. Also there is a possibility of formation of AgO in the ion tracks as O atoms released from metal oxide could combine with Ag atoms forming silver oxide. The reduction in transmittance at higher fluence may take place due to scattering from the metal atoms sputtered from the metal layer and distributed in the oxide layer. The transmittance values support the candidature of staked multilayer films as electrode in touch screen and flat panel display applications. The optical bandgap of trilayered structure was calculated using Tauc's equation by plotting $(\alpha h\upsilon)^2$ v/s energy ($h\upsilon$) as shown in Fig. 6 [27]. The calculated bandgap energy of the multilayer was found to be ~2.91 eV for pristine film which is lower than the bandgap energy of bulk or single layer SnO_2 [28] and close to the reported value of SnO (2.5–3.0 eV) [29]. The calculated band gap is optical but the amorphous nature of thin film may not allow the proper estimation of band gap as the absorption edge is sharper (near to exact). There are few reports which claim SnO_2 having a direct bandgap energy of 4.0 eV and indirect bandgap of 2.6 eV [30]. In a similar manner, these amorphous thin film exhibits lower band gap with respect to the standard value and shows high transparency because of its highly thin nature. Generally this method, which is however a crude one, is applicable for single layer but there have been reports about using the same method to determine the band gap for multilayers [31,32] also. The formation of oxide layer i.e. SnO_x (exhibiting the

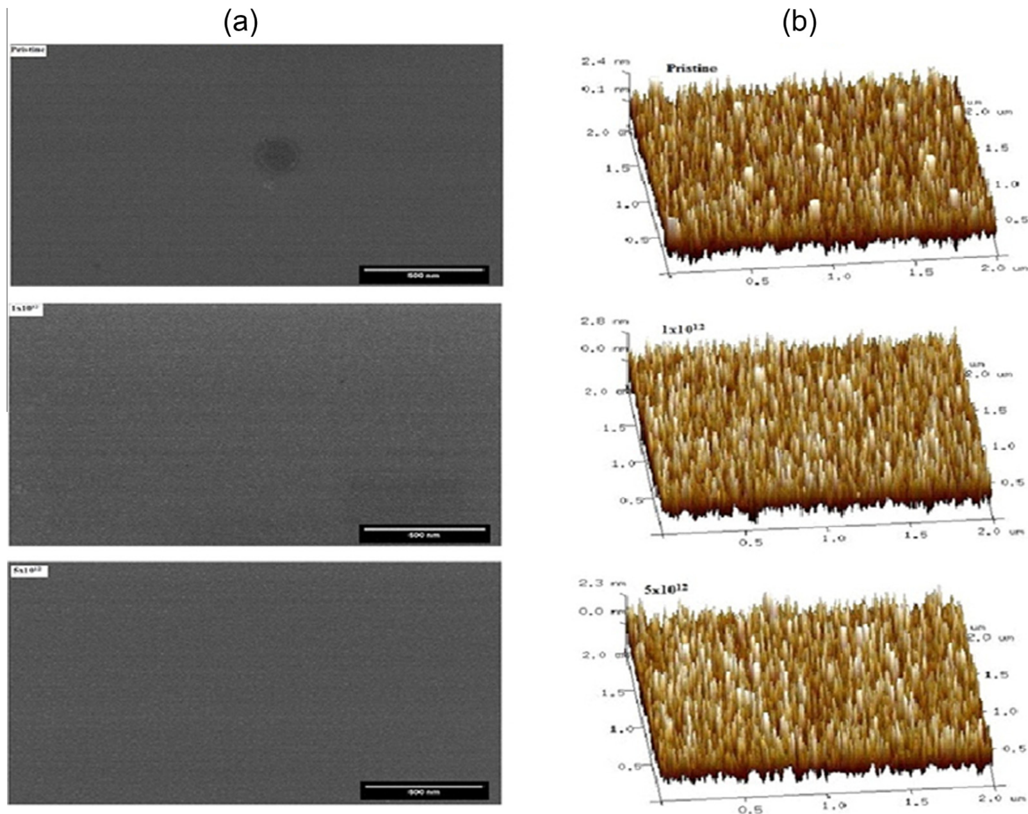

Fig. 4. The images of SnO_2/Ag/SnO_2 pristine and irradiated films (a) SEM, and (b) AFM.

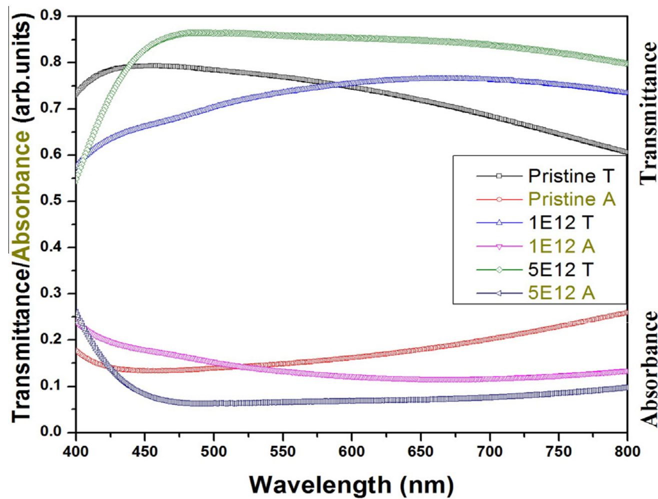

Fig. 5. Transmittance and absorbance spectra of SnO_2/Ag/SnO_2 pristine and irradiated films.

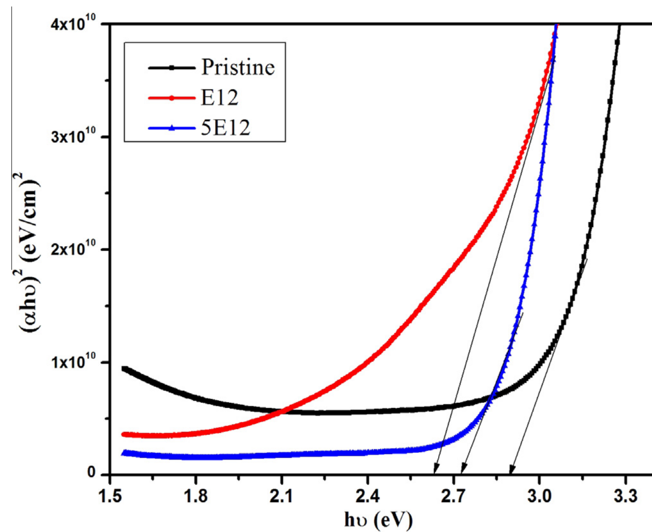

Fig. 6. Tauc plot of SnO_2/Ag/SnO_2 pristine and irradiated films.

mixture of both SnO and SnO_2) is generally expected from e-beam deposition [33]. In our previous work, we have achieved reduced bandgap explained on the basis of X-ray absorption (XAS) and X-ray emision spectroscopy (XES) results [23]. Based on these results, we can infer that the films contain proportionally more SnO compared to SnO_2. On SHI irradiation the multilayer structure shows red shift in absorption spectra which leads to decrease in optical bandgap.

Formation of defects in the tin oxide layer due to irradiation may result in the decrease in optical band gap energy. High energy ion irradiation creates lattice distortion producing defect energy levels below the conduction band in the oxide. At higher fluences the defect levels may be annealed out with the formation of narrow crystallites giving a higher band gap.

3.6. Electrical measurements

Resistivity, carrier concentration and mobility of SnO_2/Ag/SnO_2 thin films measured at room temperature are indicated in Table 1. The Hall measurement result shows that these films have *n*-type behavior. The charge carrier concentration in these samples is quite high but mobility is limited. The sheet resistance of the pristine sample is 200 Ω/□. These electrical properties of SnO_2/Ag/SnO_2 thin film justify the use of the multilayer as an electrode in flat panel display and touch screen applications.

Table 1
Resistivity, carrier concentration, mobility and sheet resistance (R_{sh}) of 100 MeV O^{7+} irradiated SnO_2/Ag/SnO_2 multilayer thin film.

S. No	Fluence (ion/cm^2)	Resistivity (Ω cm)	Carrier concentration (/cm^3)	Mobility (cm^2/v s)	R_{sh} (Ω/□)
1	Pristine	1.6×10^{-3}	4.6×10^{21}	0.85	200
2	1.0×10^{12}	4.1×10^{-3}	1.3×10^{21}	1.2	512.5
3	5.0×10^{12}	6.3×10^{-3}	6.3×10^{20}	1.6	787.5

4. Conclusion

Multilayer thin films of SnO_2/Ag/SnO_2 were fabricated using e-beam and thermal evaporation techniques. The TCE structure was irradiated with swift heavy ions of 100 MeV O^{7+} ions using two different fluences. The electrical properties showed a degradation upon irradiation and smoothing of the film surface with an increase in its transparency. However, as we increase the fluence the transparency decreases with an increase in band gap. It clearly shows that SHI irradiation can be used to modify or tune the properties of these structures on Si and glass substrates.

Acknowledgments

Authors are thankful to M.R.C., MNITJ for various fabrication and characterization facilities used for the present study and IUAC for providing the pelletron facility.

References

[1] K. Ellmer, Nat. Photonics 6 (2012) 809.
[2] C. Zhang, D. Zhao, D. Gu, H. Kim, T. Ling, Y.R. Wu, L.J. Guo, Adv. Mater. (2014), http://dx.doi.org/10.1002/adma.201306091.
[3] C. Guillén, J. Herrero, Thin Solid Films 520 (2011) 1.
[4] A. Dhar, T.L. Alford, APL Mater. 1 (2013) 012102.
[5] L. Cattin, M. Morsil, F. Dahou, S. Yapi Abe, A. Khelil, J.C. Bernede, Thin Solid Films 518 (2010) 4560.
[6] D. Zhang, H. Yebe, E. Akita, P. Wang, R. Murakami, J. Appl. Phys. 109 (2011) 104318.
[7] I. Crupi, S. Boscarino, V. Strano, S. Mirabella, F. Simone, A. Terrasi, Thin Solid Films 520 (2012) 4432.
[8] D.K. Avasthi, G.K. Mehta, Swift Heavy Ions for Materials Engineering and Nanostructuring, 145, Springer, 2001, p. XII, 280.
[9] D. Dimaria, D. Kerr, Appl. Phys. Lett. 27 (1975) 505.
[10] G. Carter, M. Nobes, I. Katardjiev, J. Whitton, Def Diff Forum 57 (58) (1988) 97.
[11] O. Tuzuna, S. Altindalb, S. Oktika, Renewable Energy 33 (2008) 286.
[12] Y.H. Tak, K.B. Kim, H.G. Park, K.H. Lee, J.R. Lee, Thin Solid Films 411 (2002) 12.
[13] H.K. Singh, D.K. Avasthi, S. Aggarwal, Nucl. Instrum. Methods Phys. Res. B 353 (2015) 35.
[14] M. Levalois, P. Marie, Nucl. Instrum. Methods Phys. Res. B 156 (1999) 64.
[15] K.M. Abhirami, P. Matheswaran, B. Gokul, R. Sathyamoorthy, D. Kanjilal, K. Asokan, Vacuum 90 (2013) 39.
[16] K.M. Abhirami, P. Matheswaran, B. Gokul, R. Sathyamoorthy, K. Asokan, Appl. Phys. A 111 (2013) 1175.
[17] S. Rani, S.C. Roy, N.K. Puri, M.C. Bhatnagar, D. Kanjilal, J. Nanomater. 2008 (2008) 395490.
[18] R.S. Chauhan, V. Kumar, D.C. Agarwal, D. Pratap, I. Sulania, A. Tripathi, Nucl. Instrum. Methods Phys. Res. B 286 (2012) 295.
[19] A. Sharma, K.D. Verma, M. Varshney, D. Singh, M. Singh, K. Asokan, R. Kumar, Rad. Eff. Def. in Solids: Incorp. Plas. Sci. Plas. Tech 165 (2010) 930.
[20] V.S.K. Chakravadhanula, Y.K. Mishra, V.G. Kotnur, D.K. Avasthi, T. Strunskus, V. Zaporotchenko, D. Fink, L. Kienle, F. Faupel, Beilstein J. Nanotechnol. 5 (2014) 1419.
[21] M. Kumar, P.K. Kulriya, J.C. Pivin, D.K. Avasthi, J. Appl. Phys. 109 (2011) 044311.
[22] M. Toofan, J. Toofan, Developments in Surface Contamination and Cleaning Wet and Dry Cleaning Methods, Chapter 5 (2015) 185.
[23] N. Zhou, D.B. Buchholz, G. Zhu, X. Yu, H. Lin, A. Facchetti, T.J. Marks, R.P.H. Chang, Adv. Mater. 26 (2014) 1098.

[24] A. Kar, M.A. Stroscio, M. Dutta, J. Kumari, M. Meyyappan, Semi. Sci. Tech. 25 (024012) (2010) 1.
[25] R.S. Chauhan, V. Kumar, A. Jain, D. Pratap, D.C. Agarwal, R.J. Chaudhary, A. Tripathi, Adv. Mater. Lett. 5 (11) (2014) 666.
[26] Z.R. Li, H. Meng, Organic Light-Emitting Materials and Devices, CRC, Boca Raton, 2007.
[27] M. Gaidi, A. Hajjaji, R. Smirani, B. Bessais, M.A. El Khakani, J. Appl. Phys. 108 (2010) 063537.
[28] S. Das, V. Jayaraman, Prog. Mater. Sci. 66 (2014) 112.
[29] C. McGuinness, C.B. Stagarescu, P.J. Ryan, J.E. Downes, D. Fu, K.E. Smith, R.G. Egdell, Phys. Rev. B 68 (2003) 165104.
[30] R. Summitt, J.A. Marley, N.F. Borrelli, J. Phys. Chem. Solids 25 (1964) 1465. Pergamon Press.
[31] H.J. Lee, J.W. Kang, S.H. Hong, S.H. Song, S.J. Park, A.C.S. Appl. Mater. Interfaces 8 (2016) 1565.
[32] A. Indluru, T.L. Alford, J. Appl. Phys. 105 (2009) 123528.
[33] V. Sharma, R. Vyas, P. Bazylewski, G.S. Chang, K. Asokan, K. Sachdev, RSC Adv. 6 (2016) 29135.